Structural and spectroscopic characterisation of Cytochrome *c'* and Cytochrome P460 from *Methylococcus capsulatus* (Bath)

Hannah Ruth Adams

A thesis submitted for the degree of PhD Biological Sciences

School of Life Sciences

University of Essex

September 2023

Abstract

Many Ammonia-oxidising nonlithotrophic bacterium (ANB) and Ammonia oxidising bacteria (AOB) have been shown to contain two phylogenetically related cytochromes: a cytochrome P460 and a cytochrome *c'*-β. Cytochrome P460s (so named due to their 460 nm peak in the ferrous state) are enzymes known to convert hydroxylamine to nitrous oxide, a key step in the metabolism of ammonia in bacteria which is considered to be one of the largest sources of nitrous oxide in the environment. Cytochromes *c'*-β are so called as they have spectral properties similar to the better studied *c'*-α but they are predicted to all have a highly beta sheet structure instead of the alpha helixes normally associated with a cytochrome *c'*. Whilst the role of Cytochrome *c'*s has not been definitively proved it has been proposed that they are involved in NO scavenging and protecting cells against nitrosoative stress. P460s have been well studied in AOB but less so in ANB, whilst very few members of the cytochrome *c'*-β have been characterised at all.

This thesis focusses on the cytochrome P460 and *c'* from *Methylococcus capsulatus* (Bath) characterising their structural and spectroscopic properties through the use of cryogenic single crystal X-ray crystallography and UV-visible and EPR spectra, along with kinetic studies and activity assays, on both the wt proteins and single point mutants, to investigate how structural differences in the distal heme pockets for two proteins with very similar overall protein folds can give rise to two very different functions.

Acknowledgments

There are so many people, without whom, I would not have been able to do this PhD and so owe my thanks to. There is however one person in particular who I wish to dedicate this whole body of work to: My Dad. My whole life you always pushed me to do my best and gave me so much love and support, even when you didn't necessarily agree with my choices or decisions. I wish you could have been here to see me complete it, but I will have to take solace in the fact that you at least saw me start and knew I'd see it through to finally beat you in being the most qualified in the family (though I think we all know you probably still won really). So, I finally did it. It may have taken eight years and a fair amount of (fairly literal) blood, sweat and tears but here it is. I always said I'd have my PhD and you always pushed me to keep going. So, this is for you Dad.

To my family: thank you for all your support, both physically and emotionally over the course of my studies. I couldn't have done this without all your help. My husband Sean: Thank you for your patience and support and for simply putting up with me over the last 8 years of studying. Also, for listening to me ramble on about proteins and scientific techniques I know you have no understanding of and for encouraging me to explain what I study to people after I've had a few drinks! My mum and my brother David: For your never-ending support and for constantly attempting to understand what I'm going on about and asking me lots of questions. I couldn't have made it through the last eight years without all your love and support.

My closest friends for believing in me and putting up with me when I was stressed – Steve: I miss our chats over a few (too many) beers, your support and advice was invaluable and greatly missed, Rob: You've always put up with so much from me and just given me wine and support in return. Juhi: For being my little bit of sanity at Essex.

The many members of the lab I've worked with whilst doing my PhD, thank you all for the advice and support over the years. In particular I'd like to thank: Marina: for both your friendship and scientific knowledge, Ryan: for your entertainment in the lab (though I do not miss your singing!), Ricky: You are the SDM King! and Demet: for teaching me so much and being very patient with me when I first started on my PhD. My fellow technicians in the department - I have had so much support from you all which I am grateful for, but especially Amanda: I don't think any student here could make it through their PhD without you, you really are the core to Core Services, but also thank you for simply being my friend. Mike Wilson: thank you for your assistance with all the kinetics studies and for the many hours of trying to explain it all to me. Your passion for science is infectious and it has been a privilege and a pleasure to be able to work with you. Dima: for all your help with the EPR and trusting me enough to run the samples on my own! Marcus: for putting up with me dropping by your office for a 'quick' chat whenever I needed someone to bounce an idea off of or just vent when things weren't going as expected.

Finally, I would like to thank my supervisors. Jonathan: Thank you for taking over my supervision for the last part of my PhD. I really appreciate you taking the time to support me through the final stages of my lab work (making sure I wasn't starting yet another new experiment!) and whilst I was writing this thesis. Mike: Thank you for agreeing to take a chance on me all those years ago. When I asked to be more involved in the research in the lab, I don't think I had really imagined what the project you offered me was going to turn into. Turning that little side project into a full-blown PhD project has changed my life and given rise to opportunities that I otherwise would not have had. I will be forever grateful for this. Thank you also for your continued support and advice after moving to DLS, I certainly could not have completed this PhD without it.

Table of Contents

Table of Figures

Figure 4.19. Distal heme pockets of K78R *Mc*P460 mutant and *c'*β^{-Met} from *N. europaea.*

Figure 4.20. Accessibility of the heme in wt *Mc*P460, computer generated simulation of R43A mutant and *Ns*ALP460.

Figure 4.21. Proposed proton relay from the heme of *Mc*P460 to the surface of the protein.

Table List

Chapter One

Introduction

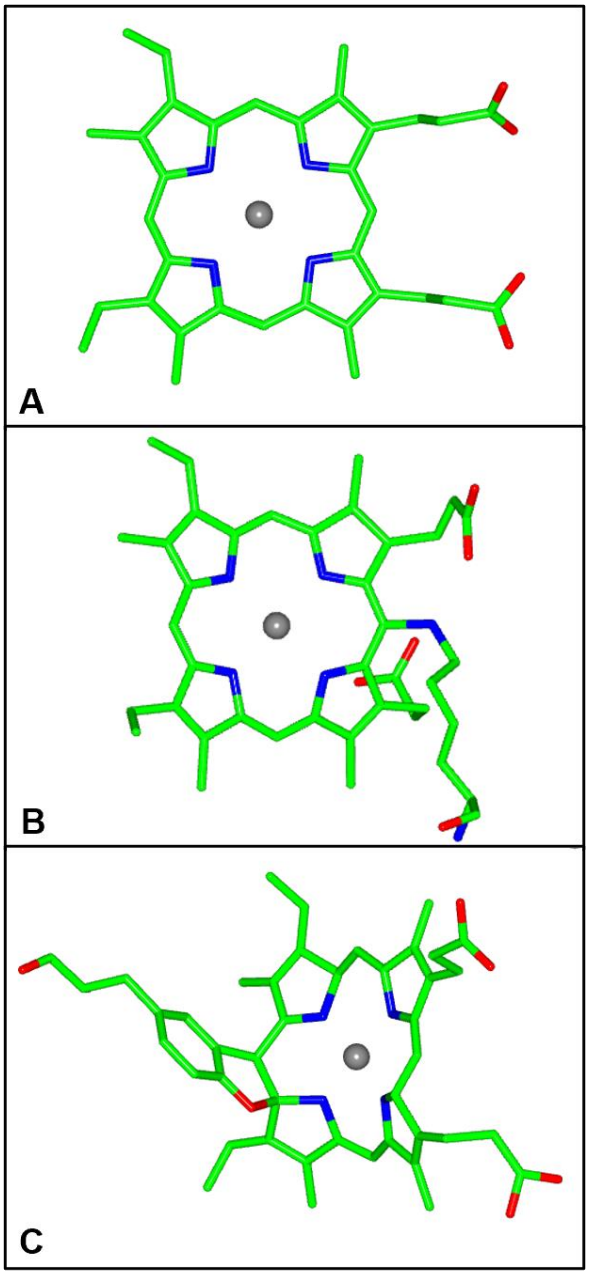

Figure 1. Hemes of cytochrome *c*' (A), cyt P460 (B) and P460 centre of HAO (C).

1.1 Bacterial Nitrification

The increase in human industrialisation and farming has had great benefits, such as the ability to produce greater amounts of crops and meat to feed more people. However, it has also had a massive impact on the balance of the global nitrogen cycle. The nitrogen cycle involves many different microorganisms whose enzymes are involved in different catalytic conversions of nitrogen compounds (Figure 1.1). For example, nitrogen fixing bacteria such as *Azotobacter*, *Rhizobium* and *Bradyrhizobium* contain nitrogenases which are able to transform dinitrogen gas into ammonium which makes nitrogen biologically available to other microorganisms (Kuypers, Marchant and Kartal, 2018). The human contribution of fixed-N to the worlds terrestrial ecosystem is believed to be more than double that of natural processes (Rockström *et al.*, 2009). The result of this includes, but is not limited to, an increased release of nitric and nitrous oxides, the enrichment of freshwater and coastal ecosystems from nitrate rich run offs resulting in increased algal and phytoplankton growth, acidification of soils, streams and lakes, and the acceleration of nitrification. A better understanding of the processes involved in each step of the nitrogen cycle is essential to allow us to produce new policies to minimise further excess production of nitric and nitrous oxides, limit the damage done to the natural environment and possibly discover ways to reverse the damage that has been already done.

Nitrous oxide (N_2O) is a potent ozone depleting greenhouse gas with a global warming potential nearly 300-fold greater than carbon dioxide. Atmospheric levels of N_2O have increased greatly due to the widespread use of fossil fuel combustion, nitric acid production and biomass burning, but mostly due to the use of fertilisers in agriculture. It is estimated that 30 % of the N_2O in the atmosphere is the result of human activity.

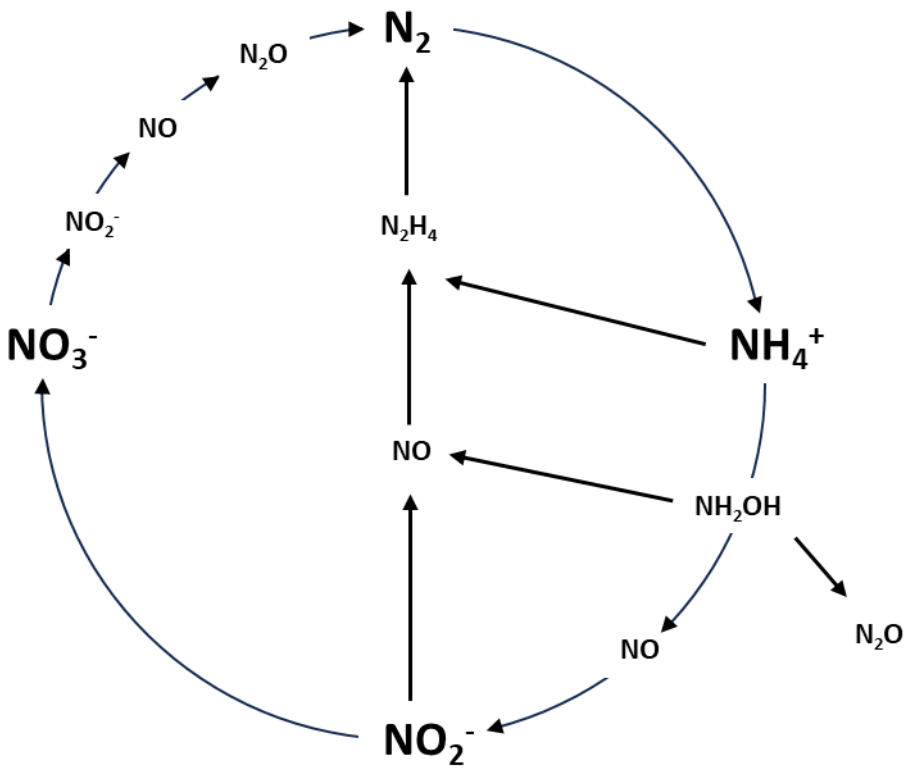

Figure 1.1. Schematic of the basic compounds of the Nitrogen Cycle.

Microbial metabolism, as a response to modern agricultural methods and the fixed-N saturation of the environment, is the largest producer of nitrous oxide. (Wuebbles, 2009) Ammonia oxidising bacteria (AOB) are proposed to emit nitrous oxide (N_2O) either as a by-product of the nitrification pathway or the product of the nitrifier denitrification pathway through the metabolism of ammonia (NH_3). This process is well studied within AOB but less so in Ammonia-oxidising nonlithotrophic bacterium (ANB), a group of organisms known to aerobically oxidise ammonia to nitrite but that do not use this as their source of energy (Trotsenko and Murrell, 2008; Soler-Jofra, Pérez and van Loosdrecht, 2021). The first step in the process is where ammonia is converted to hydroxylamine by either ammonia monooxygenase (AMO) in ammanox bacteria or methane monooxygenase (MMO) in

methanotrophic bacteria. Hydroxylamine is then converted to nitric oxide and nitrite by hydroxylamine oxidoreductase (HAO) or cytochrome P460 (P460). Nitrite reductase (NIR) reduces nitrite to nitric oxide which can be reduced to nitrous oxide by nitric oxide reductase (NOR) or cytochrome P460 (Figure 1.2).

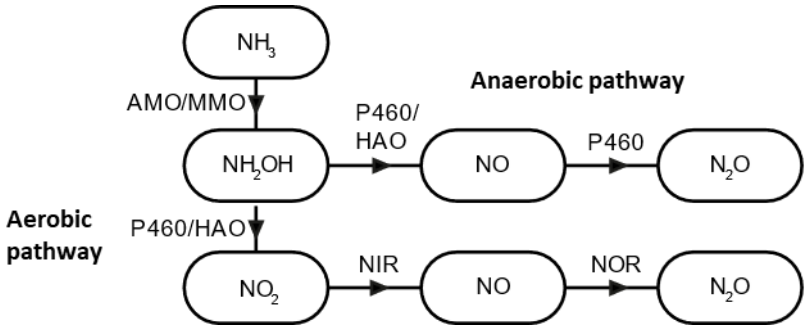

Figure 1.2. Schematic demonstrating pathways for N_2O production from NH_3 and the enzymes involved. Ammonia is converted to hydroxylamine by ammonia monooxygenase (AMO) or methane monooxygenase (MMO). Hydroxylamine is converted to nitric oxide and nitrite by hydroxylamine oxidoreductase (HAO) or cytochrome P460 (P460). Nitrite reductase (NIR) reduces nitrite to nitric oxide. Nitric oxide can be reduced to nitrous oxide by nitric oxide reductase (NOR) or cytochrome P460. The production of either N_2O or NO_2 by cytochrome P460 depends on whether the conditions are anaerobic or aerobic.

1.2 *Methylococcus capsulatus* (Bath), an ammonia-oxidising nonlithotrophic methanotroph.

Methylococcus capsulatus (Bath) is an obligate methanotroph or methane oxidising bacteria (MOB) meaning it utilises methane as its sole source of carbon and energy (Nazaries *et al.*, 2013) The use of methane monooxygenases to catalyse the oxidation of methane to methanol is one of the defining characteristics of methanotrophs. Methanotrophs can be divided into 3 types depending on the pathways used for the assimilation of formaldehyde, an intermediate in the catabolism and anabolism of methanotrophs (Hanson *et al.*, 1991). 'Type I' methanotrophs use the ribulose monophosphate (RuMP) pathway and include the genera *Methylomonas* and *Methylobacter* and 'type II' methanotrophs use the Serine pathway and include the genera *Methylosinus* and *Methylocystis.* 'Type X' also use the RuMP pathway for formaldehyde assimilation however they are distinguished from 'type I' methanotrophs because they also possess low levels of enzymes of the serine pathway. They also grow at higher temperatures than type I and type II methanotrophs and possess DNA with a higher percent G/C content than that of most type I methanotrophs (Zahn, Duncan and DiSpirito, 1994) (Whittenbury and Dalton, 1981). *Methylococcus capsulatus* (Bath) therefore is classified as a 'type X' methanotroph as it uses the RuMP pathway whilst growing at a higher temperature and having a higher G/C DNA content than most 'type 1' methanotrophs. *Methylococcus capsulatus* (Bath) is however also an ammonia-oxidising nonlithotrophic bacterium which contains cytochrome P460 (*Mc*P460), hydroxylamine oxidoreductase (*Mc*HAO) and a cytochrome *c'* (*Mc*CP) (Zahn, Duncan et al. 1994).

1.3 Cytochromes: An Overview

Cytochromes are heme containing proteins that are found in a wide range of bacterial, plants and animal cells. They can be classified into types a, b, c and d (depending on the heme group they contain), of which the c type cytochromes are believed to make up at least half of the known heme proteins (Paoli, Marles-Wright and Smith, 2002)

Proteins containing heme groups were first studied as far back as the 1850's and have since continued to be of keen interest to researchers due to their functional diversity and presence in a wide range of organisms from bacteria to humans. This diverse range of biological functions ranges from the transfer and storage of oxygen (haemoglobin and myoglobin), to transcriptional regulation (Paoli, Marles-Wright and Smith, 2002) (Sun *et al.*, 2002), (Mense and Zhang, 2006), to microRNA processing (Weitz *et al.*, 2014) and electron transfer (eg CYT c (Paoli, Marles-Wright and Smith, 2002)). The large range of functions of heme proteins is due to differences in both the proteins and the heme group itself, which depends on the nature of the substituents on the porphyrin macrocycle (Bowman and Bren, 2008). This includes factors such as the distribution of polar and charged groups around the heme environment, the extent to which the heme is buried within the protein, solvent accessibility to the heme, the number and nature of protein donated axial ligands to the heme and the degree of structural rearrangement upon ligand binding (Paoli, Marles-Wright and Smith, 2002) (MacMunn, 1884) (Li, Bonkovsky and Guo, 2011).

Heme (iron protoporphyrin IX) consists of four pyrrole rings with a central iron atom. It is characterised by the linkage of four β - pyrrole rings by methylene bridges with the iron coordinated by four nitrogen atoms of the porphyrin ring. There are six different types of heme group (*a, b, c, d, f* and *o* type), with *a, b, c* being the most common (Figure 1.3). Heme containing proteins are classified depending on which of these heme groups they contain.

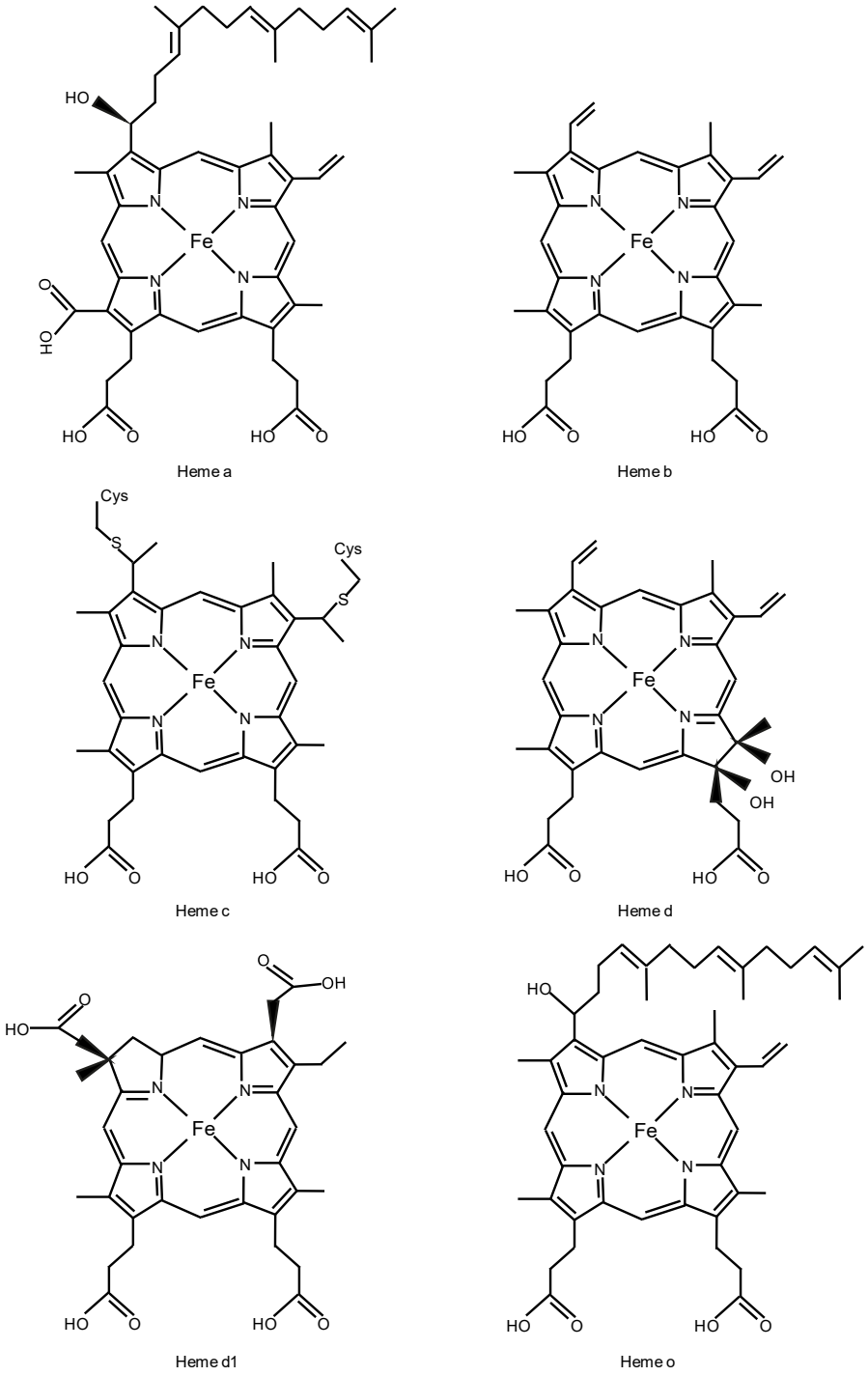

Figure 1.3. Bacterial heme types. Heme *a* (A), heme *b* (B), heme *c* (C), heme *d* (D), heme *d1* (E), heme *o* (F) (Adapted from (Liu *et al.*, 2014))

Cytochromes c (Cyts c) were first discovered in 1884 by Charles MacMunn (MacMunn, 1884). In 1925 they were rediscovered by David Keilin who described their function in the electron transport chain (Keilin, 1925).

Cytochromes c, which all contain a c-type heme, are traditionally divided into four classes depending on the type and number of hemes present, the position and identity of axial ligands and the reduction potentials they have (Figure 1.4) (Ambler, 1991).

Class I Cyts c are α-helical in structure and have a mono heme at the N-terminus which is bound to the axial His ligand by its fifth coordination site. The second axial ligand is often a Met but can also be His or Asn (Klarskov *et al.*, 1998) or be absent. They also display a wide range of reduction potentials from -390 to +450 mV (Liu, Chakraborty et al. 2014). The Class I Cyts c can be further divided into 16 subgroups which includes cytochrome c_2 from *Rhodopila globiformis* (Benning, Meyer and Holden, 1996) and mitochondrial Cyt c which has been confirmed to have a role in apoptosis by regulating the activation of caspases, the key components of apoptosis in eukaryotic cells (Liu *et al.*, 1996).

Class II Cyts c contain a mono heme which is bound to the C terminus by a fifth axial His residue and via thioether bonds to two Cys residues. Their structure consists of an antiparallel α-helical bundle. The reduction potentials of the Class II Cyts c range from -200 to +200 mV. They can be further divided into Class IIa and Class IIb depending on their heme-iron spin states. The Class IIa Cyts c include the high spin cytochromes *c'* (Cyt *c'*) such as those from *Chromatium vinosum* (*Cv*CP) and *Rhodobacter capsulatus* (*Rc*CP), whilst Class IIb includes low spin Cyts *c'* such as *Rhodospirillium molischianum* (*Rm*CP).

Class III Cyts c have multiple hemes with bis-HIS ligation and have reduction potentials ranging from -20 to -380 mV. Their structures are unlike any other Cyts c, consisting of two β-sheets and three α-helices.

Class IV Cyts c have multiple hemes with either His-Met ligation or bis-His ligation and are typically large in size (35-40 kDa). An example of Class IV Cyts c are flavocytochromes c which also contain other prosthetic groups (Liu *et al.*, 2014).

As more c type cytochromes are being identified and characterised it is however becoming clear that these traditional classifications do not always fit and new classes and types may be needed to more accurately classify this group of cytochromes. Cytochrome P460 and *c'*-β are both good examples of this as they have characteristics which could allow them to be defined as Class II (such as having a mono, C terminus heme and HS spin states) whilst their β-sheet structures would occlude them from the same Class (Figure 1.4).

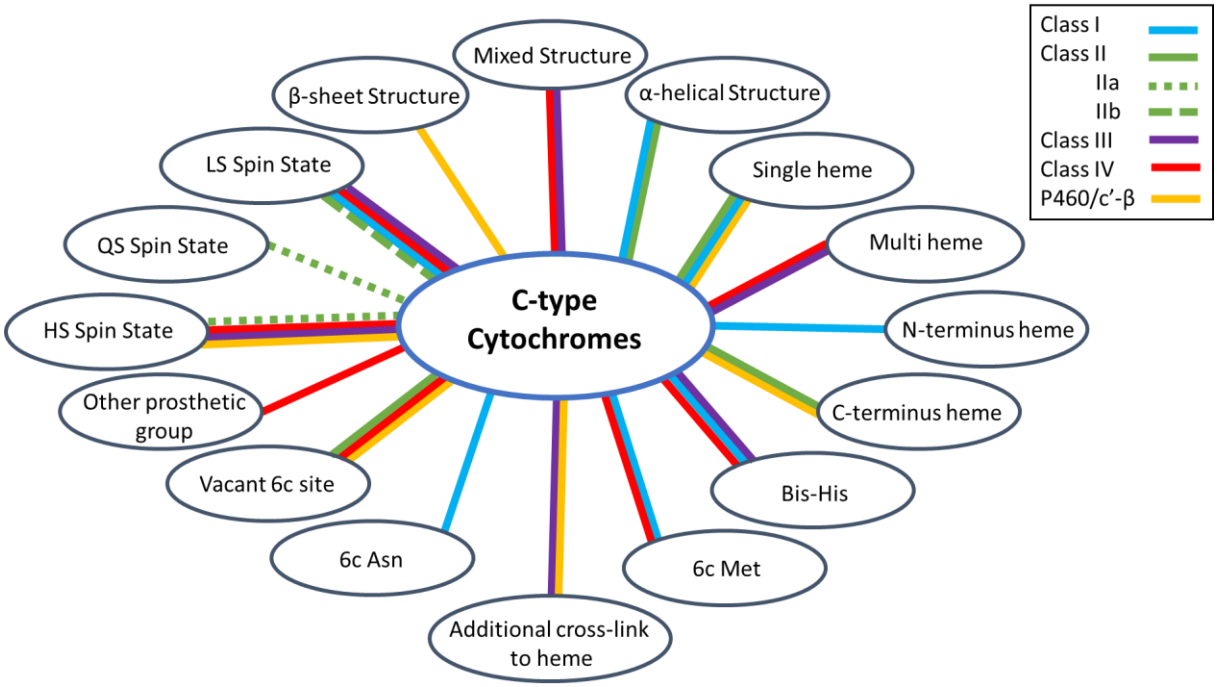

Figure 1.4. Classification of c-type cytochromes. Cytochromes c are traditionally put into four different classes based on the type and number of hemes present, the position and identity of axial ligands and the reduction potentials they have. Some c type cytochromes such as P460 and c'-β however cannot be classified in this manner as they have characteristics which occlude them from each group.

1.4 Cytochrome *c'* α and β

Cytochromes *c'* were first discovered by Vernon and Kamen in 1954 (Kamen and Vernon, 1954) in purple photosynthetic bacteria, who referred to it as pseudohaemoglobin. They are now known to be present in the periplasm of a wide range of denitrifying, methanotrophic, sulphur oxidising, nitrogen fixing and photosynthetic bacteria (Ambler, 1991), (Ambler *et al.*, 1981), (Watmough *et al.*, 1999). The precise biochemical or physiological role of any cytochrome *c'* is yet to be determined despite their widespread occurrence in nature, however roles such as cellular defence against nitrosoative stress and in nitric oxide trafficking have been proposed (Yoshimura *et al.*, 1988), (Yoshimura *et al.*, 1993), (Hough and Andrew, 2015), (Cross *et al.*, 2000).

The crystal structure of *Rhodospirillum molischianium* cytochrome *c'* (*Rm*CP) at 1.67 Å resolution was the first cytochrome *c'* structure to be characterised (Weber *et al.*, 1980). The structure revealed the monomer to be a left-handed, antiparallel, elongated 4 α-helical bundle connected by several short loops. The overall shape of the monomer is that of a truncated cone, with the four helices packing closely together at the top, and being forced further apart at the bottom to accommodate the heme, as the conserved CXXCH haem motif is located towards the c-terminus of the protein sequence and the bottom of the cone (Hough and Andrew, 2015) (Figure 1.5). Further crystal structures demonstrated that whilst the sequence identity in cytochromes *c*' is quite low (Dobbs *et al.*, 1996), (Ambler *et al.*, 1986) the monomeric structure is highly conserved.(Dobbs *et al.*, 1996), (Kekilli *et al.*, 2014), (Tahirov *et al.*, 1996), (Ramirez *et al.*, 2003), (Shibata *et al.*, 1998), (Benini *et al.*, 2008), (Yasui *et al.*, 1992), (Benini *et al.*, 2008), (Manole *et al.*, 2015), (Hirano *et al.*, 2012).

Cytochromes *c'* are known to exist as homodimers, monomers or occupying a monomer/dimer equilibrium state and thus the cytochromes *c'* have been classified into different 'types' based on their interface properties (Weber *et al.*, 1980), (Finzel *et al.*, 1985).

‘Type 1’ cytochromes *c’* demonstrate an X shaped pair of monomers, where helices A and B from each monomer are involved in an extensive interface largely made up of hydrophobic residues. The ‘type 2’ cytochromes *c’* have a greater propensity towards dimer dissociation and are much more diverse in their interface interactions than the ‘type 1’ cytochromes *c’*. They tend to have a much higher amount of charged and hydrophilic residues in the A/B helices interface than the ‘type 1’ cytochromes *c*’ resulting in the monomers lying near parallel to each other. Other cytochromes *c’* demonstrate interface properties intermediate between type 1 and 2 such as *Rhodobacter sphaeroides* (*Rs*CP) within which a flattened X shaped dimer occurs. Cytochromes *c’* can also be categorised into two structural groups (Tahirov *et al.*, 1996). In group 1 cytochromes *c’* (*Rc*CP, *Cv*CP) the subunits are folded in such a way to create a deep channel between the helices creating direct solvent accessibility to the haem distal pocket. Group 2 cytochromes *c’* (*Rhodospirillum rubrum* (*Rr*CP), *Alcaligenes xylosoxidans* (*Ax*CP), *Rm*CP) do not have this channel restricting solvent accessibility.

Cytochromes *c’* have been shown to bind small gaseous ligands such as CO and NO. CO has been shown to bind with a 6-coordinate geometry to the distal face of the heme whilst NO has been shown to bind with either 6cNO and/or 5cNO depending on the organism and sample conditions (Antonyuk *et al.*, 2011), (Hough *et al.*, 2011), (Lawson *et al.*, 2003). *Chromatium vinosum* cytochrome *c’* (*Cv*CP) and *Rhodobacter capsulatus* cytochrome *c’* (*Rc*CP), for example, both have a mixture of 5cNO and 6cNO at around pH 7, whilst *Ax*CP only has a transient 6cNO as a precursor to its proximal 5cNO product and *Sf*CP only appears to show 5cNO (Hough and Andrew, 2015). For most *c’*-αs the 5cNO form appears to predominate at equilibrium at all published pH. Whilst *c’*-αs tend to show predominately 5cNO geometry, most heme proteins actually retain a 6cNO geometry due to conformational constraints of the protein scaffold that help retain the endogenous (His) protein ligand. This

5cNO complex has been shown to occur on the proximal heme face in place of the endogenous His ligand via a series of distal NO complexes (Kekilli *et al.*, 2017). This distal to proximal switch is due to various different factors including: the steric constraints imposed by the residues in the distal pocket which lie close to the heme (Andrew *et al.*, 2001), (Andrew *et al.*, 2005); solvent accessibility to the distal face of the heme and the flexibility of the distal site residues to undergo structural rearrangements (Andrew *et al.*, 2005).

Analysis of samples during purification of *Mc*P460 (Zahn, Duncan and DiSpirito, 1994), using spectral and electrophoretic methods, demonstrated the separation of three other proteins from cytochrome P460 preceded a UV-visible spectral shift from 460 nm in cell extracts to 450 nm in the purified sample. These were two non-heme containing proteins (61.2 kDa and 26 kDa) and a cytochrome *c'*. The properties of this cytochrome *c*' were described in 1996 by Zahn et al (Zahn *et al.*, 1996). The protein was shown by electron paramagnetic resonance spectra to have a high spin, S = 5/2, heme centre and the UV-visible spectra of the ferric and ferrous protein were characteristic of cytochromes *c*'. However, the redox potential was found to be much lower than any other known cytochrome *c*' (E_{m7} = -205 mV).

The amino acid sequence of *Mc*CP showed very low sequence similarity (6-11 %) to other known cytochromes c' (Bergmann, Zahn and DiSpirito, 2000), but when compared to the sequences of cytochrome P460 from both *M. capsulatus* and *N. europaea* a higher level of similarity was found (31 % and 18 % respectively). It was postulated that this high sequence similarity indicated an evolutionary relationship between the cytochrome *c*' of *M. capsulatus* and cytochrome P460. Further sequence analysis (Elmore *et al.*, 2007) has supported this hypothesis of an evolutionary relationship and a new 'family' of cytochromes. Furthermore, using secondary structure prediction tools, all the members of this new 'family' were predicted to have a highly beta sheet structure in contrast to the typical alpha helical

structure of all other known cytochromes *c'* leading to these being referred to as cytochromes *c'*-β.

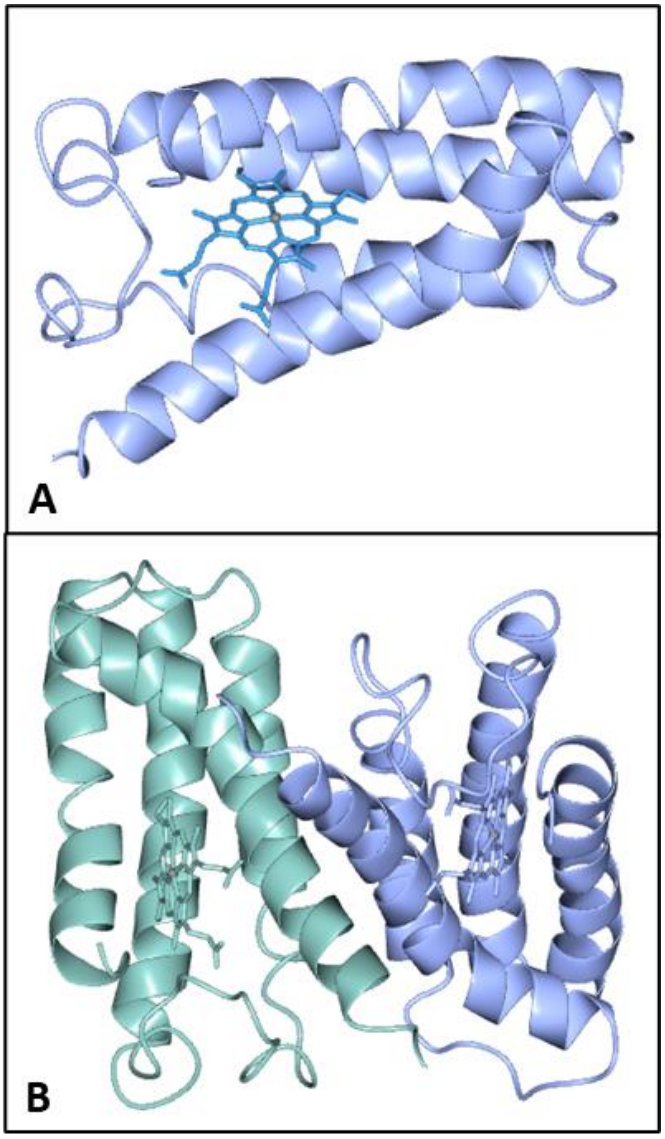

Figure 1.5. The crystal structure of *Rhodospirillum molischianium* cytochrome *c'* (2CCY) at 1.67 Å, the monomer demonstrating the left-handed, antiparallel, elongated 4 α-helical bundle connected by several short loops (A) and the homodimer of *Rm*CP displaying the X-Shaped arrangement typical of 'Type 1' cytochromes *c'*. (B).

More recently another member of the *c'*-β family has been investigated revealing their highly beta sheet structures. The crystal structure of *Thermus thermophilus* cytochrome *c'* (*Tt*CP-β) was reported to 1.74 Å showing an overall highly beta sheet structure (Figure 1.6) very similar to that of *Ne*P460 (Yoshimi *et al.*, 2022). Comparison of the amino acid sequences of *Tt*CP and *Mc*CP suggest a highly conserved distal pocket and overall structure but differences in the homodimeric interface. *Thermus thermophilus* is a thermophilic bacteria, and it is has been suggested these differences may help protect the protein from denaturation at these high temperature.

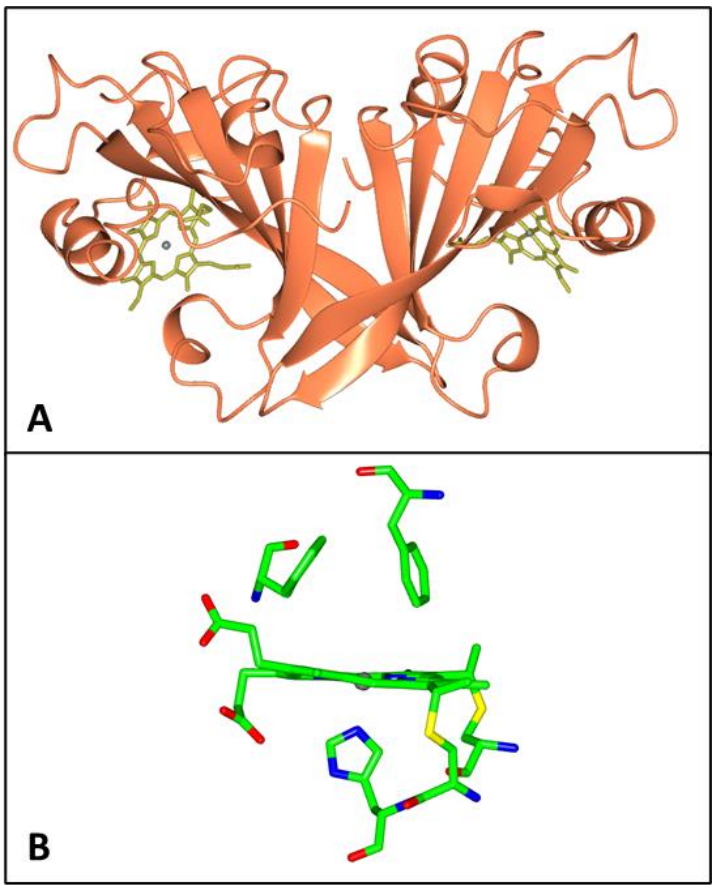

Figure 1.6. The cytochrome *c'*-β of *Thermus thermophilus* (7EAD). Overall structure (A) showing a highly beta sheet structure and heme with two Phe capping residues on the distal side (B).

1.5 Cytochrome P460 and HAO

Cytochrome P460 from *Nitrosomonas europaea* (*Ne*P460) was first discovered by Erickson and Hooper in 1972 (Erickson and Hooper, 1972) and described as a CO binding heme protein with a major absorption peak at 463 nm in the reduced-*minus*-oxidised absorption spectrum, thus resulting in the designation P460. Further research confirmed the spectroscopic characterisation with Soret absorption maxima at approximately 435, 460 and 450 nm in the ferric, ferrous and ferrous-CO forms respectively (Miller David, Wood Paul and Nicholas, 1984) and showed that the heme of P460 was a c-type heme (Numata *et al.*, 1990), (Bergmann and Hooper, 1994). This was further supported by EPR measurements showing that *Ne*P460 had a high spin heme (s=5/2) centre (Caranto, Vilbert and Lancaster, 2016). These unique features of the optical spectra of cytochrome P460 are shared by the 'heme-P460' of hydroxylamine oxidoreductase of *N. europaea* (*Ne*HAO), a homo-trimer of octa-heme subunits (Figure 1.7) which catalyses high rates of dehydrogenation of hydroxylamine (Hooper and Nason, 1965), (Arciero and Hooper, 1993). This second step in the oxidation of ammonia is a critical step in the nitrogen cycle.

The oxidation of hydroxylamine by cytochrome P460 was originally suggested to produce nitric oxide and nitrite under aerobic conditions (Zahn, Duncan and DiSpirito, 1994) however recent work has shown that although nitrite is formed under aerobic conditions, the concentration is not stoichiometric to the concentration of hydroxylamine (Caranto, Vilbert and Lancaster, 2016). Under anaerobic conditions however it was demonstrated that the enzyme uses four oxidising equivalents to convert two equivalents of hydroxylamine to nitrous oxide. This suggests that oxidation of hydroxylamine by cytochrome P460 contributes to nitric oxide and nitrous oxide emissions from nitrifying bacteria (Figure 1.8). The proposed mechanism by which this occurs in *Ne*P460 is as follows: Hydroxylamine binds to the heme of the ferric protein and is oxidised to form an $\{Fe\text{-}NO\}^6$ (in Enemark-Feltham

notation) product via a 6c{Fe-NO}^{7} intermediate. This {Fe-NO}^{6} product then undergoes nucleophilic attack by a second hydroxylamine to produce nitrous oxide and water. The heme is then free to start the cycle over again (Caranto and Lancaster, 2017), (A. Smith *et al.*, 2019), (Smith and Lancaster, 2018). The mechanism of hydroxylamine oxidation in the P460 sub unit of HAO differs slightly from that of cytochrome P460 (Figure 1.8): Whilst in Cytochrome P460 the NO product remains bound for a sufficiently long period of time to allow the production of nitrous oxide, in the P460 subunit of HAO the NO quickly dissociates leading to the production of nitrite by other enzymes instead (Fernández, Estrin and Bari, 2008), (Coleman and Lancaster, 2020).

The cytochrome P460 of *Methylococcus capsulatus* (Bath) was first described in 1994 as an enzyme capable of the oxidation of hydroxylamine to nitrite (Zahn, Duncan and DiSpirito, 1994) The protein was shown to have similar molecular weight, amino acid composition, EPR spectra, enzymatic activities and spectral properties in cell extracts to the cytochrome P460 of *N. europaea*. However, the purified ferrous protein displayed a shift in its UV-visible spectra, with a Soret band of 463 nm in the cell extract to 450 nm in the purified sample. Due to the similarity of the protein to the properties of *N. europaea* cytochrome P460, and the differences to the P450 cytochrome class of proteins, the authors named the enzyme from *M. capsulatus* as a cytochrome P460. Further comparison of the sequences of the *N. europaea* and *M. capsulatus* cytochrome P460 showed little sequence similarity (24.3 % identical residues) (Bergmann *et al.*, 1998) but that there were a few short sections of conserved residues, including the C-terminal CXXCH heme motif and a lysine residue (Lys 78 in *Mc*P460).

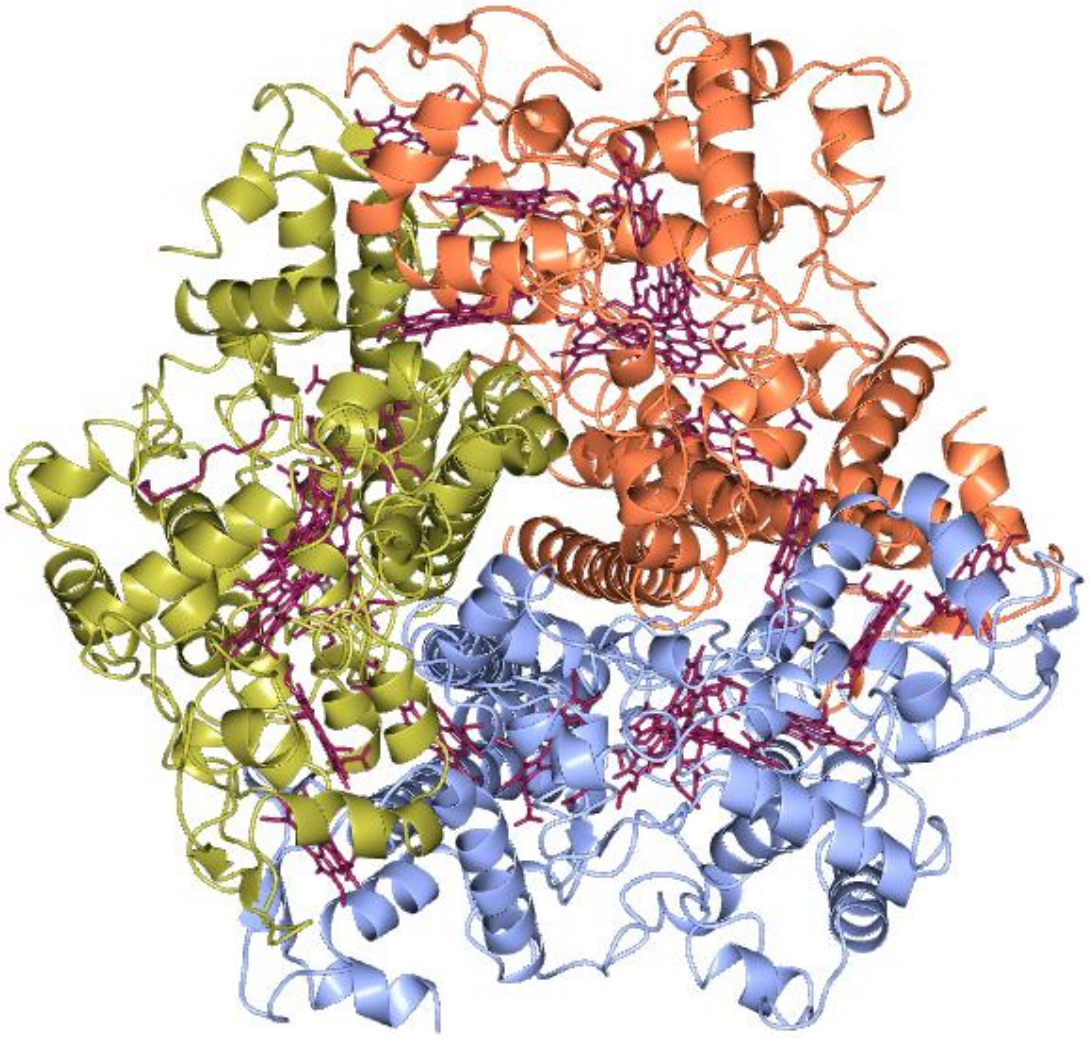

Figure 1.7. *Crystal structure of* hydroxylamine oxidoreductase (HAO) of *N. europaea*, (4FAS) a homo-trimer (with each monomer represented in a different colour). Each subunit contains eight hemes (shown in purple), seven c-type hemes and one P460-type heme.

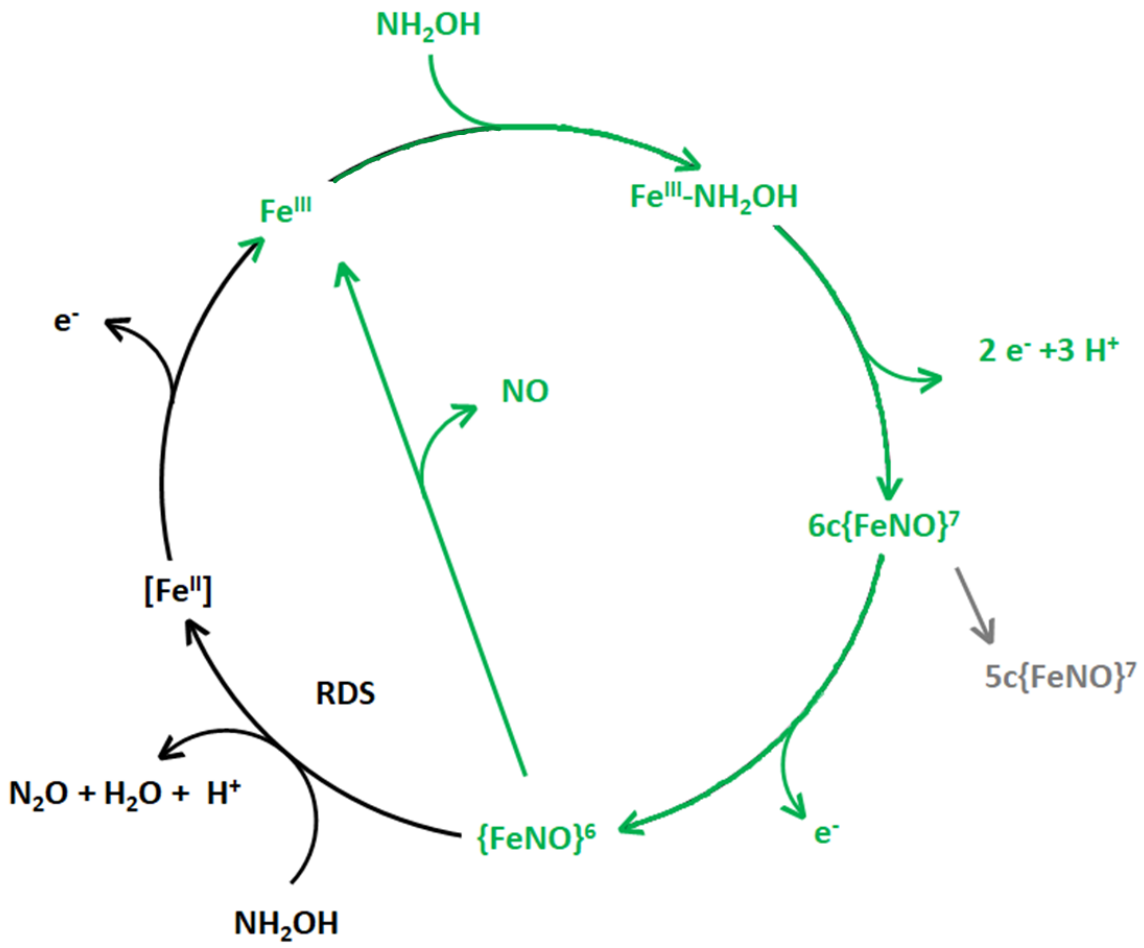

Figure 1.8. Proposed mechanism of oxidation of hydroxylamine by P460s showing key compounds in the catalytic cycle using Enemark-Feltham notation. Steps in black are those which have been observed only in P460 whilst those in red have been observed in both HAO and P460. Grey represents an off-pathway species. Hydroxylamine binds to the heme of the ferric protein and is oxidised to form an {Fe-NO}^{6} product via a 6c{Fe-NO}^{7} intermediate. This {Fe-NO}^{6} product then undergoes nucleophilic attack by a second hydroxylamine to produce nitrous oxide and water. The heme is then free to start the cycle over again. Adapted from Caranto et al 2017.

The crystal structure of *Ne*P460 confirmed the predicted highly beta sheet structure (Arciero and Hooper, 1997), (Pearson *et al.*, 2007), (Elmore *et al.*, 2006), revealing a structure consisting of a twisted five stranded antiparallel β-sheet, three large helices, three helical turns and a short two strand β hairpin (Figure 1.9 A). The structure also demonstrated that in addition to the two cysteine thioether links to the heme typically seen in c-type hemes, there is a third crosslink involving the conserved lysine (Lys 70 in *Ne*P460) as had been previously suggested (Arciero and Hooper, 1997). A further crystal structure of the cytochrome P460 from *Nitrosomonas* sp. AL212 (*Ns*ALP460) was published in 2018 (Smith and Lancaster, 2018) providing a more complete structure as the previous *N. europaea* structure was missing residues predicted to wrap around the heme (Figure 1.9 B). This new structure also demonstrated a slightly different distal pocket with less charged residues present and a single phenylalanine residue above the heme.

Mutant versions of *Ne*P460, where Lys 70 had been changed to either arginine, alanine or tyrosine, demonstrated the importance in the lysine crosslink to the unique optical spectra and catalysis of the protein (Bergmann and Hooper, 2003). It also further demonstrated the evolutionary relationship with the cytochrome *c'*-β as the removal of the crosslink gave rise to spectra more similar to cytochromes *c*' along with a loss of catalytic ability, whilst retaining ligand binding ability. Further spectroscopic characterisation of the proposed mechanism of oxidation of hydroxylamine by cytochrome P460 (C. Vilbert, D. Caranto and M. Lancaster, 2018) has also supported the importance of the crosslink in the catalytic activity of the protein. This work suggested that the Lys-heme crosslink confers a rigidity to the positioning of the P460 heme cofactor in order to avoid the formation of stable off-pathway species. Interestingly the *Ns*ALP460 variant, despite having the lysine crosslink, was shown to be unable to oxidise hydroxylamine suggesting that the crosslink alone is not enough to confer catalytic activity (A. Smith *et al.*, 2019).

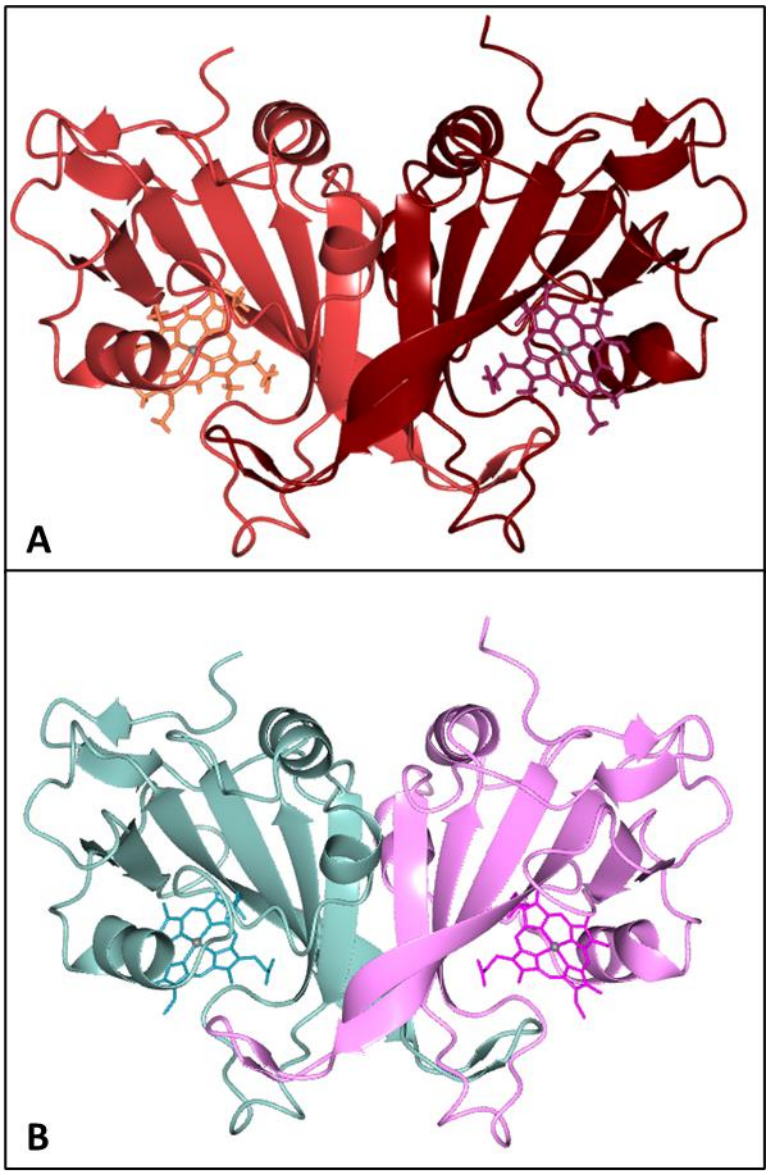

Figure 1.9. Overall crystal structure of N. *europaea* Cytochrome P460 (2JE3) (A) and *Nitrosomonas* sp. AL212 (6AMG) (B) demonstrating the highly beta sheet structure.

The additional covalent link between the porphyrin ring and the protein side chain was also observed for the P460-heme in the 2.8 Å crystal structure of the HAO of *Nitrosomonas europaea* (Igarashi *et al.*, 1997) where a conserved tyrosine residue takes the place of the lysine seen in cytochrome P460 (Figure 1.10 C). This was originally believed to be a single covalent link between a tyrosine-ring c atom and a heme meso C atom as predicted by Arciero and colleagues (Arciero and Hooper, 1993). Later higher resolution structures of *Ne*HAO to 2.1 Å (Cedervall, Hooper and Wilmot, 2013) and *Candidatus Kuenenia stuttgartiensis* HAO to 1.8 Å (Maalcke *et al.*, 2014) demonstrated that there were actually two covalent bonds between the tyrosine and the porphyrin ring with the second being between the C4 atom of the porphyrin ring and the O atom of the tyrosine.

Analysis of the crystal structure of *N. europaea* HAO using normal-coordinate structural decomposition (NSD) showed that the crosslink to the tyrosine induces severe distortion of the heme away from planarity (Figure 1.10) (Fernández, Estrin and Bari, 2008). Normal-Coordinate Structural Decomposition is an analysis method, originally developed (Jentzen, Song and Shelnutt, 1997) to quantify out-of-plane distortions of heme using vibrational normal coordinates. The out-of-plane deformations can be described in terms of six distinct displacements from idealized symmetry (Figure 1.10 A). The most common out-of-plane distortions are doming (a_{2u}), saddling (b_{2u}), and ruffling (b_{1u}). This increased level of ruffling and saddling distortions was also seen, although to a lesser extent, using the same method with the structure of *Nitrosomonas* sp. AL212 cytochrome P460 (Smith and Lancaster, 2018). It has been proposed that properties such as lower reduction potentials (Liptak, Wen and Bren, 2010) and stronger bonding between the Fe and axial ligand (Kleingardner, Bowman and Bren, 2013) are due to an increased level of ruffling within the heme, suggesting that these distortions are important in creating the correct heme environment for the functions of the P460 cytochromes. Research on *Ne*P460 has shown

though, through the production of crosslink deficient mutants, that the crosslink itself is not responsible for the ruffling of the heme. Inspection of the *Ne*P460 distal pocket showed that Arg 44 was in a position to interact with the heme 6-βpyrrolic propionate (M. Bollmeyer *et al.*, 2023). Mutation of this residue to an alanine caused a significant perturbation of the propionate and lowering the heme ruffling by about 7-fold less when compared to the wt *Ne*P460 heme.

Mutation of *Ne*P460 and the *Ns*ALP460 variant have given insights into other residues that may be important in the ability of P460's to convert hydroxylamine to nitrous oxide (A. Smith *et al.*, 2019), (M. Bollmeyer *et al.*, 2023), (Bollmeyer *et al.*, 2023). There are several residues in the distal pocket which are within a close enough distance to the heme to potentially be involved in hydroxylamine oxidation. One of these, glutamate 97 in *Ne*P460 sits over the heme next to the crosslinked lysine. Smith et al noticed that the corresponding residue in the inactive AL212 variant was an alanine residue. Mutating Glu 97 to an alanine removed activity from *Ne*P460, whilst mutating the corresponding alanine in *Ns*ALP46 (Ala 131) to a glutamate residue gave rise to activity in the previously inactive protein. Mutation of Ala 131 to other residues with similar properties (including to the Asp residue that would be present in *Mc*P460) did not confer any activity to the proteins. This suggested that an appropriately placed basic glutamate residue is critical for activity in the Nitrosomonas P460 variants.

Another residue within the pocket of the *Nitrosomonas* P460s which may influence ligand binding is a capping phenylalanine residue. The positioning of this residue has only been confirmed in the inactive Al212 variant, as in *Ne*P460 it is part of the loop that is missing from the crystal structures, however it is predicted to be in relatively the same position in both *Nitrosomonas* P460s. It was demonstrated that this residue has an effect on the turnover rate of hydroxylamine oxidation by creating a Phe to Ala mutant in *Ne*P460

(M. Bollmeyer *et al.*, 2023). The unexpected result was a reduction in the turnover rate leading to the suggestion that this residue helps to control the rate determining step of the reaction by protecting bound NO from the surrounding solvent.

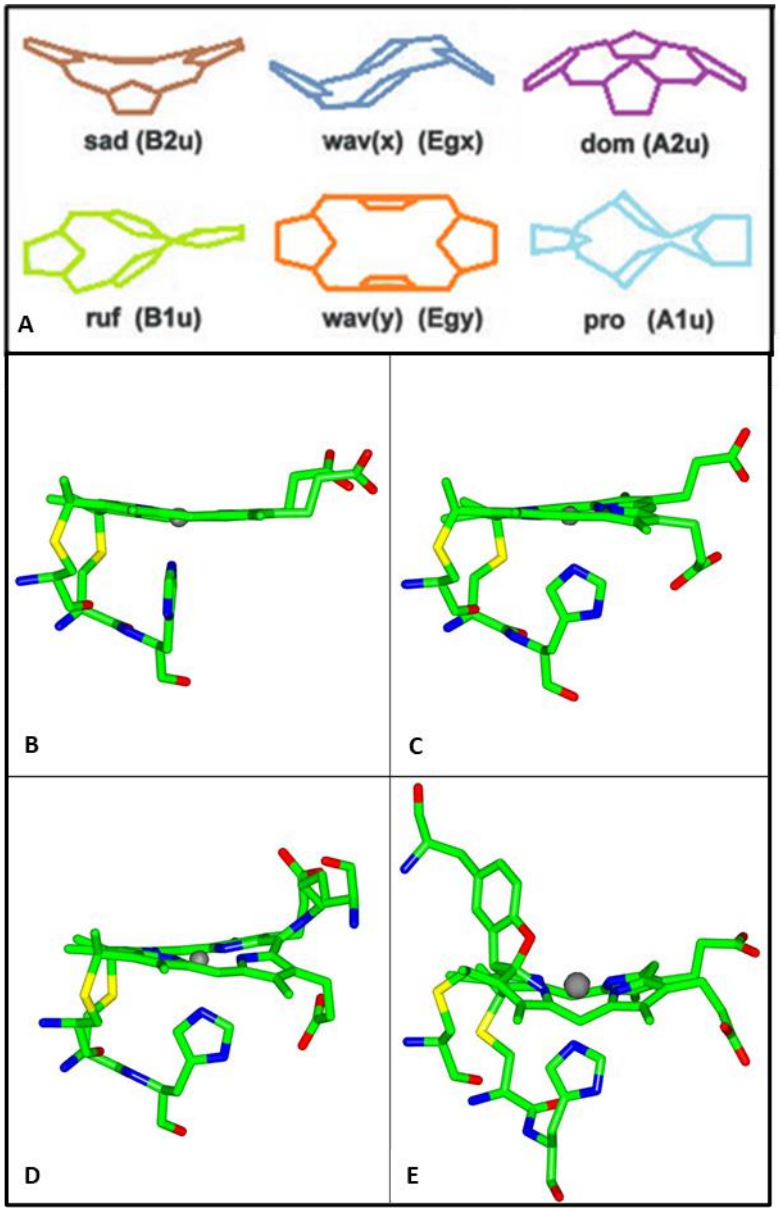

Figure 1.10. Heme Distortions. The different types of distortion of the heme from planarity are shown in panel A. Typical c-type heme of *Shewanella frigidmarina* (4ULV) (B), *c'*-β heme of *Tt*CP (7EAD) (C), the heme of *N. europaea* Cytochrome P460 (2JE3) demonstrating the additional conserved lysine crosslink (D) and the P460 heme of *N. europaea* HAO (PDB 4FAS) showing the conserved tyrosine crosslink (E).

More recently a new member of the cytochrome P460 superfamily has been discovered in *Nitrosomonas europaea*: *c'*β^{-met} (Liew *et al.*, 2020), (Abendroth *et al.*, 2022). This protein has the same overall β-sheet structure as the P460s and *c'*βs, but instead of the lysine crosslink residue there is a methionine residue which sits over the distal face of the heme and an arginine residue in place of the Phenylalanine. There is also a large lasso-like loop on top of the protein and a smaller one nearer to the heme which is not seen in other members of the P460 superfamily. The large loop is hypothesised to be involved in stabilising the dimer of P460 whilst the smaller loop could possibly be involved in both stabilising the protein dimer and involved in accessibility to the heme. Whether *Ne c'*β^{-met} exists as either a monomer or dimer in solution is yet to be determined, although the position of this smaller loop does suggest it should exist as a monomer as residues from the loop would clash if the dimer was formed in a similar manner to other known P460 family members. Further investigation into this should give better insight into the role of these loops and their importance in the dimer formation of the proteins. The changes in the distal pocket residues give rise to a very different potential function of the *c'*-β^{-met} proteins: *Ne c'*β^{-met} is incapable of hydroxylamine oxidation much like the other *c'*-β, most likely due to the lack of the crosslinked lysine residue (Liew *et al.*, 2020). It has however been shown to have low peroxidase activity which has not been previously reported for any other members of the P460 superfamily. In true peroxidases there is a well conserved histidine-arginine pair which are required for catalysis (Dunford, 2010). It is possible that the arginine which is seen to replace part of the Phe-cap acts in a similar manner to allow peroxidase activity in *Ne c'*β^{-met}, however the residue corresponding to the histidine in true peroxidases is yet to be determined. This wide range of different distal pocket residues and ability to bind/turnover different substrates in the P460 family suggests that each subgroup has a very different purpose within its host organism.

1.6 Focus of Thesis

The obligate methantroph and ammonia-oxidising nonlithotrophic bacterium *Methylococcus capsulatus* (Bath) has been shown to contain a cytochrome *c'*, cytochrome P460 and hydroxylamine oxidoreductase. Transcriptomics studies (Poret-Peterson *et al.*, 2008) have shown that both *Mc*HAO and *Mc*CP show increased expression in response to exposure to ammonia, but not *Mc*P460. This strongly suggests a role for *Mc*CP in NO scavenging and protection against nitrosoative stress, for example dealing with NO produced HAO and P460. The lack of up regulation of *Mc*P460 suggests that in *M. capsulatus* (Bath) HAO plays the major role of hydroxylamine oxidation under the conditions used. The process of ammonia metabolism, and more specifically the step of hydroxylamine oxidation has been widely studied in ammonia oxidising bacteria but much less so in Ammonia-oxidising nonlithotrophic bacterium such as *M. capsulatus* (Bath).

This thesis will focus on studying *Mc*CP and *Mc*P460 using a holistic approach of spectroscopic, crystallographic and kinetic techniques to better understand the structural and functional relationship of these proteins.

Chapter 2

Structural, spectroscopic and bioinformatic characterisation of as isolated *Methylococcus capsulatus* (Bath) Cytochrome *c'* and Cytochrome P460.

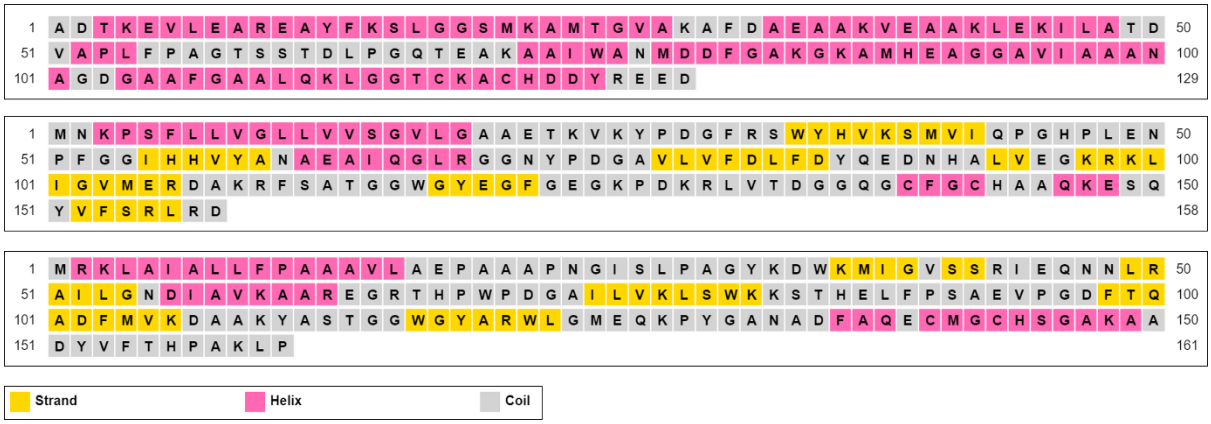

Figure 2. Predicted secondary structure of a typical *c'*-α (*Rc*CP, top), *Mc*CP (Middle) and *Mc*P460 (Bottom).

Results from this chapter have been published in: H.R. Adams, C. Krewson, J.E. Vardanega, S. Fujii, T. Moreno-Chicano, Y. Sambongi, D. Svistunenko, J. Paps, C.R. Andrew and M.A. Hough. One-fold, two functions: cytochrome P460 and cytochrome *c'*-β from the methanotroph *Methylococcus capsulatus* (Bath) *Chemical Science*, **2019**, 10, 3031-3041

2.1 Introduction

This chapter describes the structural, spectroscopic and bioinformatics characterisation of the as isolated recombinant cytochrome *c'* and cytochrome P460 from *Methylococcus capsulatus* (Bath) and how these compare to each other.

The relationship between cytochrome *c'* (*Mc*CP) and cytochrome P460 (*Mc*P460) from *Methylococcus capsulatus* (Bath) was first noted in 1994 (Zahn, Duncan and DiSpirito, 1994) during initial characterisation studies into *Mc*P460. The two proteins were co-expressed and had to be separated during purification, reportedly causing a spectral shift in the reduced *Mc*P460 from 463 nm to 450 nm. These initial studies concentrated on the amino acid composition, enzymatic activity and spectral properties of *Mc*P460 (Zahn, Duncan and DiSpirito 1994) and *Mc*CP (Zahn et al. 1996).

The spectral properties of *Mc*CP were similar to those previously reported for cytochromes *c'* which led to the protein being designated a cytochome *c'*. However futher investigation into the amino acid sequence of *Mc*CP showed very low sequence similarity (6-11 %) to other known cytochromes *c'* (Bergmann, Zahn and DiSpirito 2000), but when compared to the sequences of cytochrome P460 from both *M. capsulatus* and *N. europaea* a higher level of similarity was found (31 % and 18 %, respectively). It was postulated that this high sequence similarity indicated an evolutionary relationship between the cytochrome *c*' of *M. capsulatus* and cytochrome P460. Further sequence analysis (Elmore et al. 2007) has supported this hypothesis of an evolutionary relationship and a new 'family' of cytochromes. Furthermore, using secondary structure prediction tools, all the members of this new 'family' were predicted to have a highly beta sheet structure in contrast to the typical alpha helical structure of all other known cytochromes *c'*.

This chapter describes work that was conducted with the aim to express, purify and characterise recombinant *Mc*CP and *Mc*P460 through the use of structural, spectroscopic and bioinformatic methods. This has given rise to the first published crystal structure of a cytochrome *c'*-β and *Mc*P460 which demonstrated that *Mc*CP is a highly β-sheet structure quite unlike the previously determined *c'* structures (herein referred to as *c'*-α), but very similar to all known P460 structures. It also confirms and expands upon previously reported spectral qualities of both enzymes.

Updated bioinformatic analysis was carried out as since this was last investigated many new sequences have been made available and the computational tools to analyse them have been greatly improved. This confirmed the relationship between P460s and *c'*-βs suggesting a strong evolutionary relationship between the two families of proteins.

2.2 Experimental Procedures

2.2.1 Sub Cloning

The genes encoding both *Mc*CP (Accession number AAD39218 from the NCBI RefSeq database) and the gene encoding *Mc*P460 (Accession number AAD03548 from the NCBI RefSeq database) were commercially synthesised (Epoch Life Sciences) in pBSK plasmids with restriction enzyme sites (*EcoRI* and *XbaI*, respectively) flanking either end of the gene (Figure 2.1, Figure A.1, A.2 Appendix A). Restriction Digestion of the commercially synthesised plasmid and gene was carried out using *EcoRI* and *Xbal* restriction enzymes which were incubated at 37 ^{o}C for 1 hr. Completion of the digestion of the reaction mix was checked by running 30 µl of the reaction mix with 5 µl 6 x DNA loading dye (Fermentas) on a 1 % agarose gel at 90 V for 1 hr. The correct sized fragments were visualised using a blue light (Syngene). The gene was extracted from the agarose gel using a Qiagen Gel Extraction Kit. The yield of the purified DNA was measured using a Nanodrop 2000 spectrophotometer (Thermo Scientific).

The purified *Mc*CP and *Mc*P460 inserts were ligated into both the expression vector pMMB503EH and pBluescript II SK (+) plasmid (pBSK) for sequencing simultaneously. Both plasmids had been digested with both *EcoRI* and *XbaI* restriction enzymes to help ensure correct orientation of the insert within the plasmid. Along with the ligation reaction a negative control was set up without the insert. The reactions were incubated at 16 °C for 18 hrs.

A standard heat-shock transformation was carried out for the positive and negative controls using 100 µl of chemically competent *Escherichia coli* (*E. coli*) XL1-blue cells (Stratagene USA) and 5 µl of the negative and positive ligation mixture. The cells were streaked on LB Agar plates containing either Streptomycin (Strep) at a concentration of 50 µg ml^{-1} for the

pMMB503EH ligation or Ampicillin (Amp) at a concentration of 100 µg ml^{-1} for the pBSK plasmid and incubated at 37 °C overnight. Five single colonies from the positive plates were picked and grown at 37 °C in 10 ml Strep medium and left shaking at 220 rpm for a minimum of 18 h at 37 °C. The plasmid GeneJet Miniprep Kit (ThermoScientific) was used to extract the plasmid DNA as described by the manufacturer. The purified plasmid DNA was digested using the *EcoRI* and *XbaI* restriction enzymes. The samples were run on a 1 % DNA agarose gel with a 1 kb DNA ladder mix (Fermentas). Visualisation of the gel confirmed the presence of the gene in the plasmid for use in subsequent experiments.

CGGAATTCCATGAACAAGCCATCGTTTTTACTCGTGGGGCTCCTGGTCGTTTCCGGCG
TGCTCGGCGCAGCCGAGACCAAGGTGAAATACCCCGATGGGTTTCGCAGTTGGTACC
ACGTCAAATCCATGGTGATCCAGCCGGGACACCCGCTGGAAAATCCCTTCGGCGGGA
TCCACCACGTTTACGCCAATGCAGAAGCCATCCAGGGACTGAGGGGCGGCAACTAC
CCGGACGGAGCGGTGTTGGTATTCGACCTGTTCGACTATCAGGAGGACAACCATGCA
CTGGTGGAAGGCAAACGCAAGCTGATCGGAGTGATGGAGCGCGATGCCAAGCGTTT
TCCGCTACCGGCGGTTGGGGTTATGAAGGATTCGGTGAAGGCAAGCCGGACAAGCG
TCTGGTCACTGACGGCGGGCAGGGTTGTTTCGGCTGTCACGCTGCGCAGAAAGAGA
GCCAATACGTGTTCTCCAGGCTTCGGGACTGACTAGTCTAGACTAG

CGGAATTCCATGCGAAACTGGCCATCGCCCTGTTGTTTCCCGCCGCCGCGGTCCTTGC
CGAACCGGCAGCCGCGCCCAACGGCATTTCGCTCCCTGCCGGCTACAAGACTGGAA
GATGATCGGCGTTTCCTCACGGATCGAGCAGAACAATTTGCGCGCGATCCTCGGCAA
CGACATCGCCGTCAAGGCCGCGCGCGAAGGCAGGACCCATCCCTGGCCGGACGGC
GCGATTCTGGTCAAGCTGTCGTGGAAAAAGAGCACCCATGAGCTGTTCCCGTCGGCC
GAGGTACCCGGTGACTTCACCCAGGCCGATTTCATGGTCAAGGATGCCGCCAAGTAC
GCCTCGACCGGCGGCTGGGGCTATGCCCGGTGGCTGGGGATGGAACAGAAACCCTA
CGGCGCGAACGCCGATTTCGCCCAGGAATGCATGGGCTGCCACAGCGGCGCCAAAG
CCGCCGACTACGTCTTCACCCATCCGGCCAAGCTTCCGAGTCTAGACTAG

Figure 2.1. Top: Sequence encoding *Mc*CP (including signal peptide) Bottom: Sequence encoding *Mc*P460 (including signal peptide). Flanking restriction sites of *EcoRI* and *XbaI*, respectively, in red.

2.2.2 Heterologous protein production and purification

2.2.2.1. Preparation of transformed pEC86 plasmid in BL21 (DE3) cells

The pEC86 (Arslan *et al.*, 1998) plasmid carries the ccmA-H genes from *E. coli* necessary for the maturation of c-type cytochromes and so helps in the process of overexpressing recombinant c-type cytochromes. 2 µl of the pEC86 plasmid (Figure A.3., Appendix A) was transformed with 100 µl of *E.coli* BL21 (DE3) competent cells by a standard heat-shock transformation and was carried out as outlined in. The final transformation product was plated on LB Agar plates containing Chloramphenicol (CHL) at a concentration of 30 µg ml^{-1} and incubated overnight at 37 °C. A single colony was transferred into 10 ml LBCHL media and incubated overnight at 37 °C with continuous shaking at 220 rpm. After 16 h it was sub-cultured (1:50) into a final volume of 50 ml LBCHL media with continuous shaking at 220 rpm at 37 °C until the desired optical density was reached ($OD_{600\ nm}$ = 0.4 - 0.8). The cells were chilled on ice for 20 min and then centrifuged at 4000 rpm for 20 min at 4 °C. The supernatant was removed and the cell pellet was re-suspended in 10 ml of pre-chilled 0.1 M $CaCl_2$ followed by an incubation on ice for 20 min. The cells were centrifuged at 2500 rpm for 10 min and the supernatant was removed and 2 ml of prechilled 0.1 M $CaCl_2$ containing 15 % glycerol was used to re-suspend the cell pellet. Small aliquots of 100 µl were transferred to pre-chilled micro-centrifuge tubes, flash-frozen in liquid nitrogen then stored at -80 °C.

2.2.2.2 Protein over-production

*Mc*CP and *Mc*P460 were over-produced in pMMB503EH. Refer to Figures A.3 and A.4 (Appendix A), which contains the plasmid maps for pEC86 and pMMB503EH, respectively. A standard heat-shock transformation was carried out by adding 2 µl of the recombinant DNA plasmid to 100 µl of chemically competent *E. coli* BL21(DE3) cells transformed with the pEC86 plasmid. The cells containing both plasmids were streaked on LB agar plates containing CHL (20 µg ml^{-1}) and Strep (50 µg ml^{-1}) for pMMB503EH/pEC86 followed by an overnight incubation at 37 °C. A single colony was picked and inoculated into 10 ml LBStrep and CHL medium and incubated overnight at 37 °C with continuous shaking at 220 rpm. The 10 ml pre-culture was sub-cultured into 500 ml LB medium with the addition of Strep and CHL and left overnight at 37 °C with continuous shaking at 220 rpm. A volume of 50 ml from the overnight culture was transferred into 950 ml TB medium supplemented with the appropriate antibiotics and 0.17 M KH_2PO_4 and 0.72 M K_2HPO_4 and grown at 37 °C with continuous shaking at 200 rpm. After inoculation of the 50 ml overnight culture, proteins, which were expressed with the pMMB503EH plasmid were grown until mid-log phase (OD 600 nm = 0.4 – 0.8). This was followed by the addition of IPTG (0.12 g ml^{-1}) to induce protein synthesis under the control of the lac operon. The concentration of IPTG remains the same as it is non-hydrolysable and thus protein expression is continued until cell harvesting. After 5 h into protein expression, a volume of 330 µl of 1 M ferriprotoporphyrin IX chloride (10 µg ml^{-1}; Acros Organics) was added to the TB medium followed by 1 ml of the metal ion master mixture (2 mM Ni^{2+}, 2 mM Co^{2+}, 10 mM Zn^{2+}, 10 mM Mn^{2+} and 50 mM Fe^{3+}) after 24 h and left shaking at 220 rpm at 37 °C. Cultures were grown for 96 h and cells harvested by centrifugation for 20 min at 4 °C and at 4000 rpm.

2.2.2.3 Methylococcus capsulatus (Bath) Cytochrome c' Purification

Harvested cells were resuspended in 20 mM Tris–HCl pH 8 and disrupted by 2 passages through an EmulsiFlex (12,000 psi). The crude *Mc*CP extract was prepared by centrifugation at 18,000 rpm for 30 min followed by 24 h dialysis against ddH_2O. The extract was then centrifuged at 18,000 rpm for 20 min and loaded onto a DEAE Sepharose Fast Flow anion-exchange column previously equilibrated with two column volumes of 20 mM Tris–HCl, pH 8. *Mc*CP was eluted using 10 mM NaCl and was further purified to homogeneity by gel filtration using a Sephadex G75 column. The purity of the protein was determined by SDS-PAGE analysis and by UV–visible spectroscopy.

2.2.2.4 Methylococcus capsulatus (Bath) Cytochrome P460 Purification

Cultures were grown for 96 h and cells harvested by centrifugation for 20 min at 4 °C and at 4000 rpm to produce a green coloured pellet. Harvested cells were resuspended in 20 mM Tris–HCl pH 8 and disrupted by 2 passages through an EmulsiFlex (12,000 psi). The crude extract was prepared by centrifugation at 18,000 rpm for 30 min. A salt cut using ammonium sulphate was carried out on the protein sample to remove the protein contaminants in the sample. Ammonium sulphate was added to the protein sample in 10 % increments, whist stirring at room temperature up to 70 %. Once the salt was fully dissolved at each percentage the samples were spun at 18,000 rpm for 5 min to remove any precipitated proteins. The *Mc*P460 containing sample was buffer exchanged into 1 M ammonium sulphate, potassium phosphate pH 7 Buffer and loaded onto a hydrophobic interaction chromatography column pre equilibrated with the same buffer. The column was washed with 3 CV 1 M ammonium sulphate, potassium phosphate pH 7 Buffer. A gradient was set from 1 – 0 M ammonium sulphate, potassium phosphate pH 7 to elute the protein. Purity of the protein at this stage was

determined by SDS-PAGE analysis and by UV–visible spectroscopy. The eluted green fractions were then loaded onto a Sephadex G75 column and the purity of the protein was determined by SDS-PAGE analysis and by UV–visible spectroscopy.

2.2.3 UV-visible spectroscopy

All aerobic spectrophotometric experiments were carried out at 20 °C, unless stated otherwise, using the Varian Cary 50 spectrophotometer (Agilent Technologies). UV-visible absorption spectra were recorded between 800 - 200 nm using a 1 cm Quartz cuvette (Hellma-Analytics).

2.2.4 Initial characterisation and purity check

Protein concentrations were determined using a molar extinction coefficient (ε) for the Soret band of 78.5 mM cm^{-1} for the oxidised *Mc*P460 (Zahn, Duncan and DiSpirito, 1994) and70 mM cm^{-1} for the oxidised *Mc*CP (Zahn *et al.*, 1996). The purity of the protein was determined by the wavelength (nm) ratio of the A_{419}/A_{280} (*Mc*P460) or A_{400}/A_{280} (*Mc*CP) peak. A ratio of 3:1 was aimed for and indicated pure protein.

2.2.5 EPR spectroscopy

Electron Paramagnetic Resonance (EPR) spectra were measured using either an EMX spectrophotometer (Bruker) or a Bruker ELEXSYS E500 EPR spectrophotometer. Both EPR spectrophotometers were equipped with the spherical high quality resonator SP9703 and a liquid helium cryostat (Oxford Instruments) to measure the low temperature (10 K) EPR

spectra and were operating in continuous wave (CW) regime, at X-band (9 GHz microwave frequency), and 100 kHz field modulation frequency. The g-values were obtained using the built-in microwave frequency counter. Protein samples were 100 μM concentration in 50 mM HEPES pH 7.5. Syringes, needles and EPR tubes were flushed with nitrogen before use. A 5X MHTCP cocktail buffer containing 250 mM MES, 250 mM HEPES, 250 mM TAPS, 500 mM CAPS and 250 mM PIPES was prepared to acquire the desired pH ranges. The 1X MHTCP cocktail buffer at pH 4, 5, 6, 7, 8, 9, and 10, was used for the pH-dependent EPR experiments. Experimental conditions for the pH-dependent studies were as follows: microwave frequency 9.466 GHz, microwave power 0.0505 mW, modulation amplitude 3 G, time constant 40.96 ms, scan rate 4.77 G/s and one scan/spectrum. Simulations and spectra extractions were performed by Dr Dimitri Svistunenko using WinEPR SimFonia (Bruker).

2.2.6 Crystallisation

All proteins were buffer exchanged into 50 mM HEPES, pH 7.5 and used for subsequent crystallisation with protein concentrations ranging from 15 – 30 mg/ml. For screening for crystallisation conditions, the Art Robbins Gryphon robot and commercially available screens (Structure Screen 1+2 (Jancarik and Kim, 1991) (Wooh *et al.*, 2003), pH Clear Suite, JCSG+ (Mcpherson, 2001) (Page *et al.*, 2003), ProPlex (Radaev, Li and Sun, 2006)) were used to set up initial crystal trays. Initial crystal hits were optimised manually by the hanging drop vapour diffusion method and drop volumes ranged from 1-2 μl with equivalent volumes of the reservoir solutions.

Cryo-protection was screened by soaking multiple crystals in different conditions before flash freezing in liquid nitrogen. The frozen crystals were sent to Diamond Light Source (DLS) to test for diffraction. Cryo-protected crystals that diffracted well were chosen for further

experiments. The crystals were cryo-protected using the reservoir solution and 1.7 M sodium malonate for *Mc*P460 or 10 % glycerol for *Mc*CP for 15 – 30 s and flash-cooled in liquid nitrogen.

2.2.7 X-ray Data Collection and Processing

X-ray diffraction data for *Mc*CP crystals were collected at beamline I03, Diamond Light Source, using a Pilatus 3 6M detector. A dataset measured at a wavelength of 1.74 Å was used to solve the structure using the anomalous signal of the intrinsic heme Fe. All data were processed in Xia2 using XDS (Kabsch, 2010) and AIMLESS (Evans and Murshudov, 2013). The initial model was built using Buccaneer (Cowtan, 2006). A high-resolution dataset was measured from a second *Mc*CP crystal at a wavelength of 0.97 Å and refined from the starting model from the SAD experiment. Structures were refined by maximum likelihood methods using REFMAC5 (Murshudov *et al.*, 2011). A bespoke geometry file was used to set heme parameters during refinement (provided by Prof Hough). Model building between cycles of refinement, including addition of water molecules and ligands was performed in Coot (Emsley *et al.*, 2010).

Data for *Mc*P460 crystals were measured at beamline I04-1, Diamond Light Source. An initial dataset was measured at a wavelength of 1.74 Å to produce an initial SAD electron density map. Another dataset was then measured at a wavelength of 0.979 Å, processed using DIALS and the structure solved using Auto-Rickshaw (Panjikar *et al.*, 2005), with the initial SAD electron density map being used as the target for molecular replacement with the structure of *Ne*P460 (PDB 2JE3) (Pearson *et al.*, 2007) as the search model. Model building was completed in Arp-Warp (Cohen *et al.*, 2008) and subsequently refined as described for *Mc*CP above.

2.2.8. Validation of crystal structures

Validation of structures was carried out with *MolProbity* (Chen *et al.*, 2010) and *JCSG Quality Control Check* (Elsliger *et al.*, 2010). The pdb and mtz file were inputted to the *JCSG* server whereas only the pdb file was used for *MolProbity*. Steric clashes, poor rotamers, Ramachandran outliers, residues with improbable bonds and angles were re-modeled in Coot, followed by more refinement in Refmac5 and this was repeated until the model was of high quality.

2.2.9 Normal-Coordinate Structural Decomposition

Out of plane distortions of the heme were analysed using an online normal coordinate structural decomposition script (http://mliptak.w3.uvm.edu/nsd.html) derived from the normal-coordinate structural decomposition procedure (Jentzen, Song and Shelnutt, 1997; Graves, Graves and Liptak, 2016)

2.2.10 Bioinformatics

Protein BLAST was performed (http://blast.ncbi.nlm.nih.gov/Blast.cgi) May 2018 to identify amino acid sequences similar to those of *Methylococcus capsulatus* (Bath) cytochrome *c'*, *Methylococcus capsulatus* (Bath) P460, *Nitrosomonas europaea* P460 and *Alcaligenes xylosoxidans* cytochrome *c'*. After removal of repetitive sequences, full length protein sequences were aligned using ClustalW (Larkin *et al.*, 2007). Any sequences that did not have the crosslinking Lys residue were removed from the list of CytP460s. A total of 214 identified cytochrome *c'* (52 sequences) and P460 (144 sequences) protein sequences were used in the alignments. Maximum likelihood trees were constructed using RAxML

(Stamatakis, Hoover and Rougemont, 2008) after removal of excess and poorly aligned regions using trimAL (Capella-Gutiérrez, Silla-Martínez and Gabaldón, 2009) and annotated using MEGA7 (Kumar, Stecher and Tamura, 2016).

2.3 Results

2.3.1 Expression and Purification

Both *Mc*CP and *Mc*P460 were successfully cut out from the carrier pBSK plasmid using the restriction enzymes *EcoRI* and *XbaI* (Figure 2.2) and ligated into the pMMB503EH expression vector. The *Mc*CP or *Mc*P460 containing expression vectors were then transformed into BL21(DE3) PEC86 cells and expression was carried out as described in Experimental Procedures (Chapter 2.1).

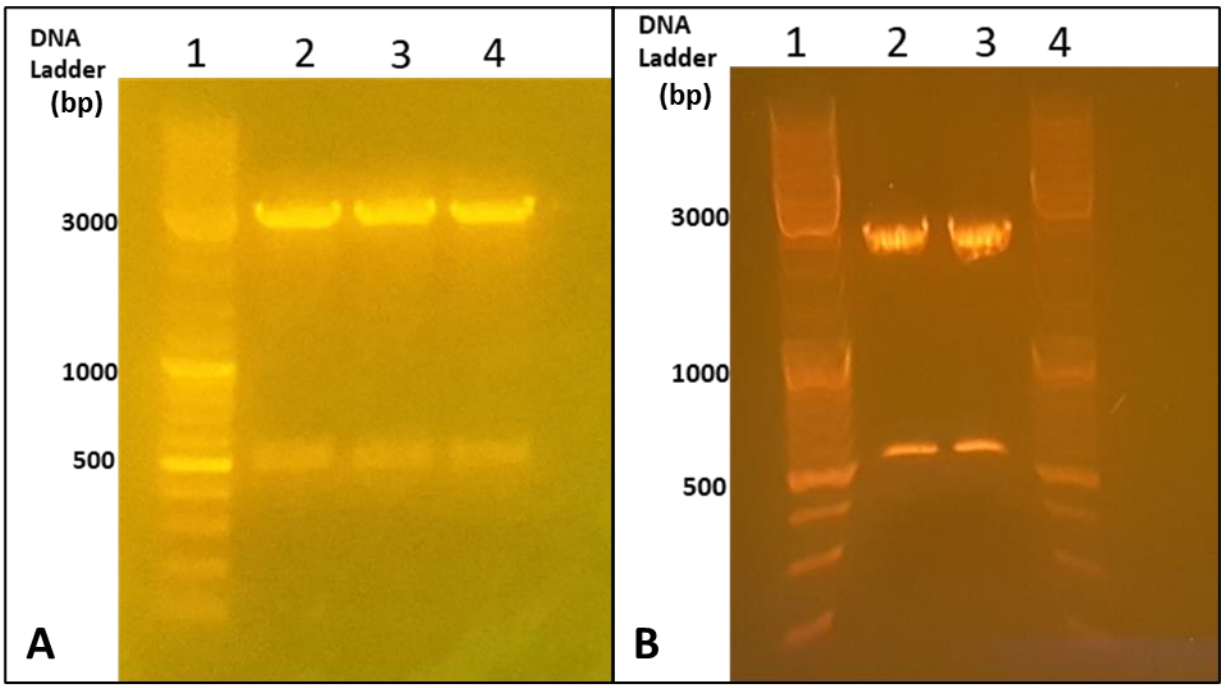

Figure 2.2. 1% Agarose Gel Electrophoresis analysis of the restriction digestion of pBSK plasmid containing (A) *Mc*CP coding insert. Lane one contains the DNA ladder (bp) and lanes 2-4 contain the digested plasmid and *Mc*CP insert. Bands for both the plasmid backbone (~3000 bp) and the *Mc*CP insert (~500 bp) can be clearly seen on the gel. (B) *Mc*P460 coding insert. Lanes 1 + 4 contain the DNA ladder (bp) and lanes 2 + 3 contain the digested plasmid and *Mc*P460 insert. Bands for both the plasmid backbone (~3000 bp) and the *Mc*P460 insert (~500 bp) can be clearly seen on the gel.

*Mc*CP was successfully overexpressed in BL21(DE3) PEC86 cells as shown by the presence of a reddish brown pellet upon harvesting of the cells (Figure 2.3 A). The presence of the protein could be easily visually monitored throughout the purification process due to its distinct reddish-brown colour (Figure 2.3 B). The purity of the protein was determined by SDS-PAGE analysis and by UV–visible spectroscopy (Figures 2.4). A final yield of 6.4 mg L^{-1} *Mc*CP was obtained.

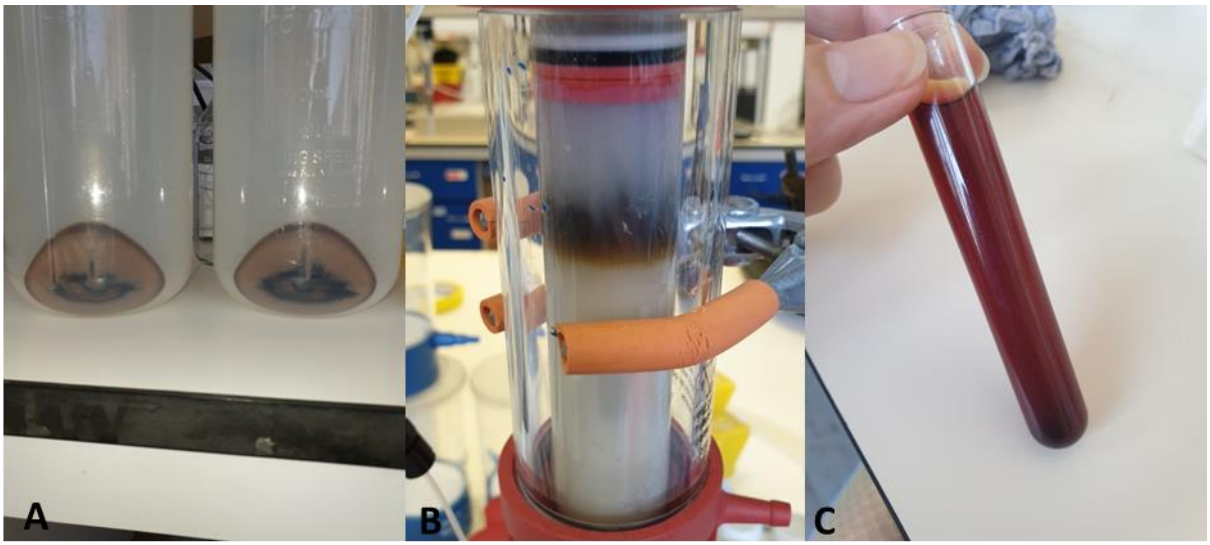

Figure 2.3. Harvesting and purification of *Mc*CP. Pelleted *E .coli* cells after over expression of *Mc*CP, the presence of *Mc*CP is indicated by the brown colouration of the pelleted cells (A). Purification of *Mc*CP on a DEAE Ion Exchange chromatography column, *Mc*CP can be clearly seen as a brown band bound to the column (B). Test tube of purified *Mc*CP, as isolated *Mc*CP has a reddish brown colour when fully purified (C).

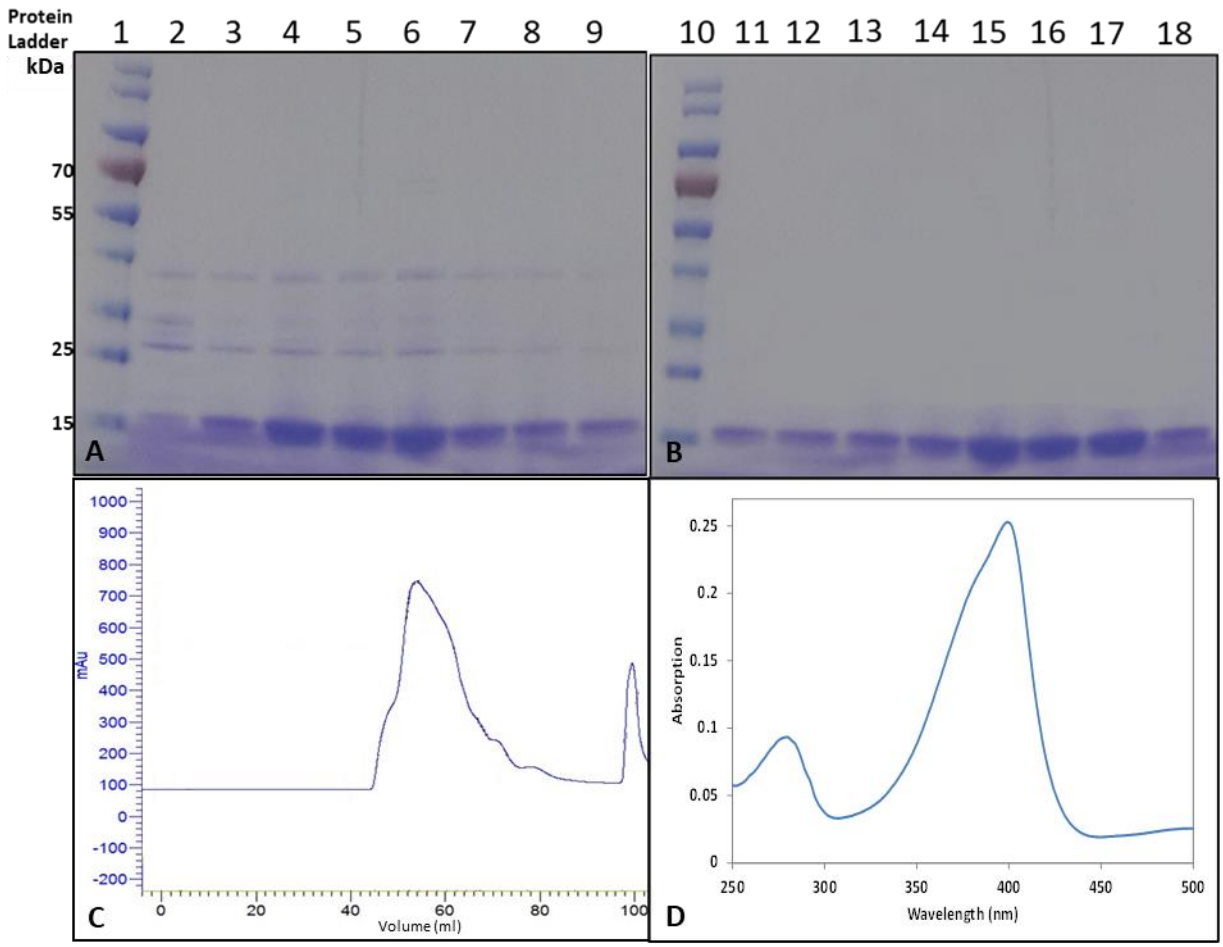

Figure 2.4. Purity checks for *Mc*CP. 15 % SDS-PAGE analysis of wt *Mc*CP. Lanes 1 + 10 contain the protein ladder. Lanes 2-9 contain protein fractions after DEAE Sepharose ion exchange chromatography with a band ~ 15 kDa, indicating the presence of *Mc*CP but also the presence of higher molecular weight proteins (A). Lanes 11-18 contain protein fractions after Sephadex G75 Gel Filtration chromatography with a band ~ 15 kDa (B), indicating the presence of *Mc*CP. Purification profile of *Mc*CP during size exclusion chromatography (C). UV-visible absorption spectra of fully purified recombinant *Mc*CP. With a A_{400}/A_{280} peak ratio of 2.5:1 suggesting a pure protein sample (D).

Harvesting of the over expressed *Mc*P460 produced a green coloured pellet (Figure 2.5 A). Initially harvested cells were resuspended in 20 mM Tris–HCl pH 8, disrupted by 2 passages through an EmulsiFlex (12,000 psi) and loaded onto an equilibrated DEAE Sepharose Fast Flow anion-exchange column following centrifugation at 18,000 rpm for 30 min. A green band was observed on the column, but this did not bind and was observed to move down the column and be eluted with the wash buffer. Assessment of the purity of the protein by SDS-PAGE analysis and UV–visible spectroscopy (Figure 2.6) showed the presence of many contaminants in the sample. A salt cut using ammonium sulphate was then carried out on the protein sample to remove the protein contaminants in the sample. Ammonium sulphate was added to the protein sample in 10 % increments up to 70 %, whist stirring at room temperature. Once the salt was fully dissolved at each percentage the samples were spun at 18,000 rpm for 5 min to remove any precipitated proteins. When the centrifuged sample produced a green pellet (leaving a colourless supernatant), the pellet was resuspended in buffer and checked for purity. Determination of the purity of the sample after each percentage of salt cut showed the 70 % sample still contained other contaminants (Figure 2.7).

The *Mc*P460 containing sample was then buffer exchanged into 1 M ammonium sulphate, potassium phosphate pH 7 Buffer and loaded onto a hydrophobic interaction chromatography column pre equilibrated with the same buffer. The protein bound to the column (Figure 2.5 B). The column was washed with 3 CV 1 M ammonium sulphate, potassium phosphate pH 7 Buffer. A gradient was set from 1 – 0 M ammonium sulphate, potassium phosphate pH 7 to elute the protein. Purity of the protein at this stage was determined by SDS-PAGE analysis and by UV–visible spectroscopy. The eluted green fractions were then loaded onto a Sephadex G75 column and the purity of the protein was determined by SDS-PAGE analysis and by UV–visible spectroscopy (Figure 2.8).

Future preparations of *Mc*P460 skipped the DEAE column step and started with the salt cut after centrifugation of the lysed cells as this provided a pure protein sample.

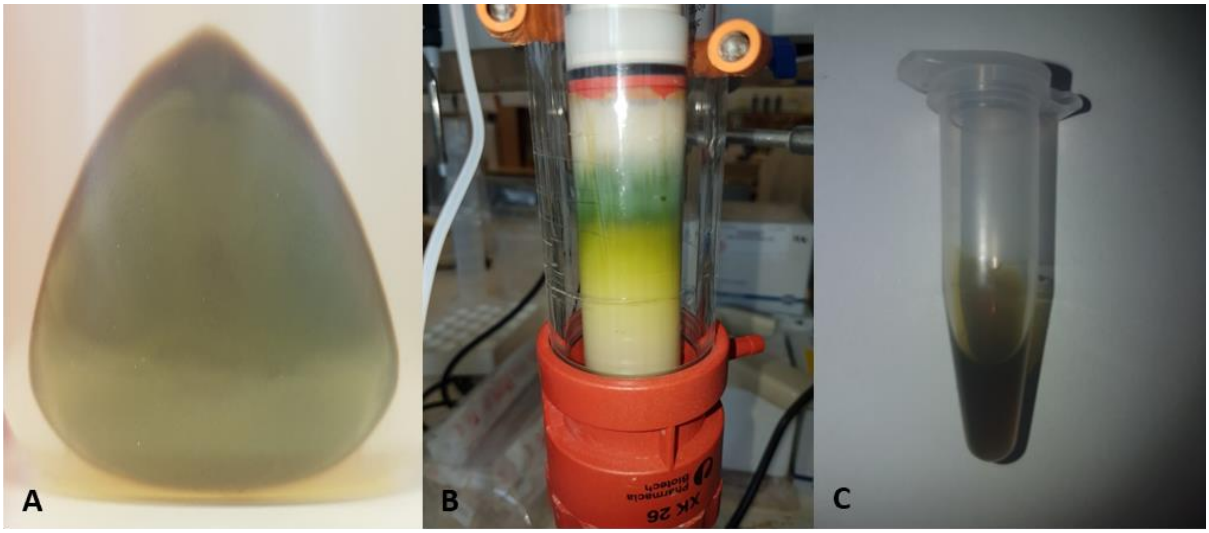

Figure 2.5. Harvesting and purification of *Mc*P460. Pelleted cultures after 96 h growth, the green colour suggests presence of the Cytochrome P460 protein (A). Purification of *Mc*P460 on a Hydrophobic Interaction chromatography column, *Mc*P460 can be clearly seen as a dark green band bound to the column (B). Eppendorf tube of purified *Mc*P460, as isolated *Mc*P460 has a brownish green colour when fully purified (C).

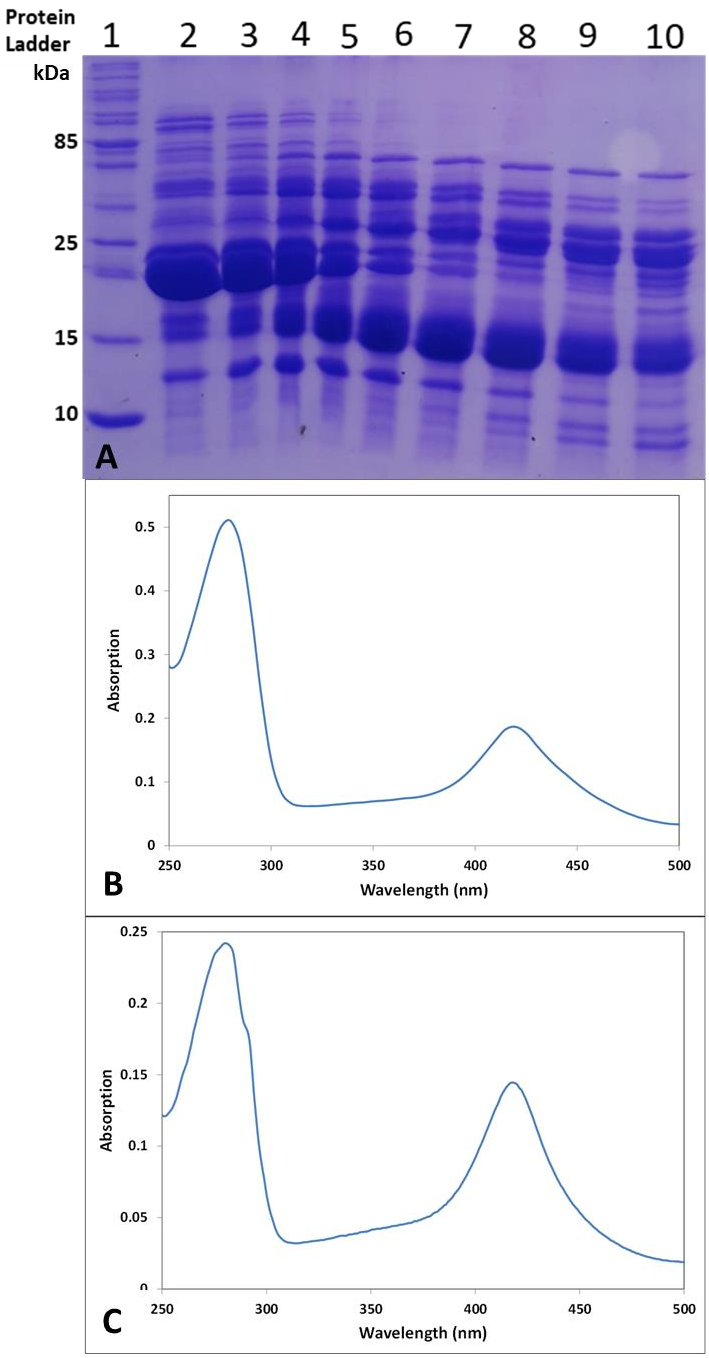

Figure 2.6. Purity checks for *Mc*P460 after DEAE and size exclusion chromatography. 15% SDS-PAGE analysis of wt *Mc*P460 (A) and UV-visible spectrum of Cytochrome P460 (B) after DEAE column, (C) after Sephadex G75 Column. SDS-PAGE after Sephadex G75 gel filtration chromatography. Lane 1 contains the protein ladder and lanes 2-9 contain protein fractions. Fractions 2-9 show a band ~ 17 kDa, indicating the presence of *Mc*P460 but also the presence of other molecular weight proteins. The A_{280}/A_{420} ratio has been lowered suggesting a slightly purer sample after size exclusion chromatography.

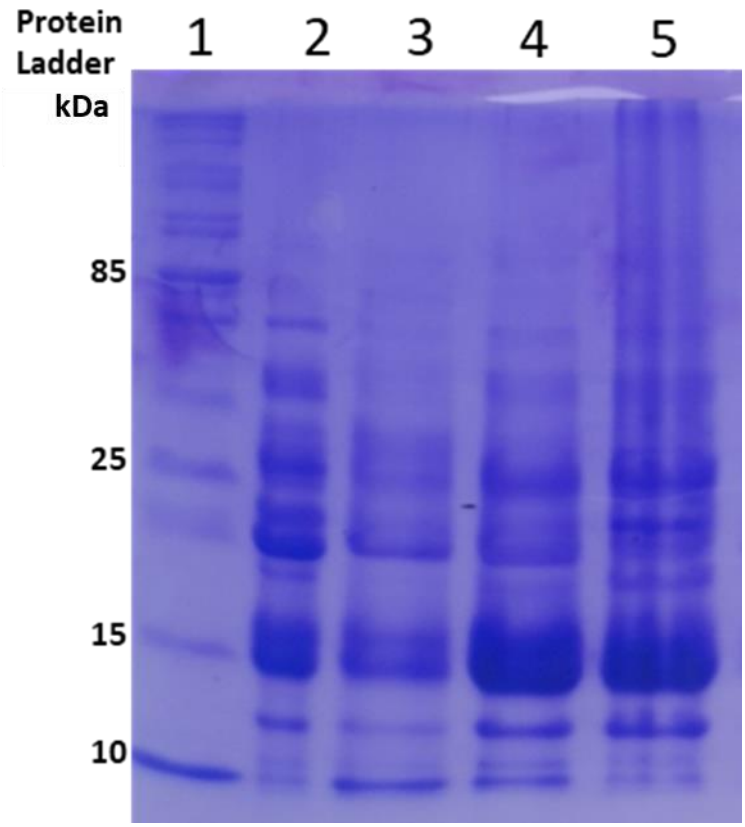

Figure 2.7. Purity checks for *Mc*P460 after salt cut. 15 % SDS-PAGE analysis of wt *Mc*P460. SDS-PAGE after ammonium sulphate salt cut. Lane 1 contains the protein ladder, lane 2 protein sample before salt cut, lane 3 50 % ammonium sulphate, lane 4 60 % ammonium sulphate, lane 5 70 % ammonium sulphate. Fractions 2-5 show a band ~ 17 kDa, indicating the presence of *Mc*P460 but also the presence of other molecular weight proteins.

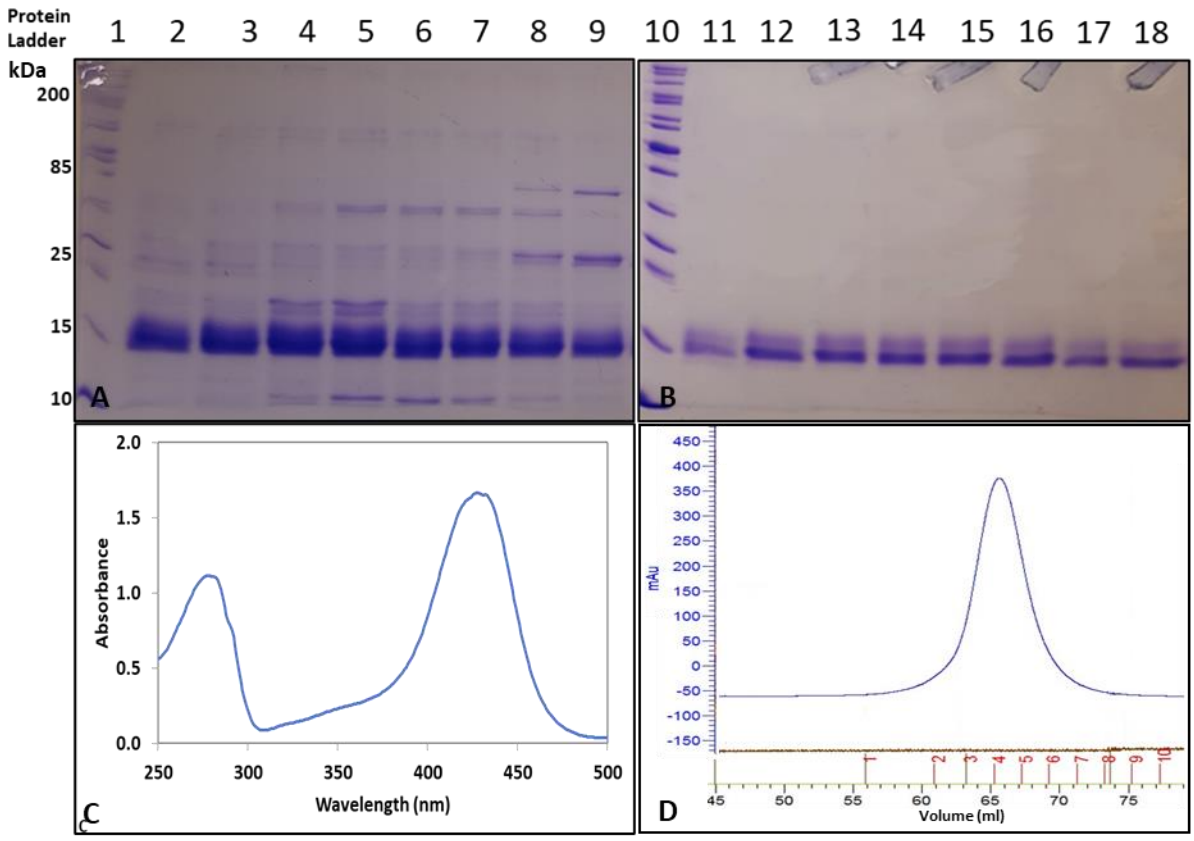

Figure 2.8. Purity checks for *Mc*P460 after Hydrophobic interaction column. 15 % SDS-PAGE analysis of wt *Mc*P460 (A, B), UV-visible Spectra of Cytochrome P460 after hydrophobic interaction chromatography (HIC) (C) and purification profile during size exclusion chromatography (D). Lanes 1 + 10 contain the protein ladder, lanes 2-9 contains protein samples after hydrophobic interaction chromatography with a band ~ 17 kDa, indicating the presence of *Mc*P460 but also the presence of a small amount other molecular weight proteins (A). Lanes 11-18 contains protein samples after sephadex G75 gel filtration chromatography with a band ~ 17 kDa, indicating the presence of *Mc*P460 and no other contaminants (B). After HIC the protein peak is much sharper suggesting that the contaminants may have been removed from the sample (C). Purification profile shows purified *Mc*P460 being eluted in a single peak (D).

2.3.2 Spectroscopy

2.3.2.1 UV-visible Spectroscopy

UV-visible absorption bands of as-isolated recombinant *Mc*CP (Figure 2.9 A, Table 2.1) are similar to those previously reported for the wt protein (Zahn, Arciero et al. 1996), with a Soret maximum at 399 nm (and weak shoulder at ~ 379 nm), together with an unresolved α/β band near 500 nm and a CT1 band at ~ 640 nm. The absorbance features are also reminiscent of the 5c quantum mechanically admixed high-spin/intermediate-spin (5cQS) state of Fe(III) cyts *c'*-α (Table 2.1). However, unlike Fe(III) cyts *c'*-α, which convert from a 5cQS to a pure 5c high-spin (5cHS) state at alkaline pH (pK_a values ~ 7 – 10) (Hough and Andrew 2015), the spectroscopic properties of Fe(III) *Mc*CP remain essentially unchanged over the pH range 4.0 – 9.0 (Figure 2.10). At pH 10.0 there is a shift in the Soret band to 403 nm, along with a decrease in intensity of the β band at 502 nm and an increase in the α band at 537 nm. This suggests a change in the iron spin state at this pH. Reduction of Fe(III) *Mc*CP with dithionite yields the Fe(II) state which exhibits a Soret maximum at 431 nm and a broad α/β band centered at 552 nm (Figure 2.9 A). The Soret band of Fe(II) *Mc*CP differs somewhat from those of Fe(II) cyts *c'*-α which typically have maxima at ~ 425 nm with a shoulder at ~ 435 nm (Table 2.1).

As-isolated Fe(III) *Mc*P460 (pH 7.0) exhibits a Soret absorption band at 419 nm, with a shift to the characteristic 460 nm band in the Fe(II) state (Figure 2.9 B, Table 2.1). This is in agreement with what was previously reported (Zahn, Duncan et al. 1994).

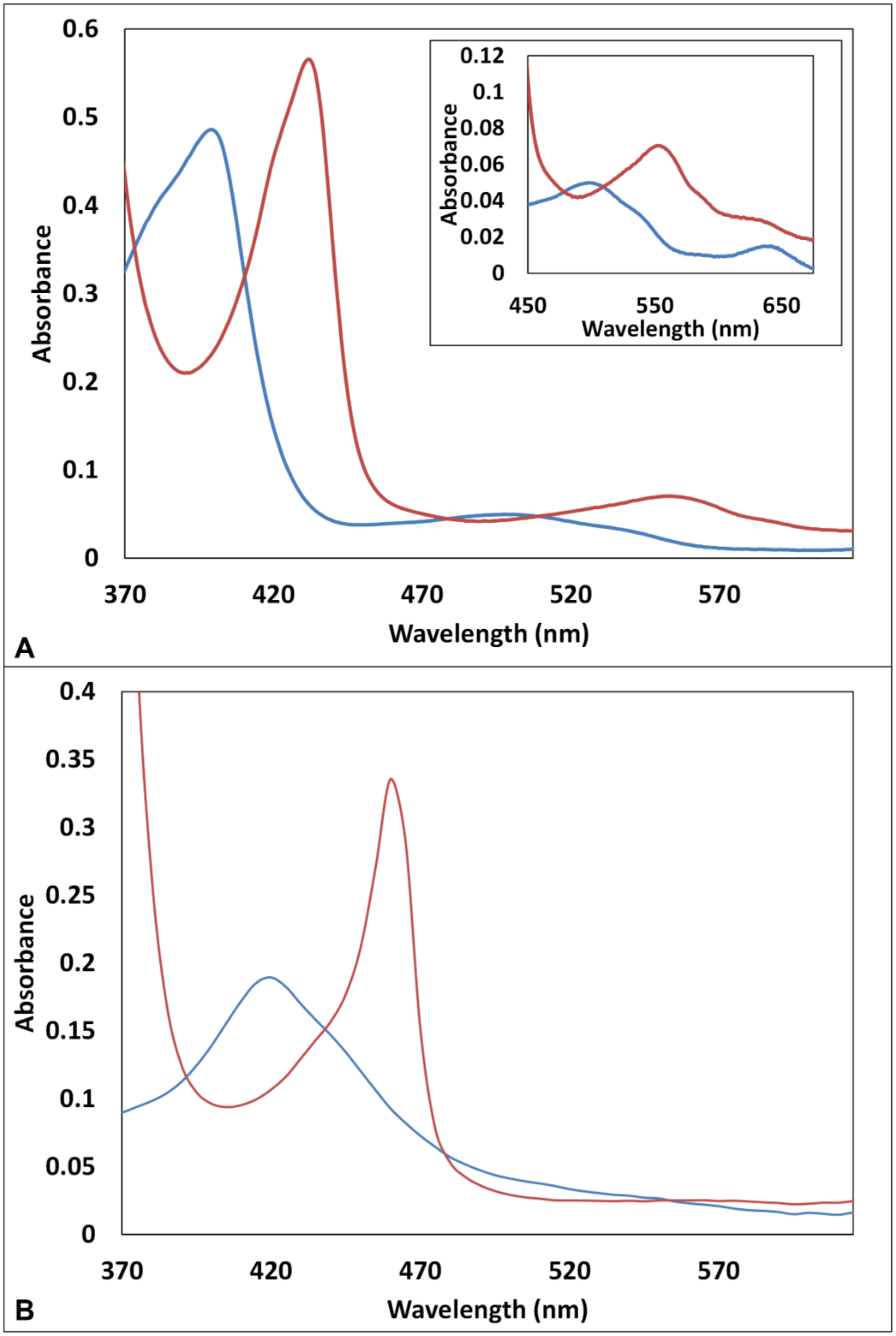

Figure 2.9. UV-visible absorbance spectra of *Mc*CP (A) and *Mc*P460 (B) in the ferric (blue) and ferrous (red) states. *Mc*CP displays a Soret maximum at 401 nm in the ferric state which shifts to 431 nm with addition of a reductant. As-isolated Fe(III) *Mc*P460 exhibits a Soret absorption band at 419 nm, with a shift to the characteristic 460 nm band in the Fe(II) state

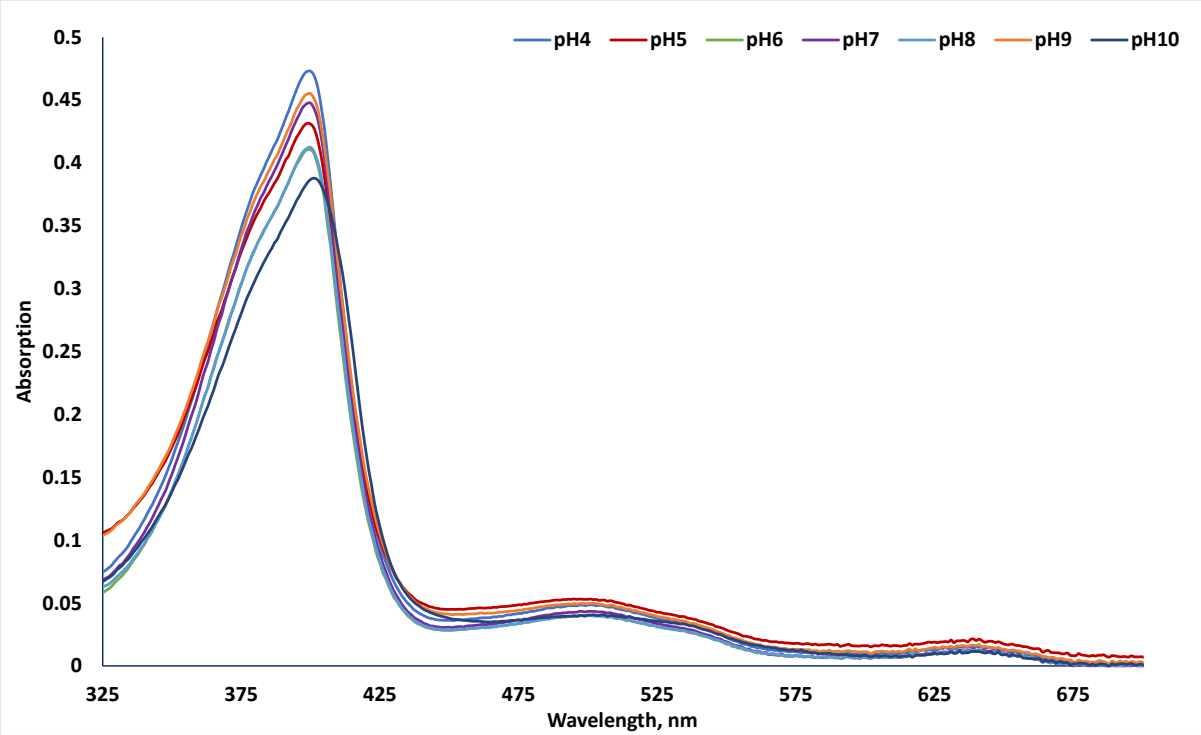

Figure 2.10. UV-visible absorption spectra of ferric *Mc*CP at varying pH (4-10). Unlike other cytochrome c' (Hough and Andrew 2015) changing the pH over the range of pH 4-9 does not change the absorbance features (a Soret band at 401 nm, a broad β-peak at 502 nm and a charge transfer band at 639 nm).

2.3.2.2 EPR Spectroscopy

EPR spectra of Fe (III) *Mc*CP reveal two high spin Fe (III) heme signals: a major species with *g* values of 6.29, 5.46, and 1.98, together with a minor species with *g* values of 6.00, 5.34, and 1.98 (Figure 2.11, Table 2.2). Previous EPR measurements of wt Fe (III) *Mc*CP also showed two Fe (III) signals, as well as a shift in the *g* values of the major species from 6.29, 5.34, 2.0 → 6.06, 5.34, 2.0 upon lowering the pH from 8.2 to 4.0 (Zahn *et al.*, 1996) However, our measurements indicated that there was no change in the predominant high spin species over the pH range 4.0 – 10.0 (Figure 2.12).

EPR spectra of *Mc*P460 showed a spectrum representative of a single high spin species (Figure 2.13) with g values of 6.17, 5.57 and 1.99 resembling that of as isolated (Numata *et al.*, 1990) and recombinant (Caranto, Vilbert et al. 2016) *Ne*P460 and the 'P460 fragment' from the *N. europaea* HAO (Andersson, Babcock and Hooper, 1991). The previously described EPR spectrum of *Mc*P460 (Zahn, Duncan et al. 1994) possibly represents a degraded form of the enzyme.

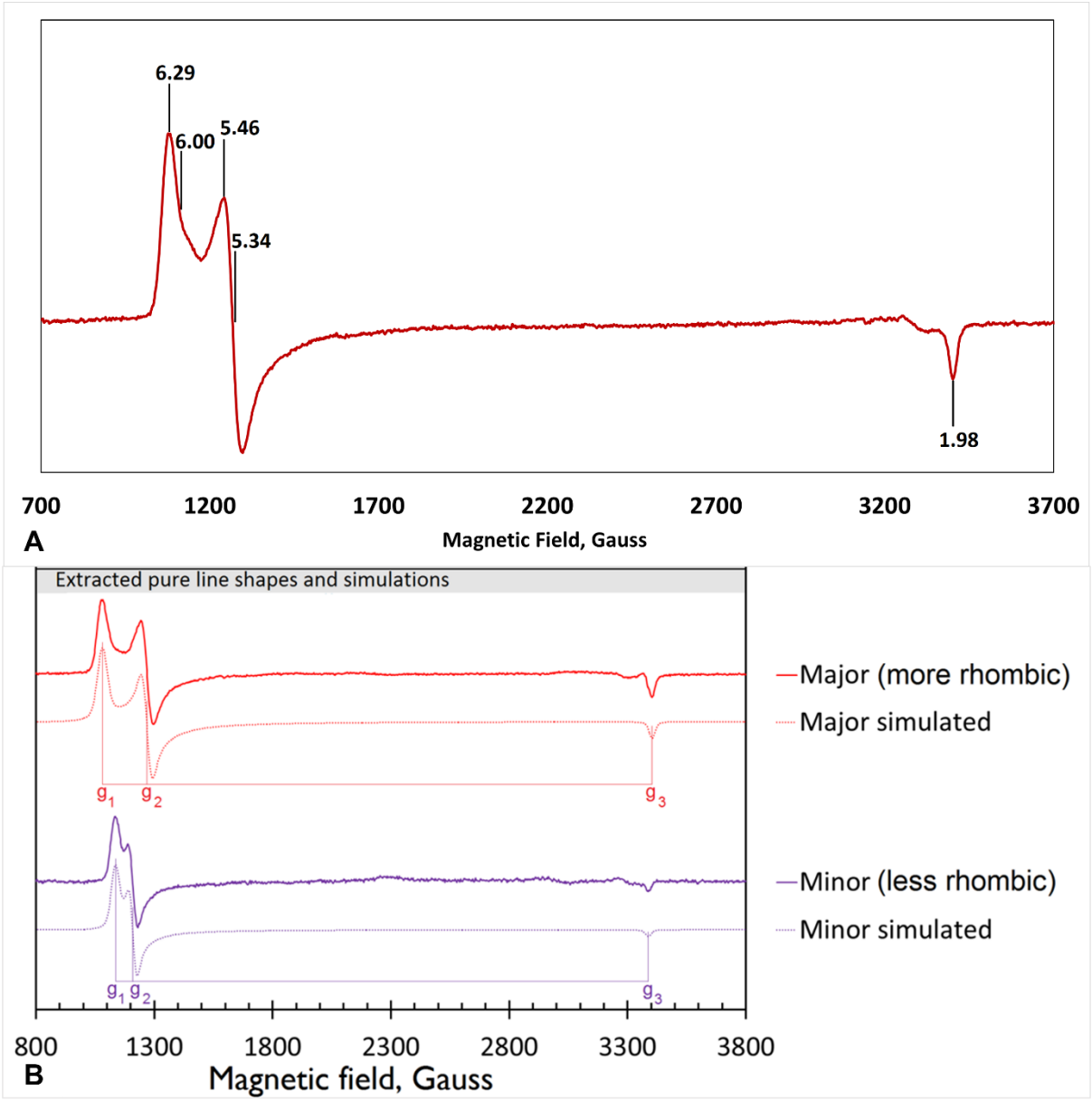

Figure 2.11. EPR spectrum of ferric *Mc*CP at pH8 (A) demonstrating two Fe(III) heme signals: a major species with *g* values of 6.29, 5.46, and 1.98, together with a minor species with *g* values of 6.00, 5.34, and 1.98. Extracted pure line shapes from the EPR spectrum in (A) and simulations of the two EPR species (B).

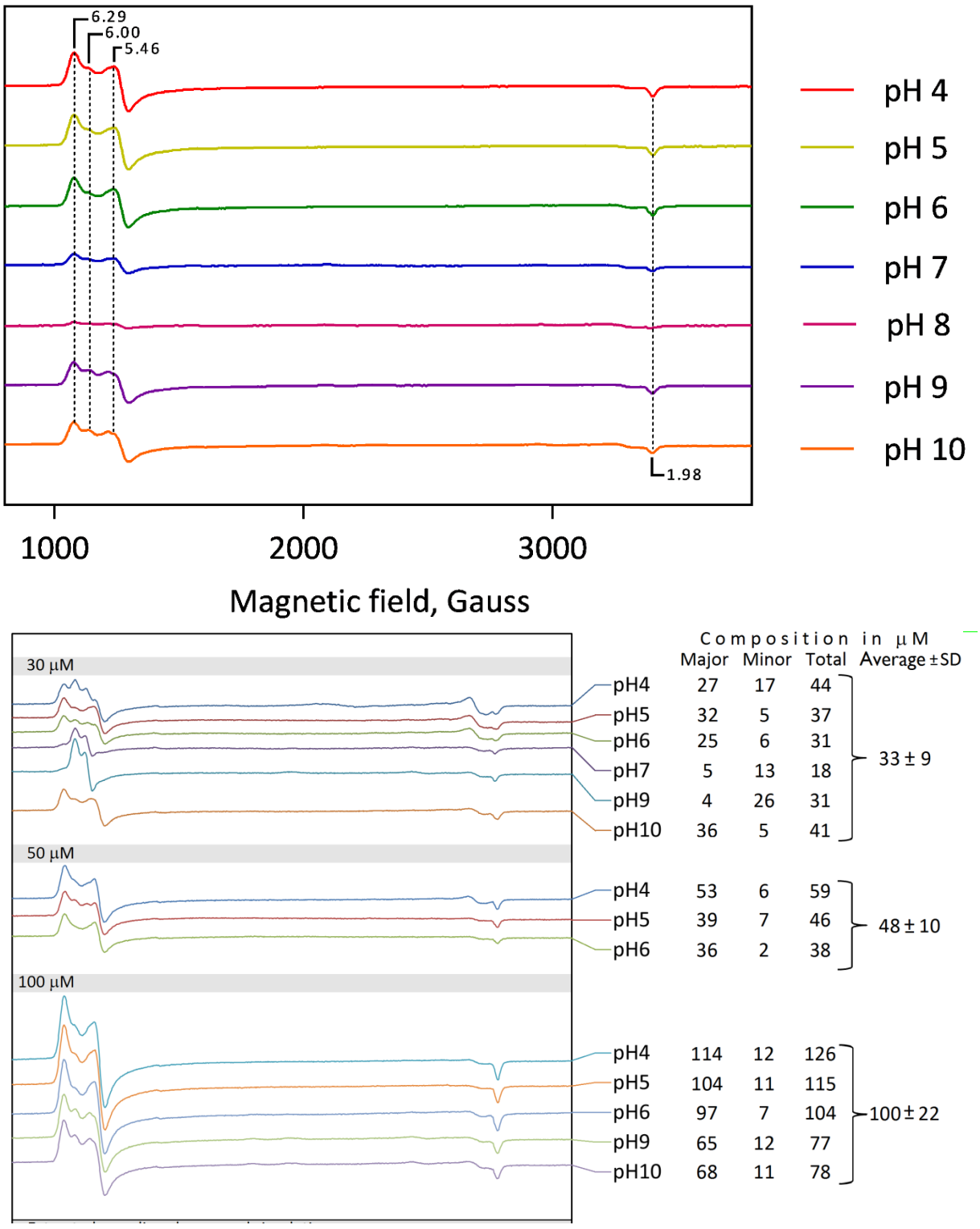

Figure 2.12. EPR spectra of ferric *Mc*CP at varying pH (4-10). Unlike previous EPR measurements of wt Fe (III) *Mc*CP (which showed a shift in the g values of the major species from 6.29, 5.34, 2.0 → 6.06, 5.34, 2.0 upon lowering the pH from 8.2 to 4.0 (Zahn, Arciero et al. 1996) there is no change seen in the predominant high spin species over the pH range 4.0 – 10.0.

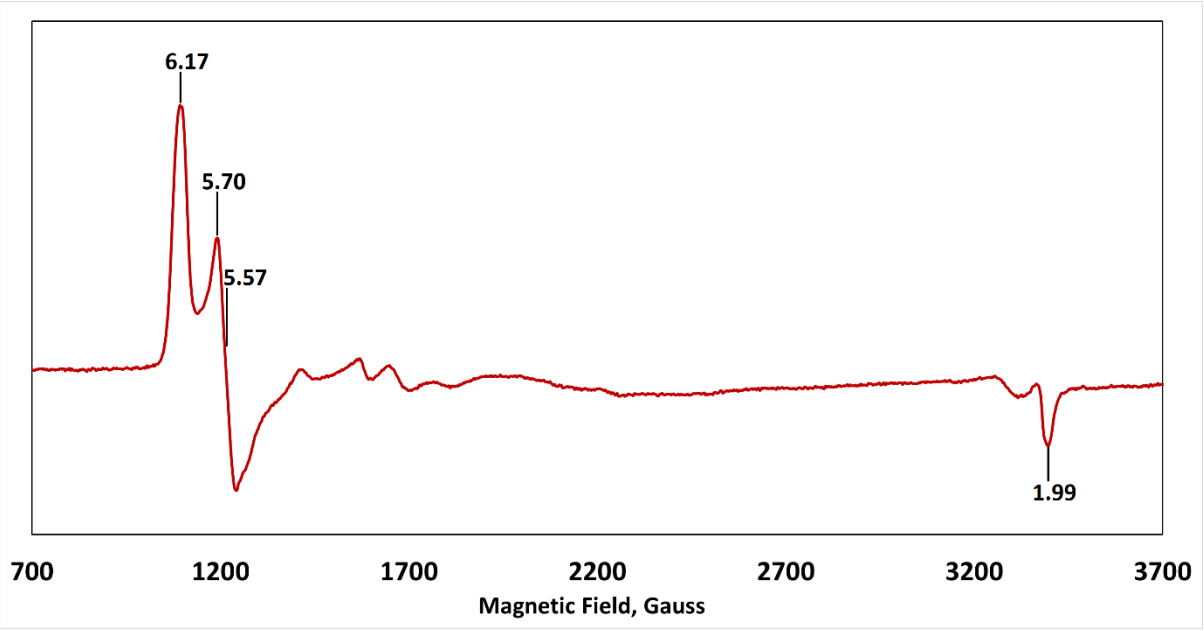

Figure 2.13. EPR spectrum of *Mc*P460 at pH 7. The spectrum with g values of 6.17 and 5.70, 5.57 and 1.99 resembles that of *Ne*P460.

Table 2.1. UV-visible absorption maxima for cyts *c'* and P460

		λ_{max} (nm)			ref
Fe(III)					
*Ax*CP-α		396	500	643	a
*Mc*CP-β	379sh	399	499	640	tw
		401	502	638	b
*Mc*P460		419			tw
		419			c
*Ne*P460		434	510sh	540	d
*Ns*ALP460		440	576	628	e
Fe(II)					
*Ax*CP-α		427, 433sh	552		a
*Mc*CP-β	372	431	552		tw
		433	552		b
*Mc*P460		460			tw
*Ne*P460		462	660	668	d

Abbreviations: tw, this work. References: a (Yoshimura *et al.*, 1985), b (Zahn, Arciero et al. 1996), c (Zahn, Duncan et al. 1994), d (Bergmann and Hooper 2003), e (Smith and Lancaster 2018).

Table 2.2. EPR parameters for cyts P460 and cyt *c'*-β.

protein	pH	temp (K)	species	g⊥		g∥	ref
				g1	g2	g3	
P460							
*Mc*P460	7	10		6.17	5.57	1.99	tw
*Ne*P460	7	4		5.91	5.63	1.99	a
Cyt *c'*-β							
*Mc*CP-β	8	10	major	6.29	5.46	1.98	tw
			minor	6.00	5.34	1.98	tw

Abbreviations: tw, this work. References: a (Numata *et al.*, 1990).

2.3.3 Crystallisation and Data Collection of McCP and McP460

Purified *Mc*CP and *Mc*P460 were both buffer exchanged into 0.1 M HEPES buffer, pH 7.5 before being screened against a selection of pre-made crystallisation conditions. The trays of crystallisation screens and proteins were incubated at 18 °C and checked daily for crystals. For *Mc*CP a single crystal was observed in a condition containing 0.01 M $ZnSO_4$, 25 % PEG 550 (v/v) and 0.1 M MES, pH 6.5, whilst for *Mc*P460 a single crystal was observed in a condition containing 0.1 M Tris-HCl, 2.4 M ammonium sulfate pH 8. For each protein further screening was carried out around the condition, varying pH, salt concentration and protein to precipitate ratios to obtain crystals of a size suitable for single crystal X-ray crystallography. The final conditions for each protein were: for *Mc*CP, 2 µl of 15 mg/ml protein in 0.1 M HEPES buffer, pH 7.5, with an equivalent volume of reservoir solution containing 0.01 M $ZnSO_4$, 35 % PEG 550 (v/v) and 0.1 M MES, pH 6.5 and for *Mc*P460 2 µl of 15 mg/ml protein in 0.1 M HEPES buffer, pH 7.5, with an equivalent volume of reservoir solution containing 0.1 M Tris, 2.4 M ammonium sulfate pH 8. For wt *Mc*CP this resulted in brown, cubic shaped crystals around 10 µM in length and for wt *Mc*P460 green orthorhombic crystals which were grown at 18 °C using the hanging drop vapour diffusion method. The crystals were cryo-protected using the reservoir solution and 1.7 M sodium malonate for *Mc*P460 or 10 % glycerol for *Mc*CP for 15 – 30 s and flash-cooled in liquid nitrogen.

Various cryoprotectants were initially trialled to establish the most suitable condition for each protein. These included 10-20 % glycerol, 10-10 % sucrose, 10-20 % glucose and 1.7 M sodium malonate. Several crystals for each protein were soaked in each cryoprotectant before flash freezing in liquid nitrogen and being sent to DLS. For the *Mc*CP crystals multiple different cryo-protected crystals diffracted, however the best resolution structures came from the 10 % (v/v) glycerol cryoprotectant soak and so this was chosen to use going forward. For the *Mc*P460 crystals diffraction was only seen with the 1.7 M sodium malonate soak.

Table 2.3. Data collection and processing statistics for the crystal structure of *Mc*CP and *Mc*P460

Dataset	*Mc*CP	*Mc*P460
Resolution (Å)	61.18 – 1.61	59.0-1.36
Space group	$P2_13$	$P2_12_12_1$
Unit cell, (Å)	a=b=c=106.0	a= 46.6 b= 81.6 c= 85.3
Unique reflections	52377	70585
Completeness (%)	99.9 (99.4)	99.9 (98.5)
Redundancy	7.6 (4.0)	5.4 (4.4)
R_{merge}	0.047 (0.93)	0.043 (1.048)
I/σ(I)	20.9 (1.4)	13.7 (1.2)
$CC_{1/2}$	0.99 (0.54)	1.00 (0.49)
Wilson B-factor ($Å^2$)	24.3	16.0
R_{work}	0.177	0.197
R_{free}	0.202	0.224
RMSD bond length (°)	0.015	0.021
RMSD bond angles (Å)	2.15	1.84
Ramachandran favoured (%)	96.1	94.6
PDB accession code	6HIH	6HIU

2.3.4 As-isolated McCP crystal structure

Brown cubic crystals of *Mc*CP were obtained after 3-5 days via the hanging drop vapour diffusion method (Figure 2.14). An initial dataset measured at a wavelength of 1.74 Å was used to solve the structure using the anomalous signal of the intrinsic heme Fe. A high resolution data set measured from a second *Mc*CP crystal was refined against this starting model to give a structure determined to 1.61 Å. Data collection and processing statistics can be seen in Table 2.3.

The as isolated structure of *Mc*CP displays a highly β-sheet fold that is quite unlike any known cytochrome *c'* structures (all previous examples being 4 α-helix bundles), yet very similar to *Mc*P460, (Figure 2.15). The crystallographic structure reveals that *Mc*CP is a dimer consisting of two chemically, but not structurally, identical monomers. The structure of each monomer consists of a twisted five-stranded antiparallel beta-sheet, three alpha helices and alpha helical turns (Figure 2.15 A).

The structure reveals a novel distal pocket structure. The distal pocket is largely hydrophobic, with two Phe residues located above the Fe in a position to sterically influence the binding of ligands (Figure 2.15 C). This residue arrangement is notably different to the single Phe residue found to lie near-parallel to and above the heme in certain *c'*-α structures (Figure 2.15 D). The proximal pocket contains the conserved haem ligand His 123 and an aromatic Phe 133 residue. This is different to *c'*-alphas where there would normally be a conserved positive, polar residue, however it is similar to the structure of *Ns*ALP460, which also has a phenylalanine in this position (Phe 150). The proximal heme ligand His 123 forms an H-bond to the carbonyl of Tyr 99. In contrast to the structure of cytochrome P460, no heme-protein crosslink is observed in the *c'*-β structure.

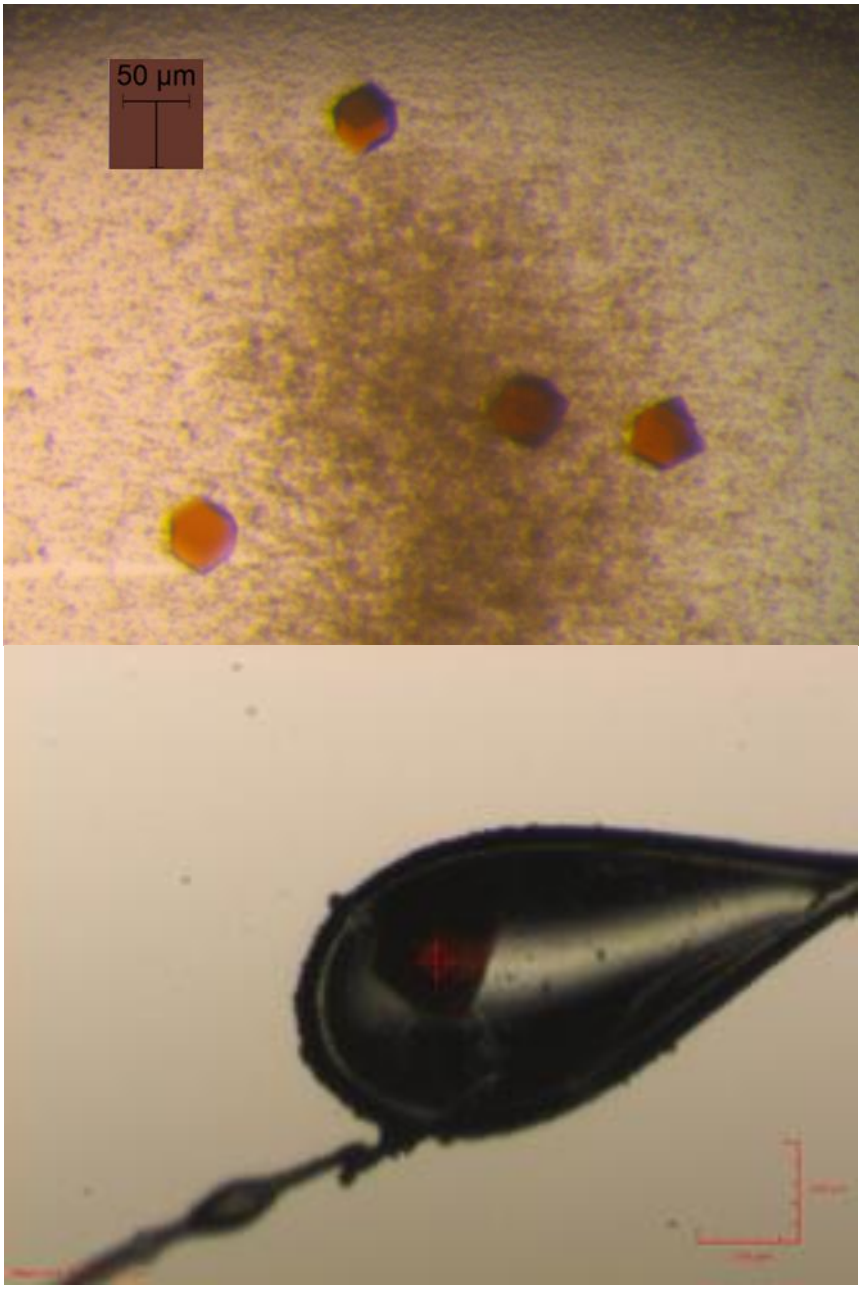

Figure 2.14. *Mc*CP forms brown cubic crystals after 3-5 days via the handing drop vapour diffusion method.

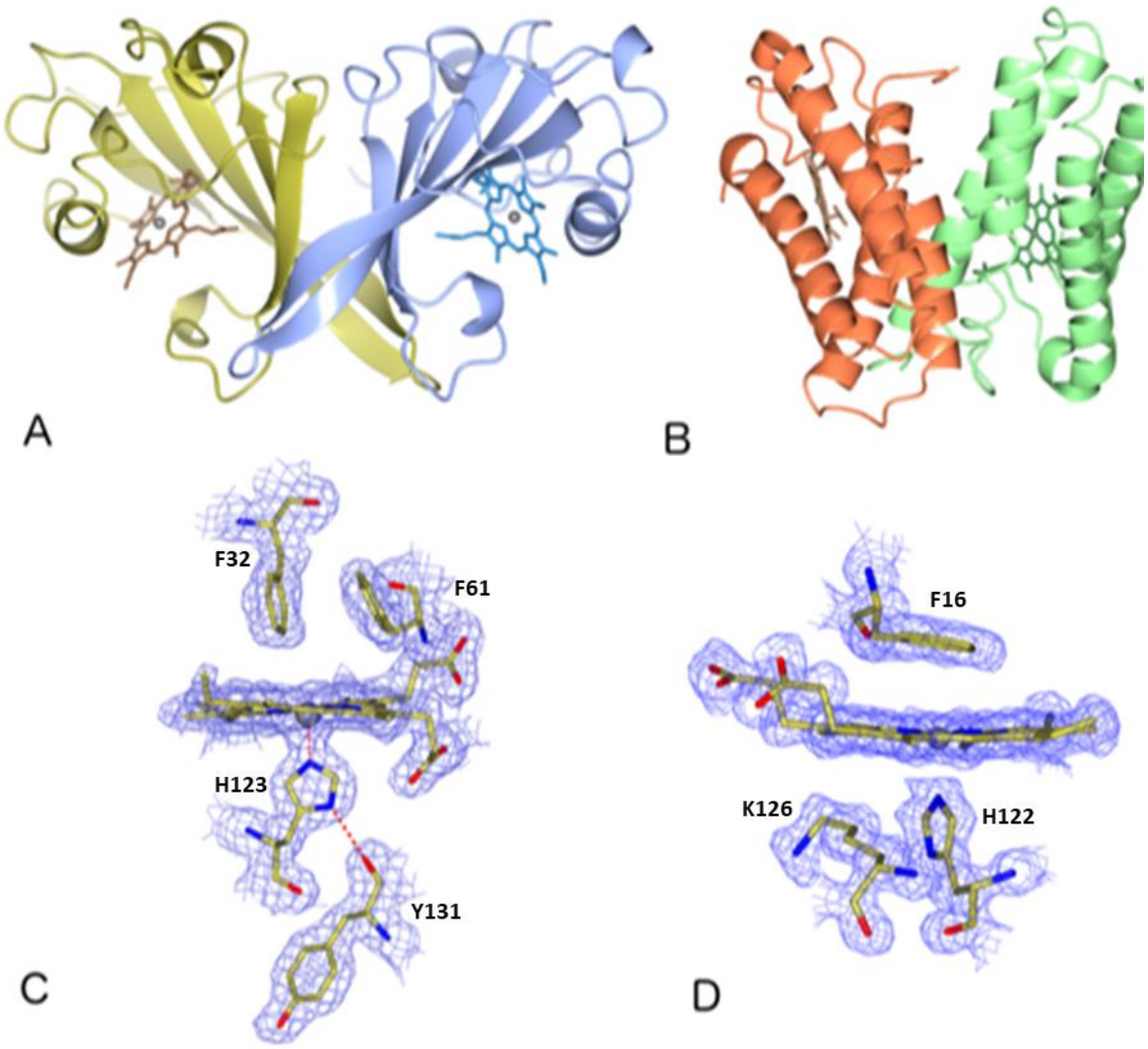

Figure 2.15. The homodimeric structures of (A) *Mc*CP showing the predominantly β-sheet fold and (B) *Sf*CP (PDB 4ULV) displaying the typical alpha helical bundle; (C) *2Fo-Fc* map contoured at 1.5 σ of the heme environment of *Mc*CP with the 'Phe Cap' of Phe 32 and Phe 61 sitting above the heme in the distal pocket (D) *2Fo-Fc* map contoured at 1.5 σ of the heme environment of *Sf*CP with Phe 16 lying near parallel to the heme in the distal pocket.

2.3.5 As-isolated McP460 crystal structure

Green orthorhombic crystals of *Mc*P460 were obtained after 4-5 days via the hanging drop vapour diffusion method (Figure 2.16). Data measured at Diamond Light Source at a wavelength of 0.979 Å was processed using DIALS and the structure solved with an initial SAD electron density map measured at a wavelength of 1.74 Å being used as the target for molecular replacement with the structure of *Ne*P460 (PDB 2JE3) (Pearson, Elmore et al. 2007) as the search model. The crystal structure of *Mc*P460 was determined to 1.36 Å resolution, revealing a highly β-sheet fold, similar to that of *Ne*P460, with which it may be superposed with an RMSD of 2.03 Å. *Mc*P460 exists as a homodimer with each monomer consisting of a twisted five-stranded antiparallel β-sheet, four α-helices and two helical turns, (Figure 2.17). As well as the two cysteines (Cys 140, Cys 143) of the CXXCH binding motif, a third covalent crosslink between Lys 78 and the 13'-*meso* carbon of the porphyrin ring is present. The distal heme pocket in *Mc*P460 is relatively exposed to solvent, with a significant number of positively charged and polar residues (Arg 43, Gln 46, Asn 48, Arg 50, Gln 100, Asp 102 and Arg 121). A water molecule is bound to the distal side of the heme at a distance of 2.26 Å to produce a 6-coordinate Fe. The proximal pocket contains the conserved haem ligand His 144, an aromatic Phe 154 residue and Met 104. The proximal heme ligand His 144 forms a H-bond to the carbonyl of Tyr 152. Using surface modelling tools (Figure 2.19 A), it can be seen that the distal side of the heme is easily accessible to solvent as there is a large opening on the side of the protein (around 11 Å wide). A narrower (4.7-6.5 Å) solvent filled channel is also present in the opposite side of the heme, created by the wrapping round of the lower loop of the other monomer leading from the propionate to the surrounding solvent.

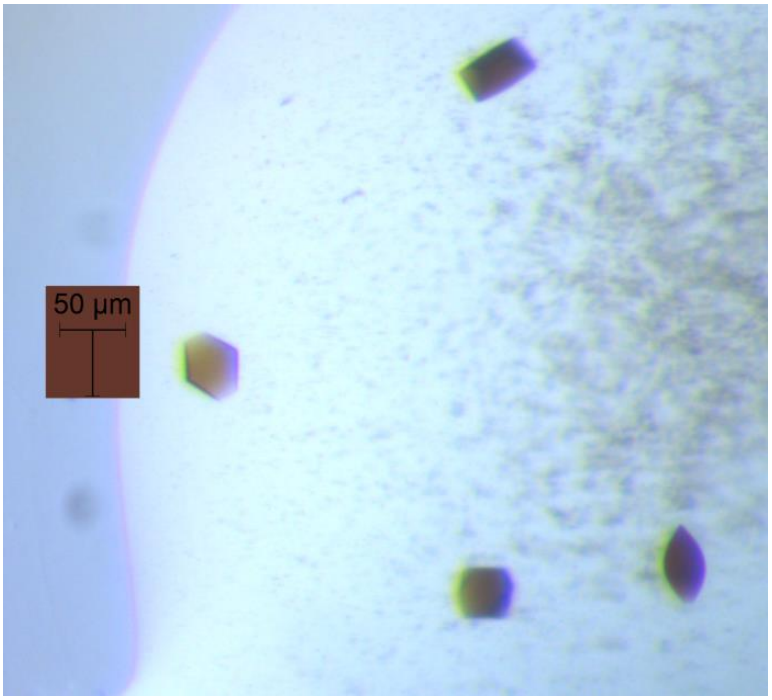

Figure 2.16. Green orthorhombic crystals of *Mc*P460 obtained after 4-5 days via the hanging drop vapour diffusion method.

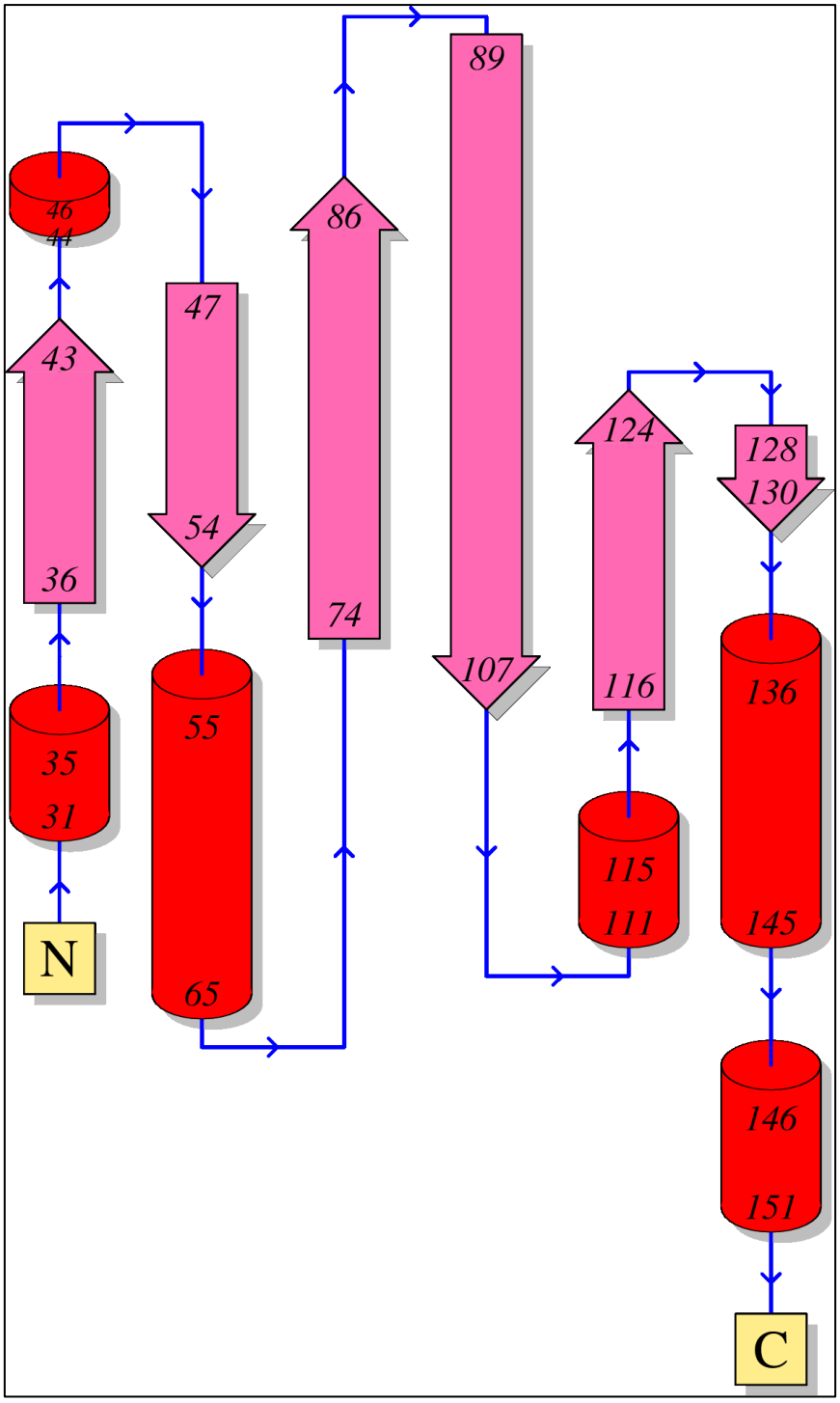

Figure 2.17. Schematic of *Mc*P460 monomer. Each monomer consists of a twisted five-stranded antiparallel β-sheet, four α-helices and two helical turns

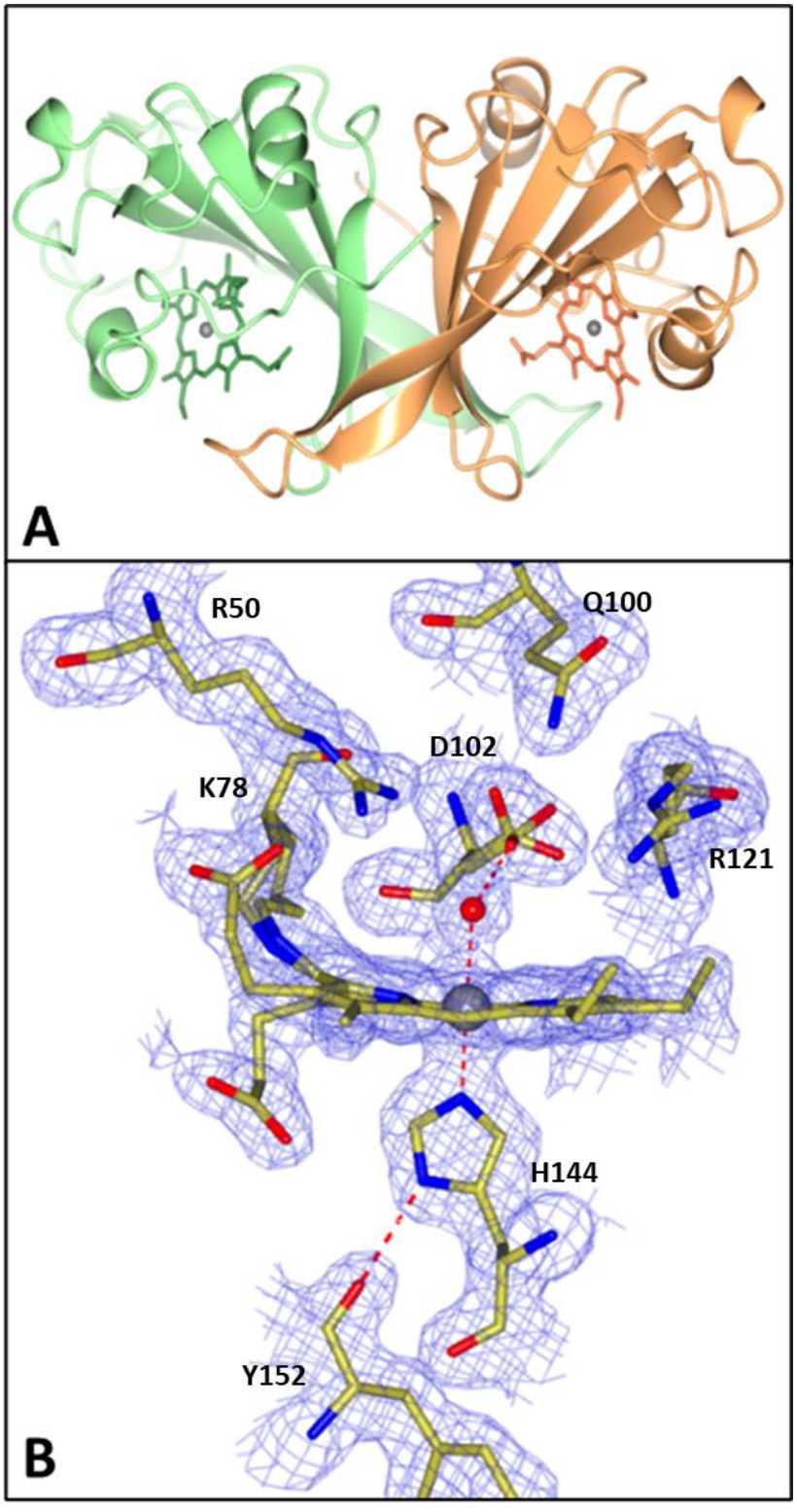

Figure 2.18. The homodimeric structure of (A) *Mc*P460 showing the predominantly β-sheet fold; (B) *2Fo-Fc* map contoured at 1.5 σ of the heme environment of *Mc*P460 with the distal water ligand and hydrophilic, charged pocket with several Arg and Asp residues in a position to interact with bound substrates.

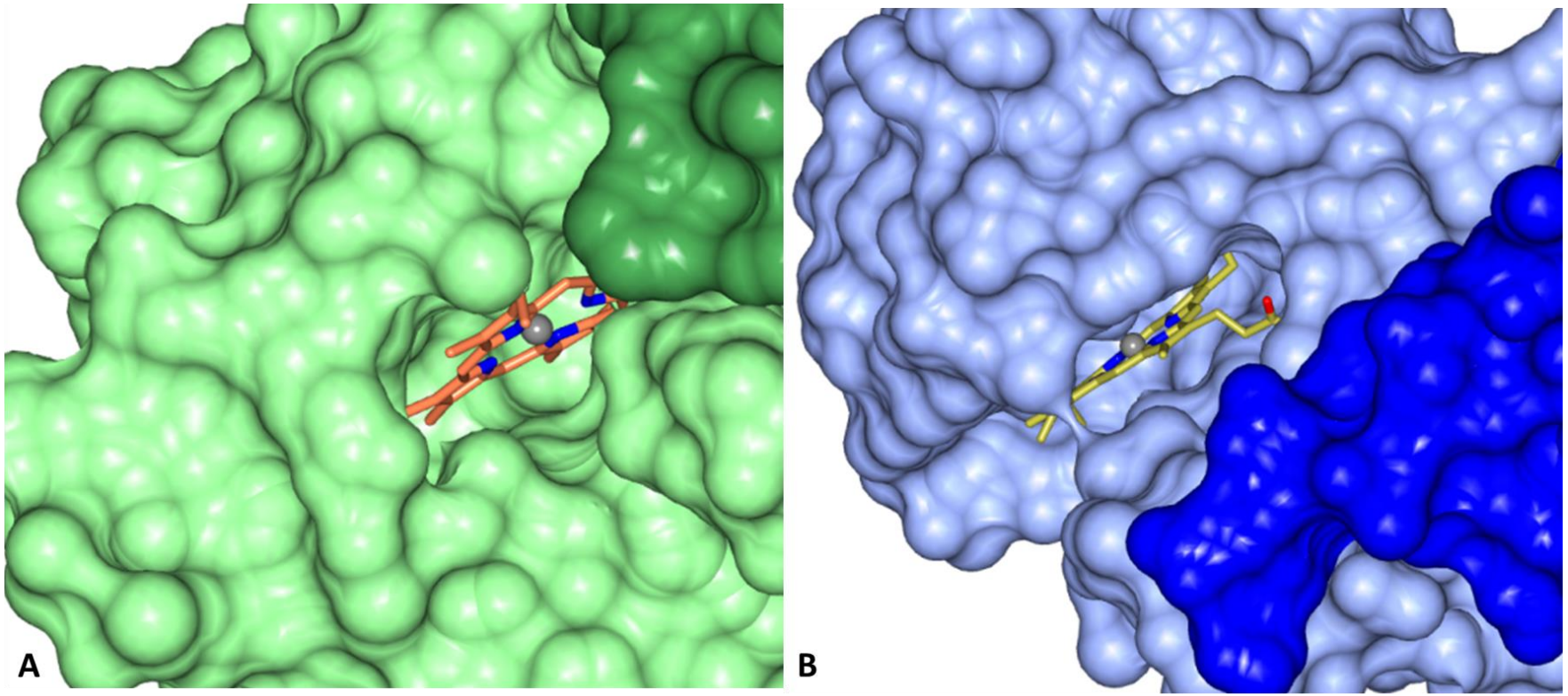

Figure 2.19. Accessibility of the heme within *Mc*P460 monomer (A). Accessibility of the heme within *Mc*CP monomer (B), light and dark colours represent each monomer.

2.3.6 Normal-Coordinate Structural Decomposition

Previously reported data (Smith and Lancaster 2018) from the structures of *Ns*ALP460 (6AMG) and *Ne*P460 (J2E3) using normal-coordinate structural decomposition (NSD) (Graves, Graves et al. 2016) showed that both had a high degree of distortion away from planarity in the heme and that there was an almost equal amount of ruffling (B1u) and saddling (B2u) distortion (Smith and Lancaster 2018). This data analysis has now been extended to include *Mc*P460, *Mc*CP and HAO (Figure 2.20, Table 2.4). *Ne*HAO has the highest level of Doop suggesting it's heme has the highest overall distortions from planetary. The next highest is *N*sALP460, followed by *Ne*P460, *Mc*P460 and finally *Mc*CP. Interestingly, *Mc*P460 and *Mc*CP have similar levels of overall distortion at 0.798 Å and 0.718 Å respectively. *Ne*HAO demonstrates the highest level of ruffling with the three P460 enzymes all having a slightly lower amount although at a similar level to each other. However, *Ne*P460 and *Ns*AL2P460 demonstrate their ruffling in a negative way away from planetary unlike both *Ne*HAO and *Mc*P460 where the ruffling is higher than planetary. *Mc*CP in contrast only displays a very low level of ruffling. Unlike *Ne*HAO both *Ne*P460 and *Ns*ALP460 demonstrate a high level of saddling. *Mc*P460 displays a smaller amount of saddling and like *Ne*HAO this is displacement is negative. *Mc*CP displays a level of ruffling more similar to *Ne*P460 and *Ns*ALP460 but again the displacement is negative. All the P460 proteins and *Ne*HAO display waving distortions, unlike *Mc*CP which only has a very small amount. This is highest in the x plane and is only in a positive direction in *Mc*P460. In this plane *Ne*P460 displays the greatest deviation from planetary, followed by *Ne*HAO, *Ns*ALP460 and *Mc*P460 respectively. There are less waving distortions in the y plane, which are again greatest in *Ne*HAO with *Ne*P460, *Ns*ALP460 and *Mc*P460 all showing a slightly lower but similar level to each other. *Mc*P460 does not demonstrate any doming distortions,

which are seen in *Ne*HAO and to a slightly lesser extent in *Ns*ALP460 and *Ne*P460. A very small amount of doming is seen in *McC*P. Only a very small amount of propellering is seen in any of the P460 enzymes. There is twice as much seen in the *Ne*HAO heme and very little seen in *Mc*CP.

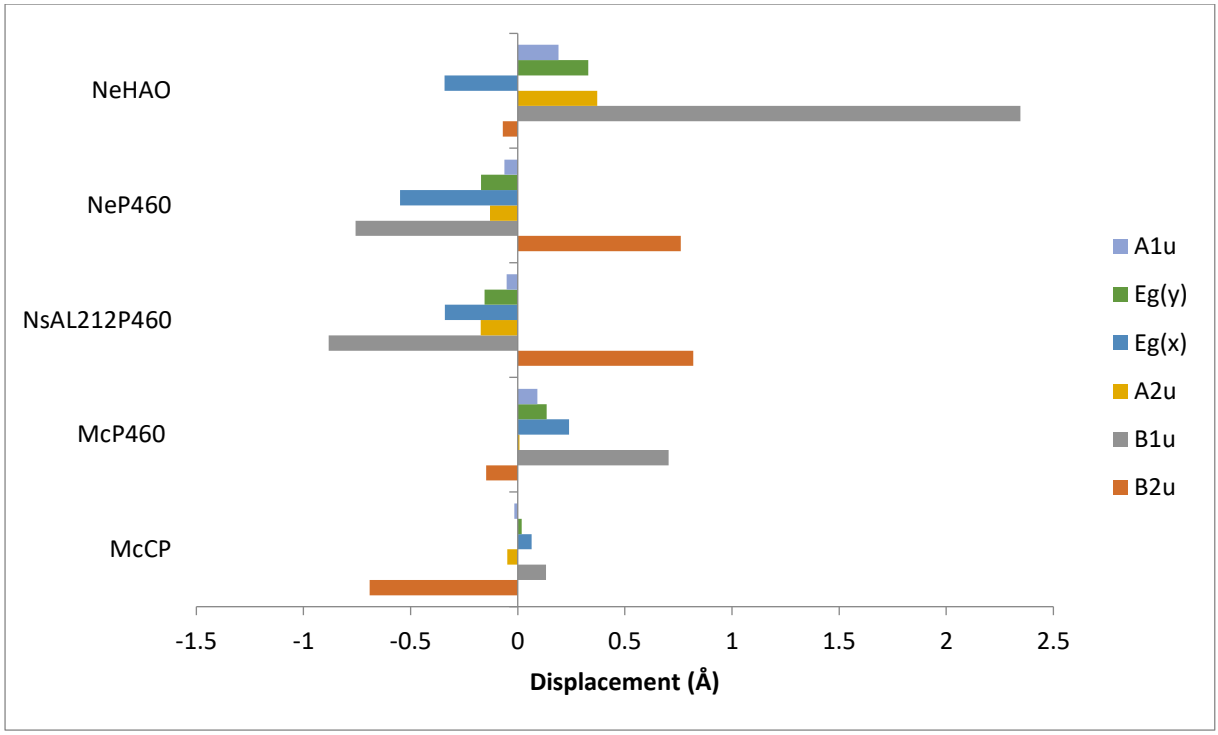

Figure 2.20. Out-of-plane displacements (minimal basis) for the hemes of *M. capsulatus (Bath)* cytochrome *c'* (6HIH), *M. capsulatus (Bath)* P460 (6HIU), *Nitrosomonas* sp. AL212 P460 (6AMG), *N. europaea* P460 (J2E3) and the P460 heme of *N. europaea* HAO (4FAS). Out of plane distortions are characterized in terms of displacements along the normal coordinates of the D_{4h}-symmetric porphyrin macrocycle. *Nitrosomonas* sp. AL212 and *N. europaea* P460 display much higher overall distortions to both *M. capsulatus (Bath)* cytochromes. *Mc*P460 displays a high amount of ruffling (B1u) which has been proposed to be important in the function of the P460 cytochromes (Smith and Lancaster 2018). In comparison to the other two cytochromes P460, *Mc*P460 does not have an equal amount of ruffling and saddling, a pattern that is more similar to that of the P460 heme of *N. europaea* HAO. *Mc*CP correspondingly does not display a high level of ruffling, although it does demonstrate a large amount of saddling (B2u).

Table 2.4. Normal-Coordinate Structural Decomposition for the hemes of *Mc*P460 (6HIU), *Mc*CP (6HIH), *Ns*ALP460 (6AMG) *Ne*P460 (J2E3) and the P460 heme of *Ne*HAO (4FAS), showing the level of deviation from planarity of the heme from saddling (B2u), ruffling (B1u), doming (A2u), waving (Eg(x) and Eg(y)) and propellering (A1u). Doop refers to the overall out-of-plane distortions (in Å).

Protein	Basis	Doop	B2u	B1u	A2u	Eg(x)	Eg(y)	A1u
*Mc*P460	Min.	0.774	-0.147	0.704	0.008	0.240	0.135	0.092
	Comp.	0.798	0.147	0.712	0.082	0.264	0.160	0.092
*Mc*CP-β	Min.	0.705	-0.691	0.131	-0.048	0.064	0.019	-0.016
	Comp.	0.718	0.702	0.131	0.056	0.064	0.037	0.021
*Ns*ALP460	Min.	1.271	0.819	-0.882	-0.172	-0.339	-0.154	-0.051
	Comp.	1.296	0.822	0.886	0.253	0.345	0.195	0.054
*Ne*P460	Min.	1.224	0.761	-0.756	-0.130	-0.548	-0.171	-0.062
	Comp.	1.250	0.782	0.766	0.142	0.558	0.172	0.066
*Ne*HAO	Min.	2.428	-0.070	2.346	0.371	-0.342	0.328	0.189
	Comp.	2.456	0.140	2.355	0.385	0.370	0.379	0.212

2.3.8 Bioinformatic analysis

In *M. capsulat*us (Bath), *Mc*CP has 31 % sequence identity to cyt P460 and possesses 18% identity to CytP460 from *N. europaea*. In contrast, Cyt *c'*-β from this organism has very low sequence homology to the well-characterised Cyt *c'*-α proteins. A maximum likelihood phylogenetic tree clearly shows that Cyt *c'*-α belong to a different evolutionary path than that of Cyt *c'*-β and the cyts P460 (Figure 2.21). The cyt P460 family has two distinct evolutionary paths. The largest group of P460 sequences (which includes *Mc*P460) follows a well-separated branch to the cyts *c'*-β. A smaller group of P460 sequences are more closely related to the cyts *c'*-β, being located on the same branch and contains both *Ne*P460 and *Ns*ALP460. It can be inferred from this result that the Cyt *c'*-β proteins evolved from the cyt P460.

There are 14 organisms within the aligned sequences which possess both a cyt P460 and a Cyt *c'*-β sequence. These genes are not close to each other on the genome, arguing against a recent gene duplication event. In all but two of these (*Nitrosococcus halophilus and Methylomonas methanica*) the cyt P460 sequences are placed on the branch that is separated from the cyts *c'*-β. No organisms identified in our study have both a Cyt *c'*-β and a Cyt *c'*-α or indeed a cyt P460 and Cyt *c'*-α.

There is low sequence conservation within the cyt *c'*-β family, with 7 other residues being fully conserved across the 52 aligned Cyt *c'*-β sequences (Trp 14, Gly 34, His 36, Tyr 39, Met 84, Thr 94, Trp 97 in *Mc*CP). This is similar to the low conservation of sequence in the Cyt *c'*-α (Ambler, Bartsch et al. 1981). Between the two Cyt *c'* families (alpha and beta) the only conservation is in the CXXCH motif. Phe 32 is highly conserved within the Cyt *c'*-β, being present in all but one of the aligned sequences (*Meiothermus ruber*). Phe 61 is slightly less conserved with the residue being present in 39 of the sequences, however all are

hydrophobic residues. The highly hydrophobic and sterically crowded distal pockets of the Cyts *c'*-α are important in their ability to discriminate between gaseous ligands by allowing small neutral ligands, such as NO and CO to bind to the heme. The importance of this type of residue within the Cyt *c'*-α family and the high conservation of Phe 32 and Phe 61 in Cyt *c'*-β is suggestive of a similar (NO) gas-binding function.

Whilst Tyr 131 in the proximal pocket is only conserved in just over two thirds of the Cyt *c'*-β sequences (36 out of 52), all other residues are hydrophobic (either Phe or Leu). Phe 133 is conserved in 38 of the 52 Cyt *c'*-β sequences suggesting the type of residue found in the proximal pocket, in comparison to the cyts *c'*-α, may be conserved across the Cyt *c'*-β.

Alignment of all 144 CytP460 sequences showed full conservation of only 5 residues (Trp 24, Gly 73, Lys 78, Lys 115 and Trp 127 in *Mc*P460) along with the CXXCH motif. The conserved lysine crosslink in cyt P460 has been shown to be important in relation to the catalytic ability of the protein (Bergmann and Hooper 2003), whilst most of the other conserved residues are, in the P460 0f *N. europaea*, clustered at the base of the monomer (Pearson, Elmore et al. 2007). The group of P460s that appear more closely related to the cyts *c'*-β have a higher level of homology to each other with an additional 20 conserved residues. The residues present in the distal pocket of *Ns*ALP460 (Phe 76 and His 80), are highly conserved within this subgroup (being present in 45 and 39 of the sequences respectively) with the alternative residues having the same properties suggesting an importance of this type of residue.

The other group of P460s (containing *Mc*P460) show five further conserved residues (Arg 50, Asn 55, Ala 58, Pro 71, Met 104 in *Mc*P460) when aligned together in comparison to the alignment of all 144 Cyt P460 sequences. Two of these residues are positioned near the heme of *Mc*P460, Met 104 being to the side of the heme in the proximal pocket and Arg 50 sitting

directly above the heme in the distal pocket. The type of residue in the distal pocket for this subgroup of P460s appears reasonably conserved with the majority of them being charged, hydrophilic, polar residues. Arg 43 for example is present in 85 (out of 95) of these sequences. As previously shown (Elmore, Bergmann et al. 2007), most of the P460 and Cyt *c'*-β sequences are from a wide range of Proteobacteria.

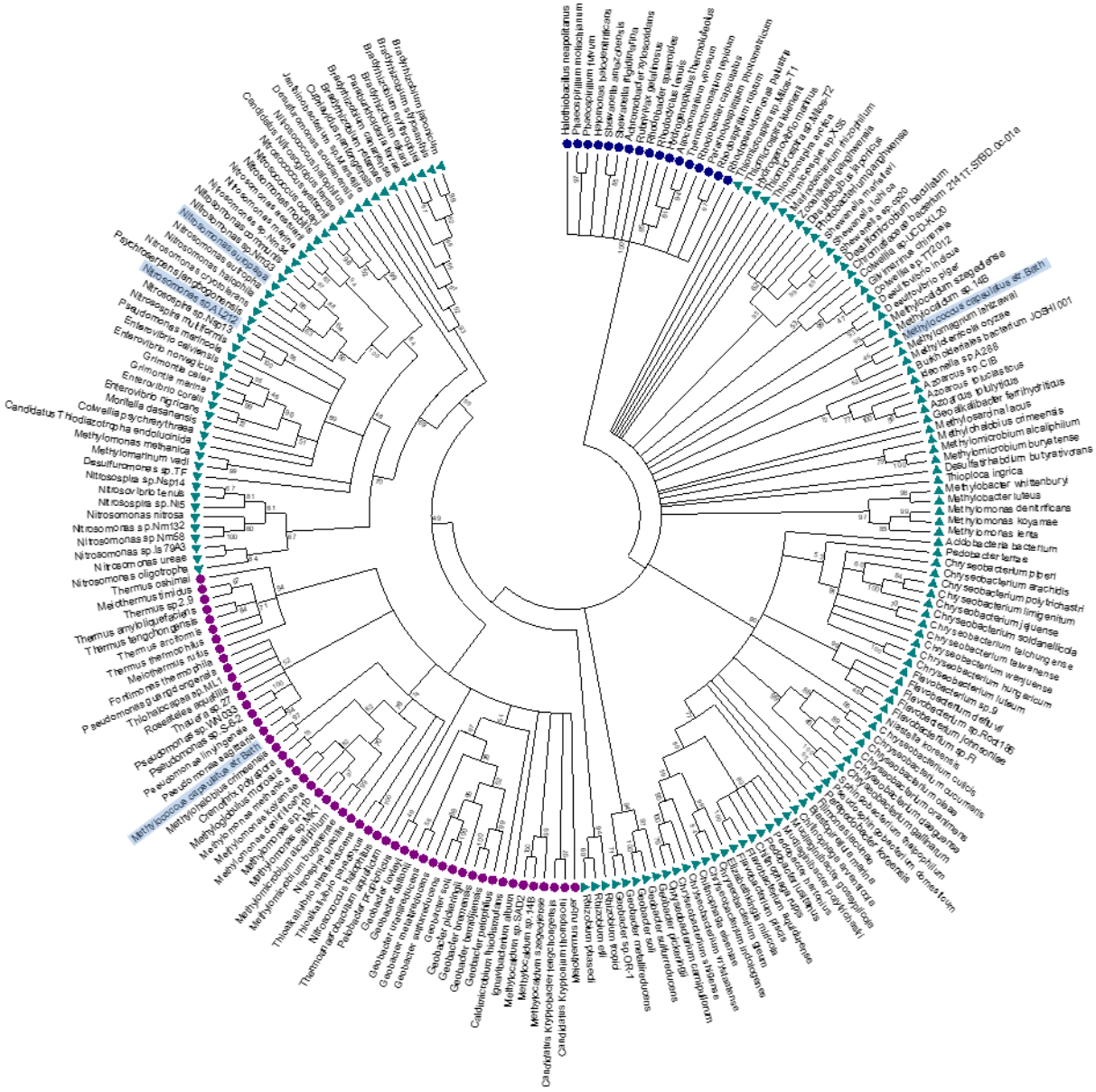

Figure 2.21. Maximum likelihood tree of cyt *c'*-α (blue circles), cyt *c'*-β (purple circles) and cyt P460 (green triangles) sequences. The Cyt *c'*-α genes are on a separate branch to the the Cyt *c'*-β and the cyts P460 genes. The cyt P460 family displays a paraphyletic structure, with a monophyletic Cyt *c'*-β nested within suggesting that the Cyt *c'*-β evolved from the cyt P460. Image was prepared using Mega7

2.4 Discussion

Recombinant *Mc*CP and *Mc*P460 were expressed, purified and analysed in order to extensively characterise each protein. UV-visible spectra of the ferric and ferrous states of *Mc*CP were similar to those previously reported (Zahn, Duncan and DiSpirito, 1994). The as isolated ferric EPR spectra showed that ferric *Mc*CP exists as two pure high spin (HS) species (S=5/2), the proportions of which do not change over varying pH. Previous work by Zahn et al also suggested two HS species were present however they also suggested that at pH 4 there was a small population of intermediate spin (QS) state (S=3/2) at around 15 %. Cytochromes *c'*-αs have been shown to exist in the ferric state as either pure HS or a mixture of HS/QS with the proportion of HS increasing at more alkaline pH, which fits with the proposal of a QS population in the pH 4 samples. This however is not corroborated by our current data where multiple data sets at different concentrations all suggest HS species. This is corroborated by the UV-visible data of the Soret maxima at 399 nm, with an unresolved α/β band near 500 nm and a CT1 band at around 640 nm which is characteristic of a 5c HS ferric heme and published RR data which showed spin-state frequencies close to those attributed to the 5cHS Fe(III) states of the *c'*-αs (Adams *et al.*, 2019).

Spectroscopically the only difference between *Mc*P460 and the other P460s is the slight blue shift in the as isolated UV-visible spectrum. This has been suggested to arise from a water molecule bound to the *Mc*CP in the as isolated structure. All other spectral features reported in this chapter are similar to those reported for *Ne*P460 and *Ns*ALP460. Spectral qualities of ligand bound P460's will be discussed in Chapter 5.

X-ray crystallography showed *Mc*CP and *Mc*P460 to have a structure that could be superimposed with an RMSD of 1.6 Å (Figure 2.22). The overall tertiary structure of the two proteins are very similar with the biggest discernible differences being within the distal

pockets suggesting that the two proteins are indeed related to each other. The phylogenetic analysis supports the theory that the two proteins are closely related, with the cyt *c'*-β having evolved from the cyt-P460s.

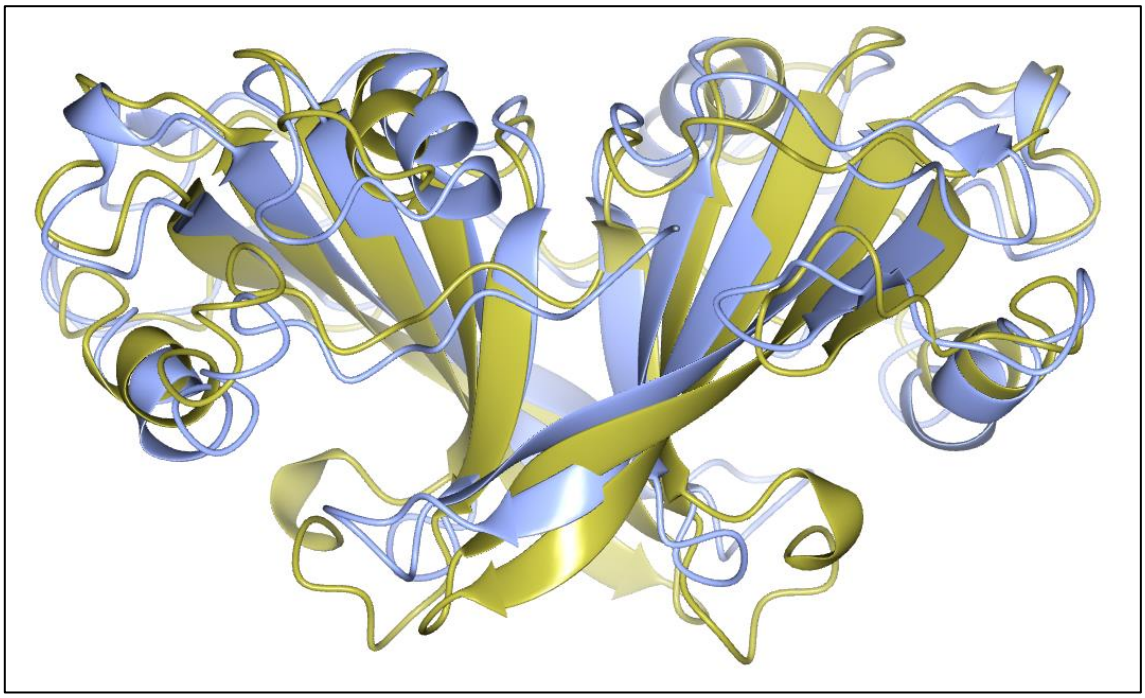

Figure 2.22. Superimposition of *Mc*CP (gold) and *Mc*P460 (blue) overall structure demonstrating the high level of similarity of the overall protein fold.

*Mc*CP displayed a highly β-sheet structure that is quite unlike any cytochrome *c'* structure that had been resolved previously whilst maintaining spectral properties that are very similar to cytochromes *c'*-α. Since publication of the *Mc*CP structure several other *c'*-β structures have been published which all consist of similar highly β-sheet monomers (Yoshimi *et al.*, 2022) (Abendroth *et al.*, 2022) although the arrangement of these monomers within the asymmetric unit is reported to be different in *Ne*CP-^{met} (where the interface is on the opposite

side to *Mc*CP and *Tt*CP). The biological assembly for these proteins is assumed to be similar to that seen in the asymmetric unit as currently no data has been published to suggest otherwise. This suggests that the tertiary structure of these proteins is not necessarily a key factor in their spectral properties or ability to carry out their function. Whilst *Mc*CP is the first reported *c'* structure to have two phenylalanine residues sitting in a capping position above the heme in the distal pocket, their placement could behave in a similar manner to residues found above the heme in the cytochromes *c'*-α. The highly hydrophobic and sterically crowded distal pockets are important in their ability to discriminate between gaseous ligands by allowing small neutral ligands, such as NO and CO to bind to the heme. The cyt *c'*-α family of proteins occur in denitrifying, photosynthetic, methanotrophic, sulphur-oxidising and nitrogen-fixing bacteria. In each of these groups, the ability to bind NO may have functional importance. In denitrifiers, NO is produced by nitrite reductases (NiRs) and further reduced to N_2O by nitric oxide reductase (NOR) enzymes. It has been proposed that cyt *c'*-α could act as a shuttle carrying this potentially dangerous free radical from NiR to the membrane bound NOR. There is also evidence that cyt *c'*-α could itself act as an NO-reductase. Studies suggesting that HAO produces NO as an end product (Hooper and Terry, 1979) (Poret-Peterson *et al.*, 2008) suggests a role for an NO sequestering protein such as *Mc*CP to work in concert with HAO to deal with excessive NO levels. The introduction of a hydrophobic distal heme environment by evolution in the cyt *c'*-β family is consistent with a functional requirement for the heme to selectively bind NO. It has already been shown that *Mc*CP can bind NO and CO (Zahn *et al.*, 1996) and these reactions will be further investigated in Chapter 4.

Two further *c'*-β structures have been made available since the publication of the *Mc*CP structure, one from *Nitrosomonas europaea* and one from *Thermus thermophilus* (*Tt*CP) (Yoshimi *et al.*, 2022), (Abendroth *et al.*, 2022). Both structures display a similar highly beta

sheet tertiary structure as seen in *Mc*CP but whilst *Tt*CP shares the 'Phe Cap' of *Mc*CP, the *c'*-β from *Nitrosomonas* does not (Figure 2.23). *Tt*CP can be superimposed to *Mc*CP with an RMSD of 1.94 Å with the greatest difference in the structures being around the interface between the two subunits of the dimer. *Thermus thermophilus* is a thermophilic bacteria with an optimum growth temperature of 72 °C and it has been suggested that the difference in the structure along the interface may give rise to greater stability of the *Tt*CP structure at higher temperatures (Yoshimi *et al.*, 2022). The other published *c'*-β structure has an arginine and methionine residue sitting over the distal face of the heme instead of the 'Phe cap' seen in *Mc*CP and *Tt*CP. The methionine residue is in the equivalent position to the lysine crosslink seen in P460s and so the protein was named as a *c'*-β-^{Met} (Abendroth *et al.*, 2022). The tertiary structure of the individual subunits appear to be similar for *Mc*CP and *Ne c'*-β-^{Met}, however the packing arrangement of the subunits in the crystals appear to be different with the interface between the subunits being on the side of the subunit on which the heme is placed, whilst in *Mc*CP, and indeed all other published *c'*-β or P460 structures, it is along the opposite side of the subunit. The reasons for this difference in subunit packing is yet to be determined. The spectral qualities of *Tt*CP were similar to that of *Mc*CP whilst those of *Ne c'*-β-^{Met} again showed differences. The *Ne c'*-β-^{Met} protein had similar ferric, ferrous and CO bound spectra, but unlike *Mc*CP it bound cyanide and also reacted with H_2O_2 to give rise to spectra similar to that seen for horseradish peroxidase (Liew *et al.*, 2020). This peroxidase like activity, which is not seen in *Mc*CP, is believed to be brought about by the lack of a crosslink and the presence of charged residues in the distal pocket positioned to interact with the peroxide molecule. This will be further discussed in Chapter 5.

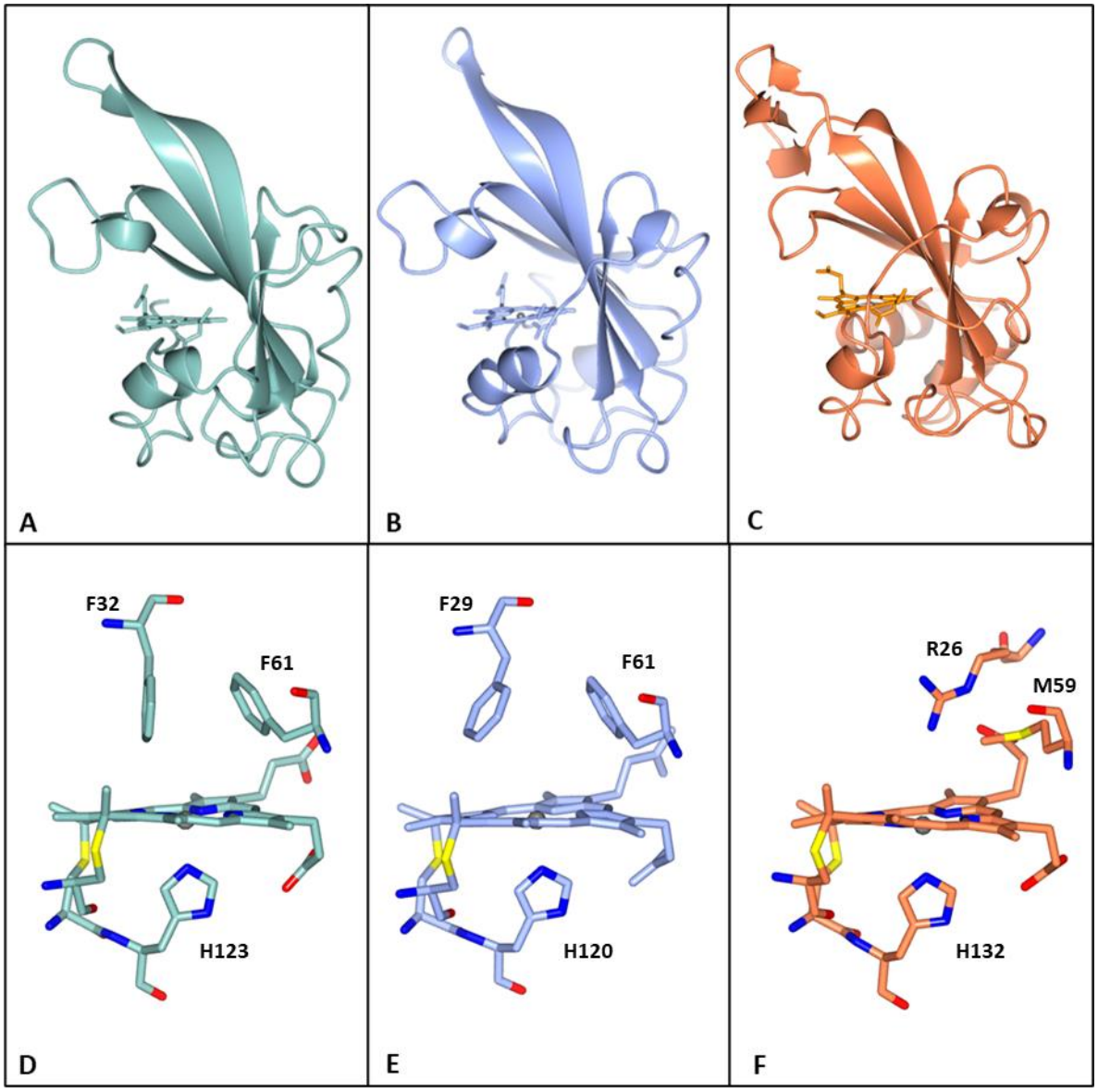

Figure 2.23. Overall structure of monomers and pocket residues from *Mc*CP (A, D), *Tt*CP (7EAD) (B, E) and *Ne c'*-β-^{met} (7S5O) (C, F). *Mc*CP and *Tt*CP have both very similar overall and pocket structures. *Ne c'*-β-^{met} whilst having a beta-sheet structure displays some differences to the other two proteins and has a different distal pocket with more charged residues instead of the 'Phe cap'.

The structure of *Mc*P460 exhibits some significant differences with those of previously determined P460 structures (Figure 2.24). In particular, *Ns*ALP460 has a much more hydrophobic distal pocket environment than *Ne*P460 or *Mc*P460, without residues likely to form a stabilising hydrogen bond to distal ligands. Indeed, in certain respects, the *Ns*ALP460 structure resembles *Mc*CP as much as it does *Ne*P460 or *Mc*P460.

Whilst *Mc*CP has the 'Phe cap' positioned to provide steric hindrance to distal ligand binding, the charged and highly hydrophilic distal pocket of *Mc*P460 is consistent with other P460 structures. However, aside from the lysine crosslink these individual pocket residues are not highly conserved across the P460 family, suggesting that the general properties of the residues present may of be more importance. Removal of a Glu residue in *Ne*P460 has been shown to stop the catalytic ability of the protein, whilst the introduction of this residue into the catalytically inactive *Ns*ALP460 created a catalytically active protein (Coleman, Vilbert and Lancaster, 2020). The equivalent residue in *Mc*P460 is an Asp residue and so has very similar properties to the Glu residue in *Ne*P460 suggesting it could carry out the same role of serving as a proton relay to effect oxidation of NH_2OH. On the other side of the crosslink, the equivalent residue to Arg 50 in *Mc*P460 has been shown to be involved in stabilising the heme through the propionate in *Ne*P460. Other residues, such as Arg 43 do not have an equivalent residue in a similar position in the published P460 structures and so their potential role in the distal pocket is yet to be elucidated. The importance of these residues will be further investigated in Chapter 5.

The proximal pocket of *Mc*P460 is quite similar to that of *Ne*P460 and *Ns*ALP460, a minor difference being that the His ligand of *Mc*P460 is H-bonded to a Tyr peptide carbonyl, whereas the His ligands of *Ne*P460 and *Ns*ALP460 are H-bonded to a Met carbonyl.

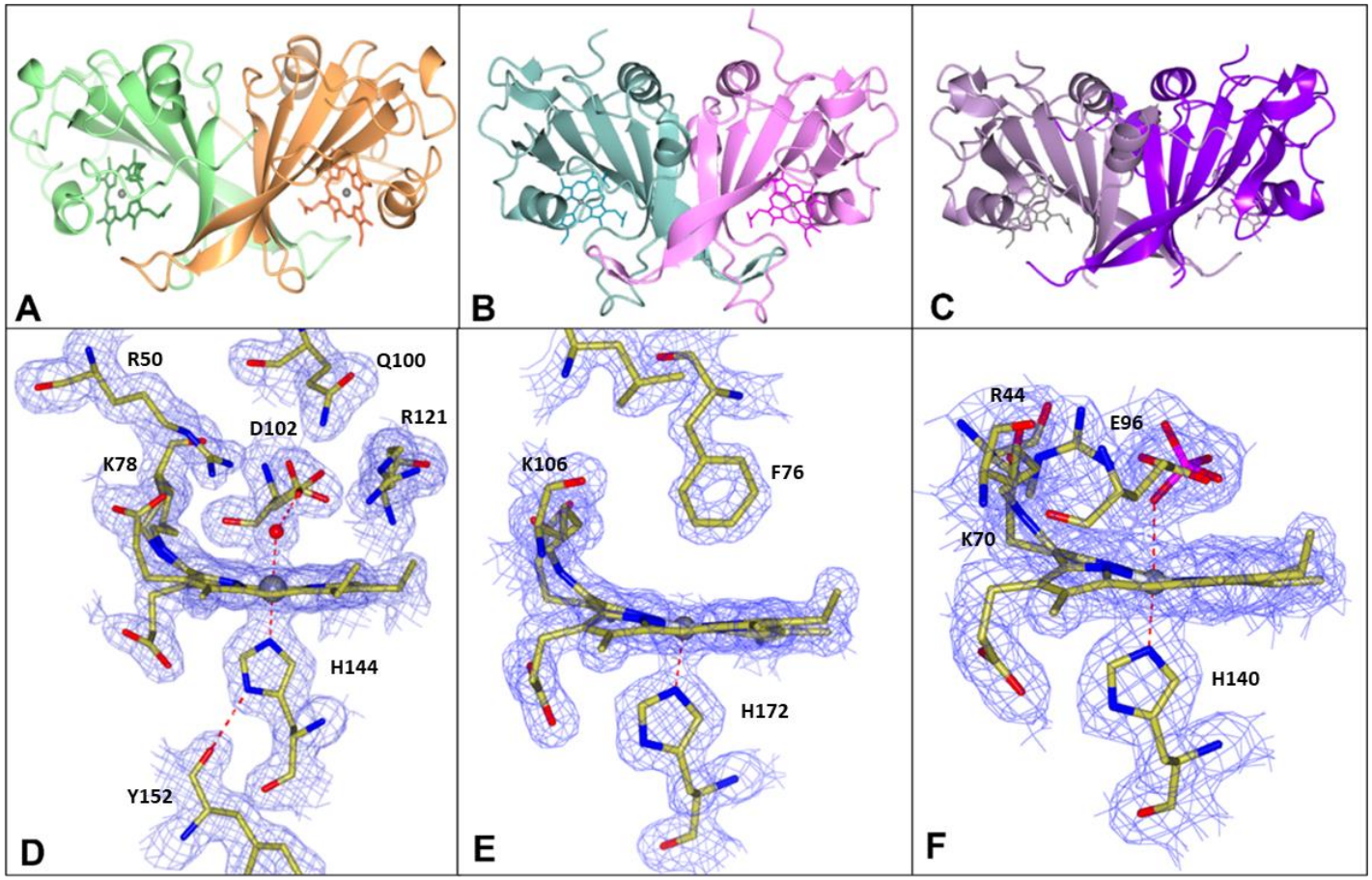

Figure 2.24. The homodimeric structures of (A) *Mc*P460, (B) *Ns*ALP460 (6AMG) and (C) *Ne*P460 (2JE3) showing the predominantly β-sheet fold. *2Fo-Fc* map contoured at 1.5 σ of (D) the heme environment of *Mc*P460 with the distal water ligand and hydrophilic, charged pocket with several Arg and Asp residues in a position to interact with bound substrates (E) the heme environment of *Ns*ALP460 displaying a much more hydrophobic distal pocket and (F) the heme environment of *Ne*P460.

P460 type hemes have been demonstrated to have significant amounts of heme distortion away from planarity (Coleman, Vilbert and Lancaster, 2020), (M. Bollmeyer *et al.*, 2023) (Figure 2.25). Normal-Coordinate Structural Decomposition is an analysis method that quantifies out-of-plane distortions of heme using vibrational normal coordiantes. Heme out-of-plane deformations can be described in terms of six distinct displacements from idealized D_{4h} symmetry: saddling, waving (along either the x or y axis) doming, ruffling and propellering. This analysis method can be applied to any set of Cartesian coordinates describing the three-dimensional structure of a molecule with a porphine moiety. This includes X-ray crystal structure data derived from the Protein Data Bank and molecular structures predicted by electronic structure calculations. NSD showed that *Mc*P460 demonstrates more heme distortion than normal c-type hemes, although it appears to have a lower level of distortion than any other reported P460s or HAO P460 hemes. The heme distortions are believed to be in part due to the extra crosslink to the P460 hemes, as demonstrated by (Coleman and Lancaster, 2020) where mutations to remove the crosslink in the HAO P460 heme and in *Ns*ALP460 resulted in less deviation from planarity. The crosslink lacking *Mc*CP unsurprisingly then also showed much less distortion than *Mc*P460. It has been proposed that properties such as lower reduction potentials (Liptak, Wen et al. 2010) and stronger bonding between the Fe and axial ligand (Kleingardner, Bowman et al. 2013) are due to an increased level of ruffling within the heme, suggesting that these distortions are important in the function of the P460 cytochromes. Properties such as the lower reduction potentials have been proposed to be the reason why HAO and P460 avoid auto-reduction upon NO binding, and indeed *Mc*CP has a much less negative reduction potential than either cyt P460 or HAO (HAO -260 mV, *Mc*P460 -300 to -380 mV and *Mc*CP -205 mV) (Hendrich *et al.*, 2001). The ability to maintain axial coordination has also been shown to be important in the enzymatic activity of cyt P460 (C. Vilbert, D. Caranto and

M. Lancaster, 2018). This would be in keeping with the proposed relationship between the level of ruffling and the function of the protein.

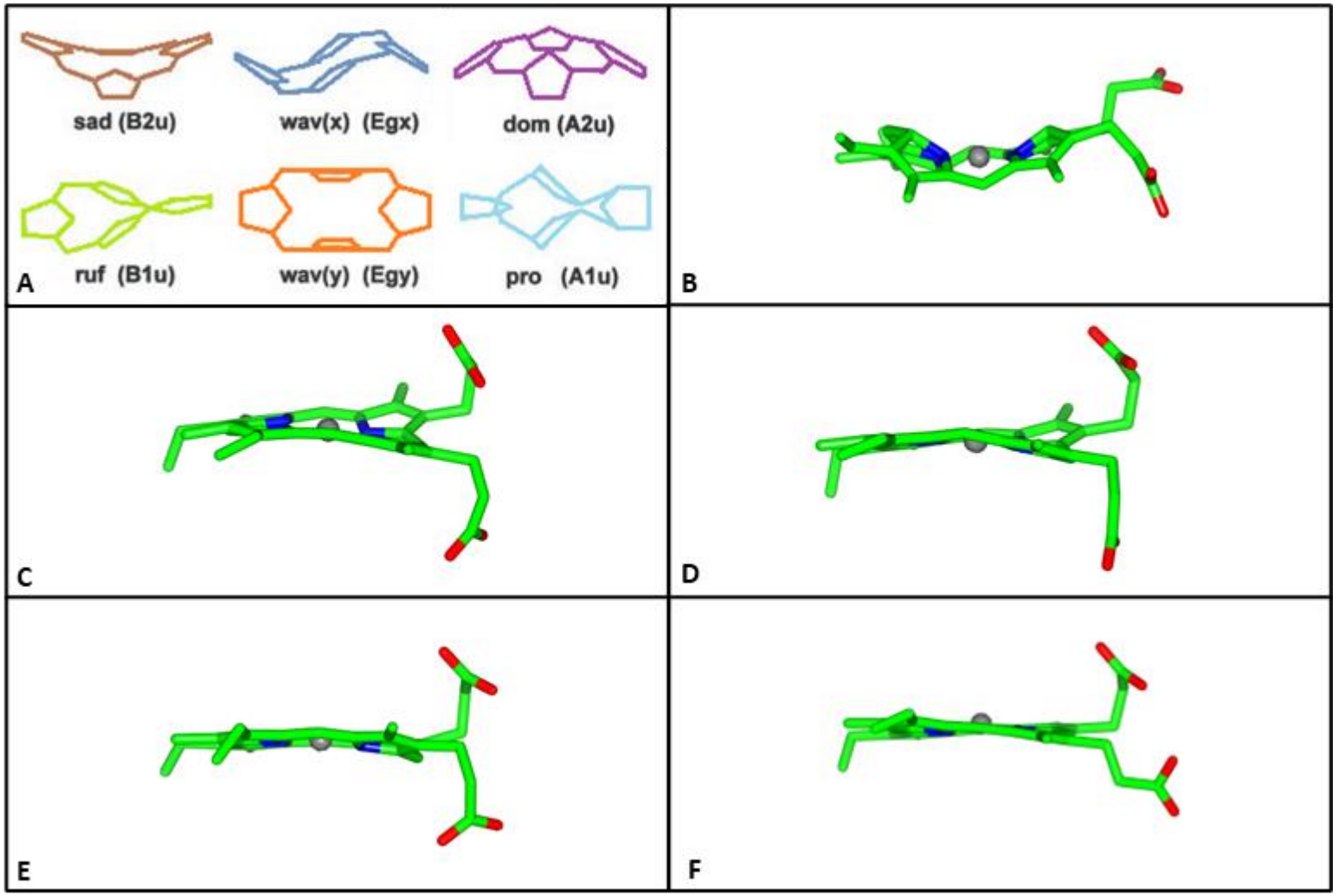

Figure 2.25. Heme distortions. The hemes of HAO (B), *Ns*ALP460 (C), *Ne*P460 (D), *Mc*P460 (E) and *Mc*CP (F) demonstrating the differing levels of distortion in each of the hemes The different types of distortion of the heme from planarity are shown in panel A.

Phylogenetic analysis of cytochromes *c'*-α, cytochromes *c'*-β and cyt P460s demonstrated a clear relationship between the three groups of proteins. The cytochromes *c'*-α were grouped in a separate clade to all the other proteins examined demonstrating that they have evolved completely separately to both the cytochromes *c'*-β and cyt P460s. The fact that none of the organisms within the analysis contained both a cty *c'*-α and a cyt *c'*-β is interesting. This suggests these bacteria never had a cyt *c'*-α in their genome and it could be inferred that the evolution of the cytochromes *c'*-β from the P460s arose due to a need to have a protein which could carry out a role similar to that of the cytochromes *c'*-α. The nesting of the cytochromes *c'*-β within the two groups of P460s clearly shows that the cyt *c'*-β evolved from the cyt P460s. This is contrary to what was previously published (Bergmann, Zahn and DiSpirito, 2000) however this discrepancy is likely to be due to the higher number of available sequences and improved phylogenetic methods.

Despite the clear evolutionary history between the cytochromes *c'*-β and cyt P460s there is very little sequence homology between the two groups. Even within each group of proteins there is low sequence homology, with 5 residues being completely conserved in P460s and 7 within the cytochromes *c'*-β along with the CXXCH motif. Whilst not fully conserved the distal pocket residues in both the cytochromes *c'*-β and cyt P460s shows reasonable conservation, and where a different residue is present it is often one of a similar property. This suggests that the type of residue present and its potential ability to interact with ligands is the important factor.

Chapter 3

Structural, spectroscopic and kinetic characterisation of ligand bound as isolated *Methylococcus capsulatus* (Bath) Cytochrome *c'* and distal pocket mutants.

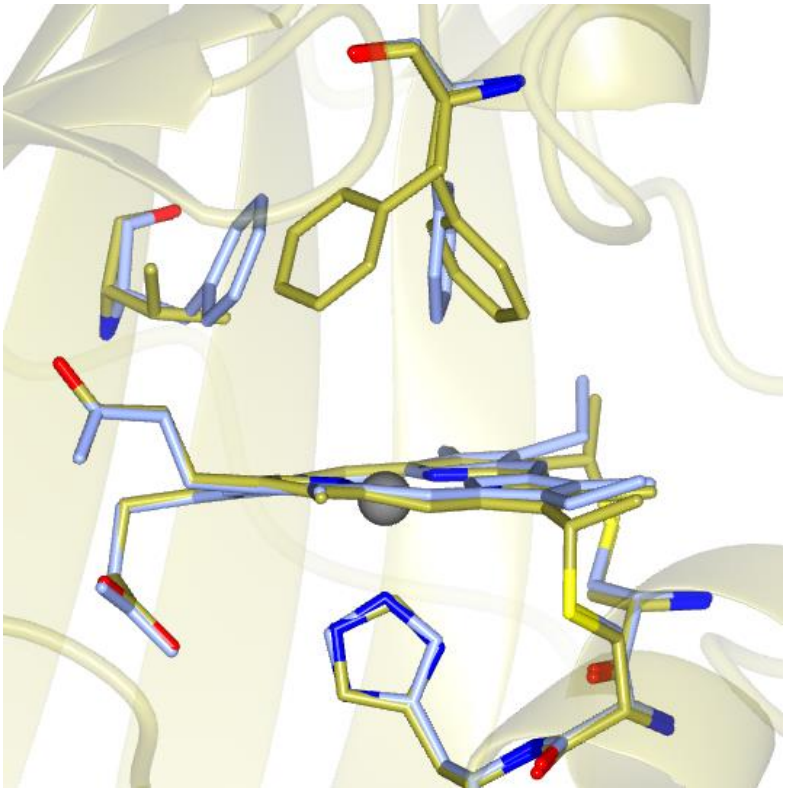

Figure 3. F61V mutation of *Mc*CP.

Results from this chapter have been published in: H.R Adams, D.A Svistunenko, M.T Wilson, S. Fujii, R.W Strange, Z.A Hardy, P.A Vazquez, T. Dabritz, G.J Streblow, C.R Andrew and M.A Hough. A heme pocket aromatic quadrupole modulates gas binding to cytochrome *c'*-β: Implications for NO sensors. Journal of Biological Chemistry, 2023, 299, 104742

3.1 Introduction

*Mc*CP was initially characterised spectroscopically and demonstrated ligand binding features similar to that reported for cytochromes *c'* (Zahn *et al.*, 1996). It was also noted that unlike the structurally similar *Mc*P460, *Mc*CP did not have any catalytic activity (Zahn, Duncan and DiSpirito, 1994). The ability of the alpha helical of cytochromes *c'* to bind small gaseous ligands such as nitric oxide (NO) and carbon monoxide (CO) has been well documented and although the true purpose of cytochromes *c'* have never been determined it is proposed that they are involved in protecting the cell from nitrosoative stress and the transport of NO (Yoshimura *et al.*, 1988) (Cross *et al.*, 2000). This chapter describes and characterises the effect of ligand binding to wt *Mc*CP and compares it to the published data for the alpha helical *c'*s and also to *Mc*P460 to assess how the differences between these proteins' structures may give rise to their different roles.

The importance of the two residues making up the 'Phe cap' of *Mc*CP was also investigated within this chapter to assess influence on ligand binding. In alpha helical *c'*s the residues on the distal side of the heme have been shown to occlude ligands and impose significant steric restraints on gas binding. Thus, each residue of the 'Phe cap' was individually mutated to see what effect the residues may have on ligand binding. The two mutations (F32V and F61V) were expressed, purified and characterized using structural, spectral and kinetic studies.

This work suggests that, unlike conventional cytochromes *c'*-α, *Mc*CP binds ligands only to the distal face of the heme and that the aromatic ring of Phe 32 in the Phe cap is important is regulating ligand binding.

3.2 Experimental Procedures

3.2.1 Site-directed mutagenesis and polymerase chain reaction

Mutations were introduced using two synthetic oligonucleotide primers carrying the desired base change (Sigma). Refer to Table A1 (Appendix A) for the primer sequences and additional information. Factors such as the percentage GC content, the length of the primers, and the melting temperature (Tm) were considered for the design of oligonucleotide primers. Site-directed mutagenesis (SDM) was carried out using the QuikChange Lightning Site-Directed Mutagenesis Kit by Stratagene (refer to Table A.2 (Appendix A) for the PCR reaction components). SDM was carried out with the template DNA of *Mc*CP in a pBluescript vector as shown in Figure A.2. (Appendix A), respectively. The PCR reaction was performed using the settings described in Table A.3 (Appendix A). The template was digested with the DpnI restriction enzyme for 2 h at 37 °C. 5 µl of the DpnI digested products were transformed into *E. coli* XL1-blue competent cells and spread on LBAmp agar plates. Single colonies were picked and grown overnight at 37 °C in 10 ml Amp media followed by plasmid miniprep extraction. DNA sequencing was carried out by Eurofins using the M13rev-29 primer. The single-point mutations were confirmed using Chromas Sequence Viewer. The genes containing the desired mutations in the cloning vector pBluescript were digested with EcoRI and XBaI restriction enzymes, ligated into the pMMB503EH expression vector and the mutated plasmids were propagated as previously described in section 2.2.1.

3.2.2 McCP F61V and F32V over-expression and purification

As isolated *Mc*CP and the F32V and F61V mutants from the pBsK plasmid were ligated into the expression vector pMMB503EH plasmid and were successfully over-produced in BL21(*DE3) E. coli* cells containing the pEC86 plasmid, refer to Chapter 3 (section 3.2.1).

The pEC86 plasmid (Figure A.3., Appendix A) is necessary to express the cytochrome *c'* maturation genes *CcmA-H* (Arslan *et al.*, 1998). TB medium was used for the over-expression of all proteins by IPTG induction. Both mutants and the wt *Mc*CP have an approximate pI of 7 with a strong positive charge at pH 8 and so were run on a DEAE column. The proteins appeared as a red/brown band and a salt gradient was used to elute the protein of interest. The collected fractions were then concentrated and run on a G75 column to produce a homogeneous sample. SDS-PAGE electrophoresis was used to assess the purity and quantity of the proteins. UV-visible absorption spectra were taken throughout all purification steps to analyse and assess the purity of the fractions. Protein concentrations were determined using a molar extinction coefficient (ε) for the Soret band of 70 $mMcm^{-1}$ for the oxidised *Mc*CP (Zahn *et al.*, 1996). The purity of the protein was determined by wavelength (nm) ratio A400/A280. A ratio of 3:1 was aimed for and indicated pure protein.

3.2.3. UV-visible spectroscopy

All aerobic spectrophotometric experiments were carried out at 20 °C, unless stated otherwise, using the Varian Cary 60 spectrophotometer (Agilent Technologies). UV-visible absorption spectra were recorded between 800 - 200 nm using a 1 cm Quartz cuvette (Hellma-Analytics). All anaerobic spectrophotometric experiments were carried out in an MBraun Unilab Pro glove box (O_2 levels < 0.1 ppm) using a Implen C40 NanoPhotometer.

3.2.4. Ligand binding studies

A few granules of sodium dithionite (Sigma) were used to reduce the proteins from ferric (Fe^{3+}) to the ferrous (Fe^{2+}) state and the reduction verified using UV-visible spectroscopy. The CO-bound protein samples were prepared by reducing the sample with sodium dithionite in a rubber-stopped sealed 1 cm quartz cuvette and bubbled with CO gas for ~ 30 s. Similarly, to prepare the NO-bound protein, 10 µl of ~ 80 mM proliNONOate (Cayman Chemicals) was injected into either the pre-reduced or ferric protein with a 10 µl Hamilton syringe (Hampton Research) to provide an excess of the ligand.

3.2.5. pH titrations

A 5 x MHTCP cocktail buffer containing 250 mM MES, 250 mM HEPES, 250 mM TAPS, 500 mM CAPS and 250 mM PIPES was prepared to acquire the desired pH ranges. The cocktail buffer was diluted to 1 x MHTCP and adjusted to pH 4, 5, 6, 7, 8, 9 and 10 with either HCl or NaOH. The ferric proteins were added to a final concentration of 5 µM in 1 ml of 1 x MHTCP buffer. For ligand bound pH titrations 10 µl of ~ 80 mM proliNONOate (Cayman Chemicals) was injected into the pre-reduced protein with a 10 µl Hamilton syringe (Hampton Research) to provide an excess of the ligand. To eliminate noise introduced into the data set by repositioning the cuvette following each pH adjustment the difference in absorbance between two wavelengths, on either side of the isosbestic point (415 and 395 nm), was used to construct the titration curve. The data were fitted to the Henderson-Hasselbalch equation (Eq. 1) for a one-proton ionisation equilibrium equation to yield the pK_a.

$$pH = pKa + log \frac{[A-]}{[HA]}$$

Equation 1.

3.2.6. Electron paramagnetic resonance spectroscopy

Electron paramagnetic resonance (EPR) spectra were measured using either an EMX spectrophotometer (Bruker) or a Bruker ELEXSYS E500 EPR spectrophotometer. Both EPR spectrophotometers were equipped with the spherical high-quality resonator SP9703 and a liquid helium cryostat (Oxford Instruments) to measure the low temperature (10 K) EPR spectra and were operating in continuous wave (CW) regime, at X-band (9 GHz microwave frequency), and 100 kHz field modulation frequency. The g-values were obtained using the built-in microwave frequency counter. Protein samples were 100 μM concentration in 50 mM HEPES pH 7.5. Syringes, needles and EPR tubes were flushed with nitrogen before use. NO-bound complexes were prepared anaerobically by the addition of 1.5 mM proliNONOate to dithionite-reduced Cyt *c'* protein samples with a total volume of 500 μl. Immediately following the NO-donor addition, 200 μl aliquots were drawn into EPR sample tubes and flash-frozen in cold methanol and once frozen, the samples were transferred to liquid nitrogen. The 1X MHTCP cocktail buffer at pH 4, 5, 6, 7, 8, 9, and 10, was used for the pH-dependent EPR experiments. Experimental conditions for the pH-dependent studies were as follows: microwave frequency 9.466 GHz, microwave power 0.0505 mW, modulation amplitude 3 G, time constant 40.96 ms, scan rate 4.77 G/s and one scan/spectrum. Simulations and spectra extractions were performed by Dr Dimitri Svistunenko using WinEPR SimFonia (Bruker).

3.2.7. Crystallisation

All proteins were buffer exchanged into 50 mM HEPES, pH 7.5 and used for subsequent crystallisation with protein concentrations ranging from 15 – 30 $mgml^{-1}$. wt *Mc*CP was crystallised as previously described in section 2.2.7. *Mc*CP mutants were initially screened against the wt protein crystallisation conditions. If this did not produce crystals the screening was widened around the wt conditions (increasing/decreasing pH, salt concentrations, varying protein: precipitant ratios) and by different crystallisation methods (hanging drop vapour diffusion vs batch crystallisation) until a suitable condition was found.

The crystals were cryo-protected using the reservoir solution and 10 % glycerol for *Mc*CP (and mutants) for 15 – 30 s and flash-cooled in liquid nitrogen. X-ray data collection was carried out using remote access at beamlines I03, I04-1 and I-24 at Diamond Light Source. All X-ray data collection was carried out at a temperature of 100 K. Data collection parameters are given later in the chapter in section 3.3.3, Table 3.3.

3.2.8. Crystal ligand-soaking

For *Mc*CP and its mutants a solution of 0.1 M ascorbic acid with the appropriate reservoir solution was prepared, transferred into 2 x 3 ml glass vials which were sealed using a rubber-seal and degassed using argon gas for 15 min. Five to six crystals were transferred to each vial solution and left to soak for ~2 h to reduce the protein crystals. The initial brown colour of the oxidised crystals was replaced by an intense red colour indicating reduction of the protein crystals. A volume of ~100 µl proliNONOate was injected into one of the sealed vials containing the reduced crystals. CO gas was bubbled through a fresh vial and the NO and CO soaked crystals were left to incubate at 18 °C for ~ 2 h. The crystals were scooped out using

plastic Pasteur pipettes and transferred to a clean sterile surface. The protein crystals were removed with a nylon UV-transparent cryo-loop (Hampton Research) and immediately soaked in a cryo-protectant for 15 - 30 s, prior to flash-cooling the crystals in liquid nitrogen.

3.2.9 X-ray data collection and processing

X-ray diffraction data for the wt *Mc*CP were measured at Diamond Light Source beamline I02 using an X-ray wavelength of 0.9795 Å and a Pilatus 6M detector and X-ray diffraction data for F32V and F61V variants were measured at Diamond Light Source beamline I04/I03 using an X-ray wavelength of 0.9795 Å and an Eiger2 XE 16M detector. All data collections were done by remote access. Data were automatically processed in xia2 using DIALS, XDS and Aimless (Kabsch, 2010) (Evans and Murshudov, 2013). Data sets were selected for further refinement by assessing the parameters R_{merge}, I/sd(I) and completeness to determine their resolution limits and data quality. The as isolated *Mc*CP structure (pdb code 6HIH) was used to refine structures through maximum likelihood methods using REFMAC5 (Murshudov, Skubak et al. 2011). A bespoke geometry file was used to set heme parameters during refinement (provided by Prof Hough). Model building between cycles of refinement, including addition of water molecules and ligands was performed in Coot (Emsley, Lohkamp et al. 2010). Data collection and refinement statistics are given in section 3.3.4.1, Table 3.4.

3.2.10. Validation of crystal structures

Validation of structures was carried out with *MolProbity* (Chen et al., 2010) and *JCSG Quality Control Check* (Elsliger et al., 2010). The pdb and mtz file were assessed with the *JCSG* server whereas only the pdb file was used for *MolProbity*. Steric clashes, poor

rotamers, Ramachandran outliers, residues with improbable bonds and angles were re-modeled in Coot, followed by refinement in Refmac5, this cycle was repeated until the model was of high quality and within the limits of the above mentioned parameters.

3.2.11 UV-visible stopped flow spectroscopy.

The SX-20 stopped-flow spectrophotometer (Applied Photophysics, Leatherhead UK) with a dead-time of ~ 1.3 ms was used for the measurements of NO binding kinetics initially at 25 °C and then at 10 °C. The dead-time of the instrument was measured by extrapolation back to t = 0 from CO recombination with a sample of constant myoglobin concentration and selected CO concentrations as described previously by Wilson & Torres, 2000. Buffer conditions of 50 mM CHES and 0.1 M NaCl, pH 8.9 were used to match previous experiments and the use of degassed buffer. Two syringes were employed for the measurements. One syringe was filled with degassed buffer containing µl amounts of proliNONOate to acquire the desire concentrations in the range of 25 – 2000 µM before mixing. The other syringe contained 10 µM of the sodium dithionite-reduced protein before mixing. The concentrations of dissolved NO were maintained at a ~ 10-fold excess over the heme binding sites (5 µM after mixing) to ensure pseudo-first-order conditions. Solutions of ferrous protein were rapidly mixed with equal volumes of the NO-saturated buffer and the reaction was monitored with monochromatic light at 415 nm and 435 nm using a photomultiplier detector. The reaction was also monitored from 300 - 700 nm for 0 – 500 s using a photodiode array. Pseudo first order rate constant at each concentration of NO was determined by fitting exponential time courses using a least-squares fitting method. Pseudo first-order rate constants for NO binding were plotted against the concentration of NO to

yield the second order rate constant and the kinetic data was analysed using the Pro-K Global Analysis Software (Applied Photophysics, Leatherhead, UK).

3.2.12 Flash Photolysis spectroscopy

The CO association kinetics were measured at room temperature with a nanosecond laser flash photolysis system (LKS.60 from Applied Photophysics Ltd., Leatherhead, UK). In this system, the 532 nm output (~ 10 ns, 110 mJ) from a Nd:YAG laser (Brilliant B from Big Sky Laser Technologies, Inc.) was employed as the photolysis beam. The output from a 150 W xenon arc lamp, at right angles to the photolysis beam, was used as the probe and was detected by a photomultiplier tube (PMT; model 1P28, Hamamatsu Corp.). The signal from the PMT was transferred to a digital oscilloscope (Infinium, Agilent Technologies) and then to a personal computer for subsequent analysis. The protein was reduced with sodium dithionite and the spectra were recorded using the as isolated protein spectrum as reference. The buffer was 50 mM Tris–HCl pH 7 and the protein concentration was 5 µM. CO was added to the ferrous protein to a concentration of 500 µM, and the spectra was recorded using the reduced protein as reference.

Global fitting was used to fit data sets to models comprising of either a single or double spectral transition using the Pro-K Global Analysis Software (Applied Photophysics, Leatherhead, UK). Prior to fitting data sets were analysed using SVD (single value decomposition) to ascertain the number of kinetic transitions required and to remove noise. The model used for CO binding to *Mc*CP is shown in Figure 3.1. Equation 2 was derived from this model which gives rise to a hyperbolic fit for the data collected. Kinetic phases were calculated using Equation 3 for a single phase and Equation 4 where two phases were seen, where a_o and b_o are the amplitudes of the two phases.

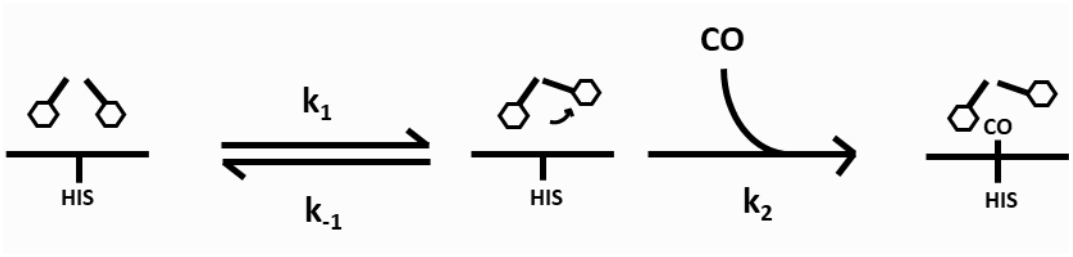

Figure 3.1. Kinetic model for CO binding to *Mc*CP

$$k_{obs} = \frac{k_1 k_2[CO]}{k_1 + k_{-1} + k_2[CO]}$$

Equation 2.

$$\Delta A = ae^{-kt}$$

Equation 3.

$$A_T = a_o e^{-k_1 t} + b_o e^{-k_2 t}$$

Equation 4.

3.3 Results

3.3.1 Mutagenesis, over-expression and purification of the McCP F61V and F32V mutants

The SDMs F32V and F61V were created as described in section 3.2.1 and the presence of the mutations confirmed by comparing the DNA sequences to the wt sequence (Figure A.5., Appendix A). Over expression in BL21(DE3) pEC 86 *E. coli* cells was considered to be successful due to the presence of reddish brown pellets upon harvesting of the bacteria (Figure 3.2). The crude extract was applied to a DEAE column where the protein could be easily followed due to its colour. The eluted reddish-brown fractions were run on an SDS-PAGE gels where a band could be seen around 17 kDa consistent with the molecular weight for *Mc*CP. The collected fractions were then concentrated and run on a G75 column to produce a homogeneous sample which was again run on an SDS-PAGE gel to check the purity of the sample. (Figure 3.3). The purity of the ferric protein was determined by measuring the ratio of the absorbance of the Soret peak at ~ 400 nm and the protein peak at 280 nm (Figure 3.3). This resulted in a ratio of 1.7:1 for F32V and 2.1:1 for F61V showing that a homogenous sample had been produced for each protein.

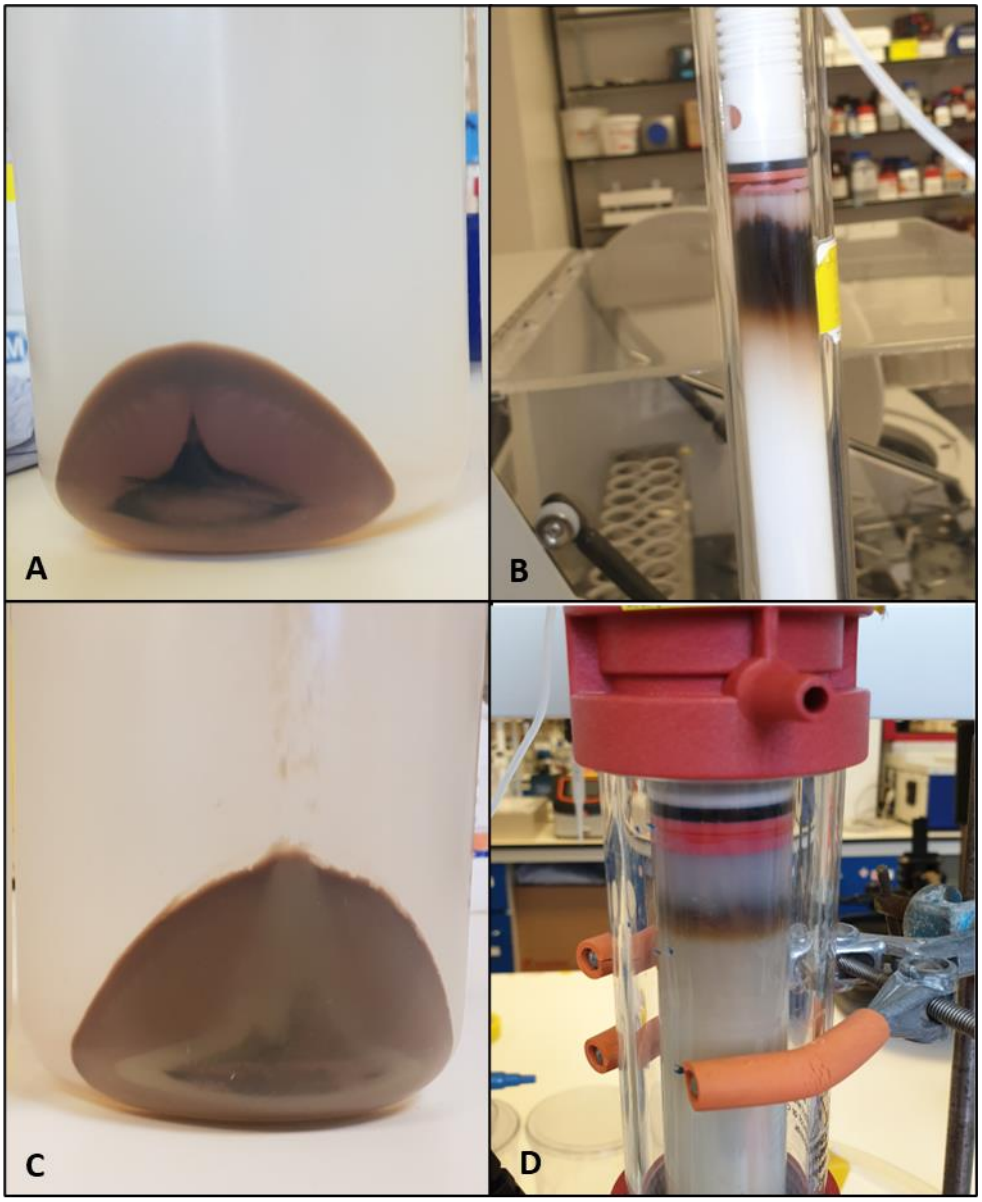

Figure 3.2. Harvesting and purification of *Mc*CP F32V and F61V. Pelleted *E .coli* cells after over expression of F32V (A) and F61V (B). The presence of the mutants is indicated by the brown colouration of the pelleted cells. Purification of F32V on a size exclusion gel filtration column (B). Purification of F61V on a DEAE Ion Exchange chromatography column (D),

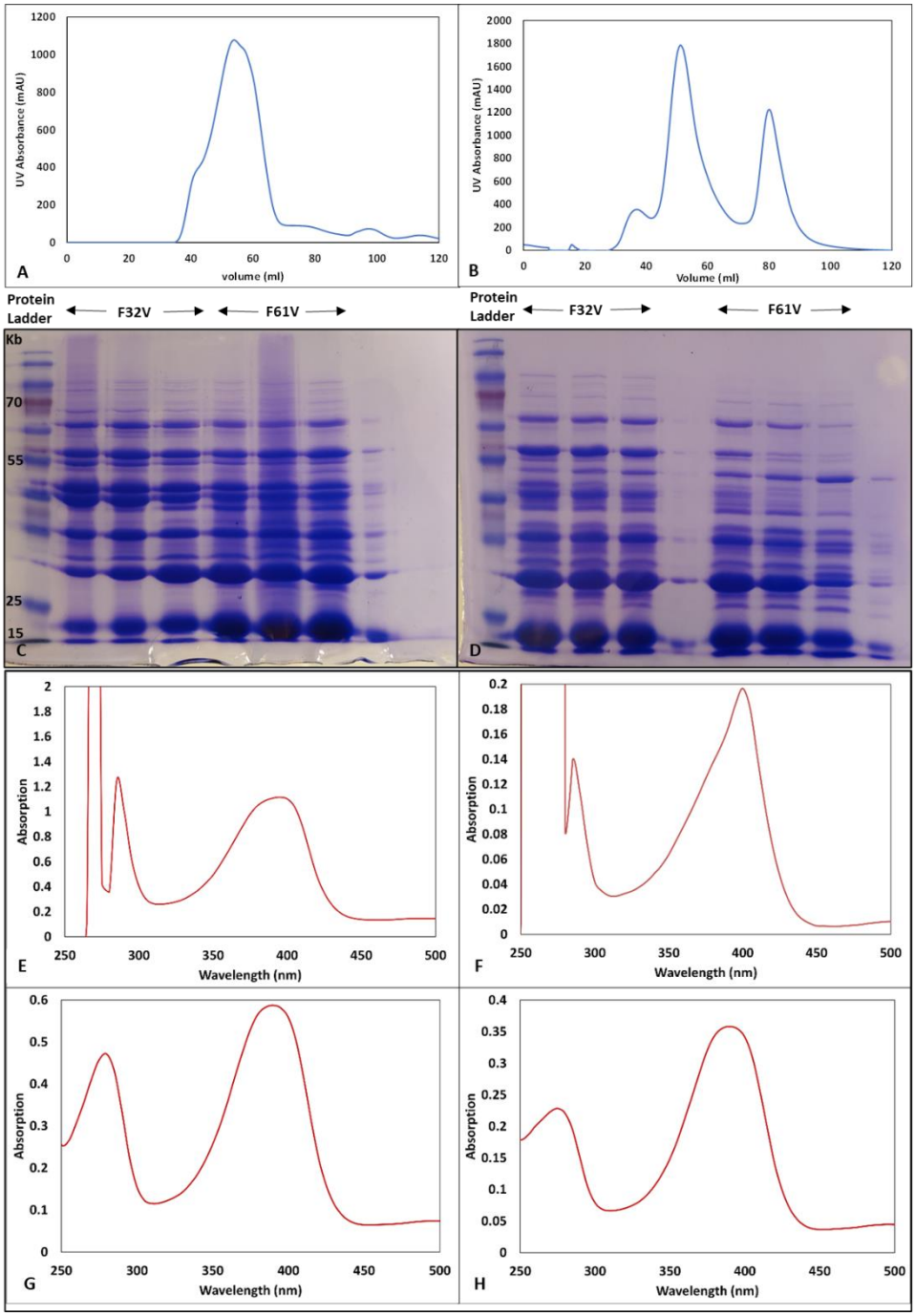

Figure 3.3. Purity checks for *Mc*CP F32V and F61V. Gel filtration profiles for F32V (A) and F61V (B). SDS Page of F32V and F61V after DEAE column (C) and gel filtration chromatography (D). UV-visible spectra of as isolated F32V *Mc*CP after DEAE column (E) and gel filtration chromatography (F). UV-visible spectra of as isolated F61V *Mc*CP after DEAE column (G) and gel filtration chromatography (H). The purity of the ferric protein was determined by measuring the ratio of the absorbance of the Soret peak at ~ 400 nm and the protein peak at 280 nm.

3.3.2 Spectroscopy of McCP F61V and F32V

3.3.2.1 UV-visible Spectroscopy

The ferric F32V mutant has a similar UV-visible spectrum to the wt protein with a Soret maximum at 399 nm (and weak shoulder at ~379 nm), together with an unresolved α/β band near 500 nm and a charge transfer (CT1) band at ~ 640 nm (Figure 3.4). Reduction of Fe (III) F32V *Mc*CP with dithionite yields the Fe (II) state which exhibits a Soret maximum at 431 nm and a broad α/β band centred at 555 nm (Table 3.1).

The ferric F61V mutant displays a broad Soret maximum centred at 400 nm, together with an unresolved α/β band near 500 nm and a CT1 band at ~645 nm (Figure 3.4, Table 3.1). Reduction of Fe (III) F61V *Mc*CP with dithionite yields the Fe (II) state which exhibits a Soret maximum at 435 nm and an α/β band centred at 530 nm.

As with the wt protein the Soret maxima for the F32V mutant remains unchanged over the range of pH 4-10, although a change in intensity can be seen at both high and low pH suggesting the protein may be unstable. The F61V mutant's Soret maxima is unchanged between pH 4-8. At very high pH (9-10) there is a shift in the Soret maximum to 410 nm (Figure 3.4).

3.3.2.2 EPR Spectroscopy

The EPR spectrum of the F61V mutant reveals two high spin Fe (III) heme signals: a major species with *g* values of 6.30, 5.46, and 1.98, together with a minor species with *g* values of 5.89, 5.34, and 1.98 (Figure 3.5, Table 3.2). The EPR spectrum of the F32V variant also reveals two high spin Fe (II) heme signals: a major species with g values of 6.34, 5.46 and 1.98, together with a minor species with g values of 5.90, 5.32 and 1.98. Both as isolated

mutant samples also showed signals around g = 4 suggesting a proportion of free iron in the samples.

Changing the pH resulted in a change in the proportions of the two species of high spin heme as seen in the wt. It also caused an increase in the free iron seen in the samples at high and low pH. This is possibly due to instability of the mutants at this pH as also noted in optical spectroscopy.

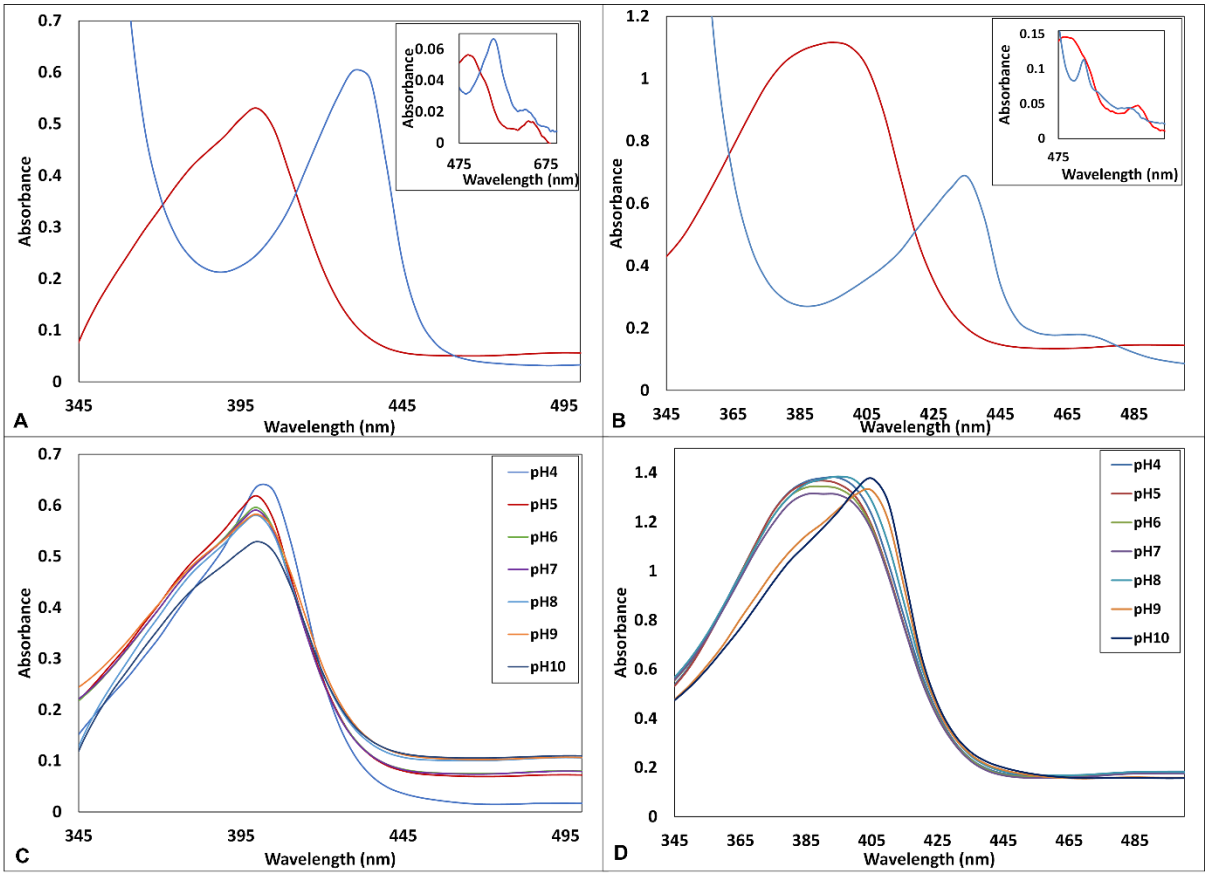

Figure 3.4. UV-visible absorption spectra of ferric and ferrous *Mc*CP F32V (A) and F61V (B) at pH 7 and ferric F32V (C) and F61V (D) over a pH range of 4 - 10. Ferric F32V has a Soret maximum of 399 nm (and weak shoulder at ~379 nm), together with an unresolved α/β band near 500 nm and a CT1 band at ~640 nm. Ferric F61V has a broad Soret maximum centred at 400 nm, together with an unresolved α/β band near 500 nm and a CT1 band at ~645 nm. The F32V variant appears to be less stable at both high and low pH, whilst the F61V variant is only unstable at very high pH (9-10). Reduction with dithionite results in a Soret maximum at 431 nm and a broad α/β band centered at 555 nm for the F32V variant and a Soret maximum at 435 nm and an α/β band centered at 530 nm for the F61V variant.

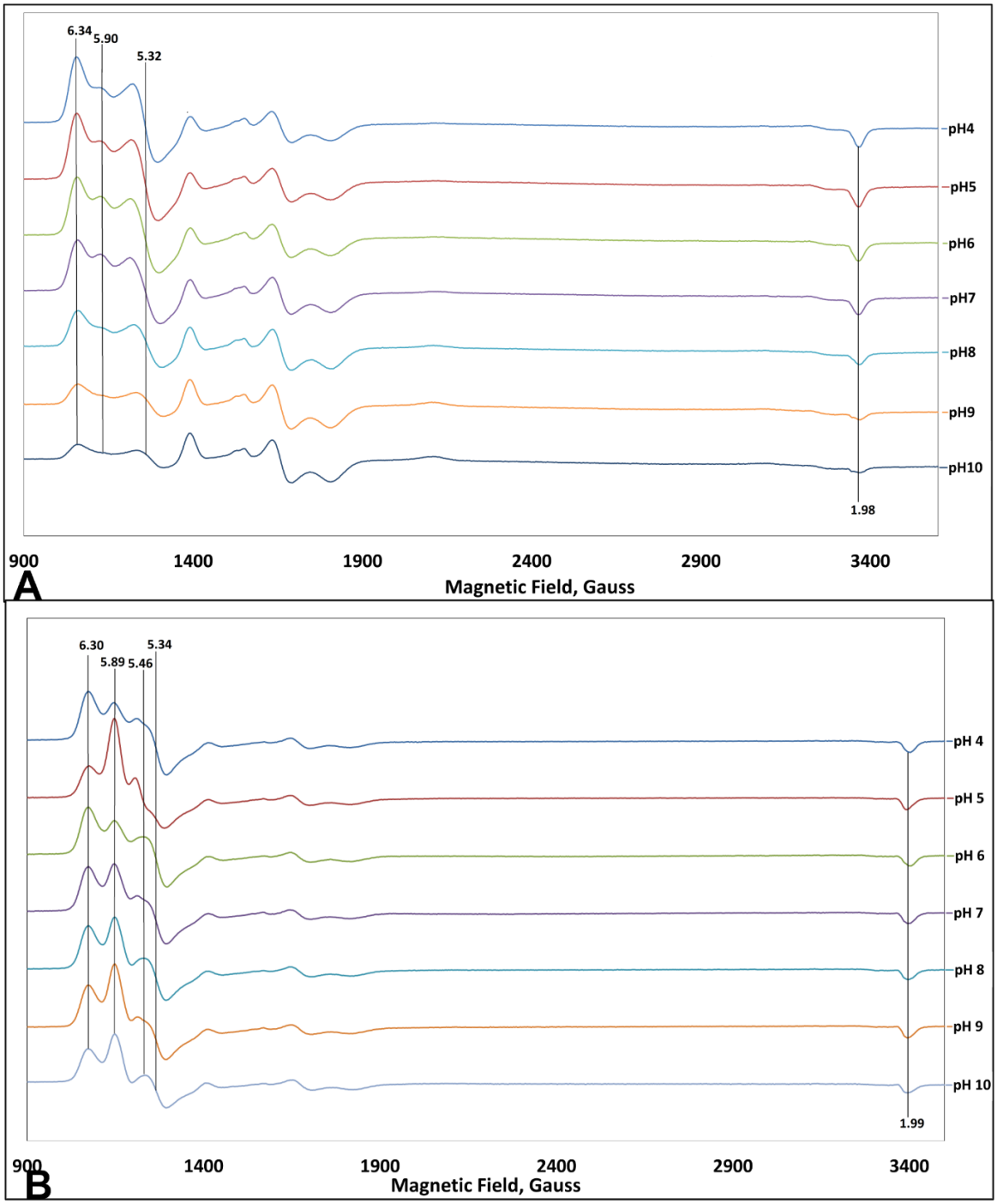

Figure 3.5. EPR spectroscopy of the F32V (A) and F61V (B) *Mc*CP mutants at varying pH. Both mutants reveal two high spin species.

Table 3.1. UV-visible parameters for cyts *c'*-β

		λ_{max} (nm)			ref
Fe(III)					
*Mc*CP	379sh	399	499	640	tw
		401	502	638	a
F32V	379sh	399	500	640	tw
F61V		400	500	645	tw
Fe(II)					
*Mc*CP	372	431	552		tw
		433	552		a
F32V		431	555		tw
F61V		435	530		tw

a (Zahn *et al.*, 1996)

Table 3.2. EPR parameters for cyts *c'*-β.

Protein	pH	temp (K)	species	g^		gçç
				g1	g2	g3
F32V	8	10	major	6.34	5.46	1.98
			minor	5.90	5.32	1.98
F61V	8	10	major	6.30	5.46	1.98
			minor	5.89	5.34	1.98
*Mc*CP	8	10	major	6.29	5.46	1.98
			minor	6.00	5.34	1.98

3.3.3 Crystallisation and data collection of the McCP F61V and F32V mutants

Crystallisation trials to grow crystals of both the F32V and F61V mutants under the same conditions as the wt *Mc*CP only produced crystals for the F61V mutant and so further screening was carried out for the F32V mutant. The screens involved increasing/decreasing the concentration of PEG 550 and changing the pH of the reservoir solution along with varying ratios of protein: reservoir solution. Only one condition gave rise to crystals which was 0.01 M $ZnSO_4$, 30 % PEG 550 (v/v) and 0.1 M MES, pH 6.5. All crystals were grown using the hanging drop vapour diffusion method at 18 °C using 2 µl of 15 mg/ml protein in 0.1 M HEPES buffer, pH 7.5 with the appropriate reservoir solution. Prior to X-ray data collection crystals were cryoprotected by transfer to reservoir solution comprising mother liquor supplemented with 10 % (v/v) glycerol and flash-cooled in liquid nitrogen. X-ray diffraction data were collected at beamlines I02/I03/I04, Diamond Light Source. All data was processed and refined as described in section 3.2.9. Data collection and processing statistics are reported in Table 3.3.

Compared to wt *Mc*CP, both mutations maintain a very similar overall fold in both the as isolated and ligand-free chemically reduced form, with structural changes essentially limited to the distal heme pocket. Both F32V and F61V can be superimposed on the wt *Mc*CP structure with RMSDs of 0.31 Å and 0.23 Å respectively demonstrating how similar the overall fold is (Figure 3.6). The overall B-Factors of the two mutants are slightly higher than that of the wt structure (28.9 $Å^2$ for F32V and 45.7 $Å^2$ for F61V), but this may simply be due to them being of a lower resolution. These result in a less crowded distal pocket and better accessibility to the heme from the surrounding solvent, although no water is evident within the Fe (II) heme pockets (Figure 3.7). In the resting state of the F61V variant there is a change in the positioning of Phe 32, this is now able to take up two possible conformations, distinct from that of the wt *Mc*CP structure. In heme A of the ligand-free chemically reduced

state, one is moved outwards from the heme by 1.2 Å and rotated by 80 ° around the Cβ-Cγ bond from the wt structure position whilst the other has moved into the space above the heme created by the Val mutation, with the face of the ring rotating by 103 ° compared to the wt structure (Figure 3.8). In heme B, one has rotated outwards from the heme by 82 ° whilst the other is again sitting over the face of the heme, where Phe 61 would previously have been, having rotated by 75 °. The F32V mutation causes no other changes to residues around the heme with the Val sitting in the same relative position as the Phe in the wt structure in both the as isolated and ligand-free chemically reduced form (Figure 3.7 and 3.8).

Table 3.3. Data collection, processing and refinement statistics for F32V and F61V in the as isolated and chemically reduced states.

Dataset	F32V	F32V Ferrous	F61V	F61V Ferrous
Resolution (Å)	74.71-1.75	52.96-1.74	74.57-1.96	47.2-2.04
Unit cell, (Å)	a=b=c=	a=b=c=	a=b=c=	a=b=c=
	105.67	105.80	105.47	105.54
Unique reflections	40548 (2016)	39950 (2001)	28359 (2087)	24699 (1706)
Completeness (%)	100 (100)	99.7 (100)	100 (100)	97.5 (100)
Redundancy	6.6 (6.8)	6.7 (6.8)	8.2 (10.3)	2.5 (2.6)
R_{meas}	0.074 (2.28)	0.062 (2.34)	0.075 (2.03)	0.064 (0.86)
I/σ(I)	17.2 (0.6)	19.4 (0.7)	14.9 (1.1)	23.3 (1.3)
$CC_{1/2}$	1.0 (0.3)	1.2 (0.03)	1.0 (0.5)	1.0 (0.6)
WilsonB-factor ($Å^2$)	28.9	32.2	45.7	42.9
R_{work}	0.186	0.182	0.187	0.184
R_{free}	0.213	0.209	0.210	0.215
RMSD bond length (°)	0.0120	0.0156	0.0115	0.0116
RMSD bond angles (Å)	2.094	2.163	2.060	2.279
Ramanchandran favoured (%)	95.90	95.90	95.15	94.78
PDB accession code	7ZS4	7ZSV	7ZRW	7ZRX

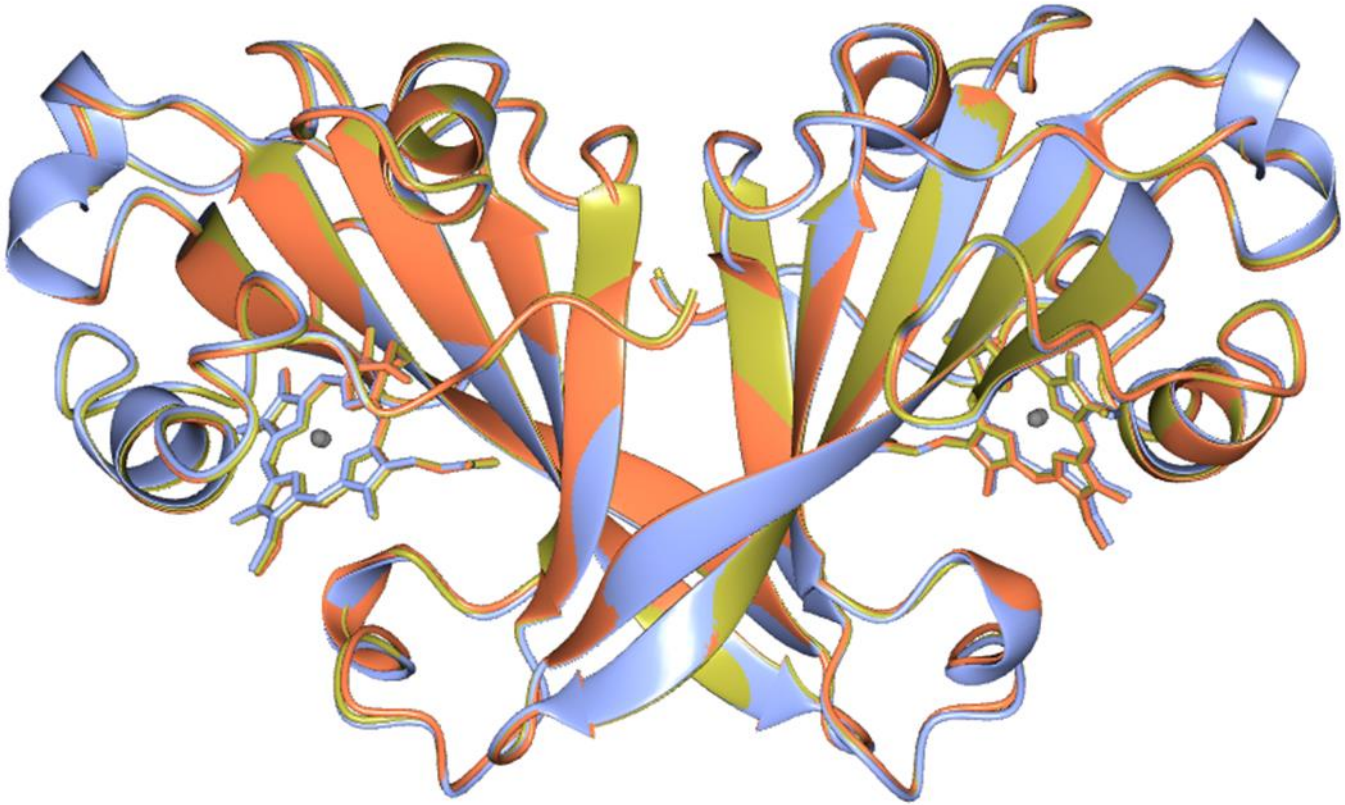

Figure 3.6. Superimposition of wt *Mc*CP (gold), F32V (blue) and F61V (coral) overall structure. F32V can be superimposed with an RMSD of 0.31 Å and F61V with an RMSD of 0.23 Å.

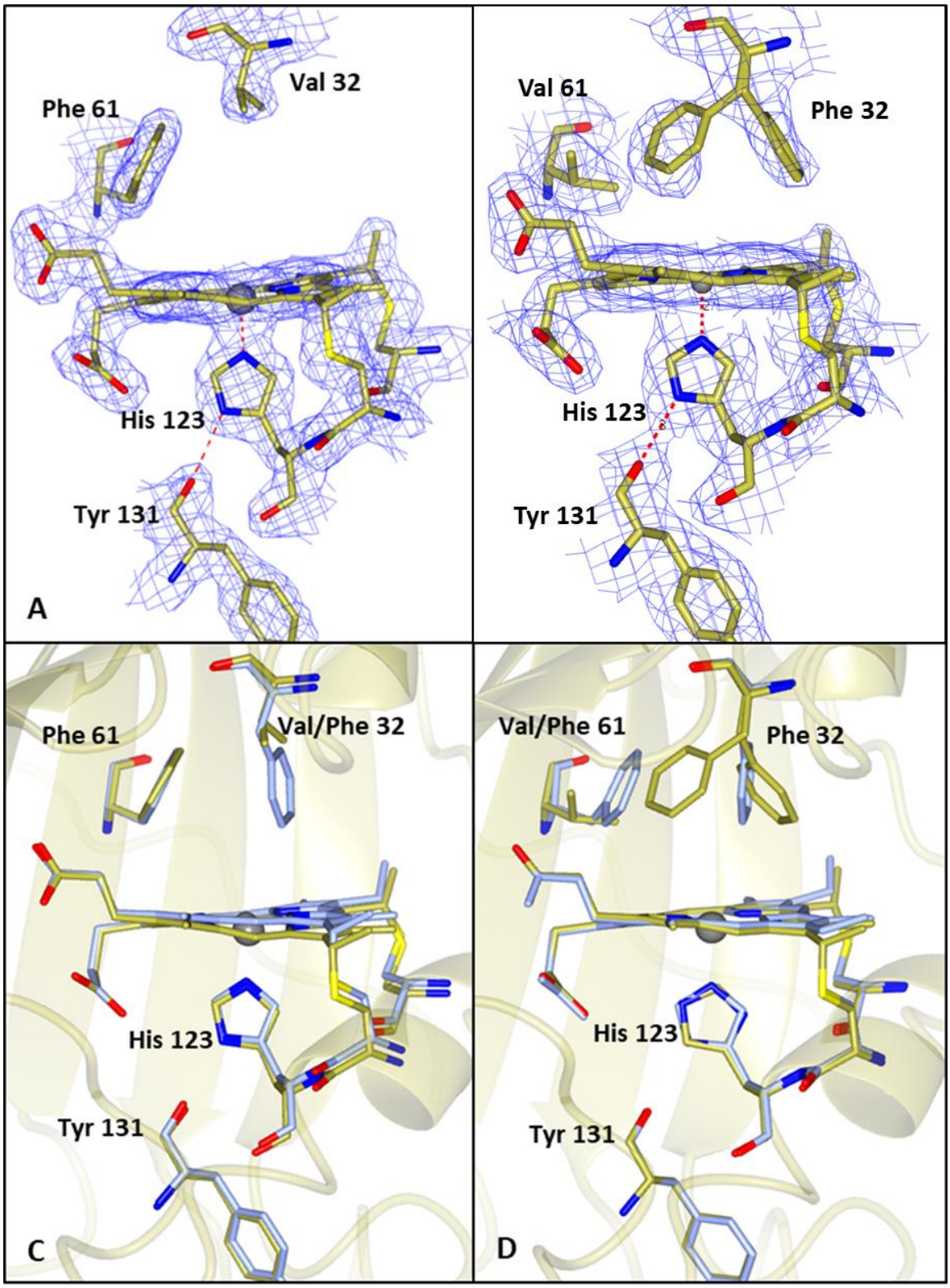

Figure 3.7. *2Fo-Fc* map contoured at 2.0 σ of the heme environments of as isolated F32V (A) and F61V (B) (Gold) mutants and comparisons to the wt *Mc*CP heme environment (C, D) (Blue). The F32V mutation creates a more open distal face to the heme. Mutating residue 61 to valine allows F32 to take up two different positions over the heme.

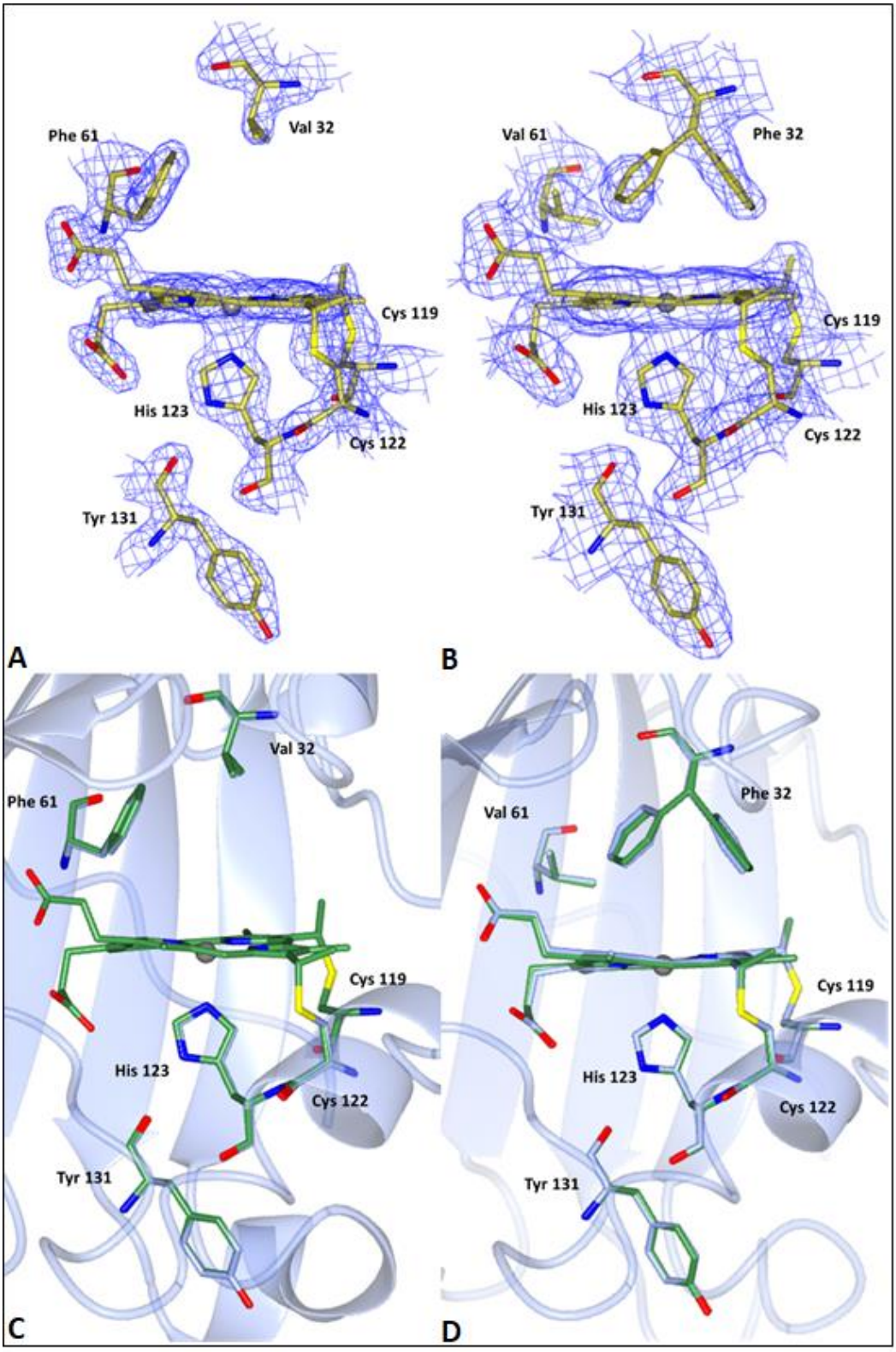

Figure 3.8. *2Fo-Fc* maps of the heme environments of chemically reduced F32V (A) and F61V (B) (Green) contoured at 1.5 σ and comparisons to the as isolated heme environments (C, D) (Blue). The F32V mutant remains unchanged upon chemical reduction. The F61V mutant shows slight movement in the two conformations of Phe 32.

3.3.4 Ligand Binding Studies

3.3.4.1 UV-visible spectroscopy and kinetics of CO bound wt McCP and F61V and F32V mutants

On addition of CO to ferrous *Mc*CP and the F32V and F61V mutants a stable hexa-coordinate carboxy adduct formed (Figure 3.9) with a Soret band at 419 nm. However, the CO binding could not be followed using stopped-flow spectroscopy as the process was complete within the dead time of the apparatus even at 20 μM CO indicating that the second-order rate constant for CO binding is > 5x 10^7 $M^{-1}s^{-1}$.

On exposing the CO adduct to laser photolysis the CO dissociates and subsequently recombines with the heme in the dark. Figure 3.9 A (and inset) shows the result of such an experiment with wt *Mc*CP where it is seen that, following photolysis, CO recombines to the heme within ~ 1 ms. The time courses for recombination comprises of the sum of two exponential processes – a fast process and a slow process. The dependences of the rate constants of these processes on CO concentration are shown in Figure 3.9 B where it is seen that for the fast process the rate constant increases with increasing CO concentration in a non-linear fashion that may be adequately fitted to hyperbolic function suggesting that the constant approaches a limiting value at high CO concentration. For the slower process the fit appears more linear and an upper limit cannot be determined. From the fit an estimate for the upper limit of the rate constant for the faster process is ~ 7000 ± 1300 s^{-1}. With the data set collected it is not possible to give an upper limit with any confidence for the slower process. The amplitudes of the two processes are also dependent on CO concentration, the amplitude of the faster process increasing with CO concentration while the amplitude of the slower decreases. This is shown in Figure 3.9 C where each amplitude is expressed as a fraction of the total amplitude of the spectral change occurring on CO binding.

Similar behaviour was observed for CO binding following photolysis of the F61V variant of *Mc*CP. The dependencies of the rate constants and fractional amplitudes of the two processes on CO concentration are shown in Figure 3.10. Although the essential elements of the behaviour observed in the wt protein is maintained in the F61V variant there are also differences, most notably the values of the rate constants are much smaller and, probably as a consequence, the CO concentration dependences generally appear more linear.

The behaviour for CO binding following photolysis of the F32V variant of *Mc*CP was different to the wt and F61V mutant suggesting there were three processes occurring. All three processes appeared more linear and thus no upper limit to the rate could be given with the collected dataset. The dependencies of the rate constants and fractional amplitudes of the three processes on CO concentration are shown in Figure 3.11.

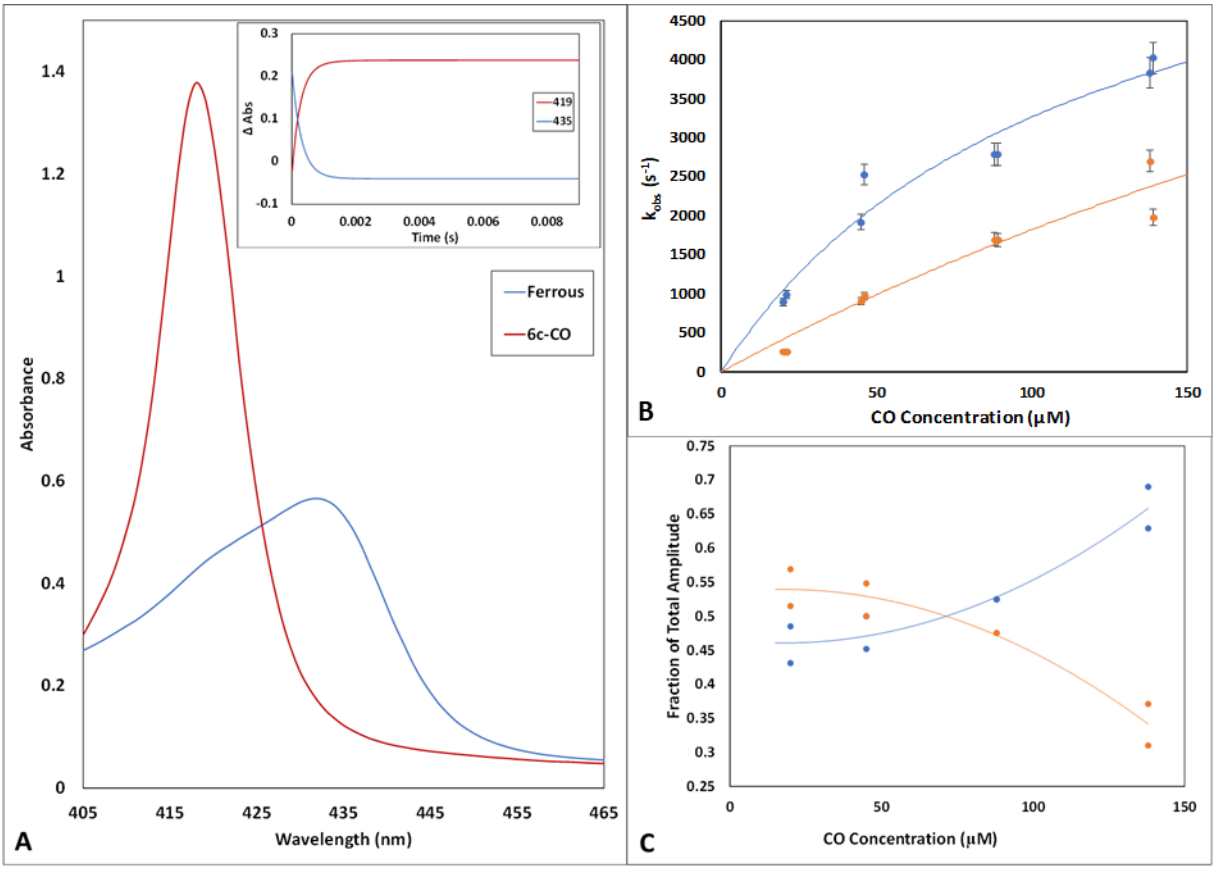

Figure 3.9. Flash photolysis of the ferrous CO complex of *Mc*CP. (A) The absorption spectra of the CO adduct and the ferrous form obtained statically. The inset shows representative time courses and their fits to double exponential functions for CO recombination following photolysis. (B) The dependences of the rate constants of the two processes (blue fast and orange slow) on CO concentration can be seen to fit a hyperbolic function in the case of the faster rate, suggesting that the constant approaches a limiting value at high CO concentration. The slower rate appears more linear in nature and no upper limit can be determined. (C) The dependences of the amplitudes of each process on CO concentration and fits to a hyperbolic function. The amplitude of the faster process (blue) increases with increasing CO concentration while the amplitude of the slower (orange) decreases.

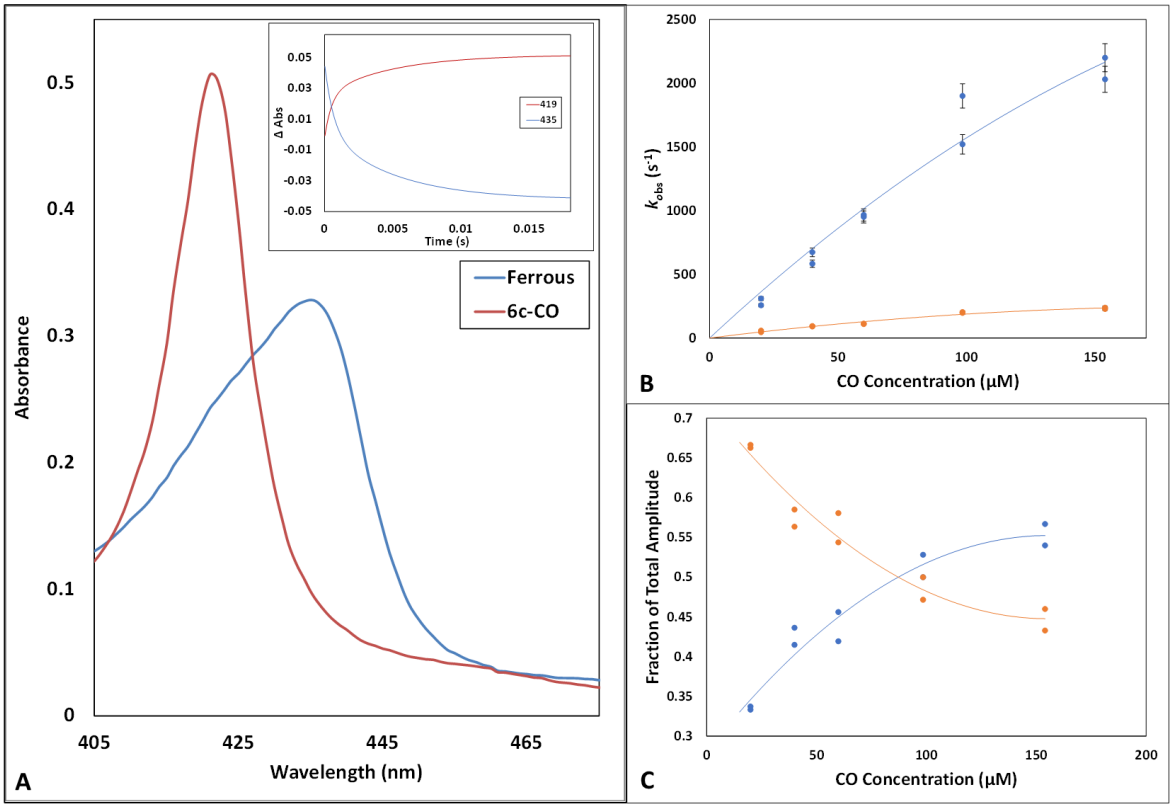

Figure 3.10. Flash photolysis of the ferrous CO complex of the F61V variant of *Mc*CP. (A) The absorption spectra of the CO adduct and the ferrous form obtained statically. The inset shows representative time courses and their fits to double exponential functions for CO recombination following photolysis. (B) The dependences of the rate constants of the two processes (blue fast and orange slow) on CO concentration can be seen to fit a hyperbolic function in the case of the faster rate, suggesting that the constant approaches a limiting value at high CO concentration. The slower rate appears more linear in nature and no upper limit can be determined. (C) The dependences of the amplitudes of each process on CO concentration and fits to a hyperbolic function. The amplitude of the faster process (blue) increases with increasing CO concentration while the amplitude of the slower (orange) decreases.

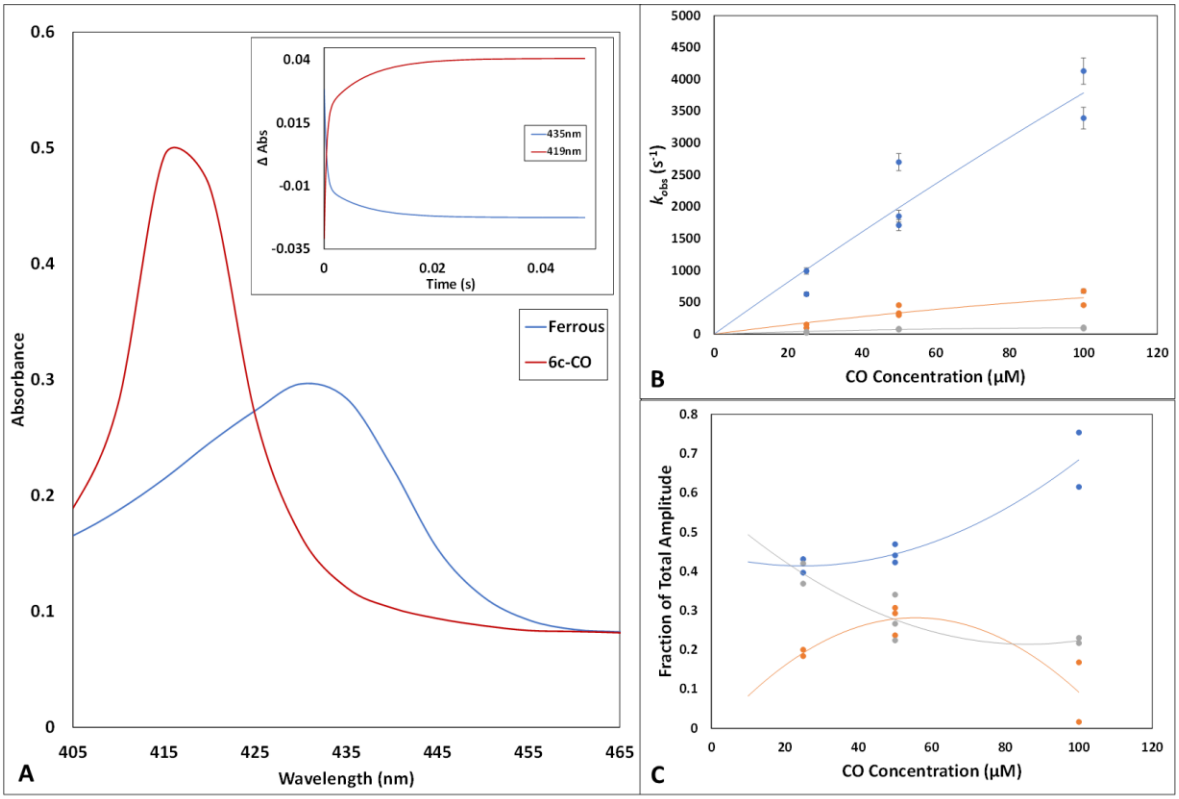

Figure 3.11. Flash photolysis of the ferrous CO complex of the F32V variant of *Mc*CP. (A) The absorption spectra of the CO adduct and the ferrous form obtained statically. The inset shows representative time courses and their fits to double exponential functions for CO recombination following photolysis. (B) The dependences of the rate constants of the three processes (blue fast and orange intermediate and grey slow) on CO concentration and can be seen to fit a linear function meaning that no upper limit to the rate can be determined with the data set measured. (C) The dependences of the amplitudes of each process on CO concentration. The amplitude of the faster process (blue) increases with increasing CO concentration while the amplitude of the slower (orange and grey) decreases.

3.3.4.2 pH Dependence of NO bound wt McCP and F61V and F32V mutants

The pH dependency of the binding of NO to *Mc*CP and both the F61V and F32V mutants was investigated using UV-visible spectroscopy and EPR over the range pH 4 – pH 10. On addition of NO to high spin penta-coordinate ferrous *Mc*CP a complex is formed the nature of which depends upon the pH of the solution. Figure 3.12 shows the UV-visible spectrum of this NO adduct at several pH values. At high pH (~ 9) the spectrum (Soret maximum 415 nm) is typical of a low spin hexa-coordinate species and may be assigned to a ferrous heme with NO occupying the distal coordination site and histidine the proximal site. At low pH (~ 5) the spectrum (Soret maximum 395 nm) is that of a penta-coordinate form in which the histidine has dissociated while the NO remains bound. Dissociation of the proximal histidine is a consequence of the trans-effect exerted by NO and has been noted to occur in many NO-heme adducts. Examination of the pH dependence shows that the transition from a hexa coordinate form (pH 9) to a pentacoordinate form at low pH conforms to a simple single proton transition. Figure 3.12 B shows the fraction of the protein in the penta-coordinate form as a function of pH together with a fit to this data that yield a pK_a for the transition of 7.17 ± 0.03. The equilibrium between 5c-NO and 6c-NO binding appears to be reached within the period of time it took to measure the samples after mixing (1-2 s) as no change was seen on further measurements at later timepoints (data not shown).

The F32V mutant showed 5c-NO binding with Soret bands at 395 nm at pH 4 and 5. At pH 6 a mixture of 5c-NO and 6c-NO can be seen with Soret bands at both 395 nm and 415 nm. pH 7 is primarily 6c-NO (415 nm) with a small amount of 5c-NO (shoulder at 395 nm). pH 8, 9 and 10 all both show 6c-NO binding (Figure 3.12 C). Further investigation revealed that the equilibrium of 5c-NO and 6c-NO binding takes time to be reached (data not shown). A pH dependence carried out between pH 5.0 and pH 7.0 showed that the point at which there appears to be an equal amount of 5c-NO and 6c-NO binding is around pH 6 after 10 min.

The F61V mutant showed 5c-NO binding with Soret bands at 395 nm at pH 4 and 5. At pH 6 it is predominately 5c (395 nm peak) but there is also a shoulder at 415 nm suggesting some 6c NO binding. At pH 7 it is primarily 6c (415 nm) with a small amount of 5c (shoulder at 395 nm). At pH 8, 9 and 10 show 6c binding of NO is observed (Figure 3.12 E). Like the wt *Mc*CP, the equilibrium between 5c-NO and 6c-NO binding appears to be reached within the period it took to measure the samples after mixing as no change was seen on further measurements (Data not shown). This equilibrium appears to be between pH 6.9 and pH 7.0 (Figure 3.12 F).

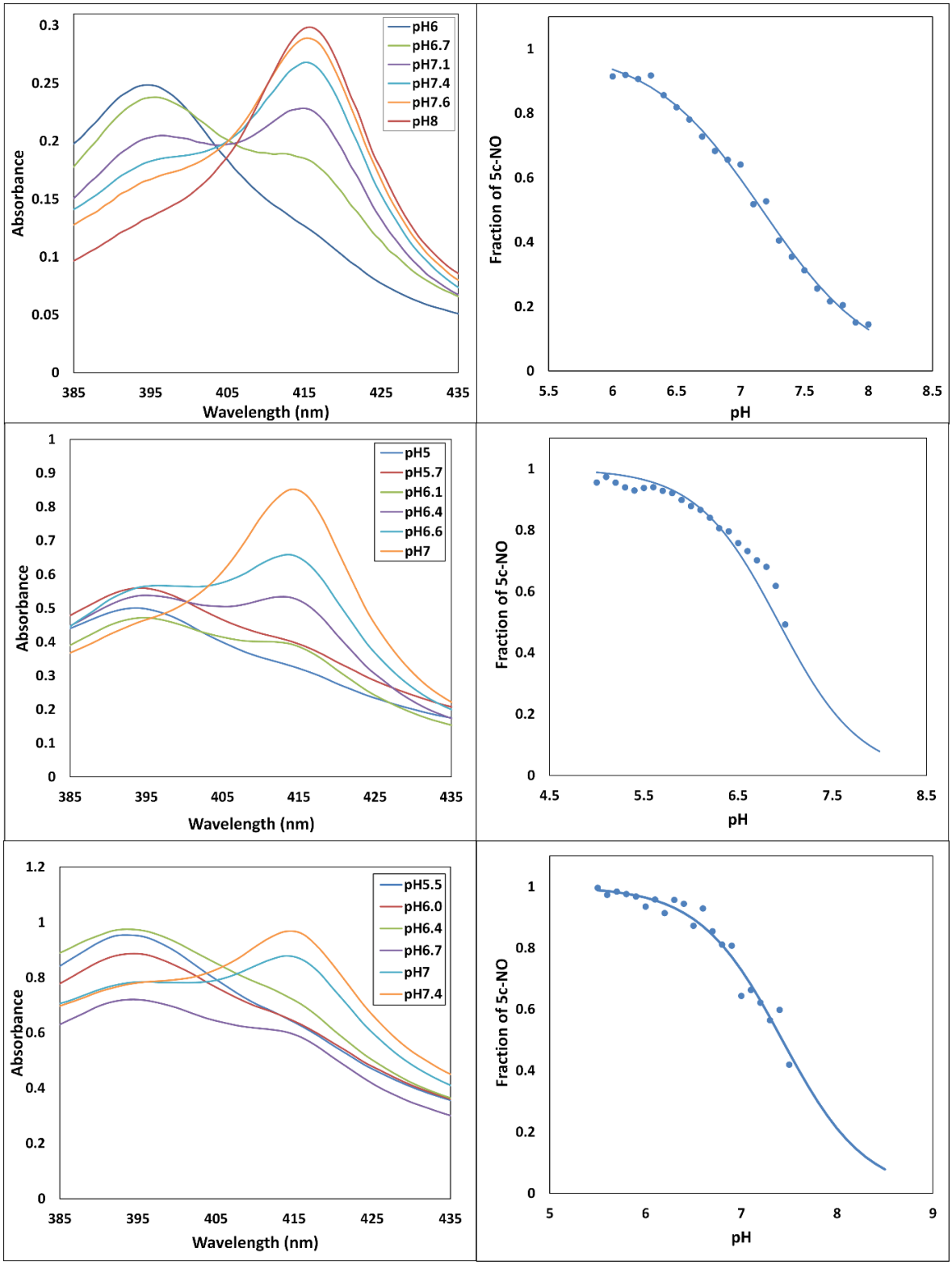

Figure 3.12. UV-visible spectrum of the NO adduct between pH 6 – 8, illustrating the change in heme coordination with pH for *Mc*CP (A), F32V (C) and F61V (E). The fraction of the protein in the penta-coordinate NO form as a function of pH for *Mc*CP (B), F32V (D) and F61V (F).

3.3.4.3 EPR Spectroscopy of NO bound wt McCP and F61V and F32V mutants

pH dependent EPR spectra of NO-bound *Mc*CP are consistent with the UV-visible data with a typical 5c-NO 3-line hyperfine pattern seen at pH 4-6 shifting to a line shape associated with 6cNO binding at pH 8-10 but with an unresolved 9-line hyperfine pattern (Figure 3.13). At pH 7 the line shape is consistent with a mixture of both 5c and 6c NO binding. A similar relationship is seen in both the mutants with the EPR data reflecting the pattern seen in the UV-visible data. For the F32V mutant at pH 4-5 a typical 5cNO 3-line hyperfine pattern can be seen, which shifts to a line shape associated with 6cNO binding at pH 8-10. At pH 6-7 the line shape is consistent with a mixture of both 5c and 6c NO binding. The F61V mutant displays a typical 5cNO line shape at pH 4-6 shifting to a line shape associated with 6cNO binding at pH 9-10 but again with an unresolved 9-line hyperfine pattern. At pH 7-8 the line shape is consistent with a mixture of both 5c and 6c NO binding.

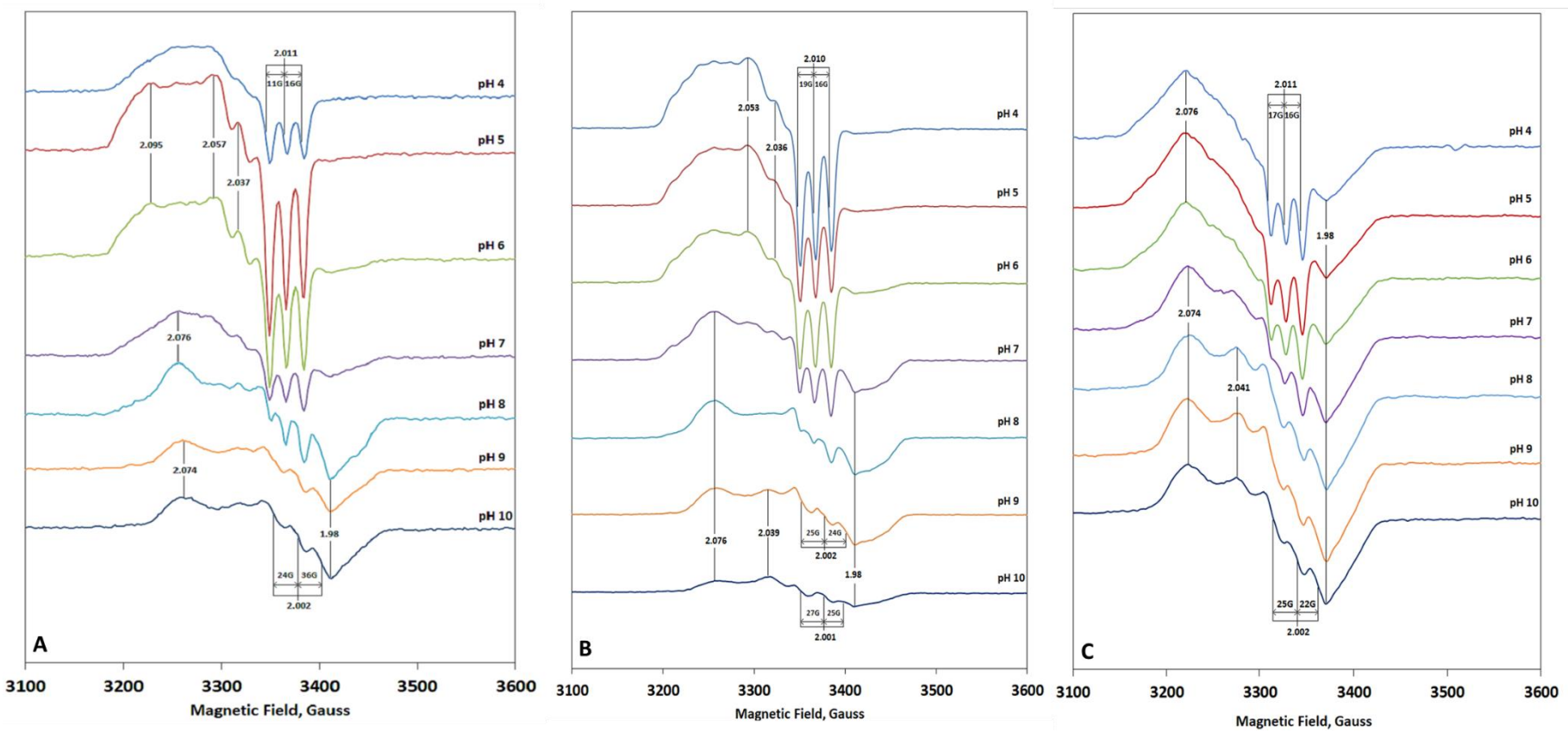

Figure 3.13. pH dependence of the EPR spectra at 10 K of NO bound *Mc*CP (A), F61V variant (B) and F32V variant (C). Low-temperature (10 K) EPR spectra of the Fe(II)NO complex shows a pH-dependent 6cNO/5cNO equilibrium, with a typical 5cNO 3-line hyperfine pattern seen at pH 4 – 6, shifting to an unresolved 9-line hyperfine pattern associated with 6cNO geometry at pH 9 – 10. The line shape at pH 7 and 8 suggests a mixture of 6cNO/5cNO.

3.3.4.4 NO Kinetics of wt McCP and F61V and F32V mutants

Stopped-flow experiments in which penta-coordinate ferrous *Mc*CP was mixed anaerobically with solutions of NO showed that the initial spectrum captured after mixing was that of the hexa-coordinate NO adduct. This was true at all pH values between pH 5 and 9. Thus, the initial binding of NO to the vacant distal coordination site is extremely rapid and occurred within the dead time of the apparatus (~ 1.5 ms). Combination of NO with the heme took place within this dead time even at the lowest NO concentration employed (5 μM) implying that the second order rate constant for combination $>10^8\ M^{-1}s^{-1}$.

Following this extremely rapid reaction a slower single exponential process occurred that can be assigned from its spectral properties (Figure 3.14) to the transition from the hexa- to penta-coordinated NO adduct. The extent to which this transition occurred was dependent on pH, the penta-coordinate form being more highly populated at lower pH (Figure 3.14) These observations are in full in agreement with the static spectra reported in Figure 3.12. The dependence of the value of the rate constant for this transition on NO concentration at two pH value (5 and 7.5) are reported in Figure 3.14 where it is seen that the rate constant tends to a plateau. Thus, the rate constant for the hexa- to penta-coordinate form is rate limited and this is consistent with this being the first order rate constant for His dissociation from the heme. From the fits to the data in Figure 3.14 D this dissociation rate constant is 2.13 s^{-1} at pH 5 and 0.73 s^{-1} at pH 7.5. The relative values of these constants are consistent with the pK_a determined from the static spectrum (Figure 3.12) suggesting that the dissociation rate constant and the extent of penta-coordinate adduct formed are controlled by the same single protonation event.

Stopped-flow experiments on the two *Mc*CP mutants (F32V and F61V) were carried out at pH 6.5 due to the instability of the mutants at high and low pH. The pH of 6.5 was chosen as

according to optical spectroscopy (See section 3.3.4.2) at this pH there should be a mixture of 5 and 6 coordinate NO populations for all of the proteins, albeit at differing percentages. The results of this showed little difference to the wt protein (1.0 s^{-1} for wt *Mc*CP, 1.03 s^{-1} for F32V and 0.95 s^{-1} for F61V) suggesting that neither mutation has an effect on the rate of transition between hexa- and penta-coordinate NO (Figure 3.15).

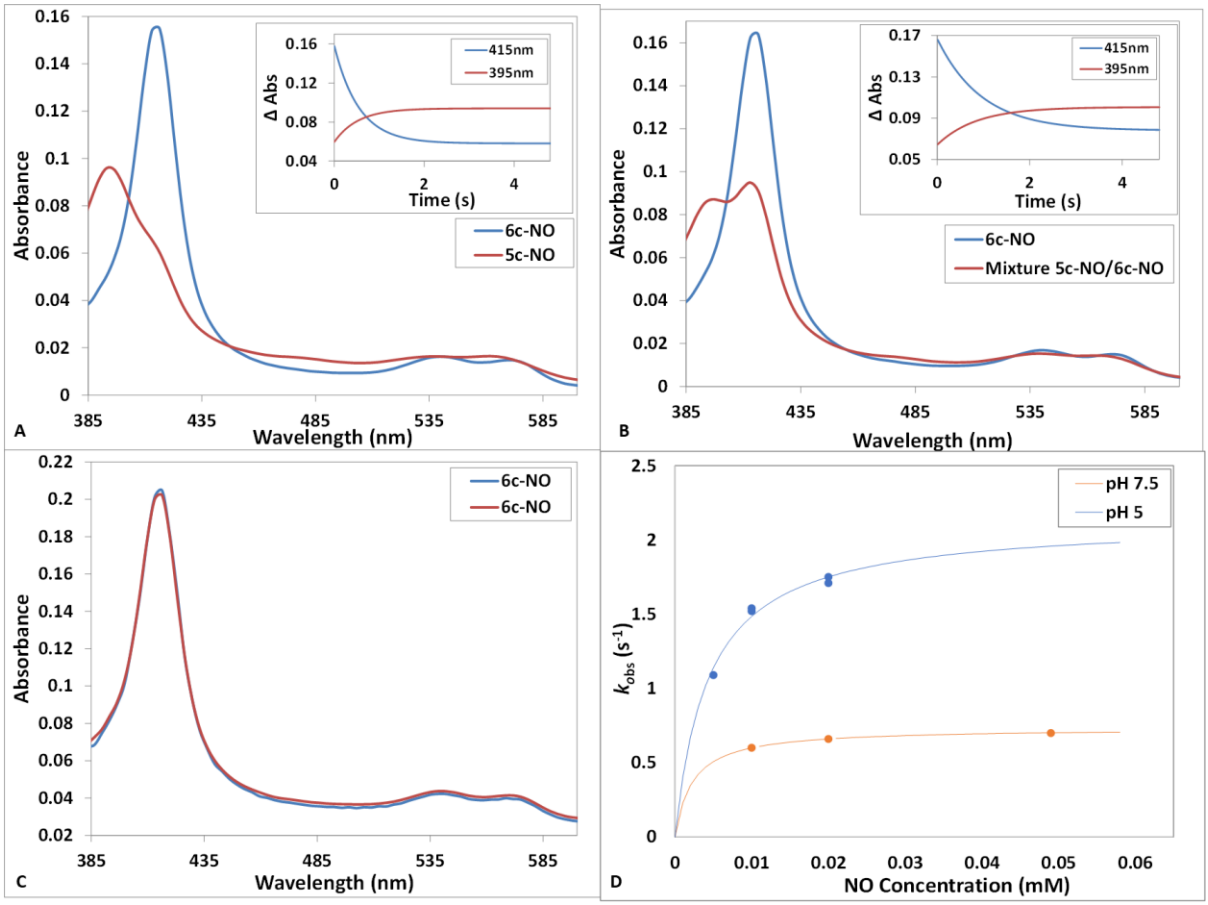

Figure 3.14. Stopped flow spectroscopy data for the reaction of ferrous *Mc*CP with NO. Panels A, B and C show the spectra at pH 5, 7.5 and 9 respectively obtained from global fitting of the diode array data to a simple **a** → **b** model where **a** represents the initial hexacoordinate NO complex and **b** the final spectrum at the end of the reaction, which shows either full conversion to the penta-coordinate for (pH 5), partial conversion (pH 7.5) or no conversion (pH 9) The insets show representative time courses collected at 415 and 395 nm, together with fits to single exponential functions. Panel D shows the rate constants k_{obs}, for the transition as functions of NO concentration together with hyperbolic fits.

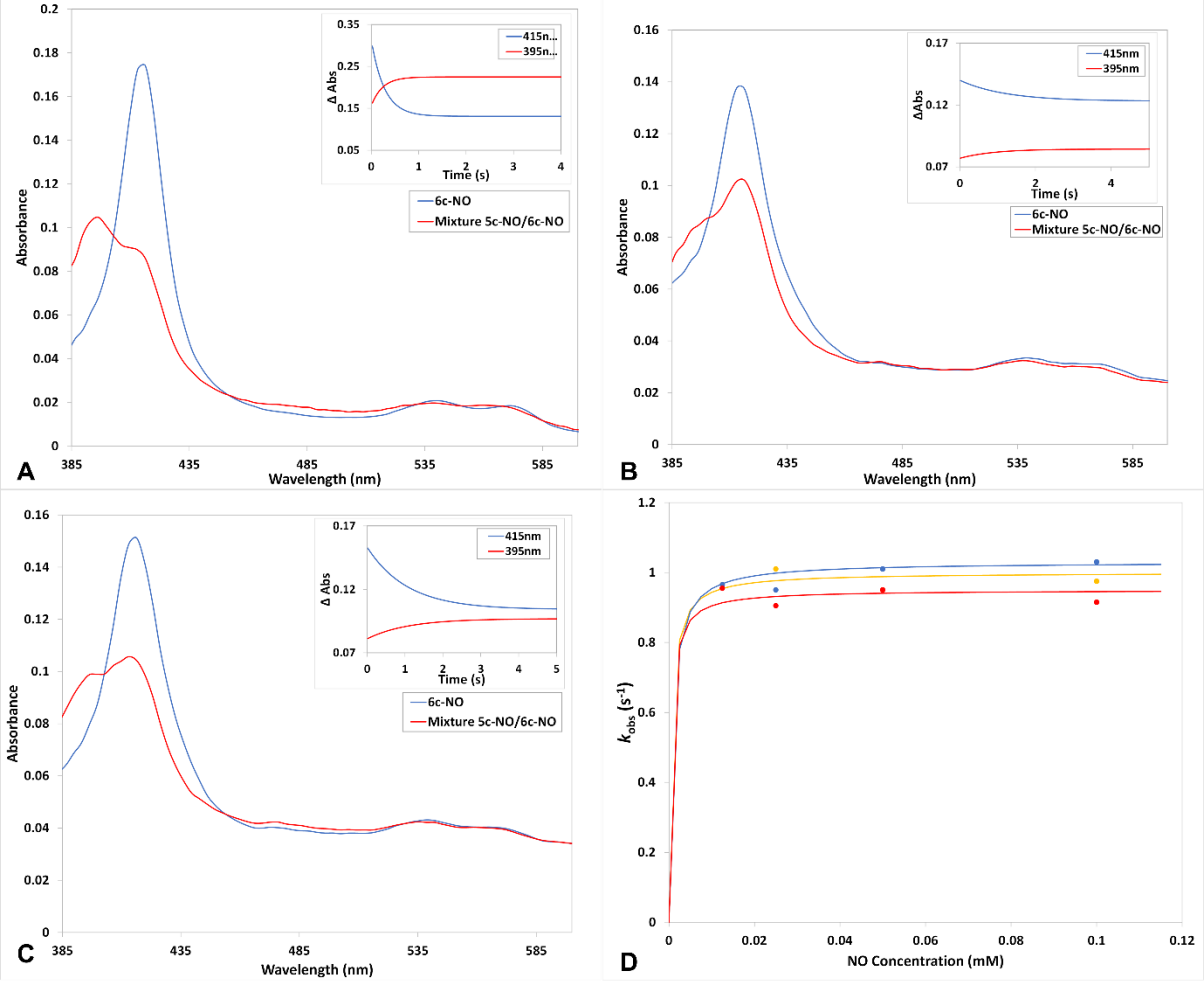

Figure 3.15. Stopped-flow spectroscopy data for the ferrous wt *Mc*CP (A), F32V variant (B) and F61V variant (C) at pH 6.5 obtained from global fitting of the diode array data to a simple **a** → **b** model where **a** represents the initial hexacoordinate NO complex and **b** the final spectrum at the end of the reaction, which shows partial conversion. The insets show representative time courses collected at 415 and 395nm, together with fits to single exponential functions. Panel D shows the rate constants k_{obs}, for the transition as functions of NO concentration together with hyperbolic fits yielding maximum values of 1.0 s^{-1} for wt *Mc*CP, 1.03 s^{-1} for F32V and 0.95 s^{-1} for F61V.

3.3.4.5 Crystallisation and Data Collection of NO and CO bound wt McCP and F61V and F32V mutants.

Crystal structures of Fe(II) *Mc*CP soaked with CO and NO were determined to 1.6 Å and 1.56 Å, respectively (Figure 3.16, Table 3.4), and compared to the chemically reduced Fe(II) *Mc*CP structure in the absence of ligands, determined at 1.68 Å (Figure 3.16, Table 3.6). The ligand-free Fe(II) structure resembles that of the as isolated *Mc*CP crystallised in the Fe(III) state (Figure 3.16). The homodimeric and tertiary structures of the Fe(II), Fe(II)CO and Fe(II)NO *Mc*CP complexes resemble those of ligand-free protein, with significant structural changes being essentially limited to the heme distal pocket (Figure 3.16).

Due to *Mc*CP having a vacant distal site in both the as isolated and chemically reduced forms it is easy to see if a ligand is bound in the maps produced by the ligand soaked crystals. Care must still be taken however to ensure the correct molecule is modelled into the map and this is ensured by using difference maps and checking the B-factors of the new ligand and adjacent Fe atom. In both the Fe (II)CO and Fe(II)NO crystal structures, the heme Fe centres are six-coordinate, and can therefore be referred to as 6cCO and 6cNO, respectively, with the gas ligand bound on the distal side opposite the proximal His 123 ligand. For the Fe (II)CO structure, the homodimer exhibits Fe-C distances of 1.78 and 1.86 Å, and near-linear Fe-C-O angles of 173 ° and 174 ° for monomer A and B, respectively (Figure 3.17 A, B). In the case of the Fe (II)NO structure, two orientations of distal NO with partial occupancy were modelled bound to the heme in monomer A, (Figure 3.17 D). One NO (occupancy = 0.5) is orientated towards Leu 28 with an Fe-N distance of 2.01 Å and an Fe-N-O angle of 148 ° whilst the other (occupancy = 0.5) is orientated in the opposite direction towards Gly 82 with an Fe-N distance of 1.87 Å and an Fe-N-O angle of 136 °. Only one

orientation of NO is seen in monomer B (Figure 3.17) (towards Gly 82) with an Fe-N distance of 1.80 Å and an Fe-N-O angle of 122 °.

The crystal structures shed light on the interaction of the distal Phe cap with exogenous gas ligands. Unlike Phe 61, which shows no significant conformational changes upon NO or CO coordination, Phe 32 can be seen to rotate around the Cβ-Cγ bond, allowing access to the distal Fe binding site and moving its aromatic ring face away from the heme (Figure 3.17). In the NO bound structures, the rotation around the Phe 32 Cβ-Cγ bond in comparison to the Fe (II) structure is 6 ° and 15 ° in hemes A and B, respectively, such that the aromatic ring face of Phe 32 presents towards the NO ligand and the ring atoms are 3.5-3.6 Å from the NO ligand (Figure 3.17 D, E). In heme A, Phe 32 also moves sideways away from the heme by 1.2 Å in comparison to the Fe (II) structure (Figure 3.17 D), no similar movement is seen in heme B (Figure 3.17 E). Within the Fe (II)CO structure, rotation around the Phe 32 Cβ-Cγ bond appears greater in one of the monomers resulting in two distal pocket conformations (Figure 3.17 A, B). In monomer A, the Phe 32 ring face is rotated 30 ° away from the CO ligand with a distance of 4.5 Å between the CO ligand and the ring atoms of Phe 32 (Figure 3.17 A). By contrast, in monomer B, the aromatic ring is presented towards the CO molecule (which more closely resembles the positioning seen in the NO complex) with a rotation of around 19 ° and a distance of 3.4 Å between the CO ligand and the Phe 32 ring atoms (Figure 3.17 B). Phe 61, which does not change its conformation, has its Cε2 atom some 3.2 Å from the O of the CO ligand, but other ring atoms as far as 3.9 Å away, consistent with a more offset position in both monomers.

Unlike α-helical Cytochromes *c'*, where 5cNO binds to the proximal side of the heme via a 6cNO distal bound intermediate, it appears that in *Mc*CP NO only binds to the distal side of the heme. Despite substantial effort including varying crystallisation pH we have been unable to produce a crystal structure of a 5cNO species in wt *Mc*CP.

In the crystal structure of the F32V variant 6cCO complex (Figure 3.18 A, B), the homodimer exhibits Fe-C distances of 2.03 and 2.07 Å, and a slightly more bent geometry than the wt ligand bound structure with Fe-C-O angles of 164 ° and 165 ° for monomer A and B, respectively. There is no observable movement of the pocket residues upon ligand binding and only one orientation of Phe 61 is observed. The F61V variant exhibits Fe-C distances of 2.01 and 2.00 Å and a similar bent geometry to the wt ligand bound structure with Fe-C-O angles of 166 ° and 177 ° for monomer A and B respectively (Figure 3.19 A, B). The F61V variant still displays two possible conformations of Phe 32 in the presence of CO. In heme A one is in a similar position to the wt CO structure, although the plane of the Phe ring is facing more towards the heme with the nearest ring atom being at a distance of 3.43 Å, whilst the one which had moved into the space above the heme (previously occupied by Phe 61) has also rotated so as to present the plane of the Phe ring to the CO oxygen with the nearest ring atom being 3.23 Å away (Figure 3.19 A). In heme B there are again two conformations of Phe 32 in similar positions; again one is in a similar position to the wt CO structure, with just a slight rotation so that the plane of the Phe ring is presenting less to the CO oxygen with the nearest ring atom being 3.14 Å away, whilst the other is in the space above the heme and slightly rotated so as to present more of the plane to the CO oxygen with the nearest ring atom being 3.08 Å away from the CO oxygen (Figure 3.19 B).

NO is bound to the distal face of the heme in both the F61V (Figure 3.19 D, E) and F32V (Figure 3.18 D, E) variants. In F61V, only one conformation of NO binding can be seen in each heme, pointing towards Gly 82 (Figure 3.19 D, E). These both have Fe-N distances of 1.86 Å and Fe-N-O angles of 130 ° and 135 ° in hemes A and B respectively. Only one conformation of the remaining Phe can be seen in each heme coming across the face of the heme towards the mutated Val residue. In F32V, only one conformation of NO binding can again be seen in each heme (Figure 3.18 D, E). However, one points towards Leu

28 (heme A) and the other towards Gly 82 (heme B) (Figure 3.18 D, E). These have Fe-N distances of 1.90 Å and 1.97 Å and Fe-N-O angles of 110 ° and 92 ° in hemes A and B respectively. There is no movement of the pocket residues observed in the F32V variant upon introduction of NO. In both NO bound variants, the Fe-His distance appears longer than expected for a 6-coordinate structure suggesting the His residue may be dissociating from the heme, giving rise to a 5-coordinate form. This is most evident in the F61V structure with Fe-His distances of 2.93 Å and 3.03 Å in hemes A and B respectively. It can be seen in the structures that the heme becomes domed as the Fe moves upwards, resulting in the extended Fe-His distances. The His residue displays a slight rotation of ~ 8 ° around the Cβ-Cγ bond and only moves downwards by about 0.2 Å. There is also a small amount of movement in the rest of the chain around the His residue. Notably the residues remain in a position to allow His 123 to remain hydrogen bonded to Tyr 131.

Table 3.4. Data collection, processing and refinement statistics for ligand bound wt *Mc*CP, F32V and F61V crystal structures.

Dataset	*McCP Fe(II)*	*Mc*CP-CO	*Mc*CP-NO	F32V-CO	F32V-NO	F61V-CO	F61V-NO
Resolution (Å)	43.09 – 1.68	47.2-1.60	47.3-1.56	52.94-1.77	61.16-1.94	52.72-2.09	33.59-1.68
Unit cell, (Å)	a=b=c=105.56	a=b=c=105.5	a=b=c=105.7	a=b=c=105.9	a=b=c=105.9	a=b=c=105.5	a=b=c=106.2
Unique reflections	42598 (2216)	51778 (2607)	56066 (2797)	38716 (1958)	29544 (1570)	23393 (1514)	45287 (2318)
Completeness (%)	100 (100)	100 (100)	100 (100)	100 (100)	100 (100)	100 (100)	99 (100)
Redundancy	6.7 (6.8)	20 (21)	20 (21)	6.7 (6.8)	10 (11)	19 (21)	3 (3)
R_{meas}	0.044 (1.31)	0.069 (2.73)	0.080 (2.52)	0.069 (2.04)	0.044 (2.94)	0.032 (5.27)	0.049 (0.91)
I/σ(I)	24.2 (1.4)	26.3 (1.4)	20.0 (1.5)	18.7 (0.6)	13.5 (0.5)	22.7 (0.6)	11.7 (1.1)
$CC_{1/2}$	1.0 (0.3)	1.0 (0.5)	1.0 (0.5)	1.0 (0.3)	1.0 (0.3)	1.0 (0.4)	1.0 (0.6)
Wilson B-factor ($Å^2$)	28.0	25.9	24.6	32.5	39.0	45.31	29.8
R_{work}	0.194	0.181	0.182	0.191	0.187	0.204	0.178
R_{free}	0.228	0.198	0.204	0.212	0.207	0.269	0.202
RMSD bond length (°)	0.015	0.014	0.015	0.015	0.013	0.013	0.015
RMSD bond angles (Å)	2.3	2.2	1.86	2.09	2.21	2.20	1.86
Ramachandran favoured (%)	97.76	96.3	95.0	95.9	95.9	94.0	98.1
PDB accession code	7ZVZ	6ZSK	7ZPS	7ZSX	7ZSW	7ZTI	7ZQZ

Table 3.5. Heme site parameters in wt *Mc*CP, F32V and F61V crystal structures

Structure	*Mc*CP Fe(III)	*Mc*CP Fe(II)	*Mc*CP-NO	*Mc*CP-CO	F32V	F32V-NO	F32V-CO	F61V	F61V-NO	F61V-CO
Fe-His (Å)	2.10/2.09	2.11/2.13	2.17/2.20	2.08/2.05	2.02, 2.05	2.53, 2.62	2.03, 2.07	2.00, 2.08	2.93, 3.03	2.10, 2.09
Fe-NO (Å)	-	-	1.89/1.99/1.77	-	-	1.90, 1.97	-	-	1.86, 1.86	-
Fe-CO (Å)	-	-	-	1.86/1.78	-	-	2.03, 2.07	-	-	2.01, 2.00
Fe-N-O (°)	-	-	135/139/123	-	-	110, 92	-	-	130, 135	-
Fe-C-O (°)	-	-	-	174/173	-	-	164, 165	-	-	166,177

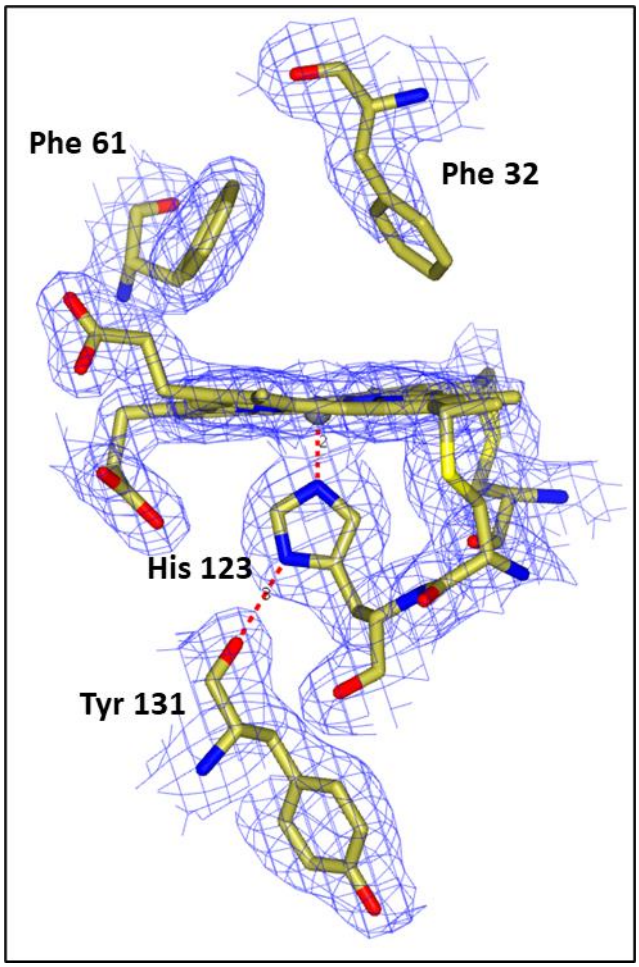

Figure 3.16. *2Fo-Fc* map contoured at 2 σ of chemically reduced *Mc*CP. The residues in both the distal and proximal pockets are in similar positions to the as isolated 'ferric' structure.

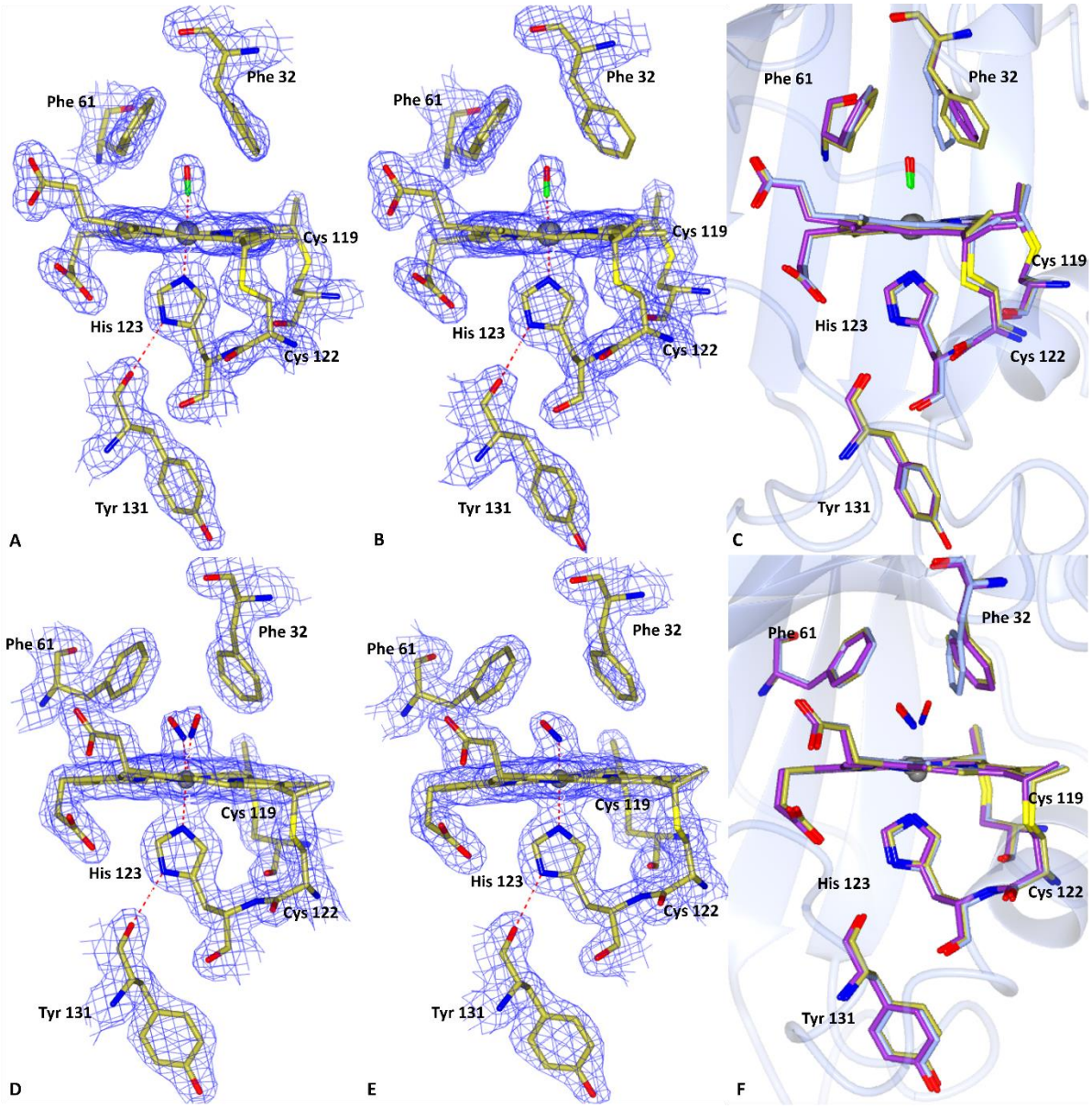

Figure 3.17. *2Fo-Fc* map contoured at 1.5 σ of hemes A and B of *Mc*CP, with either CO (A, B) or NO bound (D, E). Only one orientation of CO is seen with an angle of 170/173 °. Two orientations of NO are seen in monomer A and one in monomer B. The aromatic ring of Phe 32 can be seen to be rotated away from the CO molecule in the second heme. Comparison of wt *Mc*CP (blue) and both hemes A (purple) and B (gold) with CO (C) or NO (F) bound, Phe32 can be seen to rotate away upon introduction of a ligand to the distal side of the heme.

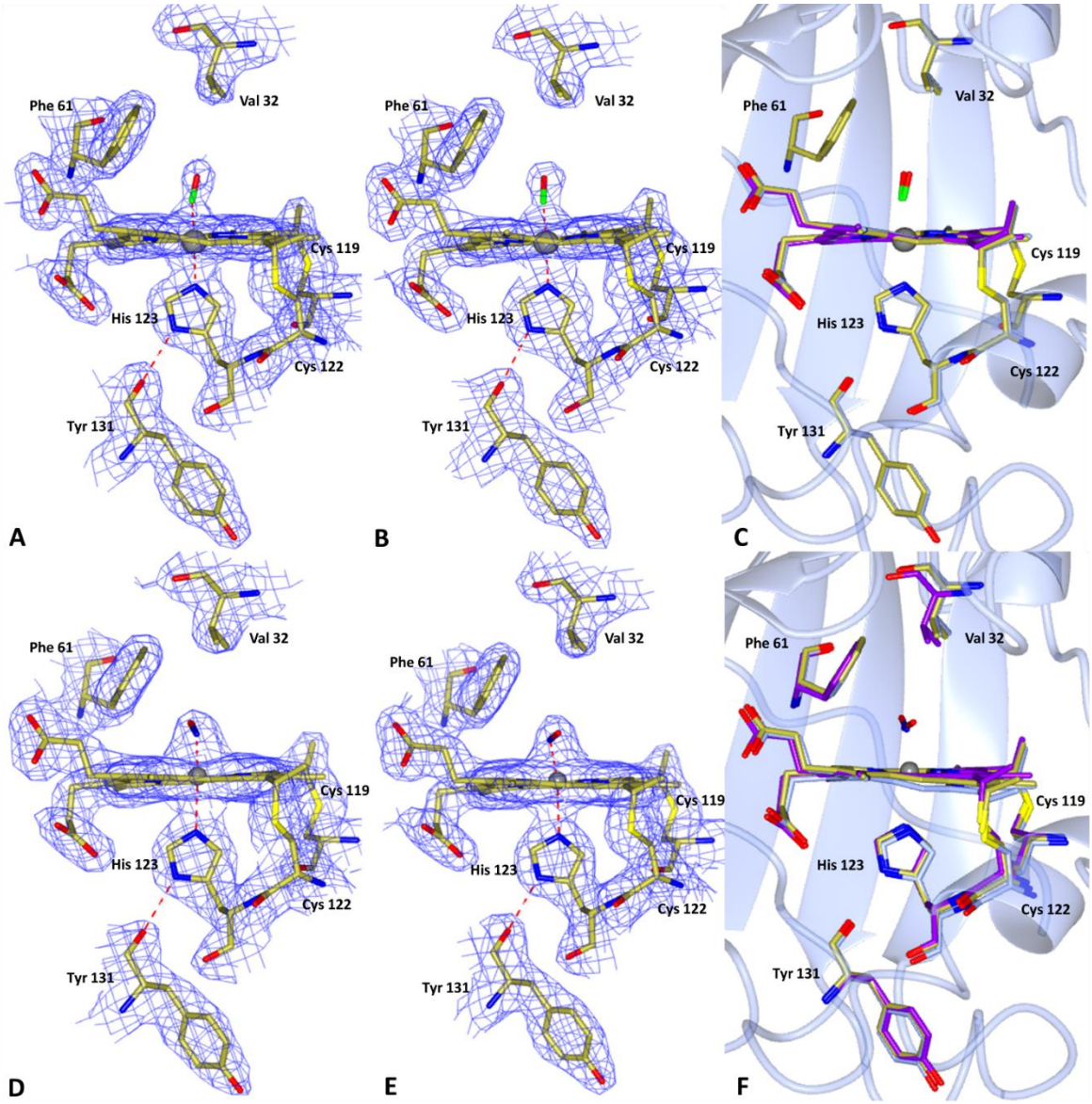

Figure 3.18. *2Fo-Fc* map contoured at 1.5 σ of hemes A and B of F32V *Mc*CP, with either CO (A, B) or NO bound (D, E). Comparison of as isolated F32V (blue) and both hemes A (purple) and B (gold) with CO (C) or NO (F) bound. Only one orientation of CO can be seen with a slightly more bent geometry than wt *Mc*CP at angles of 164/165 °. Two orientations of NO can be seen: one points towards Leu 28 (heme A) and the other towards Gly 82 (heme B). These have Fe-N distances of 1.90 Å and 1.97 Å and Fe-N-O angles of 110 ° and 92 ° in hemes A and B respectively.

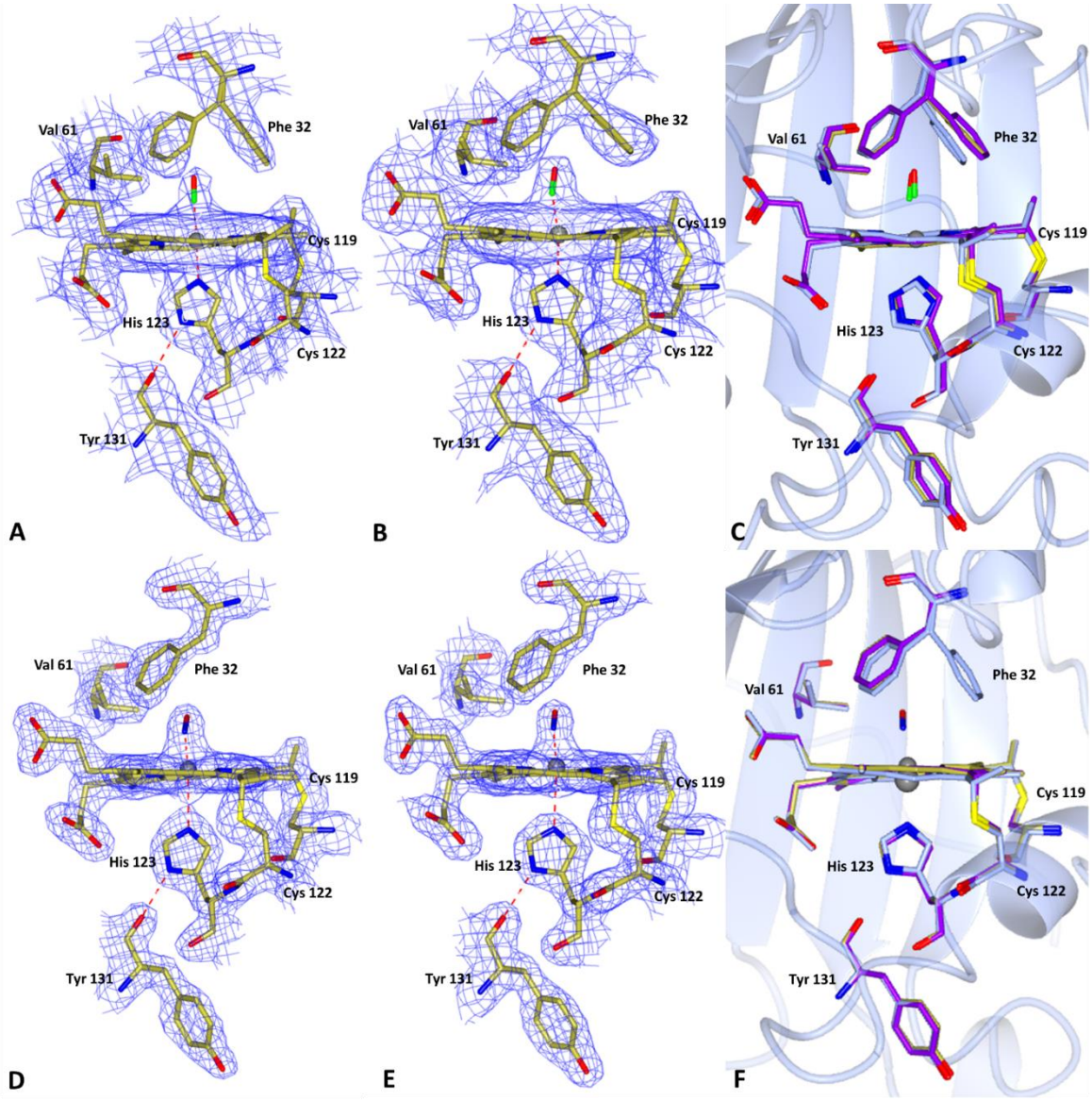

Figure 3.19. *2Fo-Fc* map contoured at 1.5 σ of hemes A and B of F61V *Mc*CP, with either CO (A, B) or NO bound (D, E). Comparison of as isolated F61V (blue) and both hemes A (purple) and B (gold) with CO (C) or NO (F) bound. Only one orientation of both CO and NO can be seen with angles of 166 ° and 177 ° (CO) and 130 ° and 135 ° (NO).

3.3.4.6 Accessibility of the heme

Using the available X-ray crystal structures, the accessibility of both the proximal and distal face of the heme of the β-sheet cytochrome *c*' of *Mc*CP (wt, F32V and F61V) and the α-helical *c' Ax*CP were investigated using Caver (Jurcik *et al.*, 2018) which allows for tunnel analysis in both static and dynamic structures. Tunnels were calculated (with a probe radius of 0.9 Å and remaining default settings) that could allow access for ligands from the outside solvent to either face of the heme.

The resulting images show that only the distal face of the heme is accessible for the ferric, ferrous, CO and NO bound structures of *Mc*CP (Figure 3.20). In the ferric and ferrous protein this consists of two tunnels coming in from either side of the protein for heme B and three tunnels for heme A with the third tunnel coming around Phe 32 (Figure 3.20). The CO bound protein displays two tunnels similar to that of heme B in the ferrous protein whilst the NO bound protein has three tunnels similar to heme A of the ferric form (Figure 3.20). The proximal face appears to be buried within the surface of the protein, not allowing any access to ligands (Figure 3.20). This gives support to binding of ligands only occurring on the distal side of the heme in cytochrome *c'*-β as has been seen in the X-ray crystal structures of ligand bound *Mc*CP. The F32V mutant displays a similar set of tunnels to the wt protein with access to the heme still only being on the distal side (Figure 3.21). The F61V mutant shows a greater amount of tunnels in comparison to wt *Mc*CP and the F32V mutant but despite this there is still no access to the proximal side of the heme suggesting that all binding occurs on the distal side of the heme (Figure 3.22).

Ferric *Ax*CP (Figure 3.23) has two tunnels, again from either side of the protein, coming in to meet at the distal face of the heme. Upon chemical reduction of the heme the number of tunnels increases, one is predicted to go across to the other monomer of the protein to its

respective heme whilst the other is heading towards Phe 79. The CO bound *Ax*CP, where the ligand is bound to the distal face of the heme, has similar tunnels to the ferrous form. The 5-coordinate NO bound *Ax*CP, where the ligand is bound to the proximal face of the heme, shows a new tunnel coming off the one that was heading towards Phe 79 which comes round to the proximal face. Superimposition of all the *Ax*CP structures (not shown) reveals only very small movement of residues around the heme in order to allow for this change in the tunnels present, with the exception of Arg 124, the proximal histidine in the NO-bound structure only and Leu 16 in the CO-bound structure only.

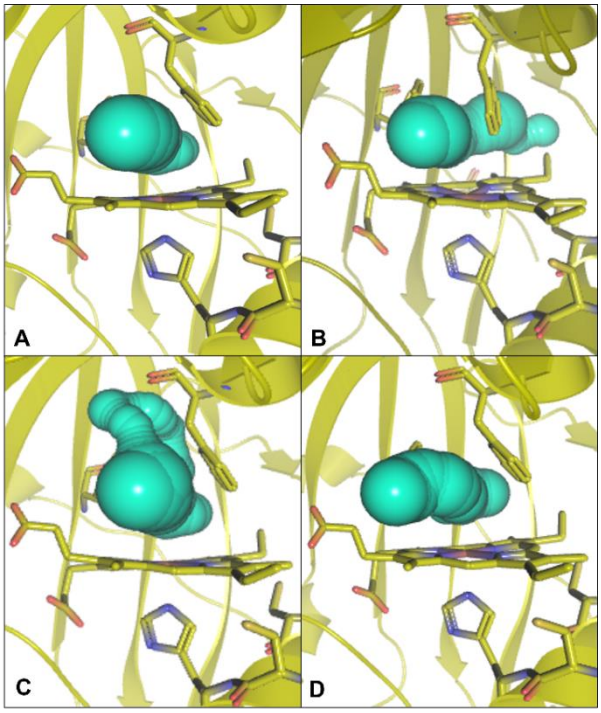

Figure 3.20. Tunnels (in green) allowing access to the heme of ferric (A), ferrous (B), CO-bound (C), NO-Bound (D) *Mc*CP. Only one heme for each form is shown as both display the same pattern of tunnels to the heme. Only the distal side of the heme is accessible in both cases.

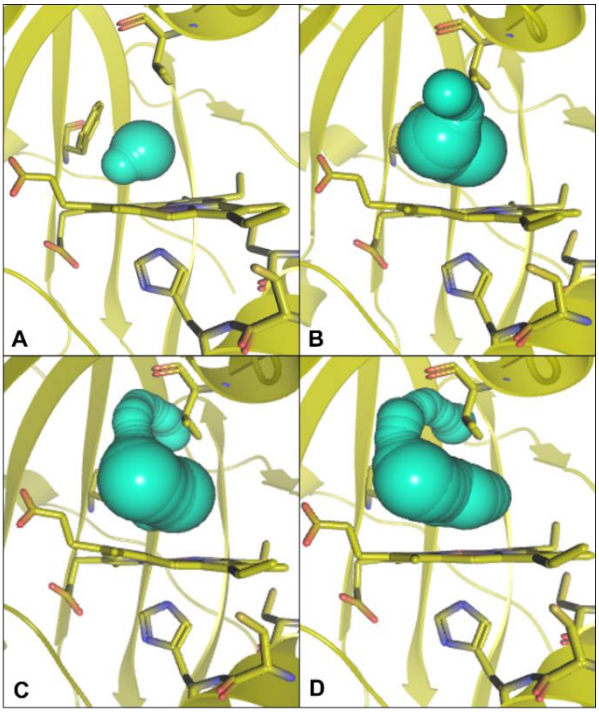

Figure 3.21. Tunnels (in green) allowing access to the heme of ferric (A), ferrous (B), CO-bound (C), NO-Bound (D) F32V. Only one heme for each form is shown as both display the same pattern of tunnels to the heme. Only the distal side of the heme is accessible in both cases.

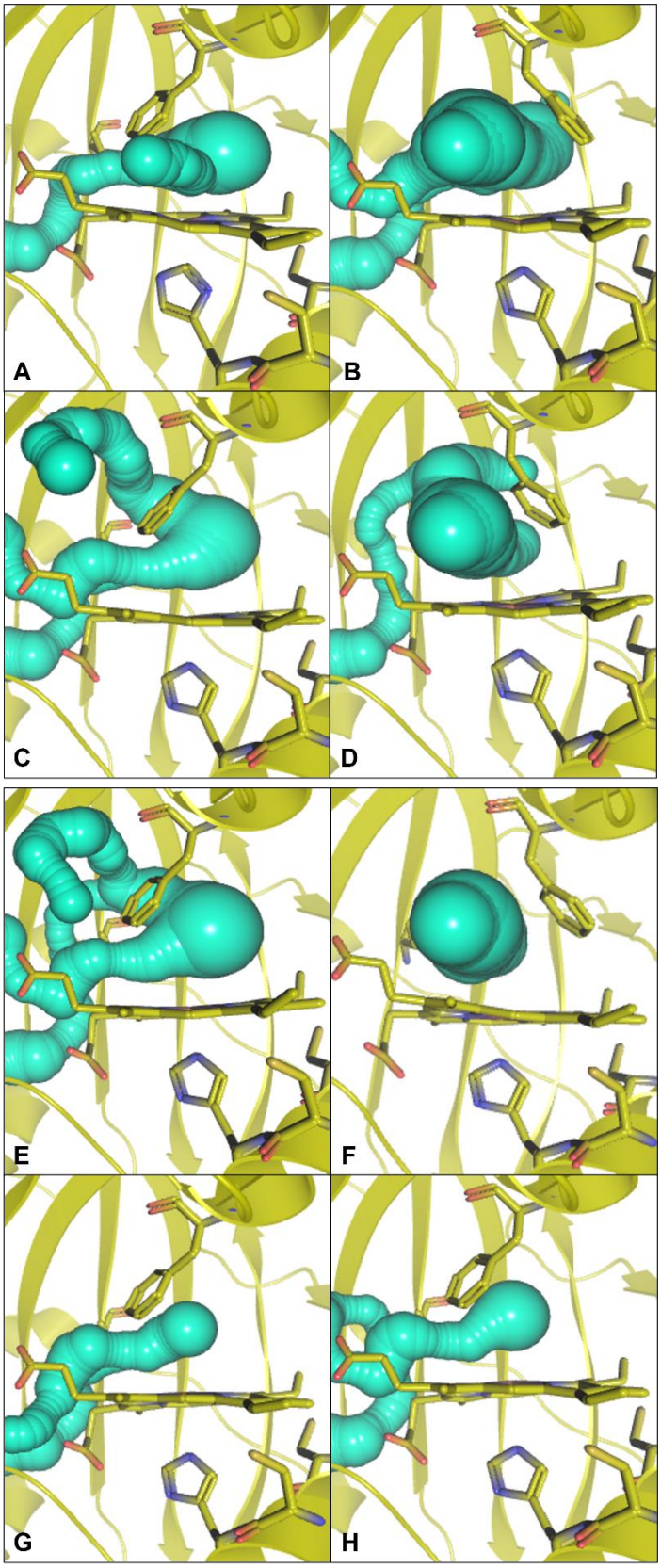

Figure 3.22. Tunnels (in green) allowing access to the heme of ferric (A, B) and ferrous (C, D) CO-bound (E, F), and NO-Bound (G, H) F61V. Only the distal side of the heme is accessible in both cases.

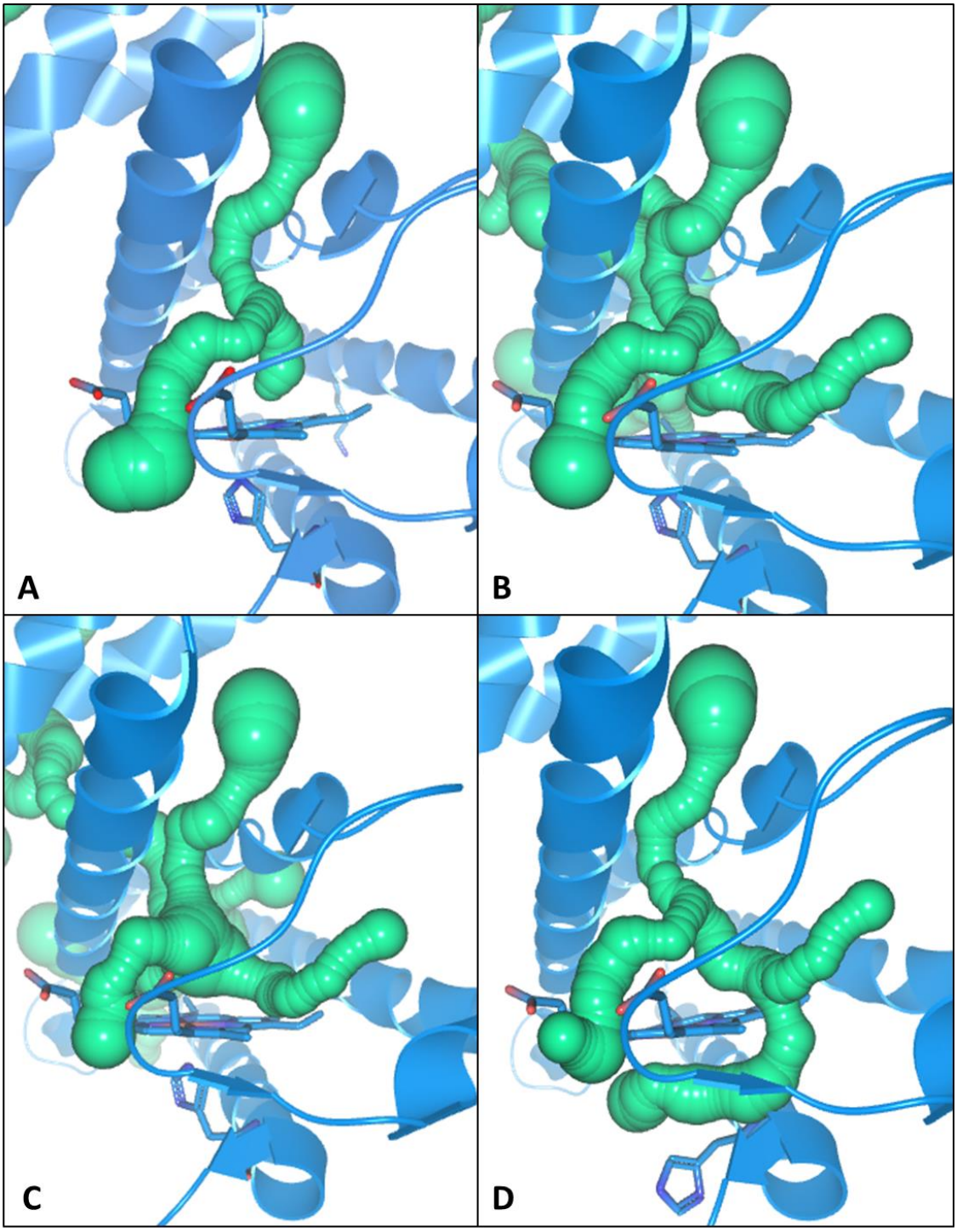

Figure 3.23. Tunnels (in green) allowing access to the heme of ferric (4CDA) (A), ferrous (4CIP) (B), CO-bound (3ZWI) (C), NO-Bound (4CJG) (D) *Ax*CP. The ferric protein shows access to the distal face of the heme. Reducing the protein (B) increases the number of tunnels present but still only allows access to the distal side of the heme. The CO-bound structure (C) has similar tunnels to the ferrous structure with access only being to the distal face of the heme. The NO-bound structure shows a new tunnel leading to the proximal face of the heme where the NO is bound.

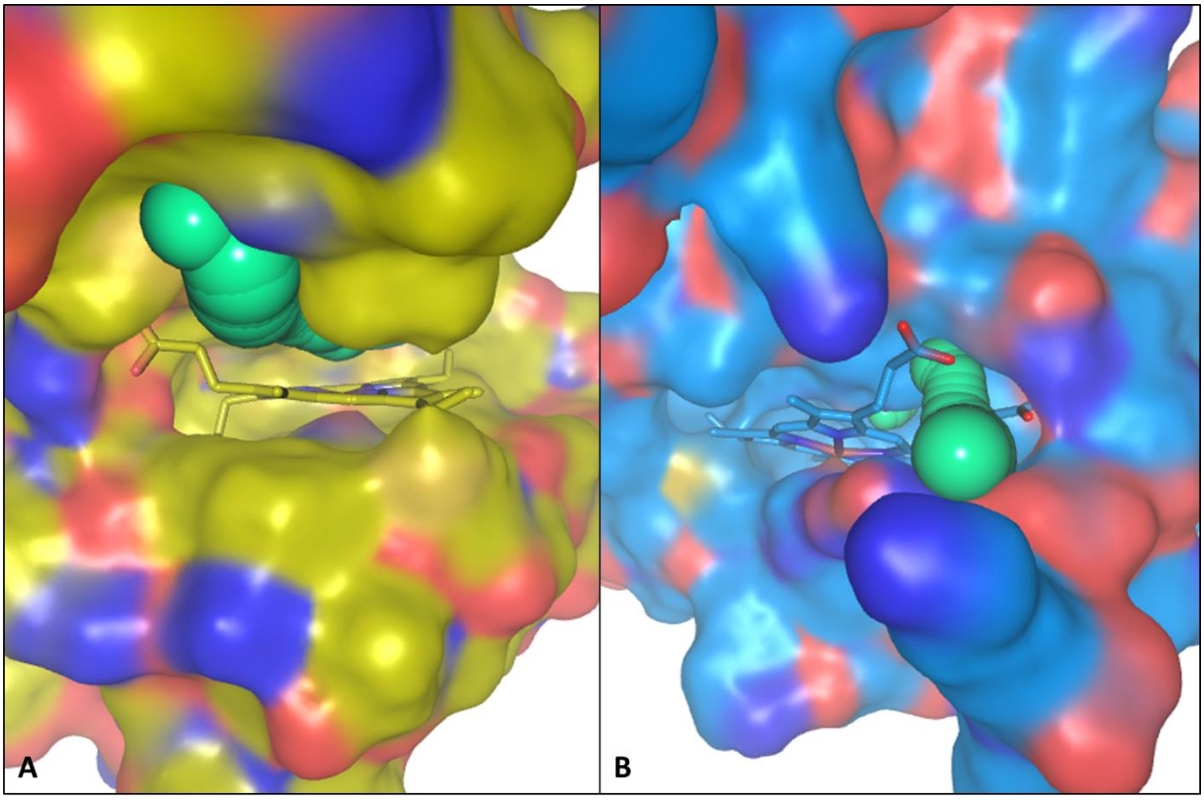

Figure 3.24. Surface modelling of *Mc*CP (6HIH) (A) and *Ax*CP (4CDA) (B) showing tunnels accessing the heme pocket.

3.4 Discussion

UV-visible spectroscopy of wt *Mc*CP showed that the protein bound both NO and CO as previously described (Zahn *et al.*, 1996). Whilst CO may not be physiologically relevant it does give insight to ligand binding properties of the protein and thus is interesting to investigate. *Mc*CP bound CO with a Soret maximum of 419 nm together with α/β bands around 565 nm and 535 nm indicative of 6 coordinate binding of the ligand. This is the same as has been reported to be seen in cytochromes *c'*-α (Hough and Andrew, 2015) and in cytochrome *c'*-β^{Met} (Liew *et al.*, 2020) which is the only other data currently published for CO binding to a *c'*-β.

Attempts to further investigate the binding of CO to *Mc*CP with stopped-flow spectroscopy were unsuccessful due to the reaction being completed within the deadtime of the instrument, even at very low (20 μM) CO concentrations indicating that the second order rate constant for CO binding is > 5x 10^7 $M^{-1}s^{-1}$. Thus, flash photolysis spectroscopy was used to monitor the reaction. Following dissociation upon exposure to the laser, CO was shown to recombine with the heme within 1 ms. The time courses comprised of the sum of two exponential processes, the dependencies of which the faster process could be fitted to hyperbolic function suggesting that the constant approaches a limiting value at high CO concentration. The faster process could be estimated to have an upper limit of ~ 7000 ± 1300 s^{-1}, however the slower process could not be given a limit with any confidence due to it being more linear in nature. The relative amplitudes of the two processes are also dependant on CO concentration such that the higher the CO concentration the larger is the fraction of the binding process that occurs in the faster phase. Such behaviour is typical for hexa-coordinate hemoglobins in which, following photolysis of the carboxy adduct, there is competition for the free coordination site between CO, that binds in a CO concentration dependent second order process, and histidine, the binding of which is first order. In *Mc*CP there is no competition

between CO and an intrinsic ligand such as His. However, this behaviour can also arise when only a penta-coordinate form of the ferrous species is present and has been described, for example, by Manole et al (2015) for a cytochrome *c'* in terms of relaxation between conformational forms within the heme pocket. The data for wt *Mc*CP is consistent with such a model, the simplest form of which proposes that the approach to the heme iron of CO is hindered by the position of a bulky group in the vicinity of the heme group. In the wt this is probably Phe 32 that can adopt two configurations, one that permits ready access to the heme while the other does not. Following photolysis, removing the CO from the heme pocket, this Phe group can adopt a position(s) that interferes with CO rebinding. This motion is likely coupled to vibrational modes in the protein and occurs in the 100 μs time range. Thus, at high CO concentration where CO binding is in this time range it competes effective with Phe movement. At lower CO concentration the Phe has time to reposition, and CO binding is hindered and becomes rate limited at very high CO concentration by motion of the Phe. This picture is complicated by the observation that the fast phase also exhibits hyperbolic dependence of the rate constant on CO concentration suggesting that there is a second configurational equilibrium in play.

NO binding in *Mc*CP displayed a pH dependent equilibrium between 5 and 6 coordinate species. At high pH a Soret maximum of 415 nm is seen which is typical of a low spin hexa-coordinate species and may be assigned to a ferrous heme with NO occupying the distal coordination site and histidine the proximal site. Whilst at low pH a Soret maximum of 395 nm is seen which is assigned to the penta-coordinate form in which the histidine has dissociated while the NO remains bound. The UV-visible data is supported by EPR spectroscopy which clearly displays the same pattern with varying pH (5c-NO 3-line hyperfine pattern seen at pH 4-6 shifting to a line shape associated with 6cNO binding at pH 8-10 but with an unresolved 9-line hyperfine pattern). Cytochromes *c'*-αs have been shown to

display 6cNO and/or 5cNO depending on the organism and sample conditions. *Chromatium vinosum* cytochrome *c'* (*Cv*CP) and *Rhodobacter capsulatus* cytochrome *c'* (*Rc*CP), for example, both have a mixture of 5cNO and 6cNO at around pH 7, whilst *Ax*CP only has a transient 6cNO as a precursor to its proximal 5cNO product and *Sf*CP only appears to show 5cNO (Hough and Andrew, 2015). *Tt*CP, the only *c'*-β with any published NO spectroscopy, appears to demonstrate mostly 5cNO binding with shoulder around 415 nm suggesting a small population of 6cNO (Yoshimi *et al.*, 2022). No pH dependency data has been published for any other *c'*-βs. For most *c'*-αs the 5cNO form appears to predominate at equilibrium at all published pH, whereas *Mc*CP displays a clear dependency based on the pH of the sample. Whilst *c'*-αs tend to show predominately 5cNO geometry, most heme proteins actually retain a 6cNO geometry due to conformational constraints of the protein scaffold that help retain the endogenous (His) protein ligand. There are however some heme protein, for example Mb, where 6cNO→5cNO conversion can be achieved by protonation of the proximal His ligand, although the pK_a for this conversion is relatively low (4.7 in the case of Mb) (Duprat *et al.*, 1995). By comparison, the 6cNO–5cNO equilibrium in *Mc*CP (attributed to protonation of the His 123 Nε) has an unusually high pK_a of ∼7.2. Analysis of the 6cNO *Mc*CP crystal structure does not indicate any obvious structural feature near the proximal heme face that might stabilize the unbound (protonated) state of the His ligand in the 5cNO population. The crystal structure also indicates that *Mc*CP retains NO on the distal heme face, thereby ruling out a distal → proximal switch in heme–NO coordination as a driver of 5cNO formation, as occurs in cyts *c*′-α (Kekilli *et al.*, 2017). It is possible that the relatively high pK_a for the 6cNO–5cNO equilibrium in *Mc*CP could arise from increased flexibility in the surrounding protein matrix.

Stopped -flow experiments in which ferrous *Mc*CP was mixed anaerobically with solutions of NO showed that the initial spectrum captured after mixing was that of the hexa-coordinate

NO adduct. Thus, the initial binding of NO to the vacant distal coordination site is extremely rapid and occurred within the dead time of the apparatus (~1.5 ms) similar to that seen for CO binding. Combination of NO with the heme took place within this dead time even at the lowest NO concentration employed (5 μM) implying that the second order rate constant for combination $>10^8$ $M^{-1}s^{-1}$. Following this a single slower exponential process occurred which could be attributed to the transition between 6cNO to 5cNO from its UV-visible spectra properties. As seen in the UV-visible spectroscopy and EPR spectroscopy this transition was pH dependant with the 5cNO being more predominant at lower pH and the 6cNO being more predominant at higher pH. This transition was shown to be NO dependant and tended to reach a plateau. This data is consistent with this being the first order rate constant for histidine dissociation from the heme with dissociation rate constants of 2.13 s^{-1} at pH 5 and 0.73 s^{-1} at pH 7.5. The relative values of these constants are consistent with the pK_a determined from the static spectrum, suggesting that the dissociation rate constant and the extent of penta-coordinate adduct formed are controlled by the same single protonation event.

The exceptionally high on rates for gas binding in *Mc*CP indicates that the Phe cap in *Mc*CP provides very little steric hinderance to heme-gas coordination unlike the residues in the distal pocket in the cytochromes *c'*-α. Structural data suggests that all ligand binding occurs on the distal face of the heme, again unlike cytochromes *c'*-α which can bind NO to the proximal side of the heme. It can be seen in the ligand bound structures that the conformation of Phe 61 remains relatively unchanged, whilst Phe 32 undergoes rotation around the Cβ-Cγ bond. It also remains within close proximity to any bound ligands with its ring face orientated towards CO in one subunit and toward NO in both subunits. Protein samples were sent to collaborators (Dr C. Andrews, Eastern Oregon University) who carried out resonance Raman (RR) measurements of the NO and CO complexes which showed evidence of unusually weak Fe(II)→XO(π∗) back-bonding, which can be attributed to the proximity of the gas ligand to

the local negative polarity of the aromatic quadrupole of the Phe 32 ring (Figure 3.25) (Adams *et al.*, 2023). It was also observed that there were two sets of ν(CO) and ν(FeCO) RR bands which correspond to the two Phe 32 orientations evident in the 6cCO structure. This further suggests that Phe 32 inhibits Fe(II)→XO(π∗) back-bonding only when its ring face presents to the XO ligand.

Mutating out each of the Phe residues in turn substantiates the suggestion that Phe 32 has an impact on gas binding. F32V and F61V mutants were successfully created and expressed using the same expression system as the wt protein. UV-visible and EPR spectroscopy of the as isolated mutants were similar to that seen for the wt protein, although both mutants appeared to be less stable at high and low pH in comparison to the wt. Both mutants bound CO with Soret maximum around 419 nm indicative of a 6cCO binding geometry. Similar behaviour to the wt protein was observed for CO binding following photolysis of the F61V variant of *Mc*CP. However, the values of the rate constants are much smaller and the CO concentration dependence appears more linear as a result of this. A very similar model to the wt protein appears to hold for the F61V variant in which the X-ray structure shows that Phe 32 can now take up a position above the heme group that hinders ligand approach. There are still two kinetic phases of the amplitudes which again demonstrates that there is a dynamic equilibrium between forms which possess different binding kinetics. The slower phase is now limited by the kinetics of movement of Phe 32 residue and by the equilibrium between forms allowing or hindering access. The behaviour for CO binding following photolysis of the F32V variant of *Mc*CP was different to the wt and F61V mutant with the suggestion that there were now three processes occurring.

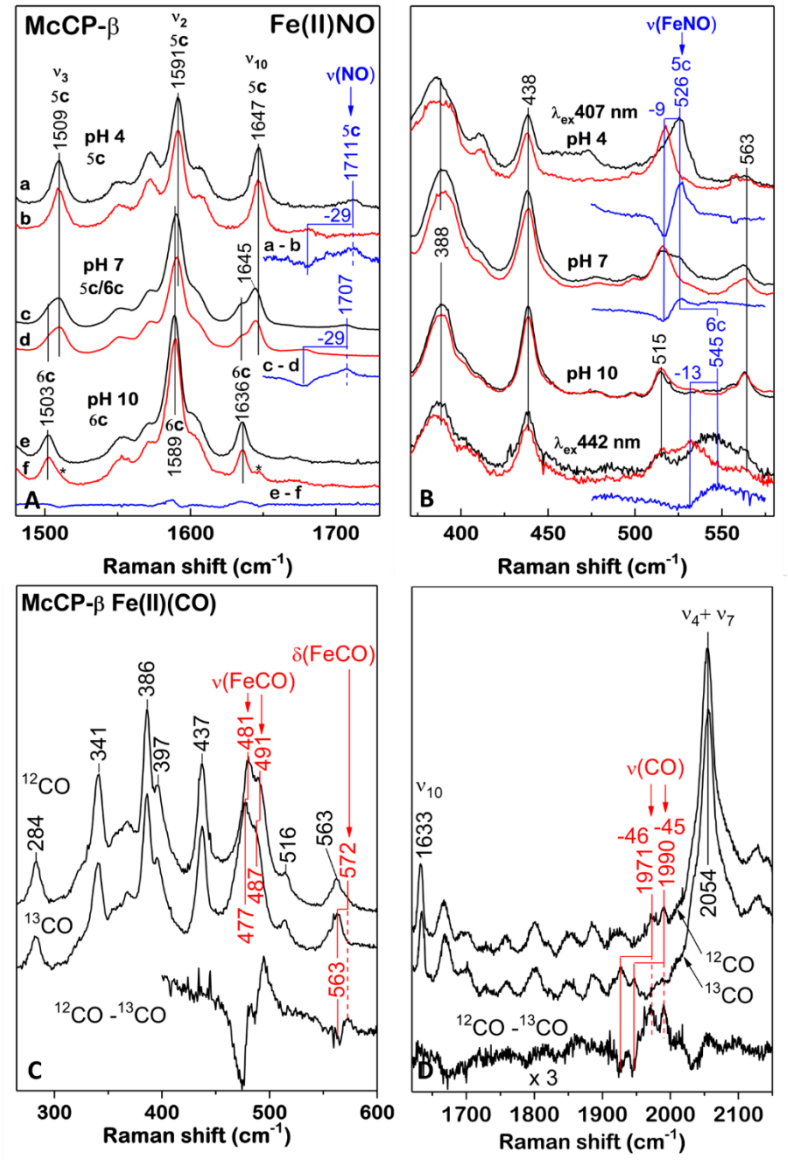

Figure 3.25. Room-temperature Resonance Raman data for wt *Mc*CP with ligands adapted from Adams et al 2023. NO bound samples were prepared with ^{14}NO (black) and ^{15}NO (red), together with ^{14}NO - ^{15}NO difference spectra (blue) in the high frequency (A) and low frequency (B) regions. Spectra at pH 4.0 correspond to a 5cNO complex, while spectra at pH 10 correspond to a 6cNO complex (asterisks denote minor contributions of 5cNO species). A mixture of 5cNO and 6cNO species is observed at pH 7.0. 6cCO *Mc*CP complexes prepared with ^{12}CO and ^{13}CO recorded in the low frequency (C) and high frequency (D) regions, together with ^{12}CO – ^{13}CO difference spectra.

As was seen for the wt protein, UV-visible and EPR spectroscopy showed that NO bound to both mutants with a 5cNO/6cNO pH dependency. The F32V (but not the F61V) mutation can be seen to lower the pK_a for the 6cNO–5cNO equilibrium from ~7.0 (wt and F61V) to ~6.0 (F32V). A possible explanation for this is that the microenvironment of the Phe 32 quadrupole could interact differently with the Fe–NO units of 6cNO and 5cNO species to influence their relative stability and favour the 5cNO form

The crystal structure of the F61V variant 6CO complex showed a similar bent geometry to the wt ligand bound structure with Fe-C-O angles of 166 ° and 177 °. This structure also showed two conformations of Phe 32, one being in a similar position to that seen in the wt protein, although with the plane of the ring facing more towards the heme, and the other moving into the space created above the face of the heme (by the removal of Phe 61) which is also rotated so as to present the plane of the Phe ring to the bound CO molecule. The F32V 6cCO complex crystal structure showed slightly more bent geometry than both the wt and F61V variant with Fe-C-O angles of 164 ° and 165 °. There was also no observable movement of the pocket residues upon CO binding.

NO is bound to the distal face of the heme in both the F32V and F61V variants. In both variants only one conformation of NO binding can be seen although the orientation differs, in F61V the oxygen atom of the NO molecule is directed towards Gly 82, whilst in F32V in one monomer it is directed towards Leu 28 and the other Gly 82. In the F61V NO complex structure only one conformation of the remaining Phe residue can now be seen which is positioned over the distal face of the heme. In F32V no movement of the remaining distal pocket residues is seen. Interestingly in both NO bound variants the Fe-His distance appears longer than would be expected for a 6-coordinate structure: 2.93 Å and 3.03 Å in F61V and

2.53 Å and 2.62 Å in F32V. This is suggestive of the histidine disassociating from the heme giving rise to a 5-coordinate structure. In both these structures the heme appears more domed as the Fe moves upwards away from the histidine resulting in the extended Fe-His distances (Figure 3.26). The histidine itself displays a small downwards movement of about 0.2 Å along with a slight rotation around the Cβ-Cγ bond. Importantly all the residues in the proximal pocket remain in a position to allow His 123 to remain hydrogen bonded to Tyr 131.

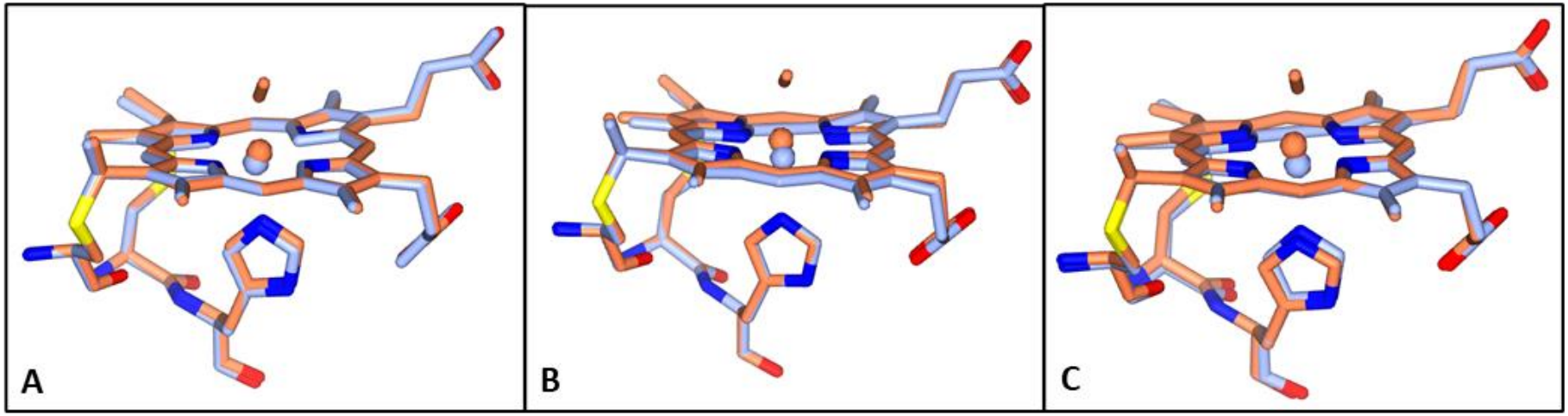

Figure 3.26. NO binding to wt *Mc*CP (A), F32V (B) and F61V (C) mutants. In both mutants the Fe atom of the heme can be seen to move upwards in the ligand bound structures causing an elongation of the Fe-His bond. In The F61V mutant the proximal histidine also moves downwards elongating the Fe-His bond further.

Published resonance ramen data (Adams *et al.*, 2023) of the mutant ligand bound complexes showed absorption features similar to those seen for the wt protein, supporting the hypothesis that the local negative polarity of the Phe 32 ring atoms limits build-up of charge associated with Fe(II)-> CO(π*). The F61V variant displayed a doublet of n(FeCO) frequencies similar to those seen in the wt protein which correspond to the two orientations seen in the crystal structure (Figure 3.27), with the lower frequency being ascribed to the local negative polarity of the aromatic quadrupole of Phe 32. The F32V variant however only displayed a single n(FECO) frequency corresponding to the single orientation seen in the crystal structure of that variant.

Thus, the spectroscopic, crystallographic and published RR data suggest that NO and CO interact with the Phe 32 ring face in both the wt and F61V mutant, but do not react with any aromatic quadrupoles in the F32V variant.

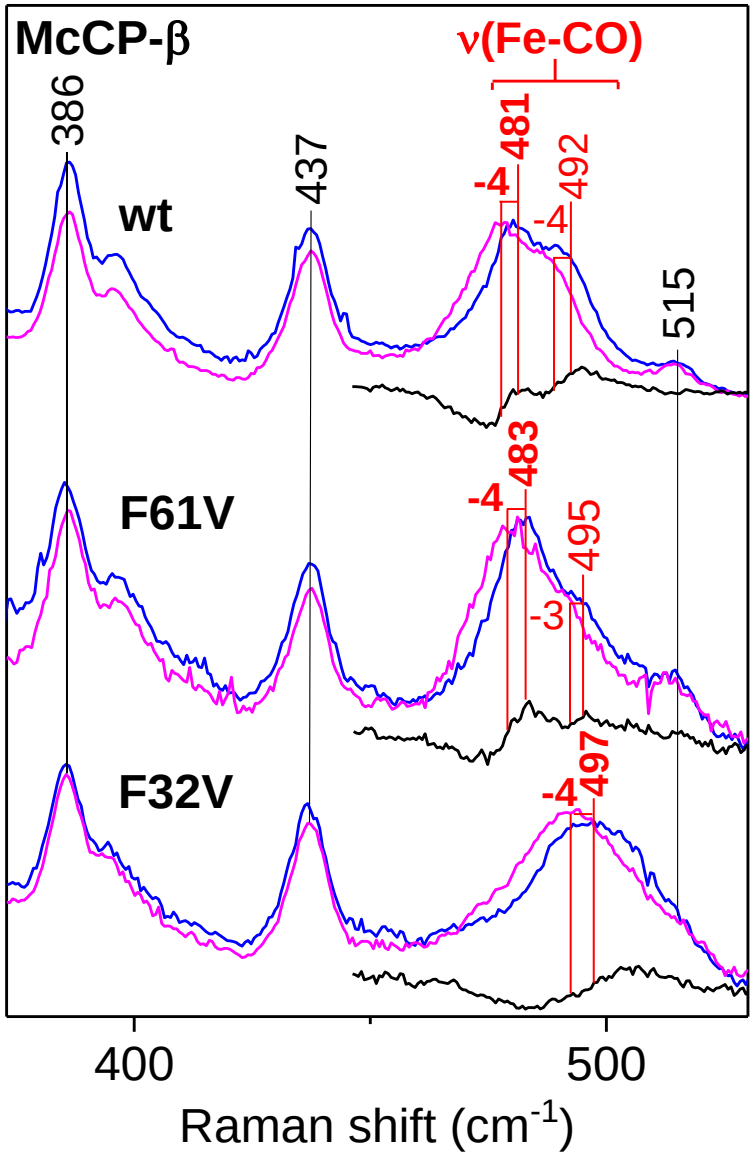

Figure 3.27. Low-frequency room temperature RR spectra of 6cCO complexes of wt, F61V, and F32V *Mc*CP taken from Adams et al 2023. Samples were prepared with ^{12}CO (blue traces) and ^{13}CO (magenta traces). The wavenumbers and isotope shifts of RR bands assigned to n(Fe–CO) modes are indicated in red.

Although attempts to generate a 5cNO wt crystal structure were unsuccessful the possible 5cNO structures seen for the two Phe mutants backs up the theory that all ligand binding occurs on the distal face of *Mc*CP. Examination of the structures using CAVER showed that there are no obvious tunnels leading to the proximal face of the heme in any of the wt and mutant structures analysed. When compared to *Ax*CP, which has proximal 5c binding in the presence of NO it can be seen that structural rearrangement is needed to create a tunnel from the distal face to the proximal side of the heme. In the ferric state *Ax*CP does not show any tunnels that could allow access to the proximal side, however upon reduction a side tunnel appears. This tunnel can also be seen in the 6cCO *Ax*CP structure. It is from the side tunnel that a further tunnel appears coming around the heme to the proximal face in the 5cNO structure. In the case of *Ax*CP the dissociation of the histidine and its subsequent rotation around its Cα-Cβ bond opens up a channel for the NO molecule to move to the proximal side. In *Mc*CP the proximal histidine is hydrogen bonded to a tyrosine which helps to hold it in position and prevents the residue from rotating away from the heme. As previously noted, it appears that the Fe atom of the heme moves further away from the proximal His, resulting in a domed heme, rather than the His moving itself.

The factors controlling heme–NO coordination in *Mc*CP may be relevant to its possible physiological relevance during nitrification. Klotz *et al*. showed using quantitative PCR that both *hao* (encoding hydroxylamine oxidoreductase) and *cytS* (encoding *Mc*CP) genes exhibited greatly increased transcript numbers when cells were exposed to ammonia, whereas in contrast, there was no increase for *cytL* encoding cytochrome P460. This may suggest a role of *Mc*CP in buffering NO (produced by hydroxylamine oxidoreductase during nitrification) or a response to other sources of nitrosative stress under these conditions.

Other gas binding heme proteins have aromatic side chains within their distal pockets which are positioned to interact with diatomic gas ligands. The mammalian heme-based NO sensor,

sGC, as well as the prokaryotic analog, *Ns* H-NOX are both examples of this (Ma *et al.*, 2007) (Kang *et al.*, 2019). The crystal structure of NS H-NOX shows that the aromatic ring of Try74 is presented towards heme bound CO and NO, and whilst the exact location of the pocket residues is yet to be resolved in sGC cryo-electron microscopy of sGC indicates that the ring face of Phe 74 is in a position to interact with distally bound gases. These proteins also demonstrate vibrational properties that are similar to those published for *Mc*CP and which are consistent with diminished Fe(II)→XO($\pi*$) backbonding resulting from the negatively polarized face of an aromatic quadrupole.

Chapter 4

Structural, spectroscopic and kinetic characterisation of as isolated ligand bound *Methylococcus capsulatus* (Bath) Cytochrome P460 and distal pocket mutants.

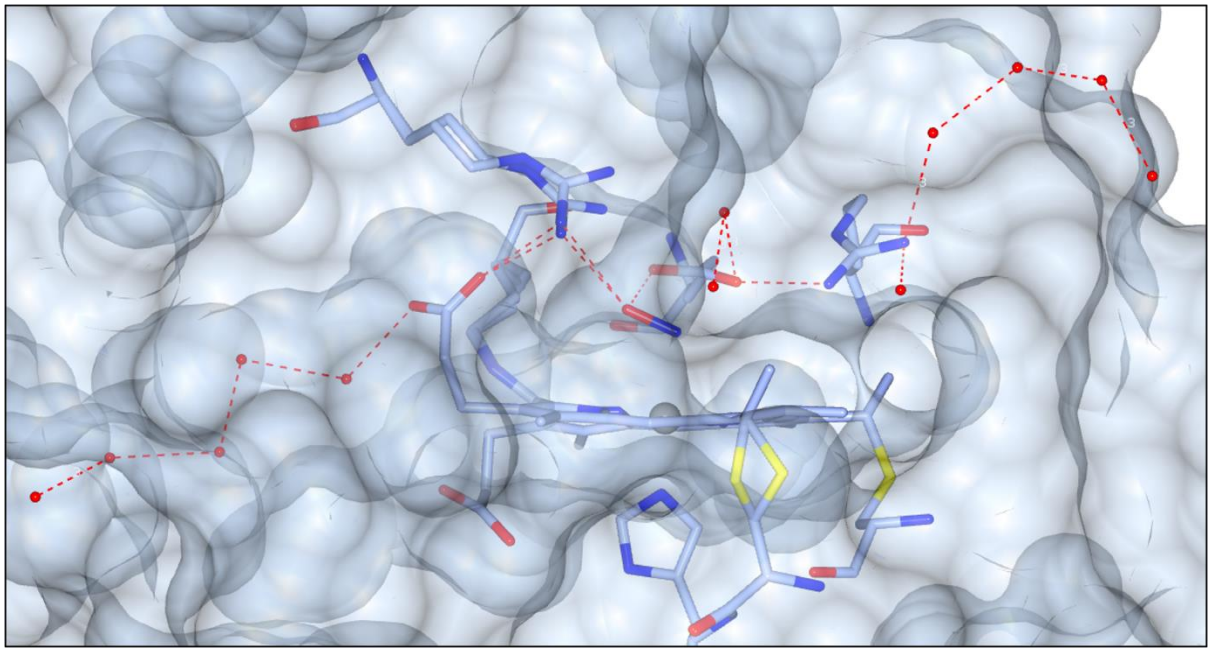

Figure 4. Proposed proton relay routes from the P460 heme to the surface of the protein.

4.1 Introduction

To probe the mechanism by which *Mc*P460 oxidises hydroxylamine various mutants were created and the effect on their structural and spectroscopic features together with activity was examined. Previous studies on *Ne*P460 (Smith and Lancaster, 2018) (A. Smith *et al.*, 2019) (Coleman, Vilbert and Lancaster, 2020) (M. Bollmeyer *et al.*, 2023) have highlighted various residues in the distal heme pocket that appear to be important in the activity of the enzyme and were used to guide the choices made when mutating residues in *Mc*P460.

The lysine crosslink is essential for catalytic activity. All crosslink deficient *Ne*P460 mutants, reveal a loss of activity (Coleman, Vilbert and Lancaster, 2020) and spectral features more similar to cytochromes *c*'. *Ne* Cytβ-^{Met}, which has a methionine in place of the lysine in P460s is also unable to catalyse the oxidation of hydroxylamine, although it has been shown to react with H_2O_2 in a manner which suggests it may have peroxidase-like activity (Liew *et al.*, 2020). Thus, a crosslink deficient *Mc*P460 mutant (K78R) was designed to test if hydroxylamine oxidation activity was supressed and whether peroxidase activity would occur.

The *Ns*ALP460 variant demonstrated the importance of correctly placing a residue in the distal heme pocket to allow proton transfer to occur. This mutant has an alanine residue instead of a glutamate next to the lysine crosslink as seen in *Ne*P460 (Smith and Lancaster, 2018). Importantly, *Ns*ALP460 shows no hydroxylamine oxidation activity implying the crosslink alone is not enough to confer enzymatic activity. Mutation of Ala 131 to a Glu in *Ns*ALP460 gave rise to activity and conversely, mutating Glu 97 to Ala in *Ne*P460 removed all activity. Interestingly, mutation of Ala 131 to an Asp (as is present in *McP*460) did not give rise to activity in the enzyme suggesting a fine tolerance for the positioning of this

residue in *Ne*P460. To assess whether the same was true for *Mc*P460, the *Mc*P460 D102E mutant was created.

In *Ne*P460 Arg 44 has been suggested to be involved in crosslink formation and stabilising the heme through hydrogen bonding with the propionate (M. Bollmeyer *et al.*, 2023). In contrast to *Ne*P460, *Mc*P460 has Arg 50 in the distal heme pocket with its sidechain orientated close to the heme face and potentially within range to affect substrate binding/catalytic activity: Thus, it was decided to mutate this residue to an Ala (i.e., *Mc*P460 R50A) to assess its effect on the enzyme and whether it has any involvement in its catalytic activity.

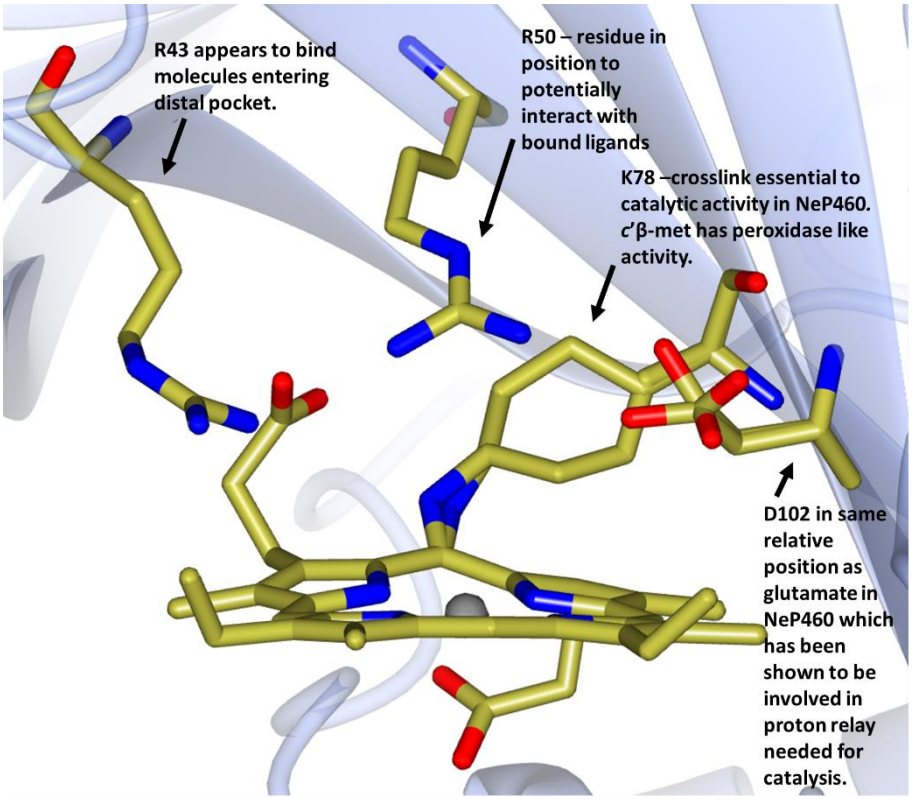

Figure 4.1. Location and rationale behind mutations to probe the mechanism of *Mc*P460 activity.

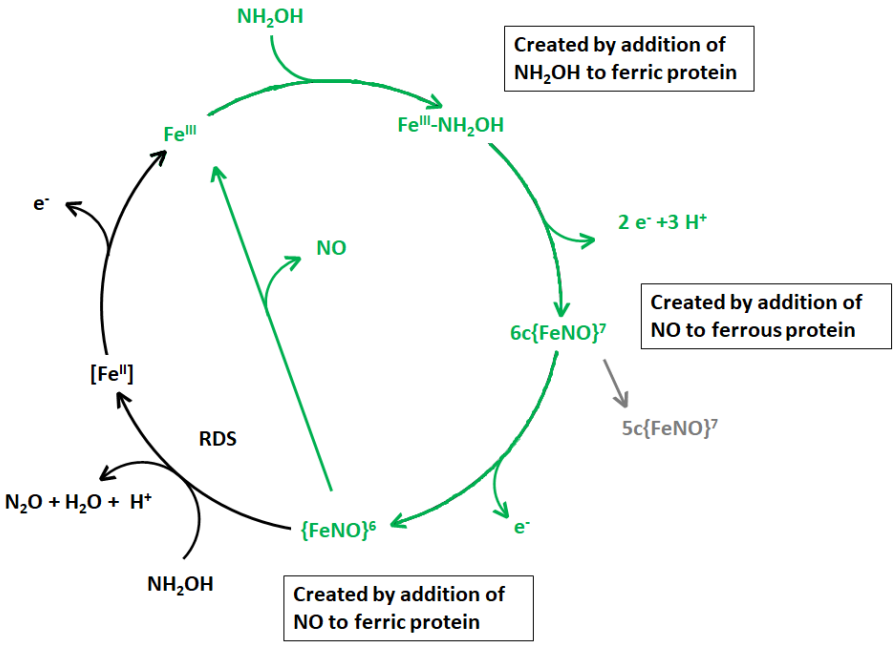

Figure 4.2. Proposed mechanism of oxidation of hydroxylamine by P460s showing key compounds in the catalytic cycle (using Enemark-Feltham notation) and the method of creation *in vitro*. Steps in black are those which have been observed only in P460 whilst those in green have been observed in both HAO and P460. Grey represents an off-pathway species. Hydroxylamine binds to the heme of the ferric protein and is oxidised to form an {Fe-NO}^{6} product via a 6c{Fe-NO}^{7} intermediate. This {Fe-NO}^{6} product then undergoes nucleophilic attack by a second hydroxylamine to produce nitrous oxide and water. The heme is then free to start the cycle over again. Adapted from (Coleman, Vilbert and Lancaster, 2020).

Finally, in the as isolated *Mc*P460 structure Arg 43 is interacting with an unknown molecule entering the distal pocket as a cryoprotectant ion could be seen potentially bound to the residue. In room temperature X-ray Free Electron Laser (XFEL) structures, where no cryo protectant is used, it has also been seen that a sulphate from the crystallisation liquor can bind in this position (Personal communication with Prof Hough and Dr Pfalzgraf). The R43A

mutant was designed to see whether this residue had any effect on ligand binding and thus the activity of the enzyme.

*Ne*P460 has been shown to react with hydroxylamine under both aerobic and anaerobic conditions, however the product of the reaction varies under the different conditions (Caranto, Vilbert and Lancaster, 2016). Similar experiments on *Mc*P460 are yet to be carried out so the exact products of *Mc*P460 hydroxylamine oxidation are yet to be determined for *Mc*P460. Under aerobic conditions *Ne*P460 has been reported to oxidise hydroxylamine to NO_2^-, however the concentrations were not stoichiometric with hydroxylamine input. It has been hypothesized that this is due to a non-enzymatic reaction of aqueous NO (released from the $\{FeNO\}^6$ species, figure 4.2) with O_2. Under anaerobic conditions *Ne*P460 has been shown to oxidise hydroxylamine to nitrous oxide. A mechanism has been proposed for P460 oxidation of hydroxylamine (Figure 4.2) by the Lancaster group (A. Smith *et al.*, 2019) based on their work on *Ne*P460. This initially involves hydroxylamine binding to the ferric heme before a two-electron oxidation step to produce a six coordinate $\{FeNO\}^7$ species. This is followed by another one electron oxidation step to produce a $\{FeNO\}^6$ species. A second hydroxylamine then reacts with the $\{FeNO\}^6$ species by nucleophilic attack to produce H_2O and N_2O in the rate determining step. It is presumed that the final oxidising equivalent regenerates the ferric enzyme however this step has not yet been observed. To see the effect each of these mutations have on ligand binding and the catalytic cycle, each of the key species was generated by either the addition of hydroxylamine (to produce Fe^{III}-NH_2OH) or ProliNONOate (to produce either 6c$\{FeNO\}^7$ by addition to ferrous protein or $\{FeNO\}^6$ by addition to ferric protein), based on previous work on *Ne*P460, along with activity assays to determine if each mutant was catalytically active or not.

4.2 Experimental Procedures

4.2.1 Methylococcus capsulatus (Bath) Cytochrome P460 Mutagenesis

The synthetic *Mc*P460 DNA in the pBsK plasmid (figure A.1, Appendix A) was used as a template for PCR to generate the single amino acid substitutions R43A, R50A, K78R and D102E, (see Chapter 2, section 2.1.4). Mutagenic primers were designed for each of the respective mutations, with GC content, primer length, and melting temperature (T_m) are reported in Table A.1 (Appendix A). Site-directed mutagenesis (SDM) was carried out using the QuikChange method. Refer to table A.2 (Appendix A) for the PCR reaction components. SDM was carried out with the template DNA of *Mc*P460 in pBluescript as shown in figure A.1 (Appendix A), respectively. PCR was performed with annealing temperatures of 60.2 °C, 60.2 °C, 58.2°C and 61.9 °C for R43A, R50A, K78R and D102E respectively and an extension time of 5 min for a total of 18 cycles (table A.3, Appendix A). The template was digested with *DpnI* enzyme for 2 hours at 37 °C. 5 µl of the *DpnI* digested products were transformed into *E.coli* XL1-blue competent cells and spread on LBAmp agar plates. Single colonies were picked and grown overnight at 37 °C in 10 ml Amp media followed by plasmid miniprep extraction. DNA sequencing was carried out by Eurofins using the M13rev-29 primer. The single-point mutations were confirmed using Chromas Sequence Viewer. The genes containing the desired mutations in the cloning vector pBluescript were digested with the *EcoRI* and *XBaI* restriction enzymes, ligated into the pMMB503EH expression vector and the mutated plasmids were propagated as previously described in section 2.2.1. DNA sequencing was carried out by Eurofins using the M13rev-29 primer. The single-point mutations were confirmed using the wt template DNA sequence as a reference guide (Figure A.5, Appendix A).

4.2.2 McP460 R43A, R50A, K78R and D102E Expression and Purification

Wt *Mc*P460 and the R43A, R50A, K78R and D102E mutants from the pBsK plasmid were ligated into the expression vector pMMB503EH plasmid and were successfully over-produced in BL21 (*DE3) E. coli* cells containing the pEC86 plasmid, refer to Chapter 2 (section 2.2.2). TB medium was used for the over-expression of all proteins following induction by IPTG. After harvesting and lysing the cells 1 M ammonium sulfate was added to the resultant protein containing fraction. Following centrifugation to remove precipitants the supernatant was added to an equilibrated HIC column where the protein containing fraction could be followed as a green (wt *Mc*P460, R43A, R50A, D102E) or reddish-brown (K78R) coloured band. The collected fractions were then concentrated and run on a G75 column to produce a homogeneous sample. SDS-PAGE electrophoresis was used to assess the purity and quantity of the proteins and indicated the correct protein band at ~17 kDa. UV-visible absorption spectra were taken throughout all purification steps to analyse and assess the purity of the fractions. Protein concentrations were determined using a molar extinction coefficient (ε) for the Soret band of 78.5 $mMcm^{-1}$ for the oxidised *Mc*P460 (Bergmann *et al.*, 1998). The purity of the protein was determined by the ratio of the A419/A280 nm, a ratio of 3:1 was aimed for and indicated pure protein.

4.2.3 UV-visible spectroscopy

All aerobic spectrophotometric experiments were carried out at 20 °C, unless stated otherwise, using the Varian Cary 50 spectrophotometer (Agilent Technologies). UV-visible absorption spectra were recorded between 800 - 200 nm using a 1 cm Quartz cuvette (Hellma-Analytics). All anaerobic spectrophotometric experiments were carried out in an MBraun Unilab Pro glove box using a Implen C40 NanoPhotometer.

4.2.4 Ligand binding studies

A few granules of sodium dithionite (Sigma) were used to reduce the proteins from ferric (Fe^{3+}) to the ferrous (Fe^{2+}) state, the effect of which was checked using UV-visible spectroscopy. The CO-bound protein samples were prepared by reducing the sample with sodium dithionite in a rubber-stopped sealed 1 cm quartz cuvette and bubbled with CO gas for ~30 s. Similarly, to prepare the NO-bound protein, 10 µl of ~80 mM proliNONOate (Cayman Chemicals) was injected into either the pre-reduced or ferric protein with a 10 µl Hamilton syringe (Hampton Research) to provide an excess of the ligand. Hydroxylamine bound protein was produced by adding 100 µl of 100 mM hydroxylamine hydrochloride (Sigma) to ferric protein samples. H_2O_2 solutions were prepared from a stock (Sigma-Aldrich) with the final concentration determined spectrophotometrically using an $\varepsilon = 43.6\ M^{-1}cm^{-1}$ at 240 nm (Gasteiger et al., 2003). One molar equivalent was added to the ferric protein. Anaerobic samples were prepared in an MBraun Unilab Pro glove box (0_2 <0.1ppm) with buffers that had all been degassed with 3 cycles of vacuum for 15 min followed by sparging with N_2 for 15 min. Aliquots of protein were equilibrated in the glovebox for 2 hours before any experiments.

4.2.5 EPR spectroscopy

Electron Paramagnetic resonance (EPR) spectra were measured using either an EMX spectrophotometer (Bruker) or a Bruker ELEXSYS E500 EPR spectrophotometer. Both EPR spectrophotometers were equipped with the spherical high quality resonator SP9703 and a liquid helium cryostat (Oxford Instruments) to measure the low temperature (10 K) EPR spectra and were operating in continuous wave (CW) regime, at X-band (9 GHz microwave frequency), and 100 kHz field modulation frequency. The g-values were obtained using the

built-in microwave frequency counter. Protein samples were 100 μM concentration in 50 mM HEPES pH 7.5. Anaerobic samples were prepared in an MBraun Unilab Pro glove box with buffers that had all been degassed with 3 cycles of vacuum for 15 min followed by sparging with N_2 for 15 min. Aliquots of protein were equilibrated in the glovebox for 2 hours before any experiments. Hydroxylamine bound samples were prepared by adding 100 mM NH_2OH to ferric samples and NO bound complexes by adding proliNONOate to either ferric or dithionite reduced samples as described above. 200 μl aliquots were drawn into EPR sample tubes, stoppered with a rubber stopped and removed from the glovebox before being flash-frozen in cold methanol and once frozen, the samples were then transferred to liquid nitrogen. Simulations and spectra extractions were performed by Dr Dimitri Svistunenko using WinEPR SimFonia (Bruker).

4.2.6 Crystallisation of McP460 R43A, R50A, K78R and D102E

Crystals of wt *Mc*P460 were grown as previously described (Chapter 2.2.6). Crystals of R50A, K78R and D102E *Mc*P460 were grown in batch at 18 °C using 100 μl of 15-30 mg/ml protein in 20 mM Tris, pH 8, with an equivalent volume of reservoir solution containing 0.1 M Tris, 3.8-4.0 M Ammonium sulfate in an Eppendorf tube. Crystals took 5-7 days to appear. Prior to X-ray data collection crystals were cryoprotected by transfer to reservoir solution comprising mother liquor supplemented with 1.7 M sodium malonate and flash-cooled in liquid nitrogen.

4.2.7 Crystal Ligand Soaking

For *Mc*P460 and mutants, the reservoir solution was prepared and transferred into 3 ml glass vials which were sealed using a rubber-seal and degassed using argon gas for 15 min. Five to six crystals were transferred to each vial solution. A volume of ~100 µl proliNONOate was injected into the sealed vial containing the crystals. The crystals were scooped out using plastic pasteur pipettes and transferred to a clean sterile surface. The protein crystals were removed with a nylon UV-transparent cryo-loop (Hampton Research) and immediately soaked in a cryo-protectant for 15 - 30 s, prior to flash-cooling the crystals in liquid nitrogen.

Hydroxylamine-soaked crystals were prepared by adding 100 mM hydroxylamine hydrochloride to the reservoir solution in a 1:1 ratio. Crystals were fished out with a nylon UV-transparent cryo-loop (Hampton Research) and left to soak in the hydroxylamine: reservoir solution for up to 5 mins prior to flash-cooling in liquid nitrogen.

4.2.8 X-ray data collection and processing

Data was measured at beamlines I04-1 and I24, Diamond Light Source at a wavelength of 0.979 Å and auto-processed using DIALS. Structures were refined by maximum likelihood methods initially using REFMAC5 (Murshudov *et al.*, 2011) and for final refinement using Phenix (Liebschner *et al.*, 2019). Model building between cycles of refinement, including addition of water molecules and ligands was performed in Coot (Emsley *et al.*, 2010). Data collection and processing statistics can be seen in Tables 4.1-4.

4.2.9 Validation of crystal structures

Validation of structures was carried out with *MolProbity* (Chen et al., 2010) and *JCSG Quality Control Check* (Elsliger et al., 2010). The pdb and mtz file were inputted into the *JCSG* server whereas only the pdb file was used for *MolProbity*. Steric clashes, poor rotamers, Ramachandran outliers, residues with improbable bonds and angles were re-modelled in Coot, followed by more refinement in Refmac5 and this was repeated until the model was of high quality and within the limits of the above mentioned parameters.

4.2.10 Activity Assays

$NH_2OH \cdot HCl$ (Sigma) was equilibrated in an anaerobic environment overnight and then dissolved in 1 mL of deoxygenated water to yield a 1 M solution. This solution was serially diluted 20,000-fold in deoxygenated water and assayed by the method of Frear and Burrell (Frear and Burrell, 1955) for accurate determination of the stock NH_2OH concentration. Final concentrations of 50 μM 2,6-dichlorophenolindophenol (DCPIP) (Sigma), 6 μM phenazine methosulfate (PMS) (Sigma), and 1 μM P460 were added to 2 mL of deoxygenated 50 mM sodium phosphate (pH 8.0). The reaction was initiated by adding an appropriate volume of the NH_2OH stock solution to the reaction mixture through the septum with a Hamilton syringe. The reaction progress was followed by monitoring the absorption of DCPIP at 605 nm. The rate of the first 10% of the total oxidant consumption was determined through linear regression. This rate was converted to the rate of oxidant consumed by using $\varepsilon_{605\ nm} = 20.6\ mM^{-1}\ cm^{-1}$ (Williamson and Engel, 1984). At least three trials for each NH_2OH concentration were averaged and the standard deviations plotted. The initial rates were plotted versus NH_2OH concentration, and the resulting plot was fit using linear regression.

4.3 Results

4.3.1 Mutant Expression and Purification

Creation of all the *Mc*P460 single point mutations in the plasmid were confirmed by comparison to the wt enzyme sequence (Figure A.5, Appendix A). Upon confirmation the mutants were expressed and purified using the optimised method for wt *Mc*P460 described in Chapter 2.2.2.4. R43A, R50A and D102E all produced a green pellet which could be followed throughout all the purification steps (Figure 4.3). K78R expression produced a reddish brown cell pellet which could also be followed throughout the purification steps. The purity of the samples was checked throughout purification through the use of SDS-PAGE gels and UV-visible spectroscopy (Figure 4.4, 4.5).

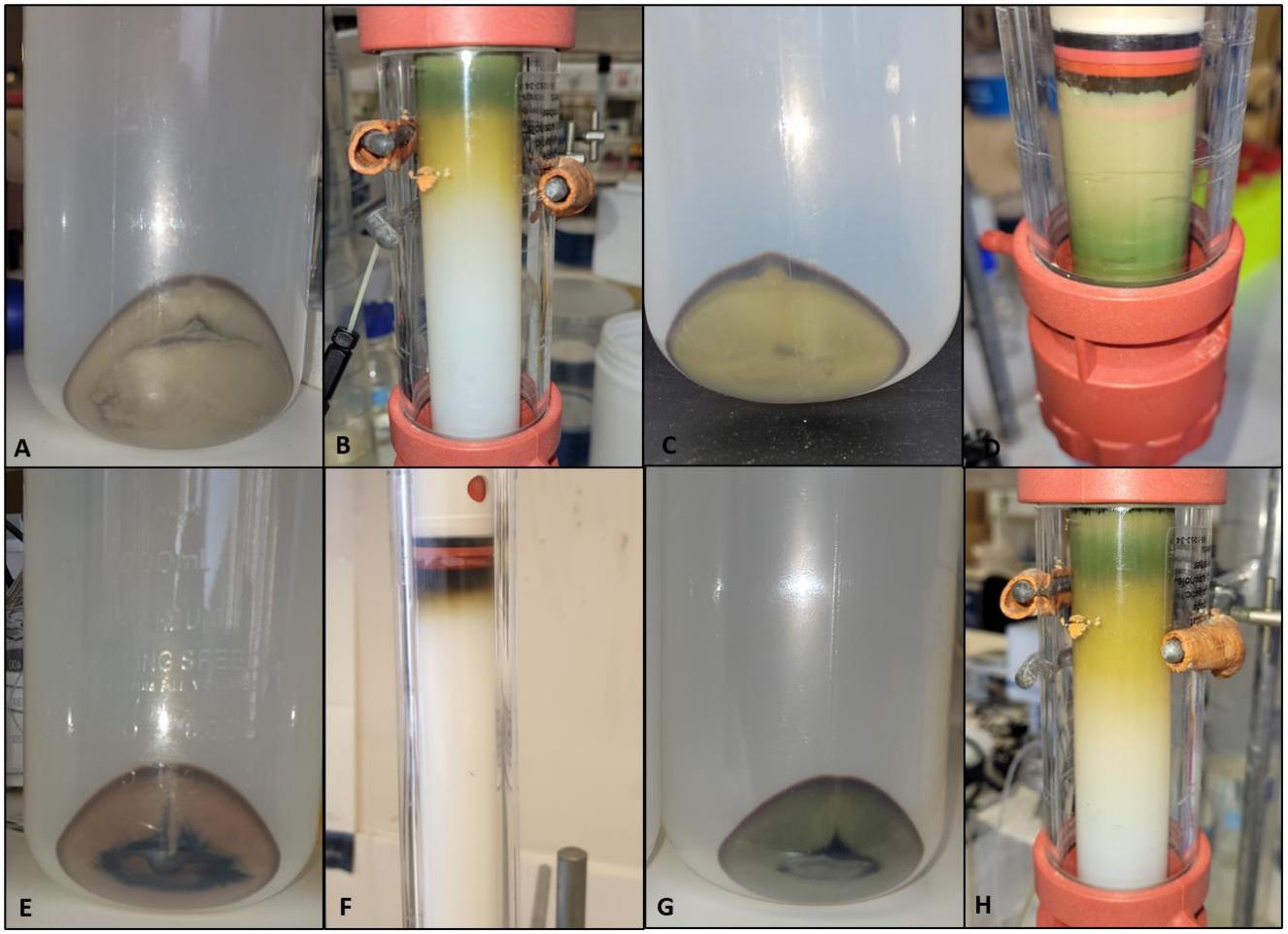

Figure 4.3. Harvesting and purification of *Mc*P460 R43A, R50A, K78R and D102E. Pelleted *E.coli* cells after over expression of R43A (A), R50A (C), K78R (E) and D102E (G). The presence of the mutants is indicated by the green or brown colouration of the pelleted cells. Purification of R43A (B), R50A (D), K78R (F) and D102E (H) on either a size exclusion gel filtration or hydrophobic interaction column,

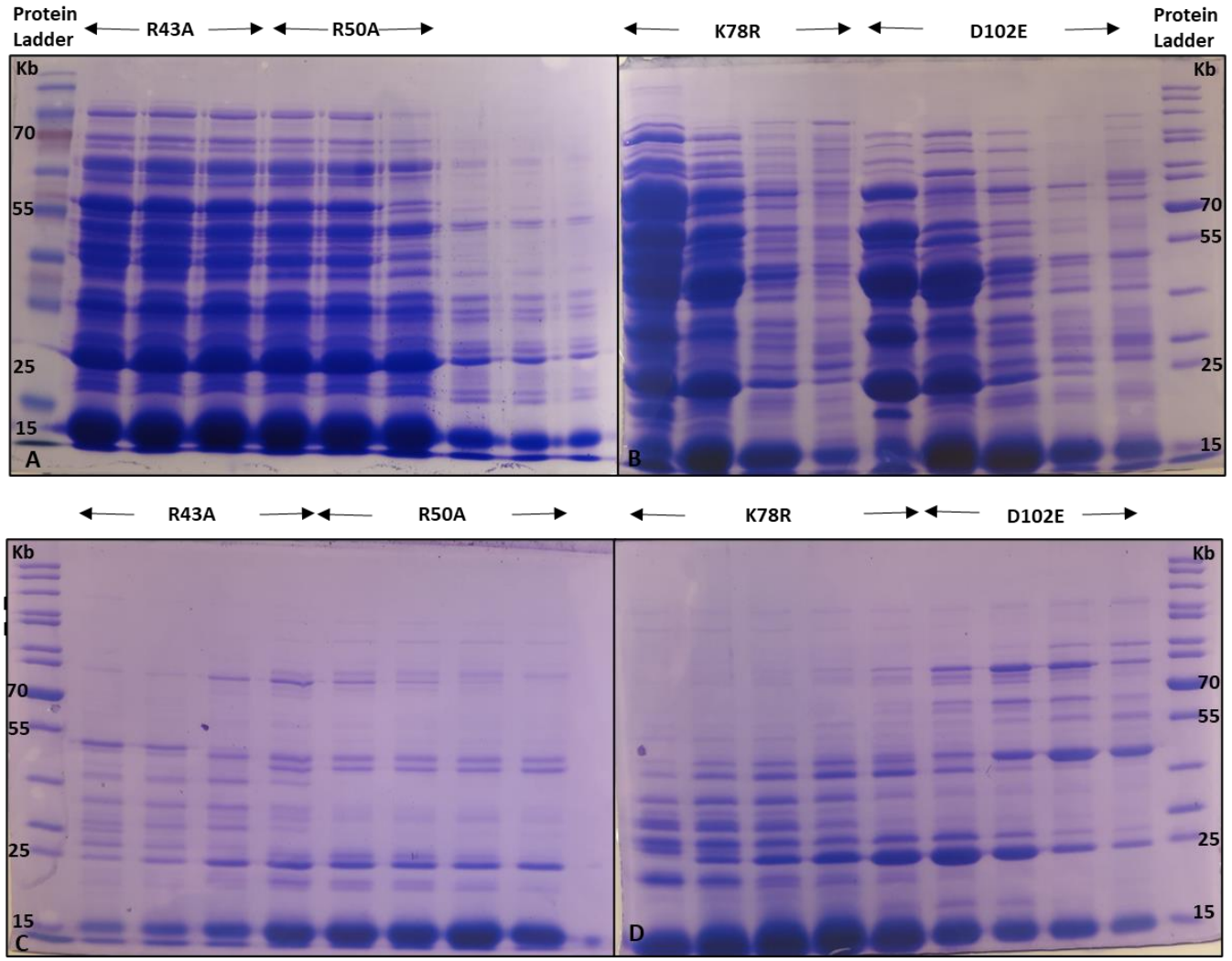

Figure 4.4. SDS-PAGE of R43A, R50A, K78R and D102E after HIC column (A, B) and after size exclusion gel filtration chromatography (C, D)

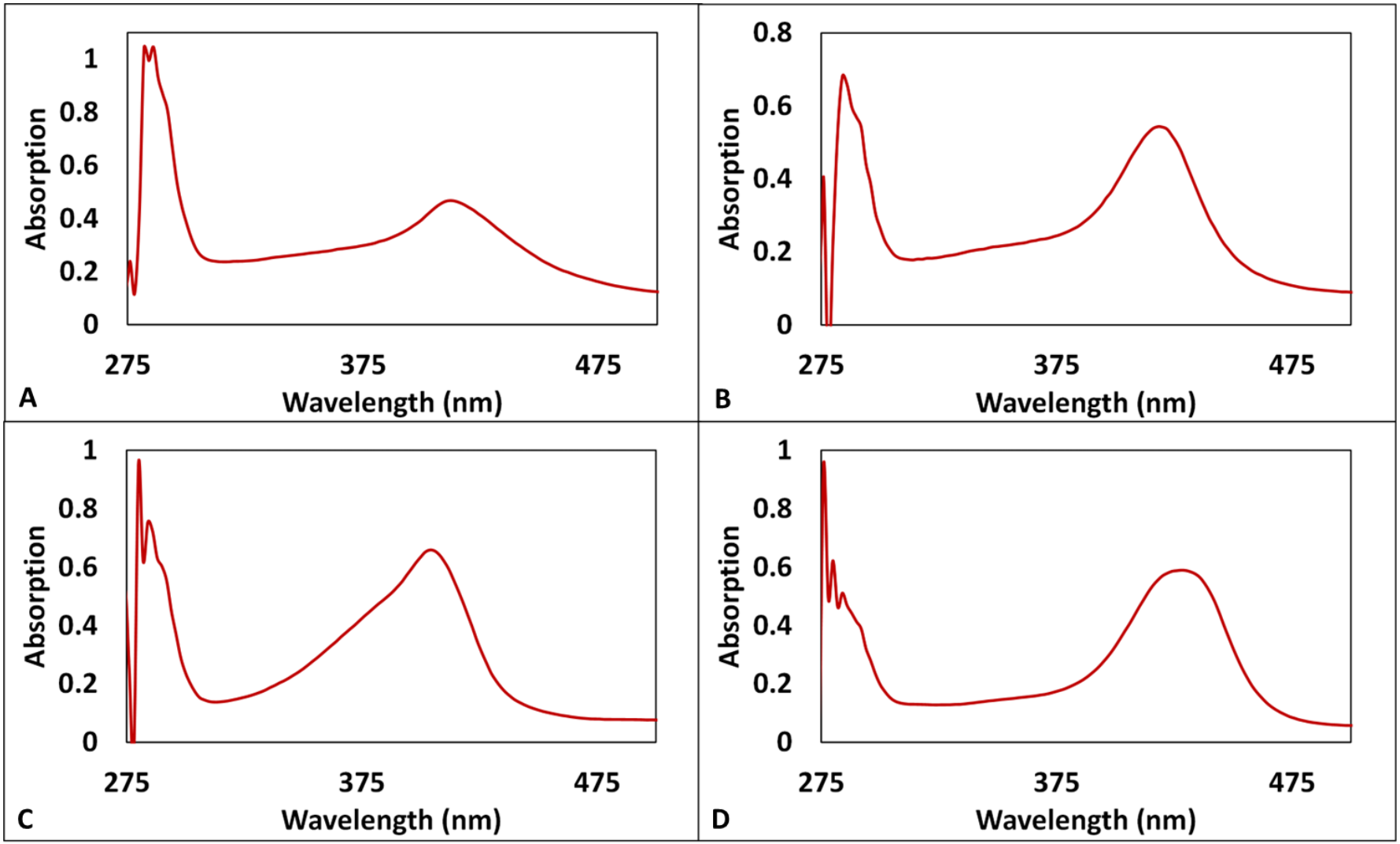

Figure 4.5. UV-visible spectra of R43A (A), R50A (B), K78R (C) and D102E (D) after size exclusion column. The purity of the ferric protein was determined by measuring the ratio of the absorbance of the Soret peak at ~ 420 nm and the protein peak at 280 nm.

4.3.2 As isolated UV-visible and EPR Spectroscopy

The R43A and R50A mutants displayed similar Soret maxima in the ferric state to the wt P460 at 418 nm and 419 nm respectively (Figures 4.6 B, C, table 4.1). Their α/β band was slightly shifted however at 562 nm and 570 nm in comparison to the wt (at ~500 nm). D102E (Figure 4.6 E, Table 4.1) showed a shift in its Soret maximum to 433 nm and α/β bands at 570 nm and 630 nm more similar to that reported for *Ne*P460 (434 nm, 570 nm and 627nm respectively) (Numata *et al.,* 1990). It was proposed that the blue shift in the spectrum for *Mc*P460 was due to the distally bound water seen in the crystal structure (Adams *et al.,* 2019), however as a similarly bound water is seen in the D102E mutant it is now unlikely that this is the case. With the only change in the D102E mutant being the single point mutation it would suggest the shift is due to the residue itself and its interaction with the heme. Chemically reducing the proteins with sodium dithionite caused a shift in the Soret maximum to 460 nm in the D102E mutant only with R43A having a Soret maximum of 443 nm and R50A of 441 nm respectively.

The K78R crosslink deficient mutant displayed a UV-visible spectrum more similar to that of cytochrome *c'* than of cytochrome P460 with a Soret maximum of 402 nm (Figure 4.6 D). Upon reduction with dithionite the Soret maximum shifted to 433 nm, again more in common with cytochrome *c'*.

EPR spectroscopy of the as isolated form of the D102E, R50A and R43A mutants all showed a single high spin species with g values similar to that reported for the wild type protein (g^1= 6.18, 6.16, 6.05, g^2= 5.61, 5.60, 5.57, and g^3= 1.99 for D102E, R50A and R43A respectively) (Figure 4.7, Table 4.2). Suggesting the mutations had not affected the high spin properties of the proteins. The K78R mutant, whilst still being a single high spin species, displayed a distinctly different line shape to the wt *Mc*P460 and other mutants with g values of 6.00 and

1.99. As with the UV-visible spectrum this is a line shape more similar to that of a cytochrome *c'* than a cytochrome P460.

Table 4.1. UV-visible parameters for cyts P460

	λ_{max} (nm)		ref
Fe(III)			
*Mc*P460	419	628	tw
R43A	418	562	tw
R50A	419	570	tw
K78R	402	506, 645	tw
D102E	433	570, 630	tw
*Ne*P460	440	570, 627	a
Fe(II)			
*Mc*P460	460	574, 684	tw
R43A	443	570, 630	tw
R50A	441	571, 630	tw
K78R	433	556	tw
D102E	460	628, 680	tw
*Ne*P460	462	660, 668	a

a (Bergmann and Hooper, 2003)

Table 4.2. EPR spectra parameters for cyts P460.

protein	pH	temp (K)	g^		gçç
			g^1	g^2	g^3
*Mc*P460	7	10	6.18	5.57	1.99
R43A	7	10	6.05	5.57	1.99
R50A	7	10	6.16	5.60	1.99
K78R	7	10	6.00		1.99
D102E	7	10	6.18	5.61	1.99
*Ne*P460*	7	4	5.91	5.63	1.99

* (A. Smith *et al*., 2019)

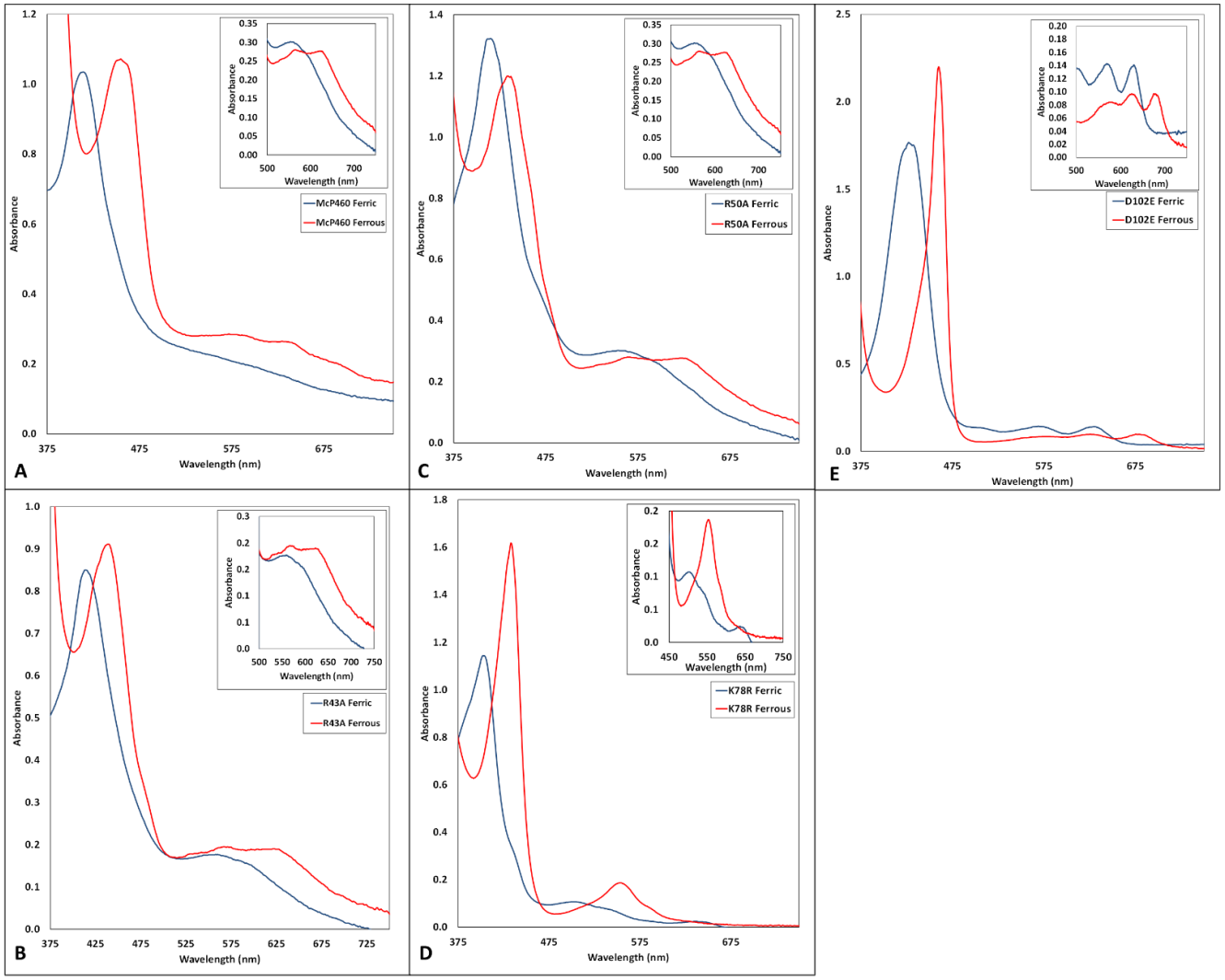

Figure.4.6. As isolated (blue) and chemically reduced (red) UV-visible spectrum for wt *Mc*P460 (A), R43A, (B), R50A, (C), K78R (D) and D102E (E) showing Soret maxima. Insets show α/β and CT bands for each protein.

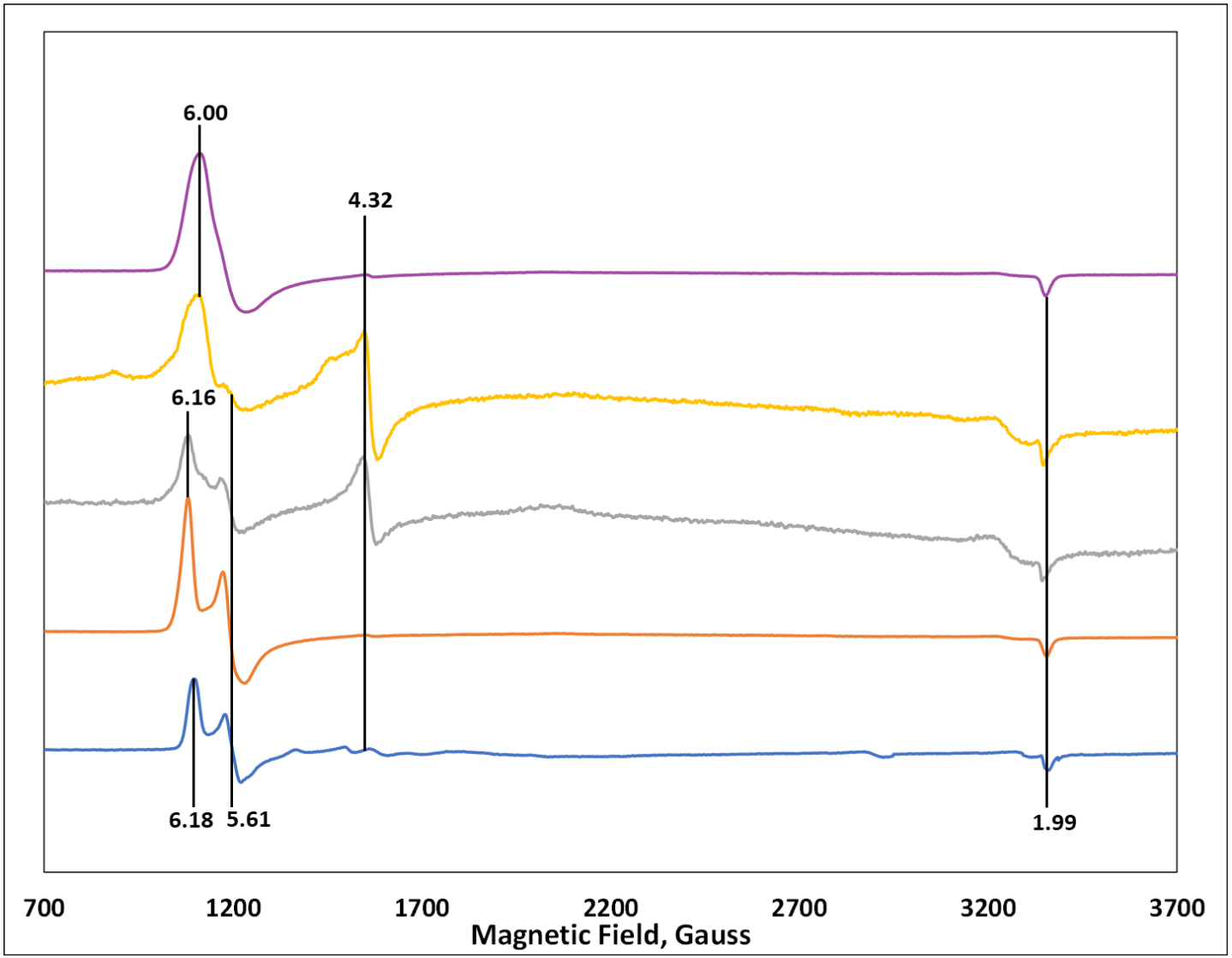

Figure.4.7. As isolated EPR spectrum for wt *Mc*P460 (blue), D102E (orange), R43A (yellow), R50A (grey) and K78R (purple).

4.3.3 X-ray structures of as isolated McP460 Mutants

All *Mc*P460 mutants were initially trialled using the wt *Mc*P460 crystallisation conditions. Trials to grow crystals of the *Mc*P460 mutants using the vapour diffusion method initially described for the wt protein were unsuccessful despite wide screening using varying concentrations of salt, different pH and varying protein: precipitant ratios. Due to this the batch crystallography method was trialled and gave rise to crystals of various sizes depending on the concentration of salt, the protein: precipitant ratio and overall volume of the batch. This allowed crystals to be made which suited different types of experiments and beamlines *i.e.,* larger single crystals for single crystal crystallography and many small crystals for serial crystallography. Thus, crystals of R50A, K78R and D102E *Mc*P460 (Figure 4.8) were grown in batch at 18 °C using 100 µl of 15-30 mg/ml protein in 20 mM Tris/HCl, pH 8, with an equivalent volume of reservoir solution containing 0.1 M Tris, 3.8-4.0 M Ammonium sulfate in an Eppendorf tube.

In order to allow the correct positioning of the heme porphyrin in all the P460 structures no geometry restraint library was used in refinement as this restricted the positioning of the atoms in the heme. Also due to an issue with the second lysine crosslink (where present in the structures) not remaining linked to the heme where the density suggested it should be Phenix was used for final refinements instead of REFMAC.

Crystals of the R50A mutant appeared green in colour and orthorhombic in shape but were small in size at 10-15 µm in length (Figure 4.8). The as isolated structure at 2.16 Å showed that the mutation created a space next to the heme which the arginine residue used to occupy (Figure 4.9 B). No other residues moved to fill this space and the distal heme environment appeared otherwise unchanged.

Crystals of the K78R mutant appeared reddish brown in colour and cubic in shape (Figure 4.8). The K78R as isolated structure was resolved at 1.30 Å. Mutation of the Lys to an Arg results in the loss of the crosslink to the heme with the arginine taking up an occluding position above the distal face of the heme (Figure 4.9 D) and so unlike wt *Mc*P460 there is no water seen bound to the face of the heme. The positioning of the arginine over the distal face has caused Arg 50 to move into a different position away from the heme and rotate by 90 ° around the CD bond. All other pocket residues remain in the same positions as seen in the wt protein. A malonate ion from the cryoprotectant can be seen in both monomers bound near to Arg 43. The overall structure of the K78R mutant is the same as the wt protein.

D102E formed large green orthorhombic crystals (Figure 4.8) in batch conditions which diffracted to 1.18 Å. The high resolution of this structure meant that anisotropic B-factors needed to be taken into consideration rather than just the isotropic B-factors used in refinement of lower resolution structures. Model building was also more complicated as the higher resolution allows alternative conformations of residues and molecules to be more easily defined. Mutation of the aspartate residue to a glutamate residue resulted in two conformations of the residue sitting in a similar position to the residue in the wt protein (Figure 4.9 C). Multiple conformations of other residues in the distal pocket can be seen in the structure which could potentially correspond to two different overall pocket structures. Arg 43 has two conformations, both in a slightly different position to the wt structure. One has its NH2 atom 0.70 Å closer to the bound malonate ion than in the wt structure whilst the other is 0.56 Å further away. Arg 50 also has multiple conformations: in heme A there are two, one of which is closer to the CD atom of the crosslink (1.13 Å) and the other further away (0.77 Å) relative to the wt structure. In heme B three conformations are observed, in one the NH1 atom is 1.2 Å closer to the CE atom of the crosslink and the other two are in a similar position to that seen in the wt structure. Other residues in the distal pocket, but further

away from the heme face have also moved slightly including Arg 121, Gln 100 and Gln 46 (which shows two conformations).

For all of the P460 mutants the overall protein fold was very similar with the structures being superimposable to 0.32-0.34 Å RMSD. The overall B-factors were also very similar for the mutant structures (R50A 21.3 $Å^2$, K78R 18.6 $Å^2$ and D102E 12.8 $Å^2$).

Despite extensive screening, of both new conditions and variations around the wt *Mc*P460 crystallisation condition, crystals of the R43A mutant were not able to be created and so no structural data was obtained for this mutant.

Attempts to reduce P460 crystals (both wt and mutants) demonstrated that *Mc*P460 crystals are resistant to reduction both by chemical treatment and upon exposure to the X-ray beam. Experiments carried out by Dr Pfalzgraf at Diamond Light Source (personal correspondence) using UV-visible data in combination with X-ray crystallography showed that when soaked in ascorbic acid the UV-visible spectrum of P460 crystals still showed a peak at 420 nm consistent with a ferric form. Repeated exposure of as isolated crystals to the beam also showed no shift in the spectrum (although a broadening and background noise was seen with increased dosage) right up to the point where the crystals were so exposed, they were destroyed in the beam. Similar experiments carried out at the Swiss Light Source using Resonance Raman spectroscopy (By Prof Hough and Dr Pfalzgraf with crystals produced at the University of Essex) also showed a lack of change in the measured data upon exposure to X-rays again suggesting that the crystals were resistant to being reduced in the X-ray beam.

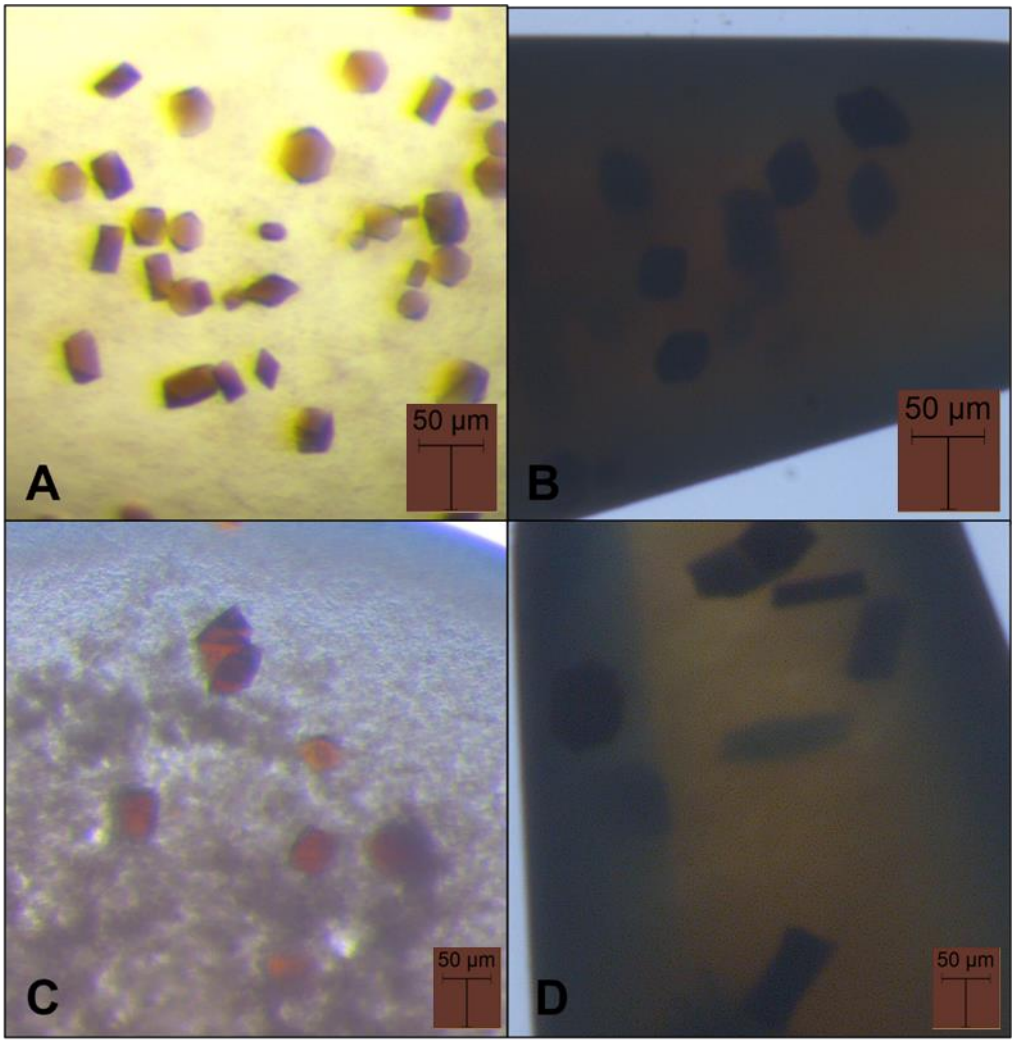

Figure 4.8. Crystals of wt *Mc*P460 (A), R50A (B), K78R (C) and D102E (D)

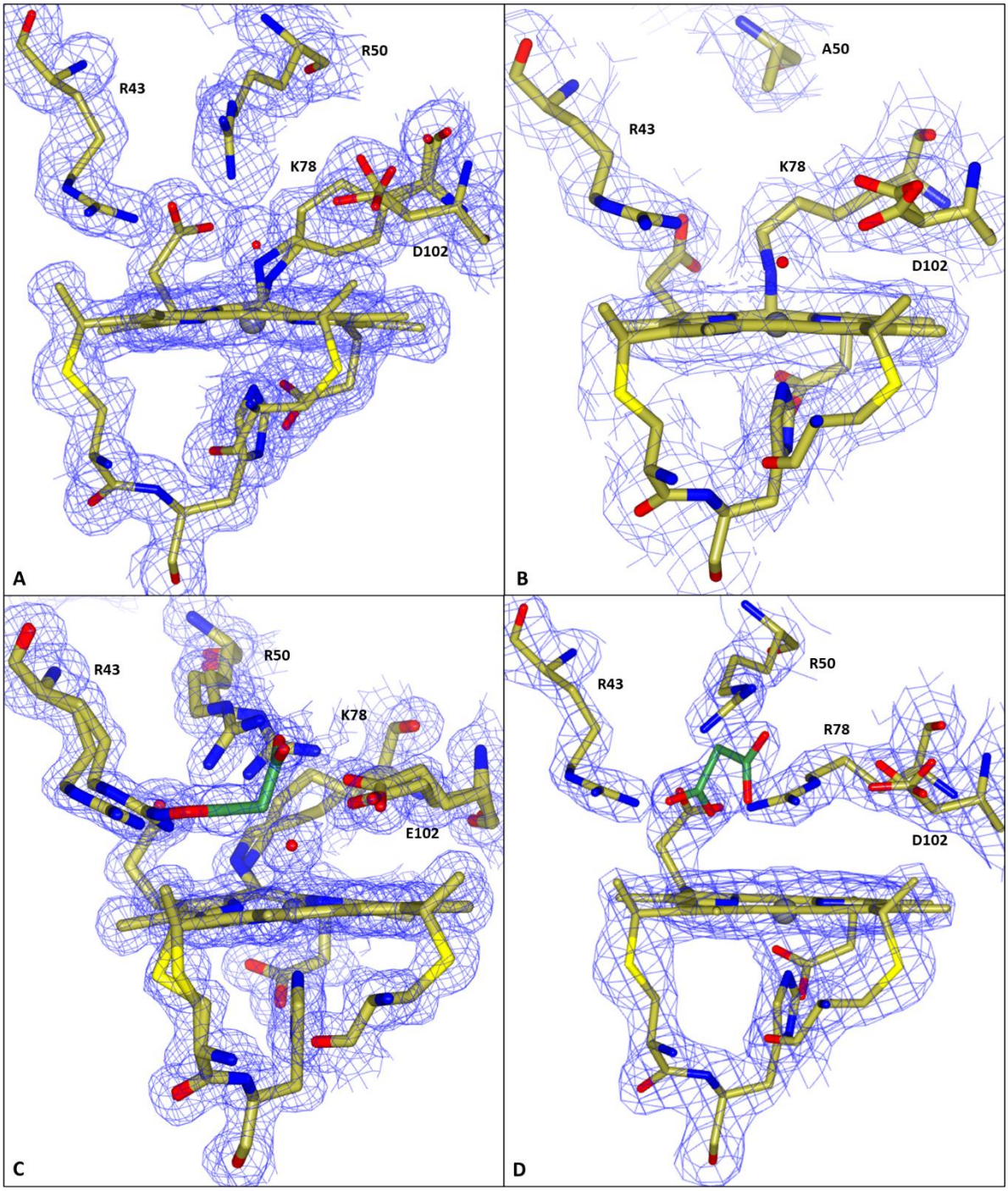

Figure 4.9. *2Fo-Fc* maps contoured at 1.5-2 σ of as isolated crystal structures of wt *Mc*P460 (A) and mutants R50A (B), D102E (C) and K78R (D). The introduced mutations can clearly be seen in the distal pocket for each structure. For the R50A (B) and D102E (C) mutations a water can still be seen bound to the distal face of the heme which is not present in the K78R (D) mutant structure.

Table 4.3. Data collection, processing and refinement statistics for R50A, K78R and D102E as isolated structures.

Dataset	R50A	K78R	D102E
Resolution (Å)	41.79 - 2.16	42.17 - 1.30	41.94 - 1.18
Unit cell, (Å)	a=45.9206 b=80.4076 c=83.5837	a=46.0816 b=80.1824 c=84.3467	a=45.6842 b=80.6604 c=83.8831
Unique reflections	17233	77387	101684
Completeness (%)	99.84 (100)	99.83 (100)	99.32 (100)
Redundancy	13.4 (13.7)	12.4 (6.5)	6.1 (3.4)
R_{meas}	0.287 (3.53)	0.074 (2.35)	0.101 (1.50)
I/σ(I)	6.3 (0.6)	16.3 (0.5)	8.3 (0.5)
$CC_{1/2}$	1.0 (0.3)	1.0 (0.3)	1.0 (0.3)
Wilson B-factor (Å^2)	21	18	12
R_{work}	0.1900	0.1756	0.1785
R_{free}	0.2440	0.1981	0.1923
RMSD bond length (°)	0.012	0.012	0.010
RMSD bond angles (Å)	1.717	1.710	1.287
Ramachandran favoured (%)	98.58	98.94	98.58

Table 4.4. Heme site parameters in *Mc*P460 WT, R50A, K78R and D102E as isolated crystal structures

Structure	Fe-His (Å)	Fe-H_2O (Å)
*Mc*P460 As Isolated	2.12, 2.13	2.37, 2.32
R50A As Isolated	2.05, 2.02	2.01, 2.05
K78R As Isolated	2.09, 2.10	-
D102E As Isolated	2.10, 2.14	2.14, 2.12

4.3.4 Ligand binding studies

4.3.4.1 Spectroscopy of ligand binding

Wt *Mc*P460 binds NO in both the ferric and ferrous states as seen in the UV-visible spectra with Soret maxima of 431 nm (Fe(III)NO) and 432 nm (Fe(II)NO) (Figure 4.10, Table 4.5). *Mc*P460 binds hydroxylamine with a Soret maximum of 433 nm. There is no previously published UV-visible data for binding either NO to ferric/ferrous *Mc*P460 or hydroxylamine to the ferric enzyme. In comparison to *Ne*P460 the Soret maxima for *Mc*P460 ligand binding are all blue shifted by around 10-20 nm.

EPR samples for NO bound wt *Mc*P460 samples in both the ferric and ferrous state were prepared in an anaerobic chamber (0_2 <0.1 ppm) using degassed buffers to minimise oxygen contamination.

The ferric NO sample displayed a large amount of unbound NO (g value 1.97) despite being prepared with the same amount of Proli-NONOate as the ferrous samples. This signal is preceded by a line shape representative of 6-coordinate NO within the sample which gave rise to g values of 2.05, 2.03 and 2.02 (Figure 4.12, Table 4.6). Generation of the $\{FeNO\}^6$ species by the addition of NO to the ferric *Ne*P460 protein (Coleman and Lancaster, 2020) produced an EPR silent species unlike what is seen in *Mc*P460.

Despite the lack of defined hyperfine splitting seen in the spectrum the line shape of the ferrous NO sample is indicative of a 6 coordinate NO (Figure 4.12). This is similar to what was seen in the *Ne*P460 EPR samples (Coleman and Lancaster, 2020) generated in a similar manner.

EPR samples for hydroxylamine bound wt were also prepared anaerobically using degassed buffers to minimise oxygen contamination. The line shape of the EPR spectrum for wt enzyme resembles that of the previously published EPR spectrum of *Ne*P460 with

hydroxylamine in the absence of oxygen (Numata *et al.*, 1990) being that of a single low spin heme (Figure 4.12).

Contamination with oxygen which gave rise to a signal thought to be the $\{FeNO\}^7$ intermediate in the published *Ns*ALP460- NH_2OH spectrum is not seen in this sample suggesting that no oxygen was present.

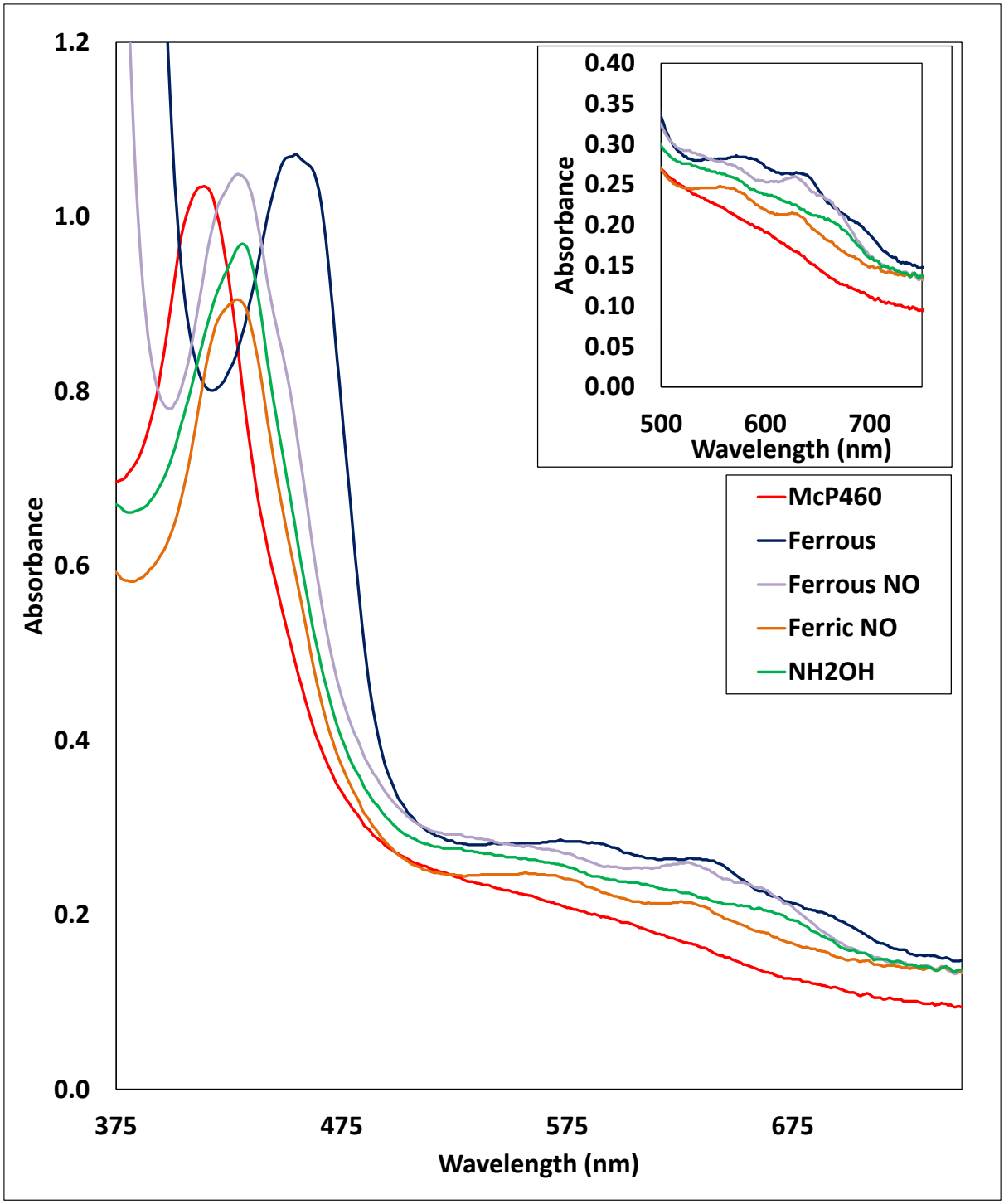

Figure 4.10. wt *Mc*P460 UV-visible spectra. The Soret maxima are shown for the ferric (red), ferrous (dark blue), ferrous-NO (purple), ferric-NO (orange) and ferric hydroxylamine bound wt *Mc*P460 and inset showing α/β bands for each.

All the *Mc*P460 pocket mutants bind NO in both the ferric and ferrous states with Soret maxima seen at 430 nm (R43A Fe(III)NO), 429 nm (R50A Fe(III)NO), 456 nm (D102E Fe(III)NO), 428 nm (R43A Fe(II)NO), 425 nm (R50A Fe(II)NO) and 447 nm (D102E Fe(II)NO) (Figure 4.11, table 4.5). This suggests that the mutations do not affect the ability to bind NO. Again, the spectra for the D102E mutant is more shifted than the other mutants giving rise to maxima more similar to those reported for *Ne*P460.

The K78R mutant binds ferrous NO with a Soret maximum at 416 nm (Figure 4.11) suggesting 6-coordinate NO binding in a fashion more similar to cytochrome *c'* than to cytochrome P460 (Hough and Andrew, 2015). K78R can also bind NO in the ferric state with a slightly shifted Soret maximum of 418 nm.

All the P460 pocket mutants bind hydroxylamine in the ferric state in anaerobic conditions with Soret maxima seen at 429 nm (R43A), 425 nm (R50A), 446 nm (D102E) and 407 nm (K78R). This suggests that the mutations do not affect the protein's ability to bind hydroxylamine. (Figure 4.11)

EPR samples for NO bound mutant P460 samples in both the ferric and ferrous state were prepared anaerobically in a glove box using degassed buffers to minimise oxygen contamination.

As seen with the wt enzyme, the ferric NO samples all displayed a large amount of unbound NO (g value 1.97) despite being prepared with the same amount of Proli-NONOate as the ferrous samples. For the R43A and R50A mutants the bound NO within the samples gave rise to g values of 2.05, 2.03 and 2.02, as seen in the wt enzyme, with a line shape indicative of 6-coordinate NO (Figure 4.11, table 4.6). In the D102E mutant only the unbound NO is seen suggesting that the $\{FeNO\}^6$ species in this mutant may be EPR silent as is seen with *Ne*P460.

Despite the lack of defined hyperfine splitting seen in the spectrum the line shape of the ferrous NO samples are indicative of a 6 coordinate NO in all of the proteins (Figure 4.11). This is similar to what was seen in both the wt *Mc*P460 and the *Ne*P460 EPR samples (Coleman and Lancaster, 2020) generated in a similar manner.

As with the wt enzyme EPR samples for hydroxylamine bound mutant *Mc*P460s were all prepared anaerobically in a glove box using degassed buffers to minimise oxygen contamination. The line shape of the EPR spectrum for the R43A, R50A and D102E mutants resembles that of the previously published EPR spectrum of *Ne*P460 with hydroxylamine in the absence of oxygen (Coleman and Lancaster, 2020) being that of a single low spin heme (Figure 4.12C). Again, contamination with oxygen which gave rise to a signal thought to be the $\{FeNO\}^7$ intermediate in the published *Ns*ALP460- NH_2OH spectrum is not seen in any of these samples suggesting that no oxygen was present.

The K78R mutant displayed a different line shape to the other proteins with g values of 6.25 and 5.55 suggesting the presence of a high spin heme despite binding of hydroxylamine.

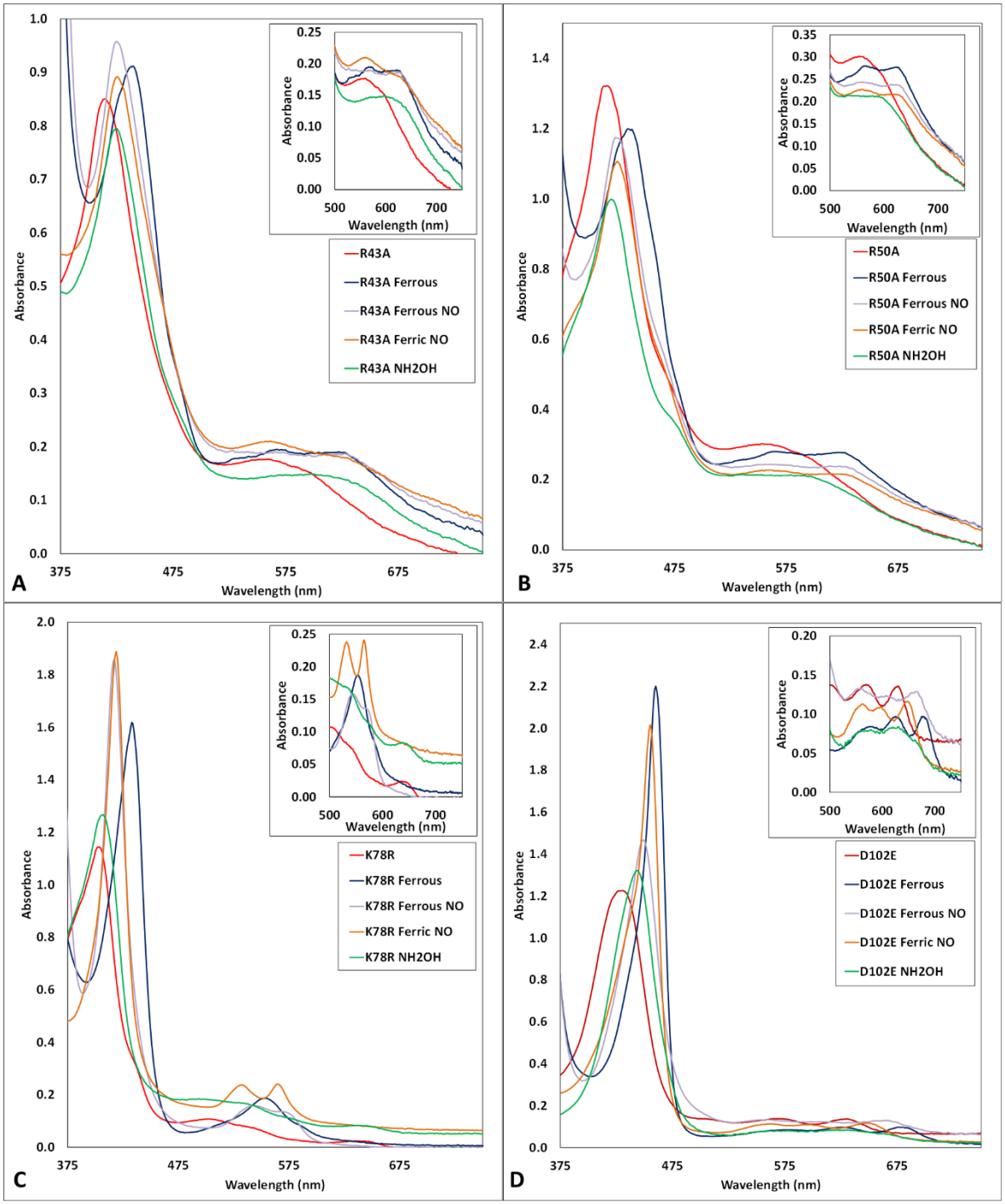

Figure 4.11. UV-visible spectra of *Mc*P460 mutants R43A (A), R50A (B), K78R (C) and D102E (D). The Soret maxima are shown for the ferric (red), ferrous (dark blue), ferrous-NO (purple), ferric-NO (orange) and ferric hydroxylamine bound *Mc*P460 mutants and insets showing α/β and CT bands for each.

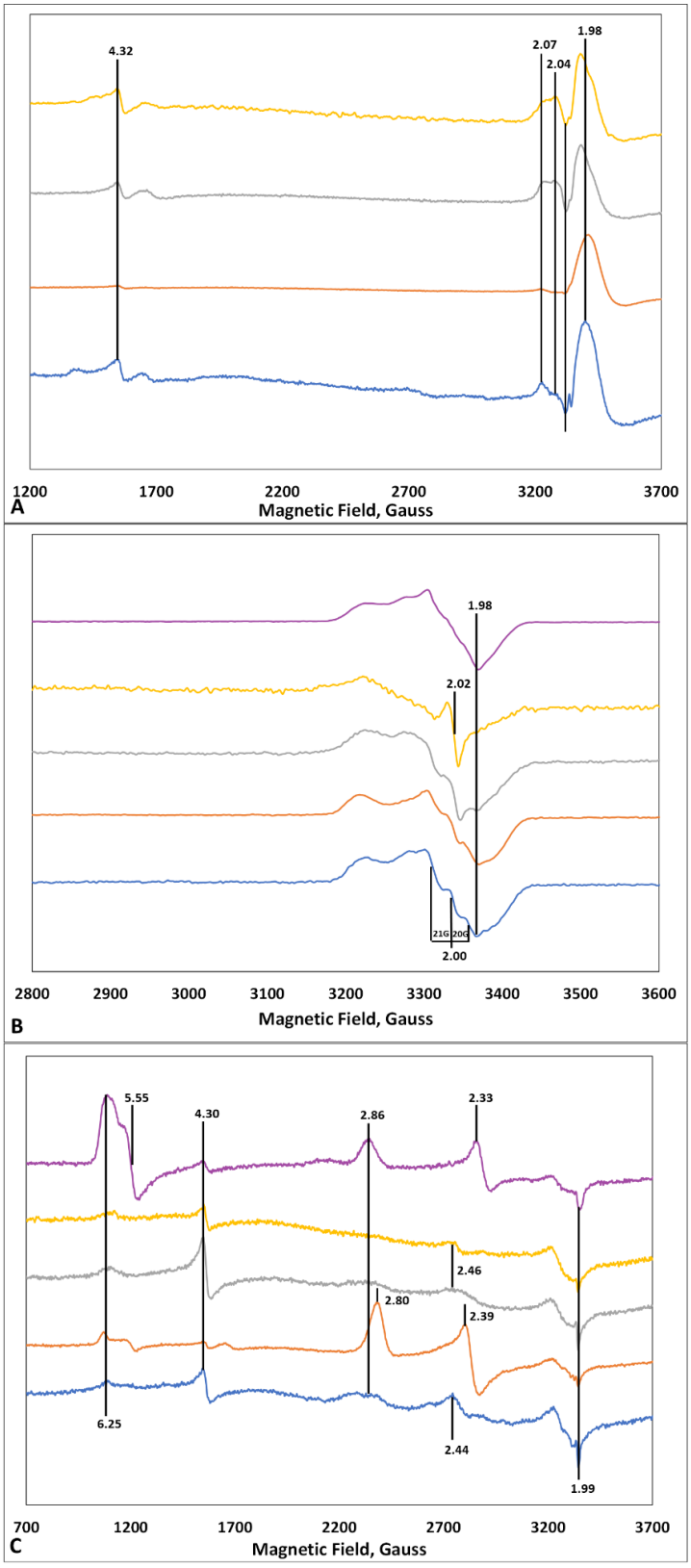

Figure 4.12. EPR spectra of *Mc*P460 (Blue), R43A (yellow), R50A (grey), K78R (purple) and D102E (orange) in either the ferric (A) or ferrous (B) state with NO and in the ferric state with hydroxylamine **(C)**

Table 4.5. UV-visible parameters for ligand bound cyts P460

	λ_{max} (nm)		ref
Fe(III)-NO			
*Mc*P460	431	556, 633	tw
R43A	428	629, 563	tw
R50A	425	563, 630	tw
K78R	419	535, 567	tw
D102E	456	566, 604, 655	tw
*Ne*P460	455	596, 650	a
Fe(II)-NO			
*Mc*P460	432	562, 636	tw
R43A	427	629	tw
R50A	426	566, 631	tw
K78R	417	545, 575	tw
D102E	447	557, 610, 668	tw
*Ne*P460	452	550, 608, 664	a
Fe(III)-HA			
*Mc*P460	433	573, 670	tw
R43A	426	606	tw
R50A	419	598	tw
K78R	408	540, 644	tw
D102E	445	572, 628	tw
*Ne*P460	445	561, 633	a

a (A. Smith *et al.*, 2019)

Table 4.6. EPR spectra parameters for ligand bound cyts P460.

protein	pH	temp (K)	g^		gçç
			g1	g2	g3
Fe(III)-NO					
*Mc*P460	7	10	4.52	2.07,2.04,2.01	1.98
R43A	7	10	4.52	2.07,2.04,2.01	1.98
R50A	7	10	4.52	2.07,2.04,2.01	1.98
D102E	7	10	EPR SILENT		
*Ne*P460*	7	10	EPR SILENT		
Fe(II)-NO					
*Mc*P460	7	10	2.02	2.00	1.99
R43A	7	10	2.05	2.02	2.00
R50A	7	10	2.02	2.00	1.99
K78R	7	10	2.02	2.00	1.99
D102E	7	10	2.02	2.00	1.99
*Ne*P460*	7	10	2.10	2.03	2.01
Fe(III)-HA					
*Mc*P460	7	10	2.86	2.44	1.99
R43A	7	10	-	2.46	1.99
R50A	7	10	-	2.46	1.99
K78R	7	10	2.86	2.33	1.99
D102E	7	10	2.80	2.39	1.99
*Ne*P460*	7	10	2.86	2.44	1.99

* (Coleman and Lancaster, 2020)

4.3.4.2 X-ray structures of ligand binding

Crystals for the wt, R50A, K78R and D102E mutants of *Mc*P460 were obtained as previously described (Chapter 4.2.6). To obtain ligand bound structures either excess proli-NONO-ate or 100 mM hydroxylamine hydrochloride were added to the crystals. Due to the fact that the P460 crystals were resistant to being reduced only structures for the ferric-ligand bound states could be investigated. All ligand soaked crystals were cryoprotected and flash frozen as previously described.

As water is present bound to the iron heme in the as isolated structures the presence of other ligands similar position in the soaked crystal structures had to be carefully assessed. A variety of methods were used to help ensure that the correct ligand (i.e., water/NO/NH_2OH) was identified in each structure. The higher resolution structures had clearer density above the distal face of the heme allowing to it be more clearly seen if a diatomic ligand was present (such as NO or NH_2OH) in comparison to a water molecule. Difference maps were also generated during the refinement to help guide the choice of ligand and it's positioning. Positive density suggests that there may be something present which has not been currently modelled into the map, whilst negative density suggests that what is currently modelled should be removed or moved to a different position. For example, if a hydroxylamine molecule was modelled in where only a water should be a patch of negative density would appear as the hydroxylamine is bigger than the water and wouldn't fit into the space. These difference maps were also used to help determine any alternate conformations of residues present in the structures. The B-factors of both the Fe centre of the heme and the bound ligand were also compared to determine the occupancy of the ligand, with the occupancy being adjusted until the B-factors were at a similar value. Again, the B-factors were also used to help determine the occupancies of any alternative conformations of residues in the

structures. The final structures were all run through online validation tools as previously described (Chapter 4.2.7). All data processing and refinement statistics are given in Table 4.7.

The wt *Mc*P460 hydroxylamine soaked crystals were measured at the Swiss Light Source beamline X10SA and diffracted to 1.35 Å. One hydroxylamine molecule can be clearly seen to be bound to heme B (Figure 4.13 D, E) and two with partial occupancies can be seen bound to heme A (Figure 4.13 E) instead of the water seen in both the as isolated structure (Figure 4.13 A). The Fe-N distances is 2.00 Å, 2.26 Å and 2.04 Å and the Fe-N-O angles 118 °, 105 ° and 127 ° in hemes A and B respectively. Each of the partial occupancy (0.5) hydroxylamine molecules are orientated in different directions in heme A, one being directed towards Arg 50 and the other towards Asp 102. In the as isolated structure a molecule of the cryoprotectant solution can be seen to be near the opening to the distal side of the heme sitting within binding distance of Arg 43. The density in this location in the hydroxylamine soaked structure is much smaller and nicely fits another molecule of hydroxylamine within 3 Å of NH2 of Arg 43. Arg 50 is positioned closer to the crosslink in both hemes with a rotation of 50 ° towards the crosslink also seen in heme B. Cysteine 143 can be seen to take up two conformations in this structure in both of the monomers.

The wt *Mc*P460 ferric proli-NONO-ate soaked crystals were measured at the Swiss Light Source beamline X10SA and diffracted to 1.43 Å. One NO molecule can be seen bound to each heme with a partial occupancy of 0.8 (Figure 4.13 B, C). They have Fe-N distances of 1.94 Å and 2.01 Å and Fe-N-O angles of 135 ° and 100 ° in hemes A and B respectively. In both cases the oxygen of the NO molecule is directed towards Asp 102. The only change seen in the distal pocket is to residue Arg 50 which displays two conformations in both hemes. In monomer A both are slightly further away from the heme (1.08 Å), and one conformation is 1.05 Å closer to the crosslink. In monomer B one sits in the same relative position to the as isolated structure whilst the other has rotated around the CD bond by 104 °. In monomer A it

has moved slightly closer to the heme face relative to the as isolated structure. Again Cys 143 can be seen to take up two conformations in this structure in both of the monomers.

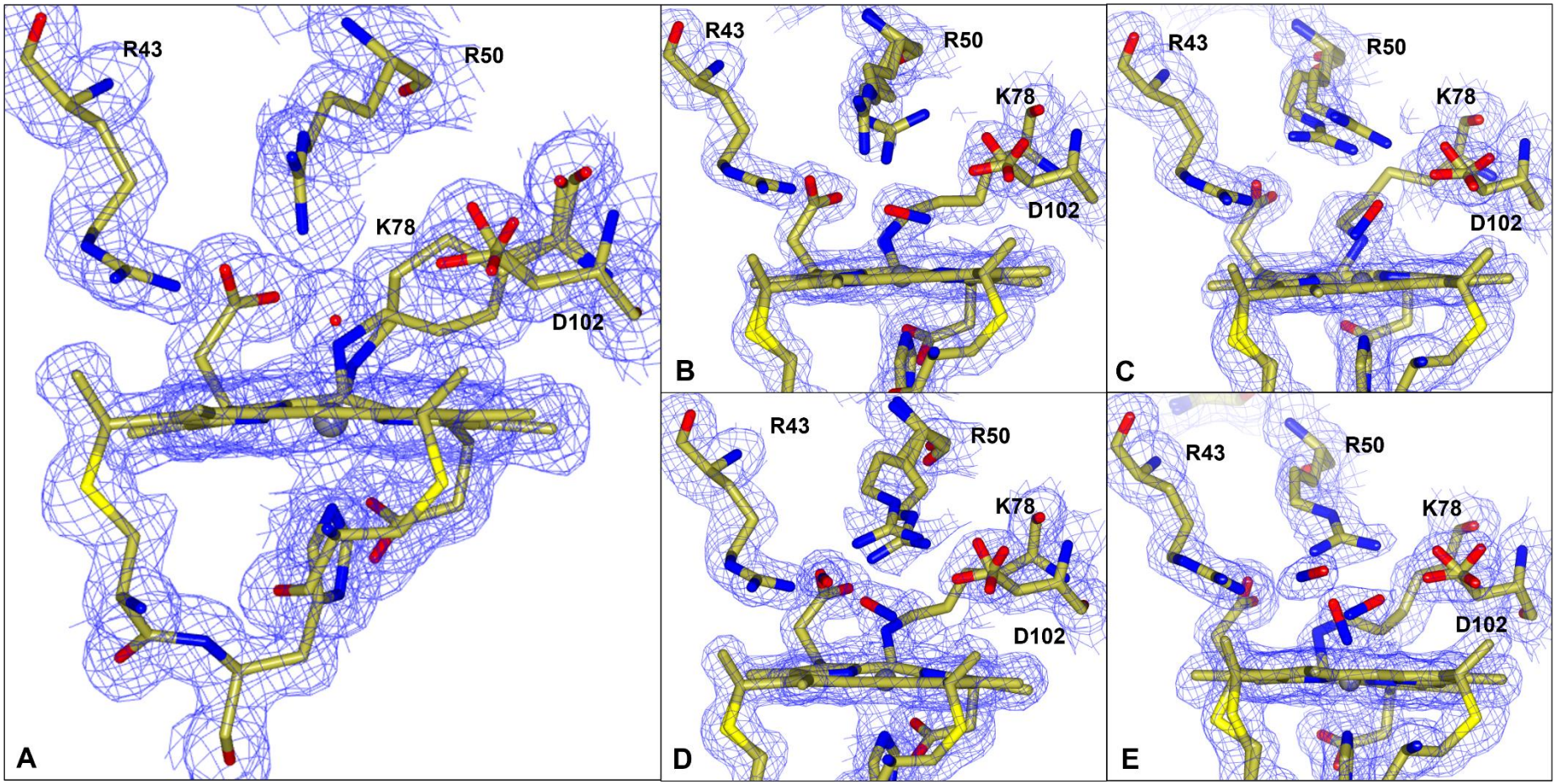

Figure 4.13. *2Fo-Fc* map contoured at 1.5 σ of wt *Mc*P460 single crystal cryogenic structures. The 'as isolated' ferric structure shows a water molecule bound to the distal face of the heme. (A) Ferric-NO soak clearly shows an NO molecule again bound to the distal face of the heme (B, C) and the ferric hydroxylamine soak shows hydroxylamine bound to the distal face. There is also a hydroxylamine seen in both monomers bound near to Arg 43 (D, E).

Table 4.7. Data collection, processing and refinement statistics for ligand bound wt *Mc*P460, R50A, K78R and D102E as isolated crystal structures.

Dataset	wt-NO	wt-HA	R50A-NO	R50A-HA	D102E-NO	D102E-HA	K78R-NO	K78R-HA
Resolution (Å)	41.67 -1.43	40.57 -1.35	57.92 -1.46	40.59 -1.63	58.14 -1.11	58.50 -1.40	45.79 - 1.52	38.61 -1.32
Unit cell, (Å)	a=45.63 b=80.98 c=83.72	a=46.23 b=81.05 c=84.63	a=45.41 b=80.51 c=83.37	a=46.3 b=80.28 c=84.33	a=45.11 b=81.38 c=83.1	a=44.94 b=82.15 c=83.33	a=42.46 b=70.86 c=91.58	a=42.50 b=71.94 c=91.50
Unique reflections	57550	64764	53966	39977	121054	61684	43200	66487
Completeness (%)	99.81 (100)	98.87 (100)	99.81 (100)	99.97 (100)	99.81 (100)	99.29 (100)	99.83 (100)	99.79 (100)
Redundancy	5.2 (4.2)	4.6 (4.0)	6.8 (6.8)	6.8 (6.9)	6.2 (3.4)	6.6 (6.9)	6.7 (6.8)	6.8 (6.8)
R_{meas}	0.068 (2.36)	0.037 (2.25)	0.097 (2.40)	0.111 (2.27)	0.078 (1.49)	0.151 (3.13)	0.112 (3.57)	0.094 (3.32)
I/σ(I)	11.5 (0.4)	18.5 (0.3)	10.2 (0.4)	9.5 (0.7)	9.6 (0.7)	7.6 (0.5)	8.8 (0.3)	11.3 (0.4)
$CC_{1/2}$	1.0 (0.3)	1.0 (0.3)	1.0 (0.3)	1.0 (0.4)	1.0 (0.3)	1.0 (0.2)	1.0 (0.3)	1.0 (0.4)
Wilson B-factor ($Å^2$)	21.84	21.93	17.04	21.69	12.06	13.17	18.75	14.21
R_{work}	0.1923	0.1945	0.1928	0.2127	0.1901	0.2221	0.2566	0.2287
R_{free}	0.2304	0.2147	0.2315	0.2433	0.2068	0.2639	0.2839	0.2519
RMSD bond length (°)	0.011	0.011	0.011	0.008	0.011	0.012	0.012	0.012
RMSD bond angles (Å)	1.181	1.269	1.207	1.021	1.246	1.417	1.718	1.715
Ramachandran favoured (%)	98.23	98.94	98.23	98.23	98.58	98.23	96.10	98.58

Table 4.8. Heme site parameters in *Mc*P460 WT, R50A, K78R and D102E crystal structures

Structure	Fe-His (Å)	Fe-H_2O (Å)	Fe-NO (Å)	Fe-HA (Å)	Fe-N-O (°)
*Mc*P460(III)-NO	2.14, 2.18	-	1.94, 2.01	-	135, 100
*Mc*P460-HA	2.01, 2.04	-	-	2.00, 2.26, 2.04	118, 105, 127
R50A As Isolated	2.05, 2.02	2.01, 2.05	-	-	-
R50A(III)-NO	2.20, 2.16	-	1.94, 1.96	-	122, 132
R50A-HA	2.16, 2.25	-	-	2.30, 2.03	105, 105
K78R As Isolated	2.09, 2.10	-	-	-	-
K78R(III)-NO	2.19, 2.08	-	1.97, 2.33, 2.34	-	152, 176, 112
K78R-HA	2.14, 2.13	-	-	1.97, 2.21	147, 165
D102E As Isolated	2.10, 2.14	2.14, 2.12	-	-	-
D102E(III)-NO	2.08, 2.08	-	1.81, 1.89	-	149, 150
D102E-HA	2.11, 1.98	-	-	1.95, 2.01	119, 120

The 1.40 Å resolution structure of the hydroxylamine soaked D102E mutant clearly shows full occupancy hydroxylamine bound to both hemes with distances of 1.95 Å and 2.01 Å and Fe-N-O bond angels of 119 ° and 120 ° in hemes A and B respectively (Figure 4.14 D, E). Both hydroxylamine molecules have their oxygen atom directed at residue Arg 50. In monomer A only one conformation of Arg 50 can now be seen, furthest from the crosslink with it NH2 atom being 4.01 Å away from the CD atom of the lysine. Only one conformation of both Glu 102 and Arg 43 are also seen the positioning of which are both between those seen in the as isolated structure. There is now only one conformation of Gln 46 which is directed towards the heme and 3.63 Å away from Arg 50 and Gln 100 is rotated by 90 ° around its CD bond. There is no density near to Arg 43 to suggest that anything is bound to it in this structure. Monomer B shows similar changes in the positions of the pocket residues except for Arg 50 which now has two conformations, having lost the one furthest from the crosslink. Only one conformation of Cys 143 can be seen bound to heme A whilst two conformations are seen in heme B.

The 1.11 Å resolution structure of the ferric NO soaked D102E shows one NO molecule bound to each heme with distances of 1.81 Å and 1.89 Å and Fe-N-O bond angles of 149 ° and 150 ° in hemes A and B respectively (Figure 4.14 B, C). Both NO molecules have full occupancy and have their oxygen atoms directed towards residue Arg 50. There are a few changes in the distal pocket residues, the conformation of Glu 102 which is the furthest from the heme has moved slightly further away from the heme in both monomers (0.42 Å and 0.53 Å respectively) and Arg 43 shows just one conformation similar to that seen in the wt as isolated protein structure. An NO molecule can be modelled into the density next to Arg 43 in both monomers at a distance of 2.77 Å from NH2 of the residue. Cysteine 143 can be seen to take up two conformations in this structure in both of the monomers.

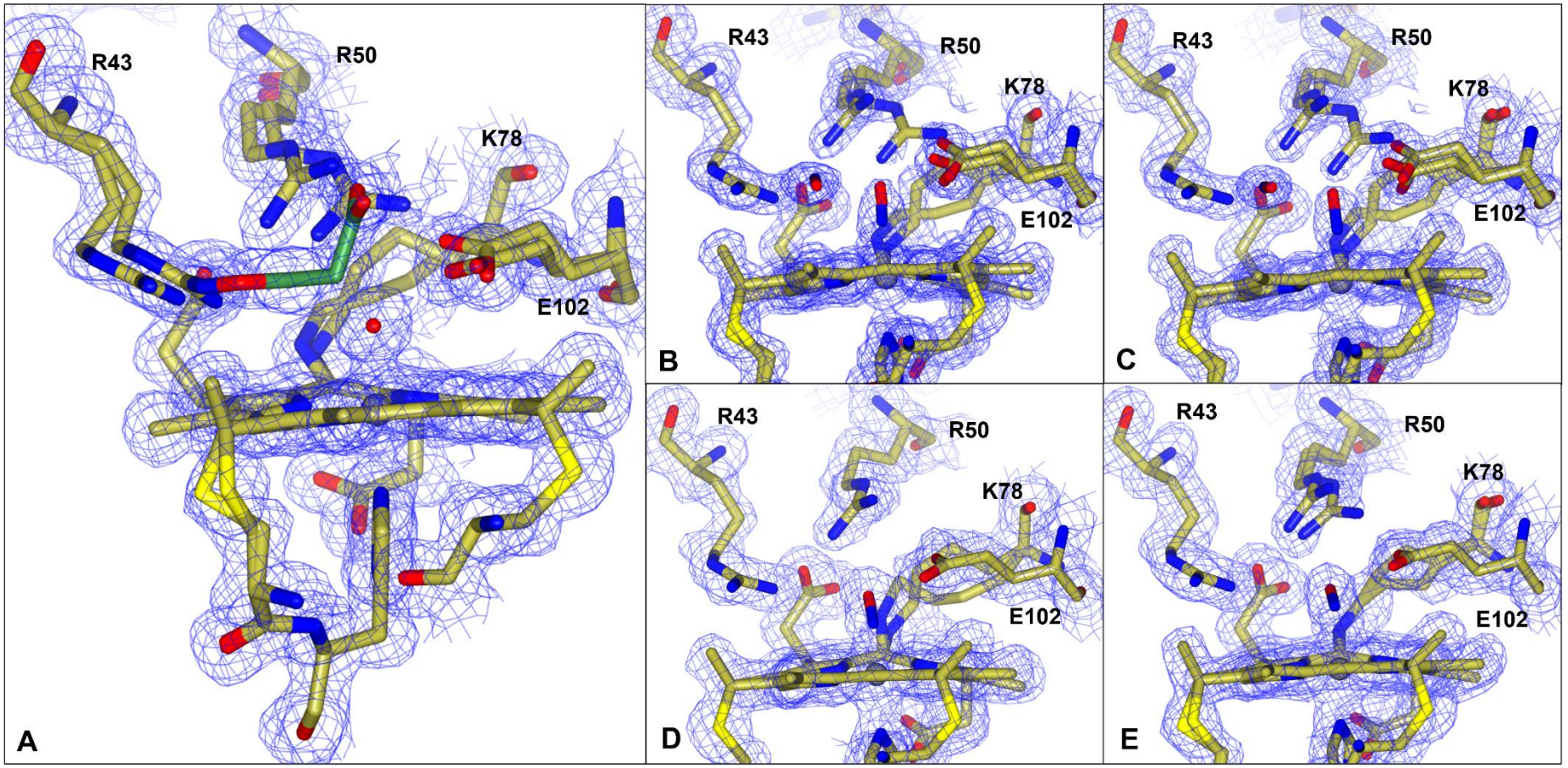

Figure 4.14. *2Fo-Fc* map contoured at 1.5 σ of *Mc*P460 D102E single crystal cryogenic structures. The as isolated ferric structure shows a water molecule bound to the heme and cryoprotectant ion bound near to Arg 43 in the distal pocket (A), the ferric NO soak shows NO molecules bound both to the distal face of the heme and to Arg 43 (B) and the ferric hydroxylamine soak shows a hydroxylamine molecule bound to the distal face of the heme but nothing bound to Arg 43 (D, E).

The 1.63 Å structure of the hydroxylamine soaked R50A mutant has one partial occupancy (0.7 and 0.8) hydroxylamine molecule bound to each heme with Fe-N distances of 2.30 Å and 2.03 Å and Fe-N-O bond angles of 105 ° in hemes A and B respectively (Figure 4.15 D, E). They each are orientated with the oxygen atom pointing in a different direction: one points between the crosslink and Asp 102 and the other between the crosslink and Arg 43. In both monomers R43 has moved a little bit away (0.4 – 1.2 Å) from the heme and Asp 102 rotated is slightly rotated whilst all other residues are in a similar position to the as isolated R50A structure. Nothing is seen to be bound to Arg 43 in either pocket.

In the 1.46 Å ferric NO soaked R50A structure one NO molecule can be seen bound in each monomer (Figure 4.15 B, C). These have Fe-N distances of 1.94 Å and 1.96 Å and Fe-N-O bond angles of 122 ° and 132 ° in hemes A and B respectively. Both NO molecules are orientated so the oxygen atom is pointing to the opposite side of the heme to the crosslink. In both monomers Arg 43 has moved a little bit away from the heme and Asp 102 rotated is slightly rotated whilst all other residues are in a similar position to the as isolated R50A structure. A malonate ion from the cryoprotectant can be seen bound to Arg 43. Cystine 143 can be seen to take up two conformations in this structure in both of the monomers.

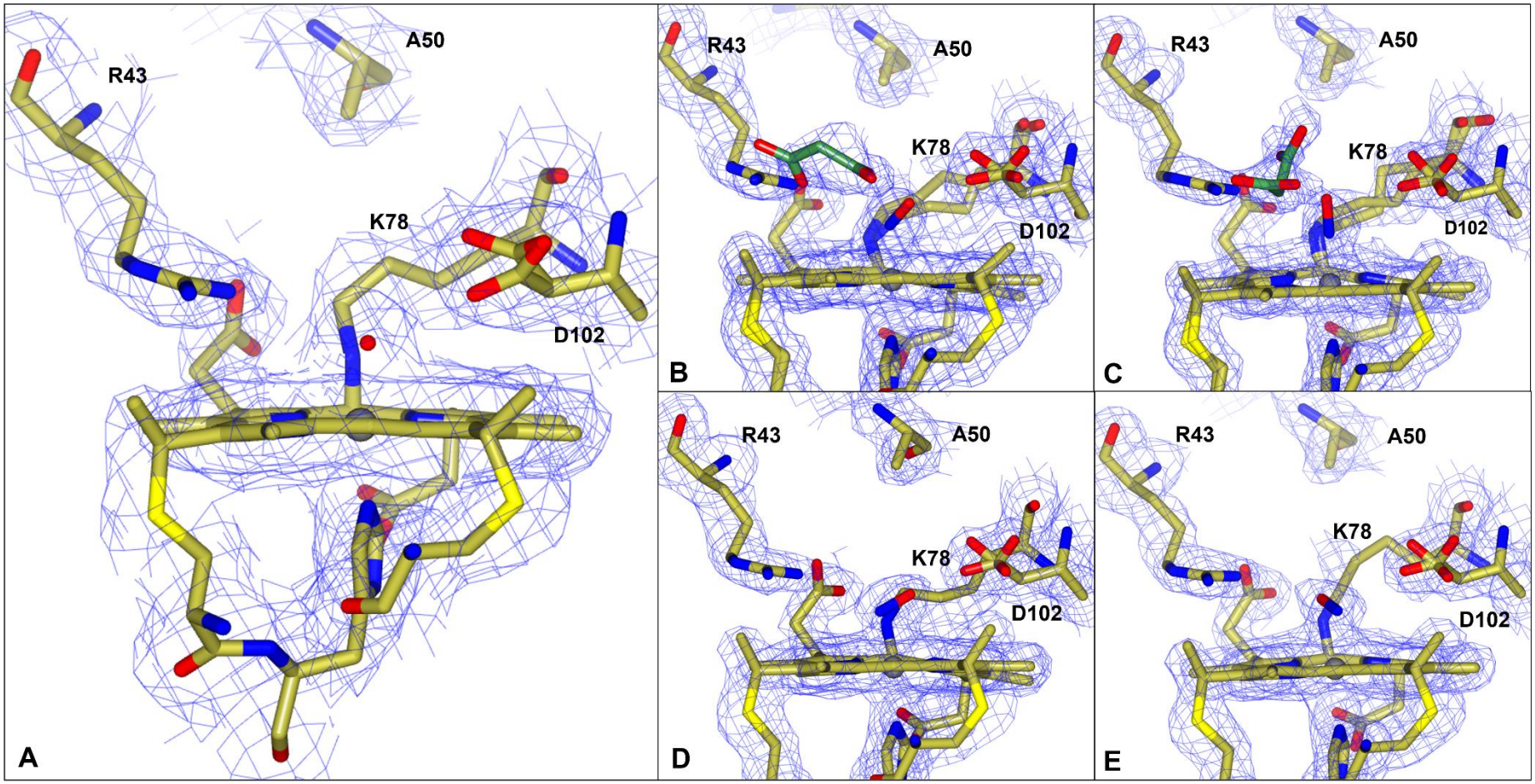

Figure 4.15. *2Fo-Fc* map contoured at 2 σ of *Mc*P460 R50A single crystal cryogenic structures. The as isolated ferric structure shows a water molecule bound to the distal face of the heme (A), the ferric NO soak shows an NO molecule bound to the distal face of each heme and a molecule of cryoprotectant bound to Arg 43 (B, C) and the ferric hydroxylamine soak shows a hydroxylamine molecule bound to the distal face of the heme (D, E).

Hydroxylamine soaked crystals of K78R diffracted to 1.32 Å and showed a single partial occupancy (0.7) hydroxylamine bound to each heme (Figure 4.16 D, E). In both monomers Arg 78 moves up away from the distal face of the heme upon introduction of a ligand, allowing it to bind. Arg 50 also moves up out of the way of residue Arg 78 and Arg 43 moves away slightly from the distal heme face. The hydroxylamine molecules are orientated with their oxygen atoms pointing in the opposite direction to Arg 78. The Fe-N distances are 1.97 Å and 2.21 Å and Fe-N-O bond angels are 147 ° and 165 ° in hemes A and B respectively.

The ferric NO soaked K78R crystals diffracted to 1.52 Å and showed one NO molecule bound in monomer A and two NO molecules bound in monomer B (Figure 4.16 B, C). The Fe-N distances are 1.97 Å, 2.33 Å and 2.34 Å and Fe-N-O bond angels are 152 °, 176 ° and 112 ° in hemes A and B respectively. The hydroxylamine molecule in monomer A is orientated with its oxygen atom pointing in the opposite direction to Arg 78 whilst in monomer B one is orientated upwards towards Arg 78 and the other is directed to the space between Arg 78 and Arg 50. Again, the presence of a bound ligand has caused Arg 78 to move upwards away from the distal heme face which in turn causes Arg 50 to move away from the heme face also. In monomer B Arg 78 is also rotated by 90 °. In both monomers a malonate ion can be modelled in the pocket bound to Arg 43.

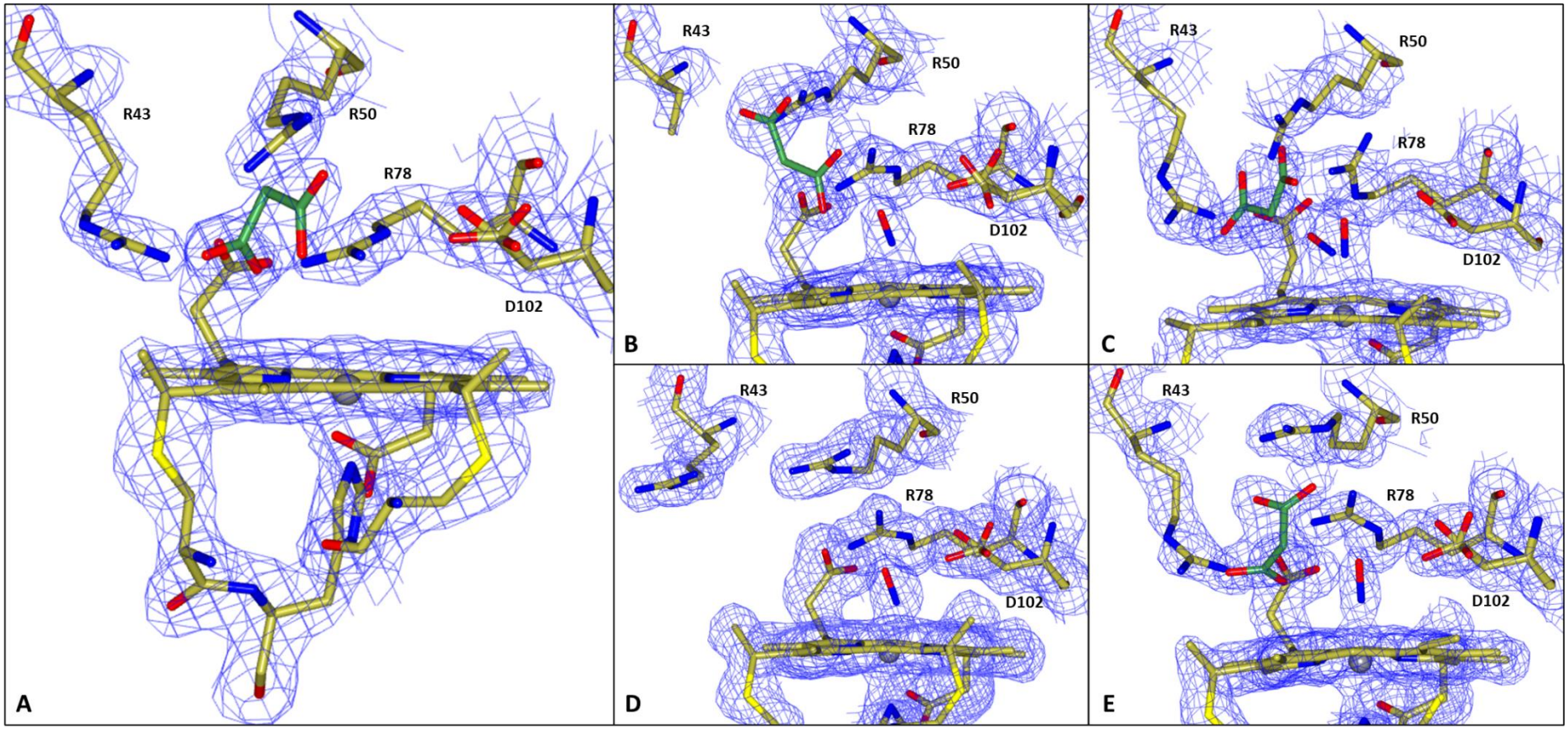

Figure 4.16. *2Fo-Fc* map contoured at 1.5 σ of *Mc*P460 K78R single crystal cryogenic structures. The as isolated ferric structure shows the Arg 78 mutation occludes water from binding to the distal face of the heme (A), the ferric NO (B, C) and ferric hydroxylamine (D, E) soaks causes Arg 43 to move away from the heme and NO/hydroxylamine to bind to the distal face in both monomers.

4.3.5 Peroxidase-like activity

When treated with H_2O_2 K78R displays a UV-visible spectra similar to that seen for compound II in peroxidases (Figure 4.17 B) with absorbance maxima seen at 410 nm, 525 nm, 555 nm and 639 nm. The spectrum then returned to the ferric state 10 min after addition of H_2O_2. This is like that seen for *Ne c'*-β^{-met} (Liew *et al.*, 2020). This change in absorbance maxima was not seen in the wt protein (Figure 4.17 A) where upon addition of hydrogen peroxide the only change was a reduction in the absorption maximum which correlated to the protein being bleached. Likewise, no changes in absorbance maxima were seen with any of the other mutants and it was also not seen in *Mc*CP or it's mutants (data not shown).

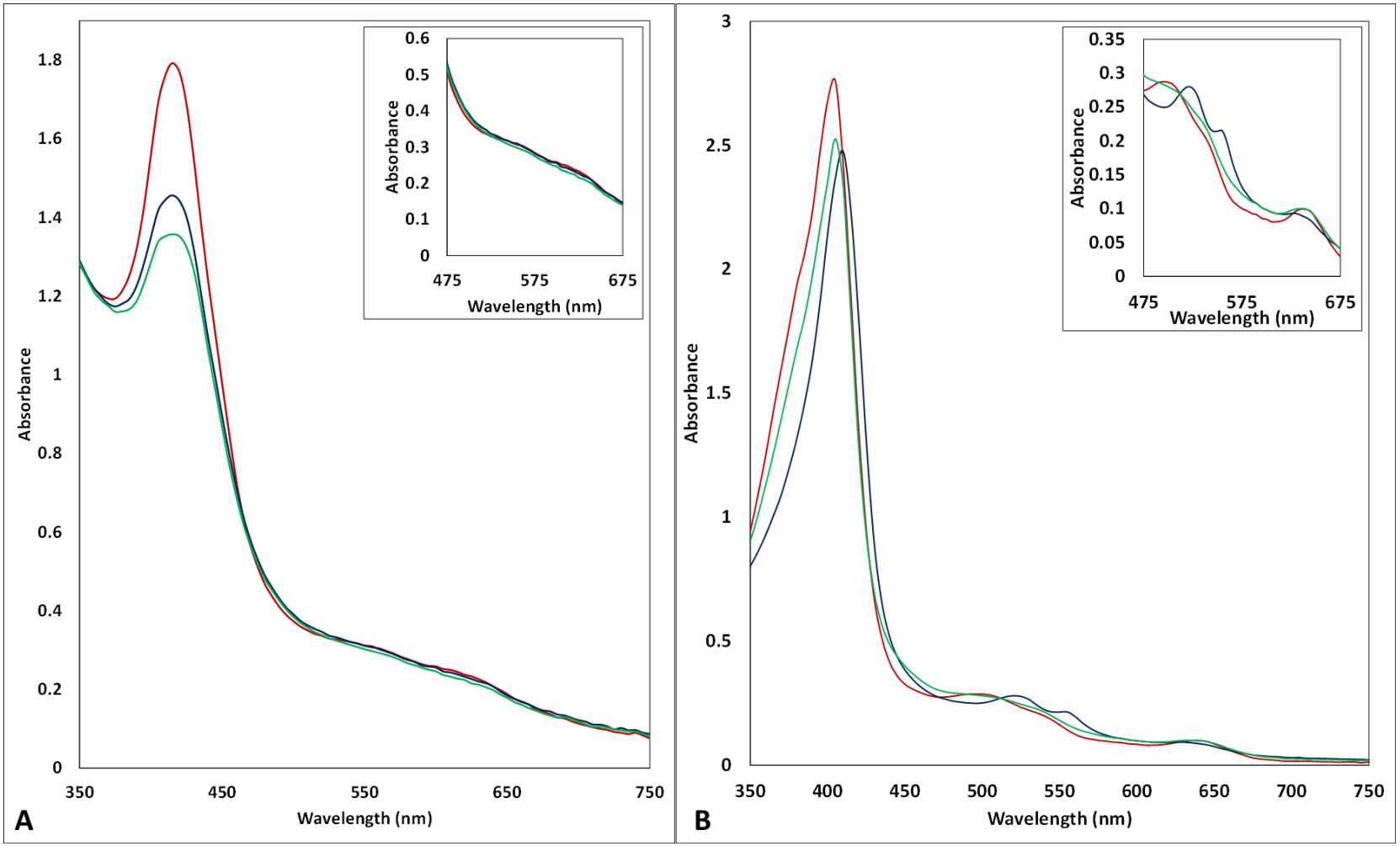

Figure 4.17. UV-visible spectra of wt *Mc*P460 (A) and K78R (B) with addition of H_2O_2 showing the starting spectrum (red), spectrum after addition of H_2O_2 (blue) and spectrum after 10 minutes (green).

4.3.6 Activity Assays

Activity assays were carried out to assess each protein's ability to oxidise hydroxylamine. The reported activity of *Ne*P460 at 4.5 μMDCPIP·(μMCytP460)$^{-1}$·(min)$^{-1}$ is around 3.8 times higher than that of *Mc*P460 (Table 4.9, figure 4.18). The activity of *Mc*P460, 1.19, is more similar to that of the *Ns*ALP460 A131E mutant at 2.1 (A. Smith *et al.*, 2019). This suggests that while *Mc*P460 is able to oxidise hydroxylamine it may not be as efficient as *Ne*P460. The D102E mutant showed similar activity to the wt *Mc*P460 at 0.93.

The R43A showed an unexpected increase in the activity of the protein at 2.84. This is 2.4 times higher than the wt *Mc*P460 but still significantly lower than the reported activity of *Ne*P460.

The R50A mutant appears to be inactive with a TOF of 0.49, similar to the reported value of the inactive *Ns*ALP460 variant, suggesting this residue is important in the activity of the protein.

The K78R crosslink deficient mutant also shows no activity as would be expected with the removal of the lysine residue with a TOF of 0.4.

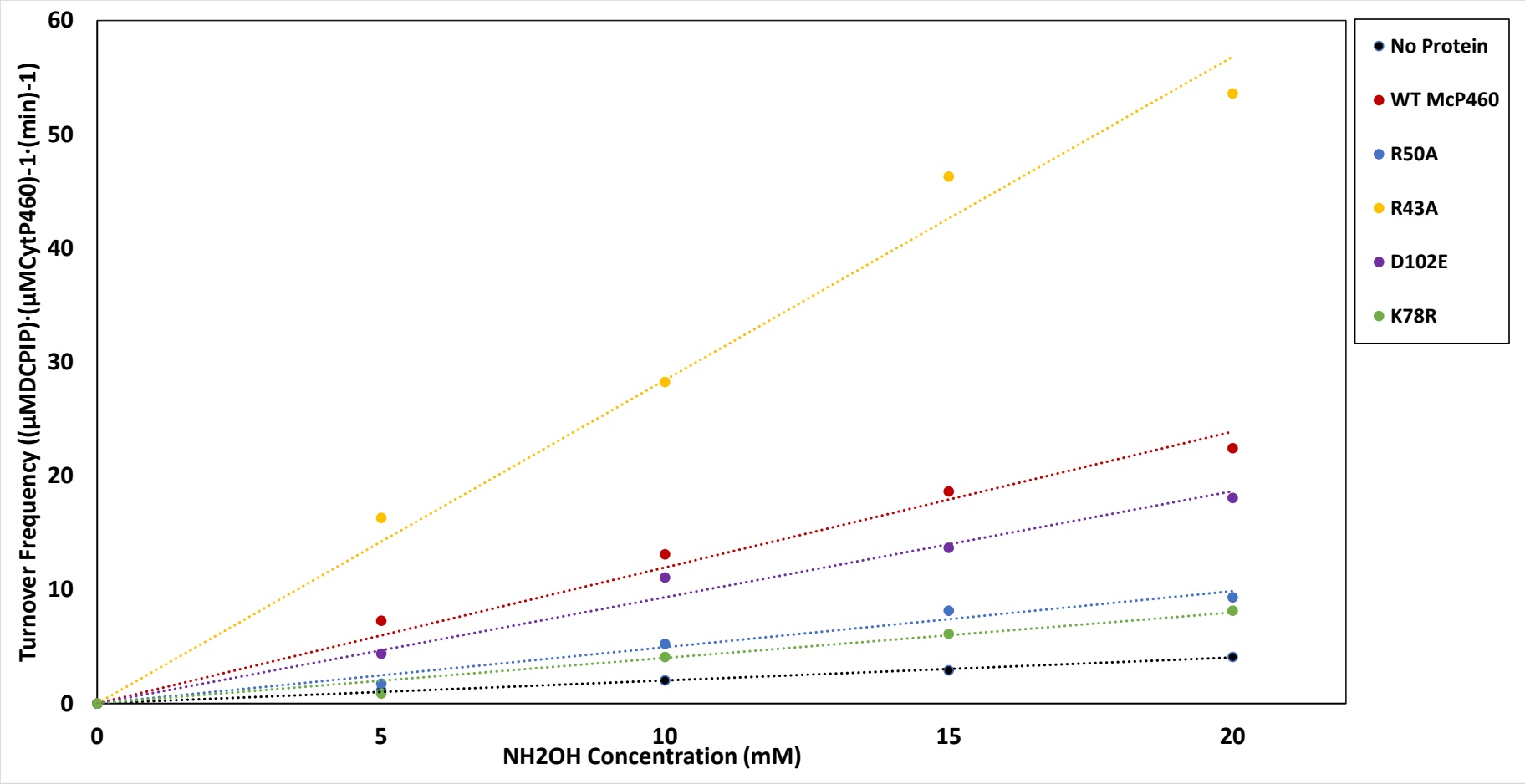

Figure 4.18. Steady-state NH_2OH oxidation activity plot for all investigated cyt P460 variants. Assay conditions were 1 µM cyt P460, 6 mM phenazine methosulfate (PMS), and 70 mM DCPIP. NH_2OH concentrations ranged from 0–20 mM. Assays were carried out anaerobically in 50 mM sodium phosphate, pH 8.0. Each data point is the average of at least three trials. The data series in black represents NH_2OH-dependent rates of DCPIP consumption under enzyme-free but otherwise identical conditions.

Table 4.9. Turnover frequencies (TOFs) of for all investigated P6460 variants and comparison to published TOFs for *Ne*P460 variants.

Protein	**TOF ((μMDCPIP)·(μMCytP460)$^{-1}$·(min)$^{-1}$)**	**ref**
*Ne*P460	4.5	Smith 2019
*Mc*P460	1.19	tw
R43A	2.84	tw
D102E	0.93	tw
*Ns*ALP460 A131E	2.1	Smith 2019
Wt *Ns*ALP460	0.43	Smith 2019
K78R	0.4	tw
R50A	0.49	tw
No Protein	0.2	tw

4.4 Discussion

The turnover frequencies (TOF) of the different *Mc*P460 mutants along with their crystal structures and spectral data give insights into the importance of the distal pocket residues in the reactivity of the protein.

The lysine crosslink present in all P460s has been previously shown to be essential in the reactivity of the protein. Thus, the lack of activity in the K78R mutant, despite clearly being able to bind hydroxylamine and NO as shown in the spectral and structural data, is not surprising. Mutating out the crosslink and replacing it with an Arg residue restricts access to the Fe of the heme on the distal face as the Arg residue sits directly on top of the heme preventing the water normally seen in wt *Mc*P460 from binding. However, access to the heme pocket is not affected by the surrounding solvent and ligands can enter the pocket just not bind without movement from the Arg residue. This is similar to the cytochrome *c'*β^{-Met} from *N. europaea* which has a methionine in this position on top of the heme (Abendroth *et al.*, 2022) and has no water bound to the heme in its as isolated crystal structure (Figure 4.19).

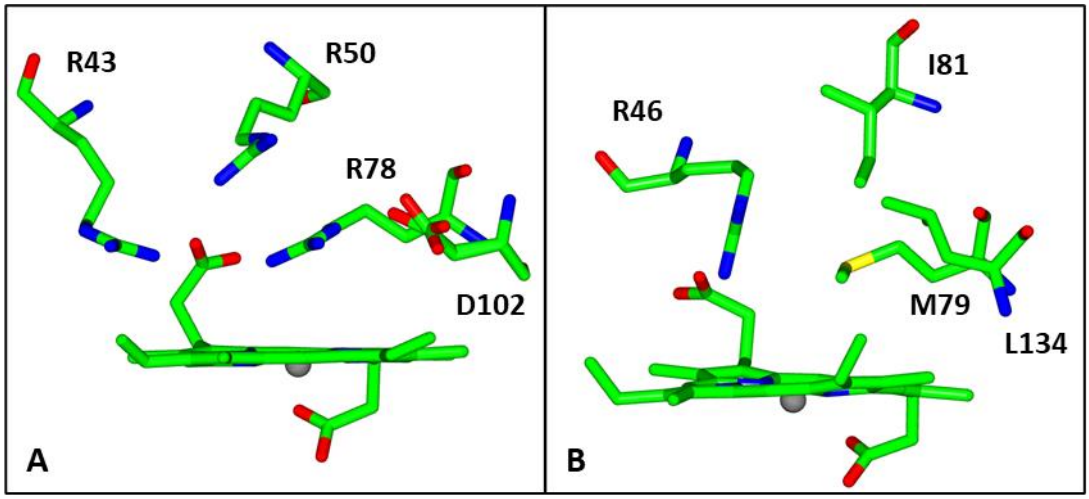

Figure 4.19. Distal heme pockets of K78R *Mc*P460 mutant (A) and *c'*β^{-Met} from *N. europaea* (7S5O) (B) showing the arginine (in K78R) and the methionine (in *Ne c'*β^{-Met}) which prevent water from binding in the as isolated state.

The peroxidase like activity seen in this mutant, similar to that seen in *Ne* c-β^{-Met} (Liew *et al.*, 2020), was unexpected and further investigations will need to be carried out to discover whether this is true peroxidase activity and if the activity is simply due to the removal of the crosslink or to the specific mutation. Addition of H_2O_2 to wt *Mc*P460 and other crosslinked *Mc*P460 mutants simply resulted in bleaching of the samples. This peroxidase like activity has also not been reported in any other crosslinked P460s and an *Ne*P460 K96A mutant (Liew *et al.*, 2020) showed that peroxidase like activity could be given to *Ne*P460 upon removal of the crosslink suggesting the presence of the crosslink prevents the reaction from occurring. It also did not show any reaction with *Mc*CP or it's mutants suggesting that there must be the correct type of residues present in the pocket for the reaction to occur.

Removal of the Arg in the R43A mutant appears to increase the TOF of *Mc*P460 to a level that is more similar to that reported for *Ne*P460 (A. Smith *et al.*, 2019). Spectral data for the Arg 43 mutant suggests that it is able to bind hydroxylamine and NO in a similar manner to the wt protein. Whilst a crystal structure for this mutant was not able to be obtained it is likely that the Arg is acting as a gatekeeping residue, binding anything that is entering the distal pocket and so reducing access and slowing down the TOF of the protein despite the distal pocket being relatively open. Making a computer generated model of *Mc*P460 with the R43A mutation, by using Coot to change Arg 44 to Ala, and carrying out surface modelling in CCP4mg it can be seen that mutation of the Arg 43 residue to an alanine would open up the access to the distal pocket (Figure 4.20). This hypothesis is supported by the crystal structures of the other mutants and wt protein where it can, more often than not, be seen that there is a ligand bound at this site (either from the cryoprotectant or a soaked ligand). The equivalent residue in *Ne*P460 is Thr 29 which does not appear to have any interactions with any ligands entering the pocket as it is positioned further away from the entrance to the distal face of the heme. In all published structures for *Ne*P460 there is a missing loop which is proposed to

come around the distal side of the heme. It had been proposed by Lancaster (M. Bollmeyer *et al.*, 2023) that Phe 41 of *Ne*P460 would sit over the heme in a position homologous to Phe 76 in the *N*sALP460 variant in a position to possibly provide some steric hinderance to incoming molecules. Whilst surface modelling suggests that this residue would possibly restrict access to the distal face of the heme (Figure 4.20 C) their research actually showed that mutation of the Phe to an Ala slowed the TOF of *Ne*P460. Interestingly this Phe residue in the *Ne*P460s sits in the same position over the distal face of the heme as Phe 32 in *Mc*CP. It has been shown that Phe 32 does not appear to provide any steric hinderance to initial ligand binding. The same appears to be true for Phe 41 which does not hinder the initial binding of hydroxylamine to the heme, but movement of the residue that occurs upon binding allows control over the second hydroxylamine in the rate determining step which returns the heme to its Fe(III) state and allows the release of N_2O. Removal of the Phe leaves the reactive intermediates open to off-pathway reactions with the surrounding solvent thus lowering the TOF.

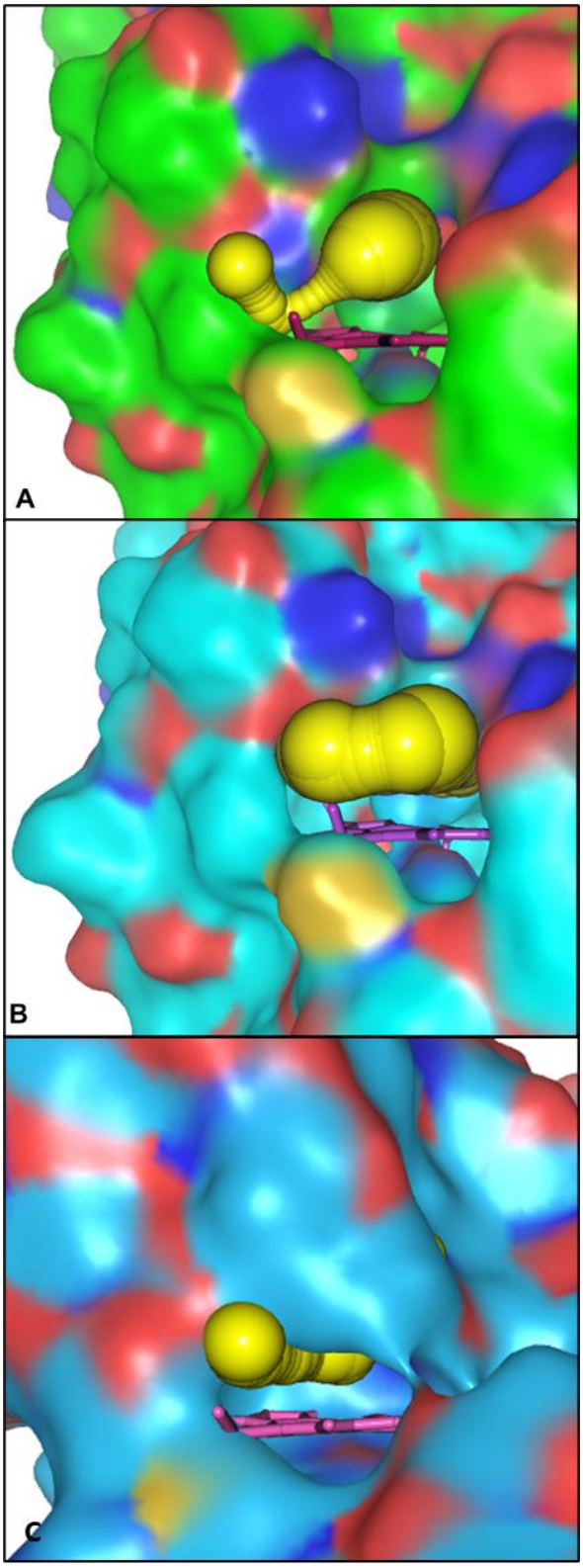

Figure 4.20. Accessibility of the heme in wt *Mc*P460 (A), computer generated simulation of R43A mutant (B) and *Ns*ALP460 (C). Mutating away the Arg 43 residue appears to open up accessibility to the distal pocket. All other mutations did not affect the accessibility to the pocket, however K78R does restrict access to the distal heme face.

The equivalent residue to Asp 102 in *Ne*P460 is Glu 96. This residue is positioned closer to the heme than Asp 102 and thus closer to any ligands bound to the distal face of the heme. It has been suggested that the correct placement of this residue is essential for catalytic activity in *Ne*P460, and that the proton relay needed in catalysis occurs through this residue in *Ne*P460. Experiments with the catalytically inactive *Ns*ALP460 variant showed that mutating the equivalent residue (Ala 131) to Glu did give rise to catalytic activity (although at a reduced rate to wt *Ne*P460) whilst mutation to an Asp resulted in an inactive mutant (A. Smith *et al.*, 2019). However, as *Mc*P460 still has catalytic activity and Asp 102 is positioned slightly further from the heme than Glu 96 it suggests that, if this residue is also involved in the proton relay, there is a looser tolerance in the positioning of this residue in *Mc*P460. Mutating the residue to be more like that of *Ne*P460 (D102E) did not significantly affect the proteins catalytic activity with similar TOFs being seen in comparison to the wt protein. There was however a change in the spectral properties of the protein which became more like those reported for *Ne*P460. As a water molecule can be seen to be bound to the heme in the D102E structure it suggests that the blue shift seen in the as isolated UV-visible spectrum of wt *Mc*P460 in comparison to *Ne*P460 is due to the residues around the heme rather than the presence of water bound to the heme as previously suggested.

The R50A mutation despite being able to bind ligands caused a complete loss of activity suggesting an important role for this residue in the catalytic activity of the protein. There is an arginine (Arg 44) in the same relative position to Arg 50 in *Ne*P460, however where Arg 50 is sitting towards the distal heme face, Arg 44 is turned away by 90° by its CD bond, stopping it from having any interaction with the face of heme or any ligands that may be present in the distal pocket. It does however appear to interact with the 6-β-pyrrolic propionate and helps to promote heme ruffling in *Ne*P460 (Bollmeyer *et al.*, 2023). In *Mc*P460 Arg 50 is positioned so that only the NH1 atom is within hydrogen bonding distance

of the propionate so whilst it may have some effect on stabilising the heme it is unlikely to be as strong an affect as seen in *Ne*P460. This is supported by the lack of movement of the propionate in the R50A structure in comparison to the published *Ns*ALP460 R44A mutant, where the propionate was significantly moved from the wt protein position, so much so that the lysine failed to create a crosslink to the heme. Normal-coordinate structural decomposition (Chapter 2.3.6) showed that the heme of *Mc*P460 was less ruffled than that of *Ne*P460. It also has been shown that *Mc*P460 'ages' and appears to lose its crosslink over time. Both may be due to the lack of a residue in a position to fully stabilise the ruffling of the heme.

The proposed mechanism for oxidation of hydroxylamine by P460 requires the abstraction of two protons to convert the hydroxylamine bound heme from Fe(III)-NH_2OH to $\{FeNO\}^7$ and then a further proton to be removed to convert it to $\{FeNO\}^6$. Under anaerobic conditions a further proton must be abstracted in order to convert the NO bound heme back to the unbound Fe(III) state. This therefore requires residues which are able to act as proton acceptors to be positioned appropriately near to the heme to be able to interact with any bound ligands and also for there to be a route for these protons to be transferred away from the heme and to the bulk solvent surrounding the protein.

In the wt *Mc*P460 hydroxylamine bound structure both Asp 102 and Arg 50 sit in a position to interact with the bound hydroxylamine molecules being 1.96 Å and 2.77 Å away from the bound hydroxylamine molecules respectively. Interestingly this positioning of two residues within distance to interact with any ligands bound to the distal face of the heme is more similar to that seen in HAO. In HAO a conserved pair of His and Asp residues sit to one side of the tyrosine crosslink within distance to interact with bound ligands (Maalcke *et al.*, 2014). It has been suggested that both residues are involved in abstracting protons from hydroxylamine.

Two chains of water molecules were also observed in the *Ne*HAO structure, leading from the aspartate to the solvent filled central channel of the protein, which could assist in the proton transfer between the active site and the surrounding solvent. The high resolution structure of the D102E hydroxylamine bound mutant also shows a series of water molecules leading away from the distal pocket suggesting possible routes for proton transfer between the heme and the surrounding solvent in *Mc*P460 (Figure 4.21 A). One of these possible routes would involve Arg 50 abstracting protons from the bound hydroxylamine molecule (Figure 4.21 B). The transfer of protons would then go through the heme propionate and to a series of water molecules in a channel which leads out to the surface of the protein and the bulk solvent. Various residues (Thr 155, His 156 and Pro 95 of the other monomer) are positioned along the channel so as to be able to stabilise the water molecules. The other possible route involves Glu 102 (Figure 4.21 C) from which the protons could either be transferred directly to a water molecule in the distal pocket which leads straight to the bulk solvent, or through Arg 121 which is within hydrogen bonding distance of several water molecules which again lead straight into the bulk solvent from the open distal pocket. Whilst residue Glu 96 has been proposed to be part of the proton relay in *Ne*P460 the full transfer pathway is yet to be determined.

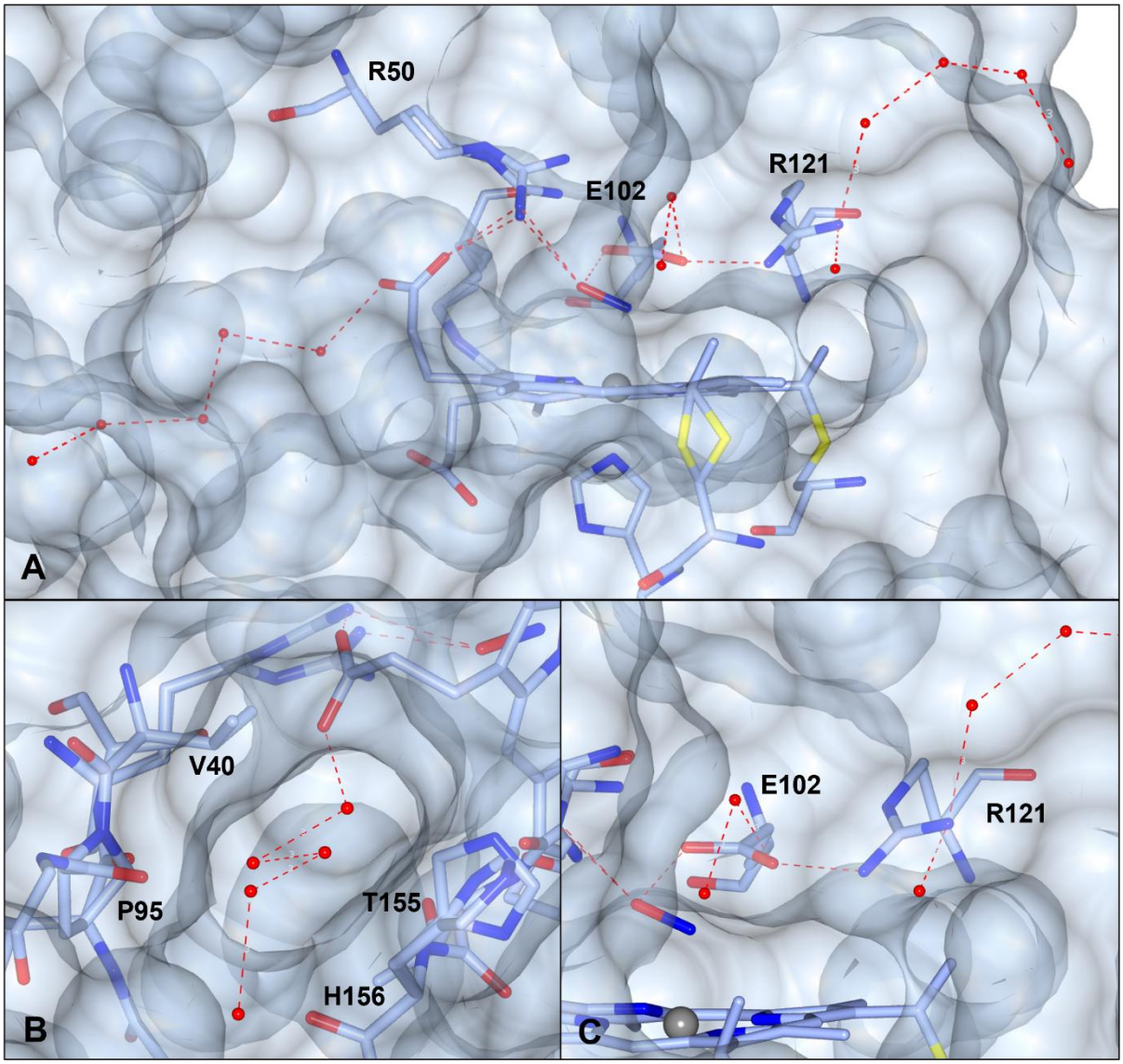

Figure 4.21. Proposed proton relay from the heme of *Mc*P460 to the surface of the protein. Two routes can be seen leading away from the heme (A), one from the propionate and through a small channel which leads out to the bulk solvent (B) and one from E102/R121 straight out of the distal pocket(C)

To confirm the importance of both Arg 50 and Asp 102 further mutants would need to be created. Knocking out Asp 102 (i.e., to Ala) should result in a loss of catalytic activity if both residues are required. Mutation of Arg 50 to either Asp or Glu would test whether any suitably charged residue able to accept protons can be in this position or if there is a finer

tolerance as seen in *Ne*P460 (A. Smith *et al.*, 2019). To further investigate the potential proton relay routes mutants could be created to either block or disrupt the proton relay. An R121A mutant should move the residue out of hydrogen bonding distance of residue 102 and so disrupt the relay in this direction. For the route leading away from the propionate several residues could be mutated to create blocks in the tunnel; Thr 155 (the nearest residue to the propionate) could be mutated to a more bulky hydrophobic residue such as a phenylalanine which might block the water from reaching the propionate or nearer to the entrance of the tunnel Pro 95 from the other monomer of the protein could also be mutated to a phenylalanine to try to block off the entrance and prevent water from the bulk solvent accessing the tunnel. It would also need to be considered if both routes were necessary for the oxidation of hydroxylamine to occur or if catalysis would still be possible with just one of the routes available. With that possibility in mind double mutants would possibly be needed to disrupt both potential proton relays. Due to time restraints none of these mutations were able to be done within this body of work.

Summary

This thesis has characterised the cytochrome *c'*-β and cytochrome P460 from the obligate methanotroph *Methylococcus capsulatus* (Bath) through the use of spectroscopic, crystallographic and kinetic studies. Ligand binding studies and point mutations in each protein has allowed a thorough investigation into each of the protein's ligand binding mechanisms and ability to carry out catalysis of hydroxylamine in the case of *Mc*P460.

Chapter 2 reports on the first published *c'*-β crystal structure. Unlike the better studied cytochromes *c'*-α which are known to have a highly alpha helical structure, it has a highly beta sheet structure much more similar to that of the P460s. Indeed, it can be seen that the overall structure is very similar to that of *Mc*P460 (RMSD 1.6 Å) which is also reported in this chapter. However, whilst these two structures share a similar overall fold their distal pockets are very different. *Mc*CP has two phenylalanine residues sitting over the distal pocket perfectly positioned to occlude ligands entering the pocket whilst the distal pocket of *Mc*P460 consists of many highly charged residues. These differences in distal pocket residues highlights the changes needed in active sites of proteins depending on their reactivity. *Mc*P460 is an enzyme which oxidises hydroxylamine to nitrous oxide and so needs charged residues in positions to interact with ligands to carry out this function. Conversely, whilst the true purpose of *Mc*CP is yet to be determined, it is proposed to be involved in processes such protecting against nitrosoative stress and so needs residues which would allow it to selectively bind and later release ligands.

NSD analysis within this chapter showed the differences in heme distortions between the P460 centre of HAO, *Ne*P460, *Ns*ALP460, *Mc*P460 and *Mc*CP. Heme distortions have been shown to be correlated with the low reduction potentials seen in the P460 family of proteins

and may have an important effect on the activity of the proteins such as being the reason why HAO and P460 avoid auto-reduction upon NO binding. The P460 centre of HAO shows the greatest amount of heme distortions, followed by *Ne*P460, *Ns*ALP460, *Mc*P460 and finally *Mc*CP which demonstrates only a minimal amount of distortion from planarity. This pattern is in keeping with the previously reported reduction potentials for the proteins.

Finally, the chapter looked at the phylogenetic relationship between the cytochromes *c'*α, the cytochromes *c'*-β and cytochromes P460s. Previous studies into the relationship between the cytochromes *c'*-β and cytochromes P460 had only looked at a small number of sequences as much less data was available at the time. A more comprehensive study using the larger databases now available allowed the relationship to be re-evaluated. This study showed that the two cytochrome *c'* families were clearly unrelated. Whilst the two families of proteins appear to carry out similar functions, they have evolved separately from each other. The cytochromes *c'*-β and P460s however do appear to have evolved from a common ancestor, with the cytochromes *c'*-β most likely having evolved from the P460s. This is contrary to what had been previously published but is most likely due to the increased number of sequences available and improved phylogenetic methodologies.

Chapter 3 probes the ligand binding properties of *Mc*CP through the use of spectroscopic, kinetic and crystallographic methods along with point mutations of the two capping phenylalanine residues. Spectroscopically *Mc*CP binds ligands such as CO and NO in a similar manner to the cytochromes *c'*-α. CO was shown to bind in a 6-coordinate manner whilst NO showed a pH dependence with 5cNO being more predominant at low pH whilst 6cNO was more predominant at high pH. This NO coordination pH dependence has been seen in the cytochromes *c'*-α however unlike the cytochromes *c'*-α which can bind NO on both the distal and proximal side of the heme it appears that *Mc*CP only binds NO on the distal side of the heme. All ligand soaked crystal structures show the ligands bound to the

distal face of the heme, whilst RR measurements carried out by collaborators suggested a distally bound ligand regardless of coordination to the heme.

Kinetic studies showed that whilst the Phe cap may provide steric hindrance to larger ligands, small ligands such as NO and CO could quickly and easily bind to the distal face of the heme with initially binding of NO occurring within the dead-time of the stopped flow apparatus suggesting an on rate of $>10^8$ $M^{-1}s^{-1}$. Mutations of either Phe residue of the 'Phe cap' to alanine probed further the interactions of these residues with ligands binding to the distal face of the heme. The structural and spectroscopic data, including RR data from collaborators, suggest that the aromatic quadrupole of Phe 32 interacts with the bound ligands influencing Fe(II)-XO(π*) backbonding.

Chapter 4 explored the distal pocket residues of *Mc*P460 in detail using spectroscopic, crystallographic and kinetic techniques. Whilst there has been much research into *Ne*P460 and its potential mechanism for the catalysis of hydroxylamine there has been very little research done into P460s from ANBs. From the crystal structure determined in Chapter 2 it could be clearly seen that there are different residues present in the distal pocket of *Mc*P460 in comparison to *Ne*P460. In order to ascertain the importance of these residues in the mechanism of hydroxylamine catalysis in *Mc*P460 each residue was mutated to a different amino acid and its properties analysed through crystallographic and spectroscopic means.

One residue which is the same in all catalytically active P460's is the lysine crosslink to the heme. Removal of this crosslink in *Ne*P460 showed a complete loss of activity, and indeed this was also the case for *Mc*P460 when the crosslink was mutated to an arginine residue. The arginine occluded the binding of water to the distal heme in the as isolated state but did not prevent ligand binding upon addition of NO or NH_2OH. This shows that the crosslink is also essential for catalytic activity in *Mc*P460. The K78R mutation also had the interesting effect

of giving rise to peroxidase like activity which is not seen in the wt *Mc*P460 (or any other mutants). This activity is seen however in other members of the P460 family, for example *Ne c'*β-^{met}. Whether this activity is down simply to removal of the lysine crosslink in *Mc*P460 or due to the specific mutation is yet to be tested. Creation of further *Mc*P460 crosslink mutants in the future would help to resolve this question.

In the wt *Mc*P460 crystal structure residue Arg 43, which lies near to the entrance to the distal pocket, was seen to be bound to a molecule of cryoprotectant. This was also true for all high resolution mutant structures. Activity assays also showed that changing the arginine to an alanine increased the catalytic activity of the enzyme. Whilst a crystal structure was not obtained, as correct crystallisation conditions for the mutant were unable to be identified, it would appear that Arg 43 acts as a gatekeeping residue, binding incoming molecules (such as hydroxylamine). A similar effect has been noted in *Ne*P460 with residue Phe 44. This residue is predicted to sit over the distal face of the heme, in a position similar to Phe 32 in *Mc*CP, and in a position to occlude incoming molecules from the distal face of the heme. Mutation of this residue to an alanine also resulted in a slight increase in catalytic activity, however it also resulted in a change in the relative amounts of NO and N_2O produced. The phenylalanine in *Ne*P460 thus appears to play an important role in controlling product selectivity. Currently the product of hydroxylamine oxidation in *Mc*P460 has not be determined. GC-MS analysis of the products from hydroxylamine oxidation of the wt *Mc*P460 and its mutants would help to ascertain if Arg 43in *Mc*P460 carries out a similar role to Phe 44 in *Ne*P460.

Asp 102 lies in a similar position in *Mc*P460 to Glu 96 in *Ne*P460. In *Ne*P460 this residue has been shown to be essential to the catalytic activity of the enzyme. Mutation in *Ne*P460 of Glu 96 to an alanine completely removed the enzyme's ability to oxidise hydroxylamine. Mutation to aspartate, as in *Mc*P460, also removed catalytic activity demonstrating that in *Ne*P460 there was only a fine tolerance for the positioning of residues involved in the

catalytic action of the enzyme. Comparatively, in *Mc*P460 mutation of Asp 102 to Glu resulted in little change to the TOF of the enzyme. Whether this residue is essential to the catalytic activity of the enzyme is yet to be tested however a mutation of Asp 102 to an alanine would answer this question. The final mutation of *Mc*P460 that was looked at within Chapter 4 was that of Arg 50 to Ala. This residue sits on the opposite side of the lysine crosslink to Asp 102 and is positioned within binding distance of any ligands bound to the Fe of the heme on the distal side. Whilst this mutation was able to bind both NO and NH_2OH all catalytic activity was lost suggesting that Arg 50 plays an important role in the oxidation of hydroxylamine in *Mc*P460.

The high resolution structure of the D102E mutant revealed a tunnel containing a chain of water molecules which lead from the propionate nearest to Arg 50 to the external solvent suggesting a possible proton relay route. It is feasible that protons could be abstracted via Arg 50, through the propionate and into the water filled channel. Indeed, in the ligand bound structures show that hydroxylamine is within distance to react with Arg 50 which is itself within a suitable distance to react with the propionate. Mutation of Arg 50 to Ala moves the residue too far away for these interactions to occur thus breaking the relay. Further research is needed into this potential proton relay route to determine if this is indeed part of the mechanism of hydroxylamine oxidation in *Mc*P460. Mutations to block the channel for example could help to determine how essential it is to the mechanism. It is also possible that *Mc*P460 could behave like the P460 centre of HAO which has been shown to have a His-Asp pair which abstract protons from the bound hydroxylamine. It may be that both residues Arg 50 and Asp 102 are needed for catalysis in *Mc*P460. Again, the previously mentioned mutation of D102A would help to investigate if this was the case.

The great variation of distal pocket residues in the P460 Family of proteins suggests that they may have wider range of functions that first thought and so much more work is to be done to understand what selection of distal pocket residues give rise to which functions.

References

Abendroth, J. *et al.* (2022) 'Structural Characterization of Cytochrome c'β-Met from an Ammonia-Oxidizing Bacterium', *Biochemistry*, 61(7), pp. 563–574. Available at: https://doi.org/10.1021/acs.biochem.1c00640.

Adams, H.R. *et al.* (2019) 'One fold, two functions: cytochrome P460 and cytochrome c '-β from the methanotroph Methylococcus capsulatus (Bath)', *Chemical Science*, 10(10), pp. 3031–3041. Available at: https://doi.org/10.1039/C8SC05210G.

Adams, H.R. *et al.* (2023) 'A heme pocket aromatic quadrupole modulates gas binding to cytochrome c'-β: Implications for NO sensors', *Journal of Biological Chemistry*, 299(6). Available at: https://doi.org/10.1016/j.jbc.2023.104742.

Ambler, R.P. *et al.* (1981) 'Amino Acid Sequences of Bacterial Cytochromes c' and c-556', *Proceedings of the National Academy of Sciences of the United States of America*, 78(11), pp. 6854–6857.

Ambler, R.P. *et al.* (1986) 'The amino acid sequence of cytochrome c-555 from the methane-oxidizing bacterium Methylococcus capsulatus', *Biochemical Journal*, 233(2), pp. 333–337. Available at: https://doi.org/10.1042/bj2330333.

Ambler, R.P. (1991) 'Sequence variability in bacterial cytochromes c', *Biochimica et biophysica acta*, 1058(1), pp. 42–47. Available at: https://doi.org/10.1016/s0005-2728(05)80266-x.

Andersson, K.K., Babcock, G.T. and Hooper, A.B. (1991) 'P460 of hydroxylamine oxidoreductase of Nitrosomonas europaea: Soret resonance Raman evidence for a novel heme-like structure', *Biochemical and Biophysical Research Communications*, 174(1), pp. 358–363. Available at: https://doi.org/10.1016/0006-291X(91)90528-F.

Andrew, C.R. *et al.* (2001) 'Resonance Raman Studies of Cytochrome c' Support the Binding of NO and CO to Opposite Sides of the Heme: Implications for Ligand Discrimination in Heme-Based Sensors', *Biochemistry*, 40(13), pp. 4115–4122. Available at: https://doi.org/10.1021/bi0023652.

Andrew, C.R. *et al.* (2005) 'Accessibility of the Distal Heme Face, Rather than Fe−His Bond Strength, Determines the Heme-Nitrosyl Coordination Number of Cytochromes c': Evidence from Spectroscopic Studies', *Biochemistry*, 44(24), pp. 8664–8672. Available at: https://doi.org/10.1021/bi050428g.

Antonyuk, S.V. *et al.* (2011) 'Carbon monoxide poisoning is prevented by the energy costs of conformational changes in gas-binding haemproteins', *Proceedings of the National Academy of Sciences of the United States of America*, 108(38), pp. 15780–15785. Available at: https://doi.org/10.1073/pnas.1109051108.

Arciero, D.M. and Hooper, A.B. (1993) 'Hydroxylamine oxidoreductase from Nitrosomonas europaea is a multimer of an octa-heme subunit', *Journal of Biological Chemistry*, 268(20), pp. 14645–14654. Available at: https://doi.org/10.1016/S0021-9258(18)82382-1.

Arciero, D.M. and Hooper, A.B. (1997) 'Evidence for a crosslink between c-heme and a lysine residue in cytochrome P460 of Nitrosomonas europaea', *FEBS Letters*, 410(2), pp. 457–460. Available at: https://doi.org/10.1016/S0014-5793(97)00635-2.

Arslan, E. *et al.* (1998) 'Overproduction of theBradyrhizobium japonicum c-Type Cytochrome Subunits of thecbb3Oxidase inEscherichia coli', *Biochemical and Biophysical Research Communications*, 251(3), pp. 744–747. Available at: https://doi.org/10.1006/bbrc.1998.9549.

A. Smith, M. *et al.* (2019) 'Controlling a burn: outer-sphere gating of hydroxylamine oxidation by a distal base in cytochrome P460', *Chemical Science*, 10(13), pp. 3756–3764. Available at: https://doi.org/10.1039/C9SC00195F.

Benini, S. *et al.* (2008) 'High resolution crystal structure of Rubrivivax gelatinosus cytochrome c'', *Journal of Inorganic Biochemistry*, 102(5), pp. 1322–1328. Available at: https://doi.org/10.1016/j.jinorgbio.2008.01.017.

Benning, M.M., Meyer, T.E. and Holden, H.M. (1996) 'Molecular Structure of a High Potential Cytochrome c2 Isolated from Rhodopila globiformis'.

Bergmann, D.J. *et al.* (1998) 'Cytochrome P460 Genes from the Methanotroph *Methylococcus capsulatus* Bath', *Journal of Bacteriology*, 180(24), pp. 6440–6445. Available at: https://doi.org/10.1128/JB.180.24.6440-6445.1998.

Bergmann, D.J. and Hooper, A.B. (1994) 'The primary structure of cytochrome P460 of Nitrosomonas europaea: Presence of a c-heme binding motif', *FEBS Letters*, 353(3), pp. 324–326. Available at: https://doi.org/10.1016/0014-5793(94)01072-2.

Bergmann, D.J. and Hooper, A.B. (2003) 'Cytochrome P460 of Nitrosomonas europaea', *European Journal of Biochemistry*, 270(9), pp. 1935–1941. Available at: https://doi.org/10.1046/j.1432-1033.2003.03550.x.

Bergmann, D.J., Zahn, J.A. and DiSpirito, A.A. (2000) 'Primary structure of cytochrome c' of Methylococcus capsulatus Bath: evidence of a phylogenetic link between P460 and c'-type cytochromes', *Archives of Microbiology*, 173(1), pp. 29–34. Available at: https://doi.org/10.1007/s002030050004.

Bollmeyer, M.M. *et al.* (2023) 'Cytochrome P460 Cofactor Maturation Proceeds via Peroxide-Dependent Post-translational Modification', *Journal of the American Chemical Society*, 145(26), pp. 14404–14416. Available at: https://doi.org/10.1021/jacs.3c03608.

Bowman, S.E.J. and Bren, K.L. (2008) 'The chemistry and biochemistry of hemec: functional bases for covalent attachment', *Natural Product Reports*, 25(6), pp. 1118–1130. Available at: https://doi.org/10.1039/B717196J.

Capella-Gutiérrez, S., Silla-Martínez, J.M. and Gabaldón, T. (2009) 'trimAl: a tool for automated alignment trimming in large-scale phylogenetic analyses', *Bioinformatics*, 25(15), pp. 1972–1973. Available at: https://doi.org/10.1093/bioinformatics/btp348.

Caranto, J.D. and Lancaster, K.M. (2017) 'Nitric oxide is an obligate bacterial nitrification intermediate produced by hydroxylamine oxidoreductase', *Proceedings of the National Academy of Sciences*, 114(31), pp. 8217–8222. Available at: https://doi.org/10.1073/pnas.1704504114.

Caranto, J.D., Vilbert, A.C. and Lancaster, K.M. (2016) 'Nitrosomonas europaea cytochrome P460 is a direct link between nitrification and nitrous oxide emission', *Proceedings of the National Academy of Sciences*, 113(51), pp. 14704–14709. Available at: https://doi.org/10.1073/pnas.1611051113.

Cedervall, P., Hooper, A.B. and Wilmot, C.M. (2013) 'Structural Studies of Hydroxylamine Oxidoreductase Reveal a Unique Heme Cofactor and a Previously Unidentified Interaction Partner', *Biochemistry*, 52(36), pp. 6211–6218. Available at: https://doi.org/10.1021/bi400960w.

Chen, V.B. *et al.* (2010) 'MolProbity: all-atom structure validation for macromolecular crystallography', *Acta Crystallographica Section D: Biological Crystallography*, 66(1), pp. 12–21. Available at: https://doi.org/10.1107/S0907444909042073.

Cohen, S.X. *et al.* (2008) 'ARP/wARP and molecular replacement: the next generation', *Acta Crystallographica Section D: Biological Crystallography*, 64(1), pp. 49–60. Available at: https://doi.org/10.1107/S0907444907047580.

Coleman, R.E. and Lancaster, K.M. (2020) 'Heme P460: A (Cross) Link to Nitric Oxide', *Accounts of Chemical Research*, 53(12), pp. 2925–2935. Available at: https://doi.org/10.1021/acs.accounts.0c00573.

Coleman, R.E., Vilbert, A.C. and Lancaster, K.M. (2020) 'The Heme–Lys Cross-Link in Cytochrome P460 Promotes Catalysis by Enforcing Secondary Coordination Sphere Architecture', *Biochemistry*, 59(24), pp. 2289–2298. Available at: https://doi.org/10.1021/acs.biochem.0c00261.

Cowtan, K. (2006) 'The Buccaneer software for automated model building. 1. Tracing protein chains', *Acta Crystallographica Section D: Biological Crystallography*, 62(9), pp. 1002–1011. Available at: https://doi.org/10.1107/S0907444906022116.

Cross, R. *et al.* (2000) 'Cytochrome c' from Rhodobacter capsulatus Confers Increased Resistance to Nitric Oxide', *Journal of Bacteriology*, 182(5), pp. 1442–1447. Available at: https://doi.org/10.1128/jb.182.5.1442-1447.2000.

C. Vilbert, A., D. Caranto, J. and M. Lancaster, K. (2018) 'Influences of the heme-lysine crosslink in cytochrome P460 over redox catalysis and nitric oxide sensitivity', *Chemical Science*, 9(2), pp. 368–379. Available at: https://doi.org/10.1039/C7SC03450D.

Dobbs, A.J. *et al.* (1996) 'Three-Dimensional Structure of Cytochrome c' from Two Alcaligenes Species and the Implications for Four-Helix Bundle Structures', *Acta Crystallographica Section D: Biological Crystallography*, 52(2), pp. 356–368. Available at: https://doi.org/10.1107/S0907444995008328.

Dunford, H.B. (2010) *Peroxidases and Catalases: Biochemistry, Biophysics, Biotechnology and Physiology*. John Wiley & Sons.

Duprat, A.F. *et al.* (1995) 'Myoglobin-NO at Low pH: Free Four-Coordinated Heme in the Protein Pocket', *Biochemistry*, 34(8), pp. 2634–2644. Available at: https://doi.org/10.1021/bi00008a030.

Elmore, B.O. *et al.* (2006) 'Expression, purification, crystallization and preliminary X-ray diffraction of a novel Nitrosomonas europaea cytochrome, cytochrome P460', *Acta Crystallographica Section F: Structural Biology and Crystallization Communications*, 62(4), pp. 395–398. Available at: https://doi.org/10.1107/S1744309106008785.

Elmore, B.O. *et al.* (2007) 'Cytochromes P460 and c'-beta; A new family of high-spin cytochromes c', *FEBS Letters*, 581(5), pp. 911–916. Available at: https://doi.org/10.1016/j.febslet.2007.01.068.

Elsliger, M.-A. *et al.* (2010) 'The JCSG high-throughput structural biology pipeline', *Acta Crystallographica Section F: Structural Biology and Crystallization Communications*, 66(10), pp. 1137–1142. Available at: https://doi.org/10.1107/S1744309110038212.

Emsley, P. *et al.* (2010) 'Features and development of Coot', *Acta Crystallographica Section D: Biological Crystallography*, 66(4), pp. 486–501. Available at: https://doi.org/10.1107/S0907444910007493.

Erickson, R.H. and Hooper, A.B. (1972) 'Preliminary characterization of a variant co-binding heme protein from Nitrosomonas', *Biochimica et Biophysica Acta (BBA) - Bioenergetics*, 275(2), pp. 231–244. Available at: https://doi.org/10.1016/0005-2728(72)90044-8.

Evans, P.R. and Murshudov, G.N. (2013) 'How good are my data and what is the resolution?', *Acta Crystallographica Section D: Biological Crystallography*, 69(7), pp. 1204–1214. Available at: https://doi.org/10.1107/S0907444913000061.

Fernández, M.L., Estrin, D.A. and Bari, S.E. (2008) 'Theoretical insight into the hydroxylamine oxidoreductase mechanism', *Journal of Inorganic Biochemistry*, 102(7), pp. 1523–1530. Available at: https://doi.org/10.1016/j.jinorgbio.2008.01.032.

Finzel, B.C. *et al.* (1985) 'Structure of ferricytochrome c' from Rhodospirillum molischianum at 1.67 Å resolution', *Journal of Molecular Biology*, 186(3), pp. 627–643. Available at: https://doi.org/10.1016/0022-2836(85)90135-4.

Frear, D.S. and Burrell, R.C. (1955) 'Spectrophotometric Method for Determining Hydroxylamine Reductase Activity in Higher Plants', *Analytical Chemistry*, 27(10), pp. 1664–1665. Available at: https://doi.org/10.1021/ac60106a054.

Graves, A.B., Graves, M.T. and Liptak, M.D. (2016) 'Measurement of Heme Ruffling Changes in MhuD Using UV–vis Spectroscopy', *The Journal of Physical Chemistry B*, 120(16), pp. 3844–3853. Available at: https://doi.org/10.1021/acs.jpcb.6b01497.

Hanson, R.S. *et al.* (1991) 'The obigate methanotrophic bacteria Methylococcus, Methylomonas, Methylosinus and related bacteria', *The Prokaryotes*, pp. 271–275.

Hendrich, M.P. *et al.* (2001) 'Correlations of Structure and Electronic Properties from EPR Spectroscopy of Hydroxylamine Oxidoreductase', *Journal of the American Chemical Society*, 123(13), pp. 2997–3005. Available at: https://doi.org/10.1021/ja002982d.

Hirano, Y. *et al.* (2012) 'Structure Analysis and Comparative Characterization of the Cytochrome c' and Flavocytochrome c from Thermophilic Purple Photosynthetic Bacterium Thermochromatium tepidum', *Biochemistry*, 51(33), pp. 6556–6567. Available at: https://doi.org/10.1021/bi3005522.

Hooper, A.B. and Nason, A. (1965) 'Characterization of Hydroxylamine-Cytochrome c Reductase from the Chemoautotrophs Nitrosomonas europaea and Nitrosocystis oceanus', *Journal of Biological Chemistry*, 240(10), pp. 4044–4057. Available at: https://doi.org/10.1016/S0021-9258(18)97148-6.

Hooper, A.B. and Terry, K.R. (1979) 'Hydroxylamine oxidoreductase of Nitrosomonas: Production of nitric oxide from hydroxylamine', *Biochimica et Biophysica Acta (BBA) - Enzymology*, 571(1), pp. 12–20. Available at: https://doi.org/10.1016/0005-2744(79)90220-1.

Hough, M.A. *et al.* (2011) 'Distal-to-Proximal NO Conversion in Hemoproteins: The Role of the Proximal Pocket', *Journal of Molecular Biology*, 405(2), pp. 395–409. Available at: https://doi.org/10.1016/j.jmb.2010.10.035.

Hough, M.A. and Andrew, C.R. (2015) 'Chapter One - Cytochromes c': Structure, Reactivity and Relevance to Haem-Based Gas Sensing', in R.K. Poole (ed.) *Advances in Microbial Physiology*. Academic Press (Recent Advances in Microbial Oxygen-Binding Proteins), pp. 1–84. Available at: https://doi.org/10.1016/bs.ampbs.2015.08.001.

Igarashi, N. *et al.* (1997) 'The 2.8 Å structure of hydroxylamine oxidoreductase from a nitrifying chemoautotrophic bacterium, Nitrosomonas europaea', *Nature Structural Biology*, 4(4), pp. 276–284. Available at: https://doi.org/10.1038/nsb0497-276.

Jancarik, J. and Kim, S.H. (1991) 'Sparse-matrix sampling a nic acid synthase and uroporphyrinogen methylase: two key control enzymes of tetrapyrrole biosynthesis and modification, Ciba screening method for crystallization of proteins', *J. Appl. Crystallogr*, 24, p. 409411.

Jentzen, W., Song, X.-Z. and Shelnutt, J.A. (1997) 'Structural Characterization of Synthetic and Protein-Bound Porphyrins in Terms of the Lowest-Frequency Normal Coordinates of the Macrocycle', *The Journal of Physical Chemistry B*, 101(9), pp. 1684–1699. Available at: https://doi.org/10.1021/jp963142h.

Jurcik, A. *et al.* (2018) 'CAVER Analyst 2.0: analysis and visualization of channels and tunnels in protein structures and molecular dynamics trajectories', *Bioinformatics*, 34(20), pp. 3586–3588. Available at: https://doi.org/10.1093/bioinformatics/bty386.

Kabsch, W. (2010) 'XDS', *Acta Crystallographica Section D: Biological Crystallography*, 66(2), pp. 125–132. Available at: https://doi.org/10.1107/S0907444909047337.

Kamen, M.D. and Vernon, L.P. (1954) 'EXISTENCE OF HAEM COMPOUNDS IN A PHOTOSYNTHETIC OBLIGATE ANAEROBE', *Journal of Bacteriology*, 67(5), pp. 617–618. Available at: https://doi.org/10.1128/jb.67.5.617-618.1954.

Kang, Y. *et al.* (2019) 'Structural insights into the mechanism of human soluble guanylate cyclase', *Nature*, 574(7777), pp. 206–210. Available at: https://doi.org/10.1038/s41586-019-1584-6.

Keilin, D. (1925) 'On Cytochrome, a Respiratory Pigment, Common to Animals, Yeast, and Higher Plants', *Proceedings of the Royal Society of London. Series B, Containing Papers of a Biological Character*, 98(690), pp. 312–339.

Kekilli, D. *et al.* (2014) 'Fingerprinting redox and ligand states in haemprotein crystal structures using resonance Raman spectroscopy', *Acta Crystallographica Section D: Biological Crystallography*, 70(5), pp. 1289–1296. Available at: https://doi.org/10.1107/S1399004714004039.

Kekilli, D. *et al.* (2017) 'Engineering proximal vs. distal heme–NO coordination via dinitrosyl dynamics: implications for NO sensor design', *Chemical Science*, 8(3), pp. 1986–1994. Available at: https://doi.org/10.1039/C6SC04190F.

Klarskov, K. *et al.* (1998) 'Ligand Binding and Covalent Structure of an Oxygen-Binding Heme Protein from Rhodobacter sphaeroides, a Representative of a New Structural Family of c-Type Cytochromes', *Biochemistry*, 37(17), pp. 5995–6002. Available at: https://doi.org/10.1021/bi972498w.

Kleingardner, J.G., Bowman, S.E.J. and Bren, K.L. (2013) 'The Influence of Heme Ruffling on Spin Densities in Ferricytochromes c Probed by Heme Core 13C NMR', *Inorganic Chemistry*, 52(22), pp. 12933–12946. Available at: https://doi.org/10.1021/ic401250d.

Kumar, S., Stecher, G. and Tamura, K. (2016) 'MEGA7: Molecular Evolutionary Genetics Analysis Version 7.0 for Bigger Datasets', *Molecular Biology and Evolution*, 33(7), pp. 1870–1874. Available at: https://doi.org/10.1093/molbev/msw054.

Kuypers, M.M.M., Marchant, H.K. and Kartal, B. (2018) 'The microbial nitrogen-cycling network', *Nature Reviews Microbiology*, 16(5), pp. 263–276. Available at: https://doi.org/10.1038/nrmicro.2018.9.

Larkin, M.A. *et al.* (2007) 'Clustal W and Clustal X version 2.0', *Bioinformatics*, 23(21), pp. 2947–2948. Available at: https://doi.org/10.1093/bioinformatics/btm404.

Lawson, D.M. *et al.* (2003) 'A two-faced molecule offers NO explanation: the proximal binding of nitric oxide to haem', *Biochemical Society Transactions*, 31(Pt 3), pp. 553–557. Available at: https://doi.org/10.1042/bst0310553.

Li, T., Bonkovsky, H.L. and Guo, J. (2011) 'Structural analysis of heme proteins: implications for design and prediction', *BMC Structural Biology*, 11(1), p. 13. Available at: https://doi.org/10.1186/1472-6807-11-13.

Liebschner, D. *et al.* (2019) 'Macromolecular structure determination using X-rays, neutrons and electrons: recent developments in Phenix', *Acta Crystallographica. Section D, Structural Biology*, 75(Pt 10), pp. 861–877. Available at: https://doi.org/10.1107/S2059798319011471.

Liew, F.N. *et al.* (2020) 'Cytochrome c'β-Met Is a Variant in the P460 Superfamily Lacking the Heme–Lysyl Cross-Link: A Peroxidase Mimic Generating a Ferryl Intermediate', *Biochemistry*, 59(5), pp. 704–716. Available at: https://doi.org/10.1021/acs.biochem.9b00810.

Liptak, M.D., Wen, X. and Bren, K.L. (2010) 'NMR and DFT Investigation of Heme Ruffling: Functional Implications for Cytochrome c', *Journal of the American Chemical Society*, 132(28), pp. 9753–9763. Available at: https://doi.org/10.1021/ja102098p.

Liu, J. *et al.* (2014) *Metalloproteins Containing Cytochrome, Iron–Sulfur, or Copper Redox Centers | Chemical Reviews*. Available at: https://pubs.acs.org/doi/full/10.1021/cr400479b (Accessed: 13 September 2023).

Liu, X. *et al.* (1996) 'Induction of Apoptotic Program in Cell-Free Extracts: Requirement for dATP and Cytochrome c', *Cell*, 86(1), pp. 147–157. Available at: https://doi.org/10.1016/S0092-8674(00)80085-9.

Ma, X. *et al.* (2007) 'NO and CO differentially activate soluble guanylyl cyclase via a heme pivot-bend mechanism', *The EMBO Journal*, 26(2), pp. 578–588. Available at: https://doi.org/10.1038/sj.emboj.7601521.

Maalcke, W.J. *et al.* (2014) 'Structural Basis of Biological NO Generation by Octaheme Oxidoreductases *', *Journal of Biological Chemistry*, 289(3), pp. 1228–1242. Available at: https://doi.org/10.1074/jbc.M113.525147.

MacMunn, C.A. (1884) *On myohaematin, an intrinsic muscle-pigment of vertebrates and invertebrates, on histohaematin, and on the spectrum of the supra-renal bodies*.

Manole, A. *et al.* (2015) 'Conformational control of the binding of diatomic gases to cytochrome c'', *JBIC Journal of Biological Inorganic Chemistry*, 20(4), pp. 675–686. Available at: https://doi.org/10.1007/s00775-015-1253-7.

M. Bollmeyer, M. *et al.* (2023) 'Outer coordination sphere influences on cofactor maturation and substrate oxidation by cytochrome P460', *Chemical Science*, 14(31), pp. 8295–8304. Available at: https://doi.org/10.1039/D3SC02288A.

Mcpherson, A. (2001) 'A comparison of salts for the crystallization of macromolecules', *Protein Science : A Publication of the Protein Society*, 10(2), pp. 418–422.

Mense, S.M. and Zhang, L. (2006) 'Heme: a versatile signaling molecule controlling the activities of diverse regulators ranging from transcription factors to MAP kinases', *Cell Research*, 16(8), pp. 681–692. Available at: https://doi.org/10.1038/sj.cr.7310086.

Miller David, J., Wood Paul, M. and Nicholas, D.J.D. (1984) 'Further Characterization of Cytochrome P-460 in Nitrosomonas europaea', *Microbiology*, 130(11), pp. 3049–3054. Available at: https://doi.org/10.1099/00221287-130-11-3049.

Murshudov, G.N. *et al.* (2011) 'REFMAC5 for the refinement of macromolecular crystal structures', *Acta Crystallographica Section D: Biological Crystallography*, 67(4), pp. 355–367. Available at: https://doi.org/10.1107/S0907444911001314.

Nazaries, L. *et al.* (2013) 'Methane, microbes and models: fundamental understanding of the soil methane cycle for future predictions', *Environmental Microbiology*, 15(9), pp. 2395–2417. Available at: https://doi.org/10.1111/1462-2920.12149.

Numata, M. *et al.* (1990) 'Cytochrome P-460 of *Nitrosomonas europaea*: Further Purification and Further Characterization', *The Journal of Biochemistry*, 108(6), pp. 1016–1021.

Page, R. *et al.* (2003) 'Shotgun crystallization strategy for structural genomics: an optimized two-tiered crystallization screen against the Thermotoga maritima proteome', *Acta Crystallographica Section D: Biological Crystallography*, 59(6), pp. 1028–1037. Available at: https://doi.org/10.1107/S0907444903007790.

Panjikar, S. *et al.* (2005) 'Auto-Rickshaw: an automated crystal structure determination platform as an efficient tool for the validation of an X-ray diffraction experiment', *Acta Crystallographica Section D: Biological Crystallography*, 61(4), pp. 449–457. Available at: https://doi.org/10.1107/S0907444905001307.

Paoli, M., Marles-Wright, J. and Smith, A. (2002) 'Structure–Function Relationships in Heme-Proteins', *DNA and Cell Biology*, 21(4), pp. 271–280. Available at: https://doi.org/10.1089/104454902753759690.

Pearson, A.R. *et al.* (2007) 'The Crystal Structure of Cytochrome P460 of Nitrosomonas europaea Reveals a Novel Cytochrome Fold and Heme−Protein Cross-link', *Biochemistry*, 46(28), pp. 8340–8349. Available at: https://doi.org/10.1021/bi700086r.

Poret-Peterson, A.T. *et al.* (2008) 'Transcription of nitrification genes by the methane-oxidizing bacterium, Methylococcus capsulatus strain Bath', *The ISME Journal*, 2(12), pp. 1213–1220. Available at: https://doi.org/10.1038/ismej.2008.71.

Radaev, S., Li, S. and Sun, P.D. (2006) 'A survey of protein-protein complex crystallizations', *Acta Crystallographica. Section D, Biological Crystallography*, 62(Pt 6), pp. 605–612. Available at: https://doi.org/10.1107/S0907444906011735.

Ramirez, L.M. *et al.* (2003) 'High resolution crystal structure of ferricytochrome c' from Rhodobacter sphaeroides', *Journal of Chemical Crystallography*, 33(5), pp. 413–424. Available at: https://doi.org/10.1023/A:1024286215637.

Rockström, J. *et al.* (2009) 'A safe operating space for humanity', *Nature*, 461(7263), pp. 472–475. Available at: https://doi.org/10.1038/461472a.

Shibata, N. *et al.* (1998) 'Basis for monomer stabilization in Rhodopseudomonas palustris cytochrome c' derived from the crystal structure1 1Edited by R. Huber', *Journal of Molecular Biology*, 284(3), pp. 751–760. Available at: https://doi.org/10.1006/jmbi.1998.2190.

Smith, M.A. and Lancaster, K.M. (2018) 'The Eponymous Cofactors in Cytochrome P460s from Ammonia-Oxidizing Bacteria Are Iron Porphyrinoids Whose Macrocycles Are Dibasic', *Biochemistry*, 57(3), pp. 334–343. Available at: https://doi.org/10.1021/acs.biochem.7b00921.

Soler-Jofra, A., Pérez, J. and van Loosdrecht, M.C.M. (2021) 'Hydroxylamine and the nitrogen cycle: A review', *Water Research*, 190, p. 116723. Available at: https://doi.org/10.1016/j.watres.2020.116723.

Stamatakis, A., Hoover, P. and Rougemont, J. (2008) 'A Rapid Bootstrap Algorithm for the RAxML Web Servers', *Systematic Biology*, 57(5), pp. 758–771. Available at: https://doi.org/10.1080/10635150802429642.

Sun, J. *et al.* (2002) 'Hemoprotein Bach1 regulates enhancer availability of heme oxygenase-1 gene', *The EMBO Journal*, 21(19), pp. 5216–5224. Available at: https://doi.org/10.1093/emboj/cdf516.

Tahirov, T.H. *et al.* (1996) 'High-resolution Crystal Structures of Two Polymorphs of Cytochromec' from the Purple Phototrophic BacteriumRhodobacter capsulatus', *Journal of Molecular Biology*, 259(3), pp. 467–479. Available at: https://doi.org/10.1006/jmbi.1996.0333.

Trotsenko, Y.A. and Murrell, J.C. (2008) 'Metabolic aspects of aerobic obligate methanotrophy', *Advances in Applied Microbiology*, 63, pp. 183–229. Available at: https://doi.org/10.1016/S0065-2164(07)00005-6.

Watmough, N.J. *et al.* (1999) 'Nitric oxide in bacteria: synthesis and consumption', *Biochimica et Biophysica Acta - Bioenergetics*, 1411(2–3), pp. 456–474. Available at: https://doi.org/10.1016/S0005-2728(99)00032-8.

Weber, P.C. *et al.* (1980) 'Structure of cytochrome c': a dimeric, high-spin haem protein', *Nature*, 286(5770), pp. 302–304. Available at: https://doi.org/10.1038/286302a0.

Weitz, S.H. *et al.* (2014) 'Processing of microRNA primary transcripts requires heme in mammalian cells', *Proceedings of the National Academy of Sciences*, 111(5), pp. 1861–1866. Available at: https://doi.org/10.1073/pnas.1309915111.

Whittenbury, R. and Dalton, H. (1981) 'The Methylotrophic Bacteria', in M.P. Starr et al. (eds) *The Prokaryotes: A Handbook on Habitats, Isolation, and Identification of Bacteria*. Berlin, Heidelberg: Springer, pp. 894–902. Available at: https://doi.org/10.1007/978-3-662-13187-9_71.

Williamson, G. and Engel, P.C. (1984) 'Butyryl-CoA dehydrogenase from Megasphaera elsdenii. Specificity of the catalytic reaction', *Biochemical Journal*, 218(2), pp. 521–529. Available at: https://doi.org/10.1042/bj2180521.

Wooh, J.W. *et al.* (2003) 'Comparison of three commercial sparse-matrix crystallization screens', *Acta Crystallographica Section D: Biological Crystallography*, 59(4), pp. 769–772. Available at: https://doi.org/10.1107/S0907444903002919.

Wuebbles, D.J. (2009) 'Atmosphere. Nitrous oxide: no laughing matter', *Science (New York, N.Y.)*, 326(5949), pp. 56–57. Available at: https://doi.org/10.1126/science.1179571.

Yasui, M. *et al.* (1992) 'Three-Dimensional Structure of Ferricytochrome c' from Rhodospirillum rubrum at 2.8 Å Resolution', *The Journal of Biochemistry*, 111(3), pp. 317–324. Available at: https://doi.org/10.1093/oxfordjournals.jbchem.a123756.

Yoshimi, T. *et al.* (2022) 'Crystal structure of thermally stable homodimeric cytochrome c'-β from Thermus thermophilus', *Acta Crystallographica Section F: Structural Biology Communications*, 78(6), pp. 217–225. Available at: https://doi.org/10.1107/S2053230X22005088.

Yoshimura, T. *et al.* (1985) 'Identification of heme axial ligands of cytochrome c' from Alcaligenes sp. N.C.I.B. 11015', *Biochimica et Biophysica Acta (BBA) - Protein Structure and Molecular Enzymology*, 831(3), pp. 267–274. Available at: https://doi.org/10.1016/0167-4838(85)90106-2.

Yoshimura, T. *et al.* (1988) 'Nitric Oxide Complex of Cytochrome c' in Cells of Denitrifying Bacteria', *The Journal of Biochemistry*, 103(6), pp. 1016–1019. Available at: https://doi.org/10.1093/oxfordjournals.jbchem.a122372.

Yoshimura, T. *et al.* (1993) 'Five coordinated nitrosylhemoprotein in the whole cells of denitrifying bacterium, Achromobacter xylosoxidans NCIB 11015', *Archives of Microbiology*, 160(6), pp. 498–500. Available at: https://doi.org/10.1007/BF00245312.

Zahn, J.A. *et al.* (1996) 'Cytochrome c' of Methylococcus Capsulatus Bath', *European Journal of Biochemistry*, 240(3), pp. 684–691. Available at: https://doi.org/10.1111/j.1432-1033.1996.0684h.x.

Zahn, J.A., Duncan, C. and DiSpirito, A.A. (1994) 'Oxidation of hydroxylamine by cytochrome P-460 of the obligate methylotroph Methylococcus capsulatus Bath', *Journal of Bacteriology*, 176(19), pp. 5879–5887. Available at: https://doi.org/10.1128/jb.176.19.5879-5887.1994.

Appendix A

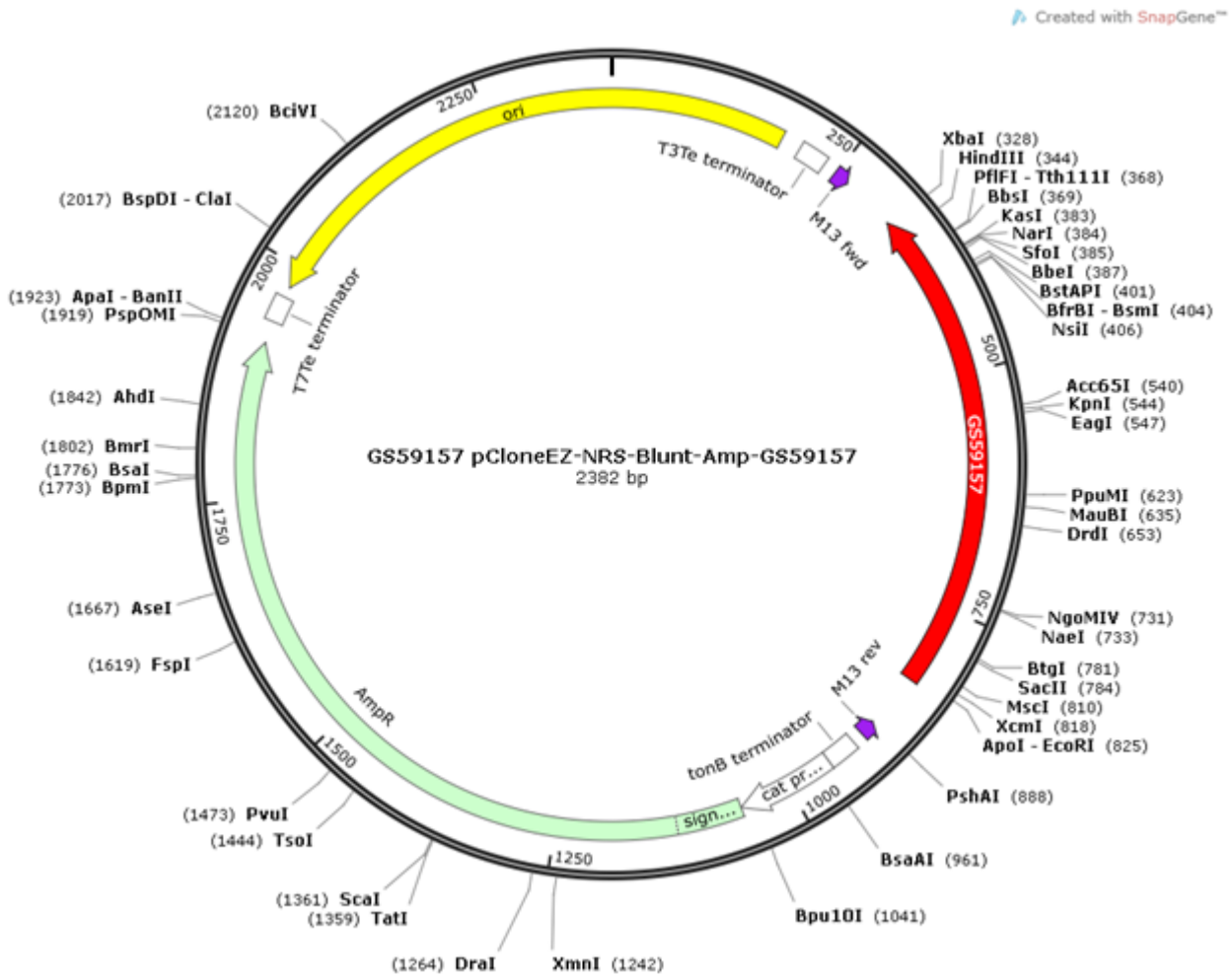

Figure A.1. *Mc*P460 cloning plasmid map. Gene for P460 is shown in red with *XbaI* and *EcoRI* restriction site at either end.

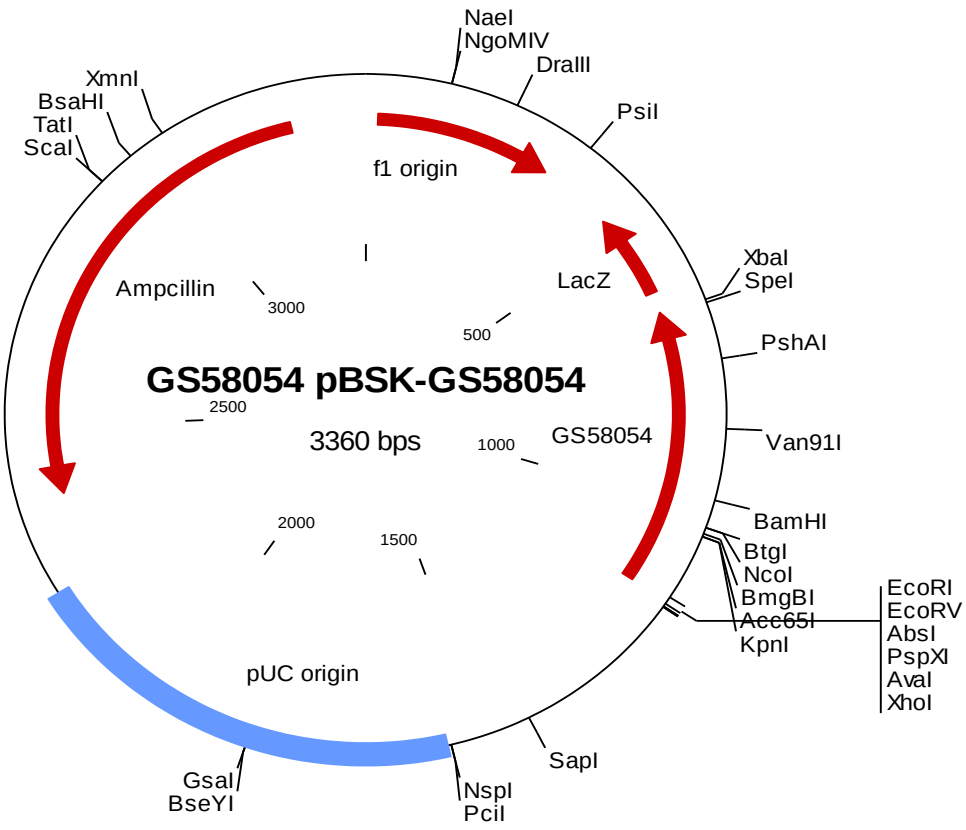

Figure A.2. *Mc*CP cloning plasmid map. Gene for *Mc*CP is shown in red and labelled as GS58054 with *XbaI* and *EcoRI* restriction site at either end.

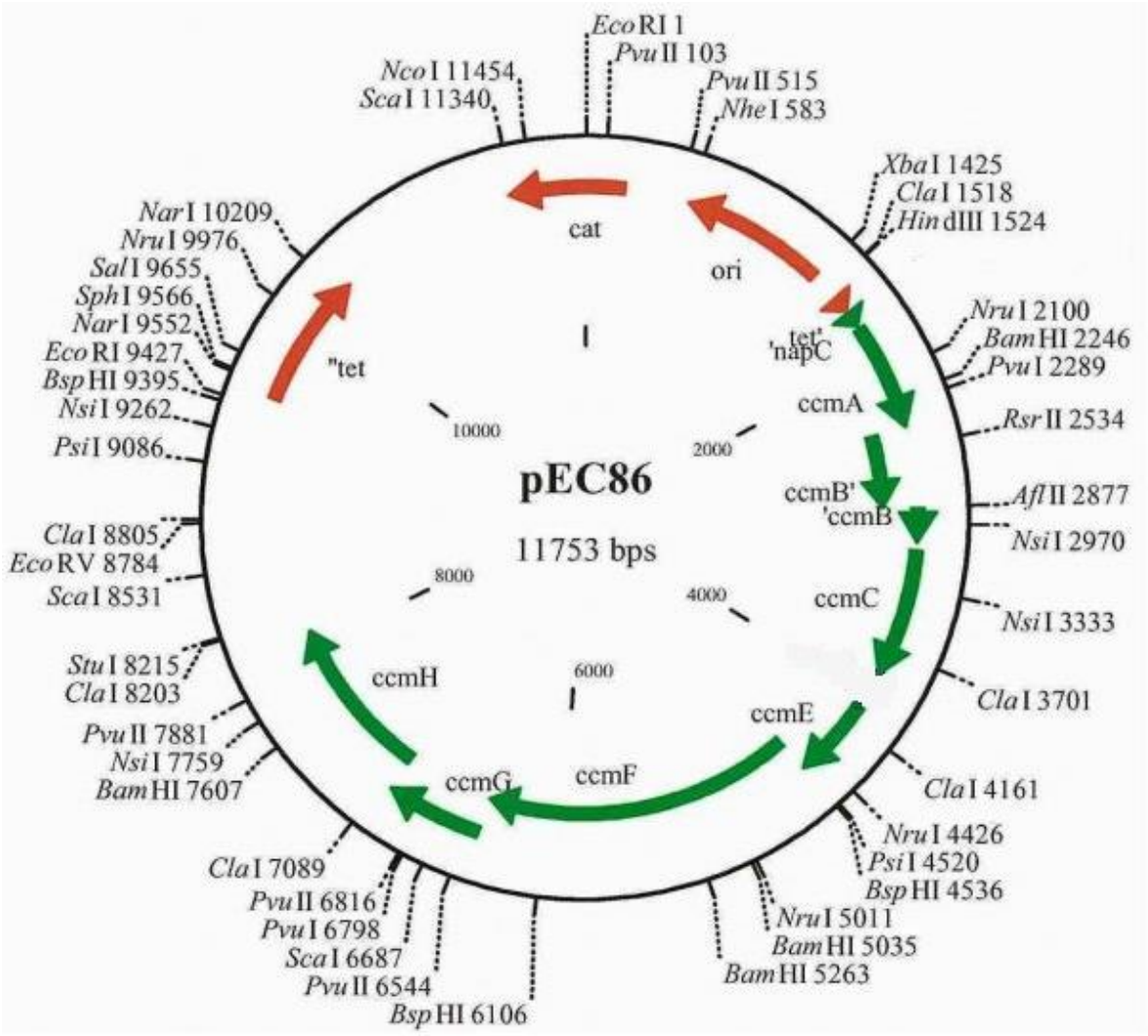

Figure A.3. pEC86 plasmid map.

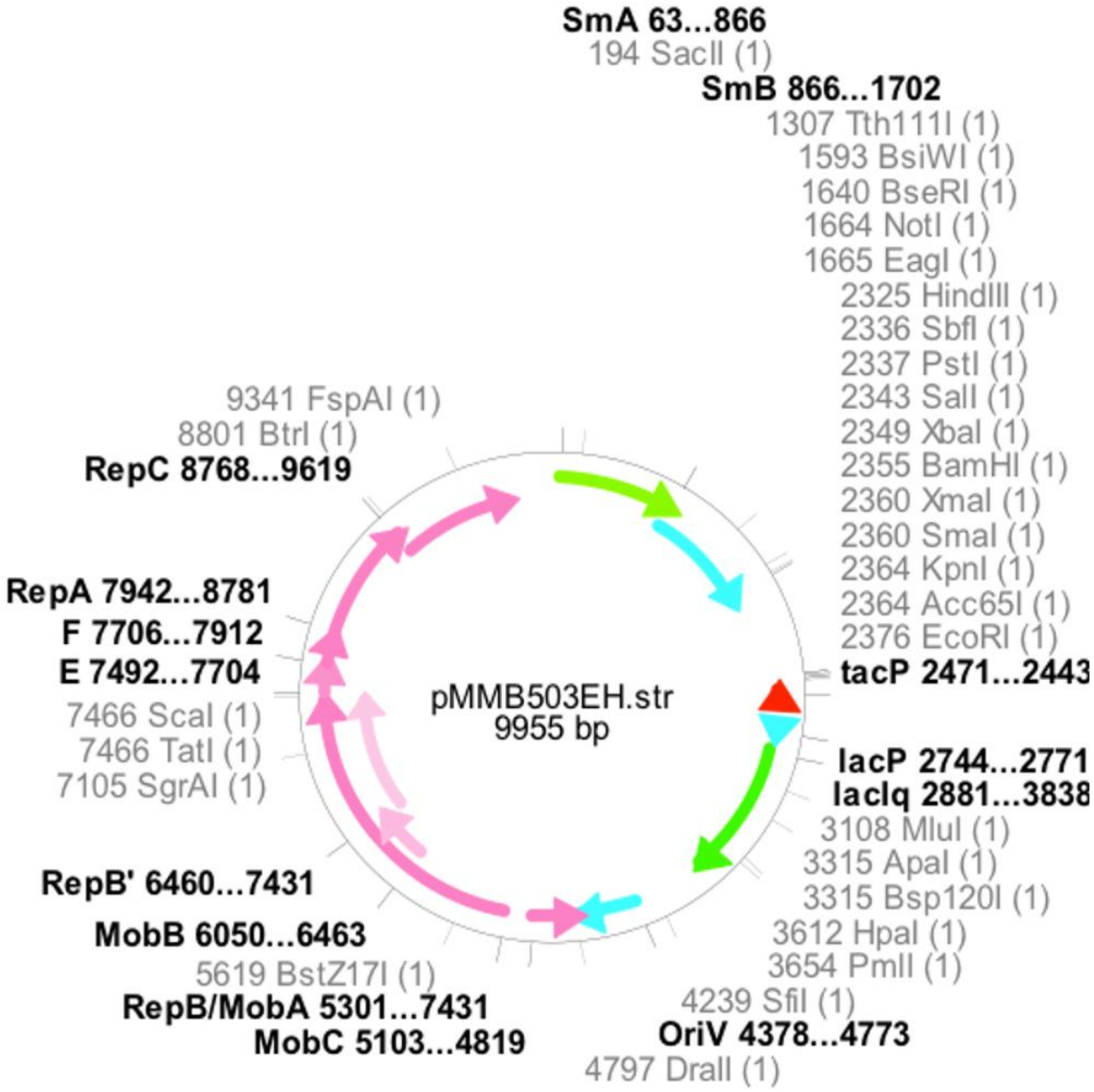

Figure A.4. pMMB503EH plasmid map.

Table A.1. Primers for *Mc*CP and *Mc*P460 mutations.

Mutant	Protein	Primer 5'-3'	Length (bp)	GC(%)	Tm (°C)
F32V Forward	*Mc*CP	GAA AAT CCC GTT GGC GGG ATC CAC	24	58	68.5
F32V Reverse		GTG GAT CCC GCC AAC GGG ATT TTC	24	58	68.5
F61V Forward	*Mc*CP	GTG TTG GTA GTT GAC CTG TTC GAC	24	50	65.2
F61V Reverse		GTC GAA CAG GTC ACC TAC CAA CAC	24	54	65.2
R43A Forward	*Mc*P460	GTT TCC TCA GCT ATC GAG CAG AAC	24	50	65.2
R43A Reverse		GTT CTG CTC GAT AGC TGA GAA AAC	24	50	65.2
R50A Forward	*Mc*P460	CAG AAC AAT TTG GCT GCG ATC CTC	24	50	65.2
R50A Reverse		GAG GAT CGC AGC CAA ATT GTT CTG	24	50	65.2
K78R Forward	*Mc*P460	GCG ATT CTG GTC AGA CTG TCG	21	57	63.2
K78R Reverse		CGA CAG TCT GAC CAG AAT CGC	21	57	63.2
D102E Forward	*Mc*P460	TTC ACC CAG GCC GAA TTC ATG GTC	24	54.1	66.9
D102E Reverse		GAC CAT GAA TTC GGC CTG GGT GAA	24	54.1	66.9

Table A.2. PCR Reaction Components

Component	**Manufacturer**	**Concentration**	**Quantity**
Template DNA		100 ng	1 ul
Forward Primer	Sigma	125 ng	1 ul
Reverse Primer	Sigma	125 ng	1 ul
10x Reaction Buffer	Agilent	1 x	5 ul
QuikChange Lightening Enzyme	Agilent	1 U	1 ul
dNTPs	Agilent	10 mM	1 ul
QuikSolution Reagent	Agilent		1.5 ul
Nuclease Free Water	Fisher		38.5 ul

Table A.3. PCR Reaction Settings

Step	**Cycles**	**Temperature**	**Duration**
Initial Denaturation	1	95 °C	2 minutes
Denaturation	18	95 °C	20 seconds
Annealing		Tm of primers	10 seconds
Extension		68 °C	1.5 minutes
Final Extension	1	68 °C	5 minutes
		4 °C	hold

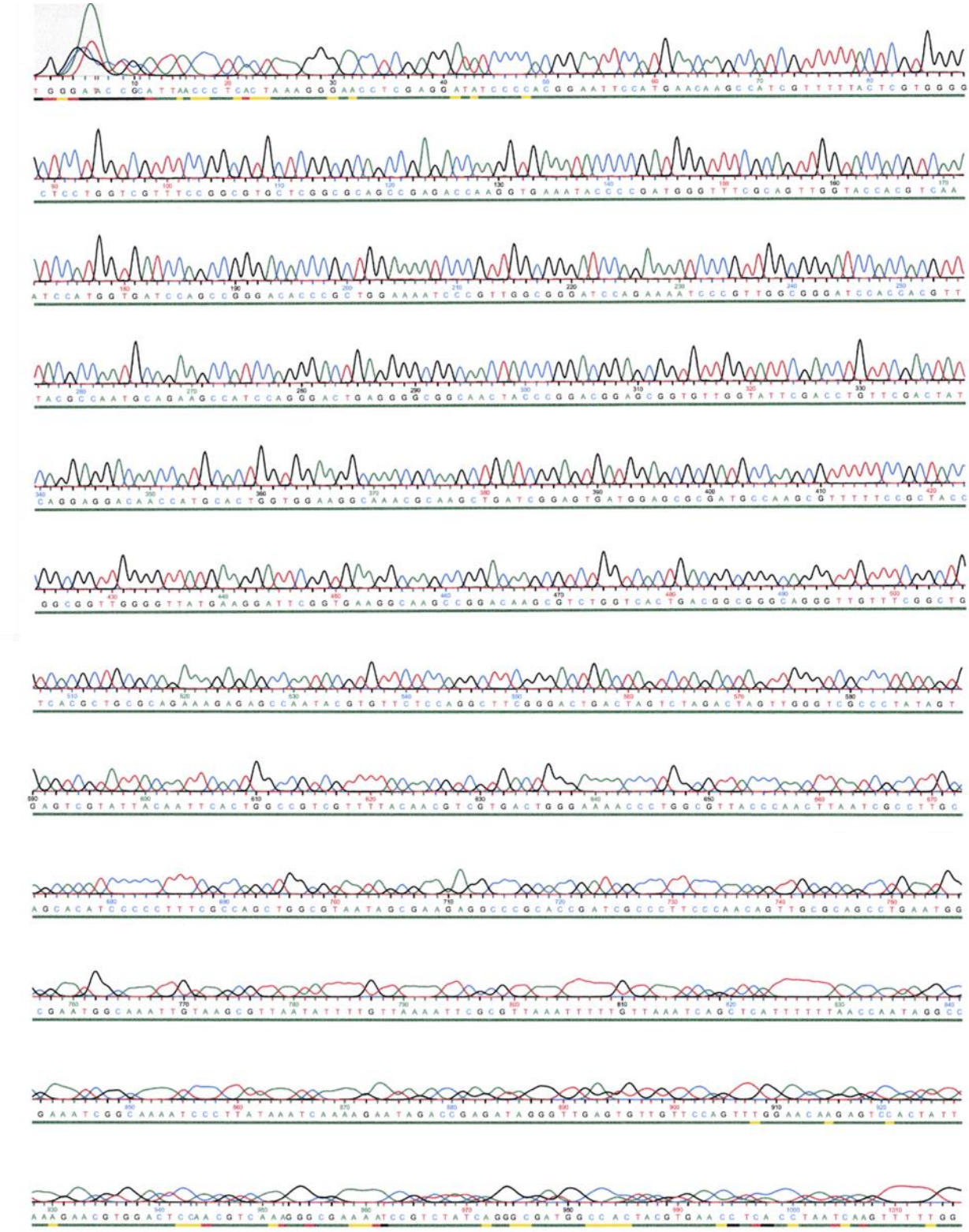

Figure A.5. Sequencing results showing the presence mutation F32V in *Mc*CP

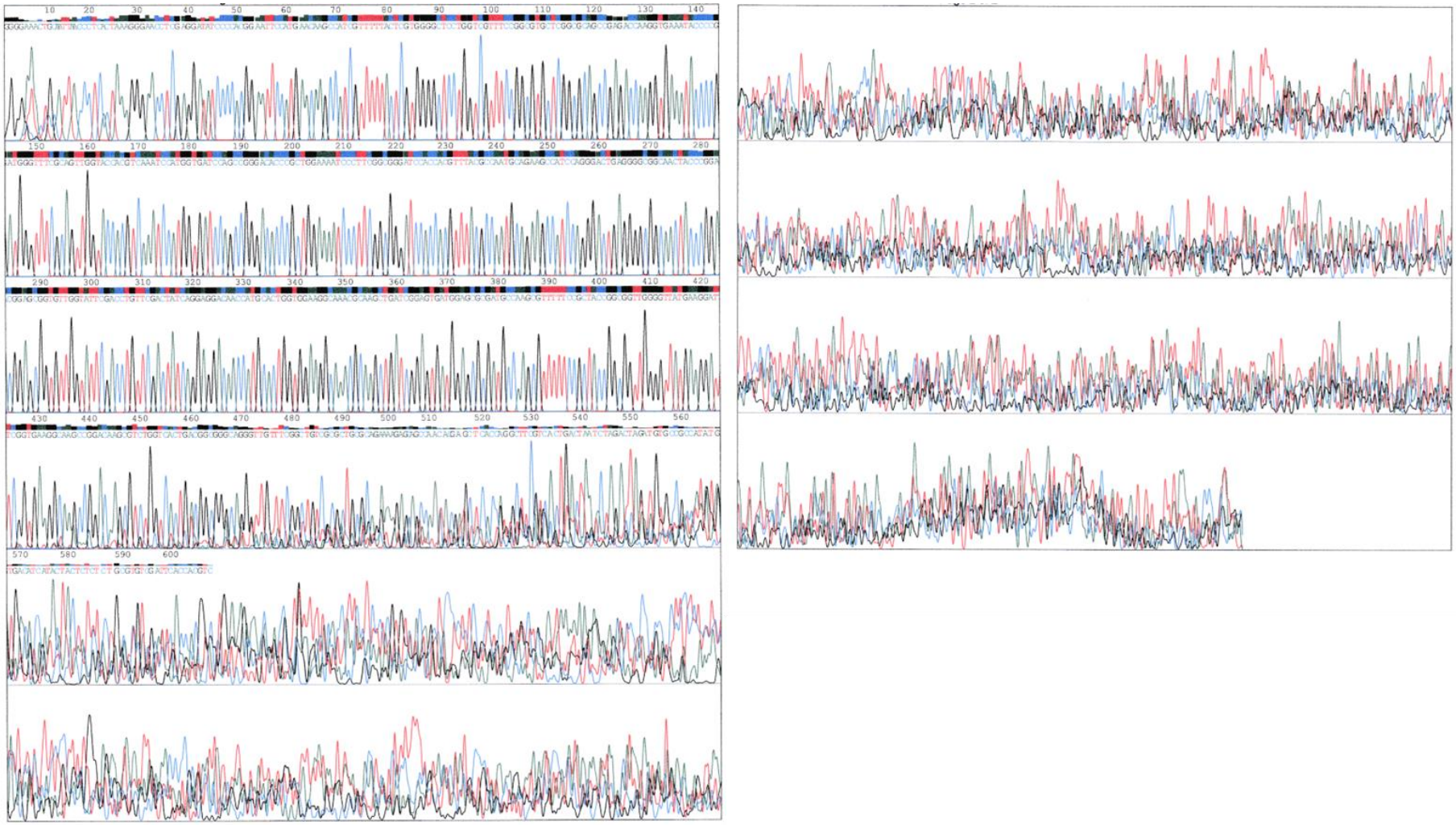

Figure A.6. Sequencing results showing the presence mutation F61V in *Mc*CP

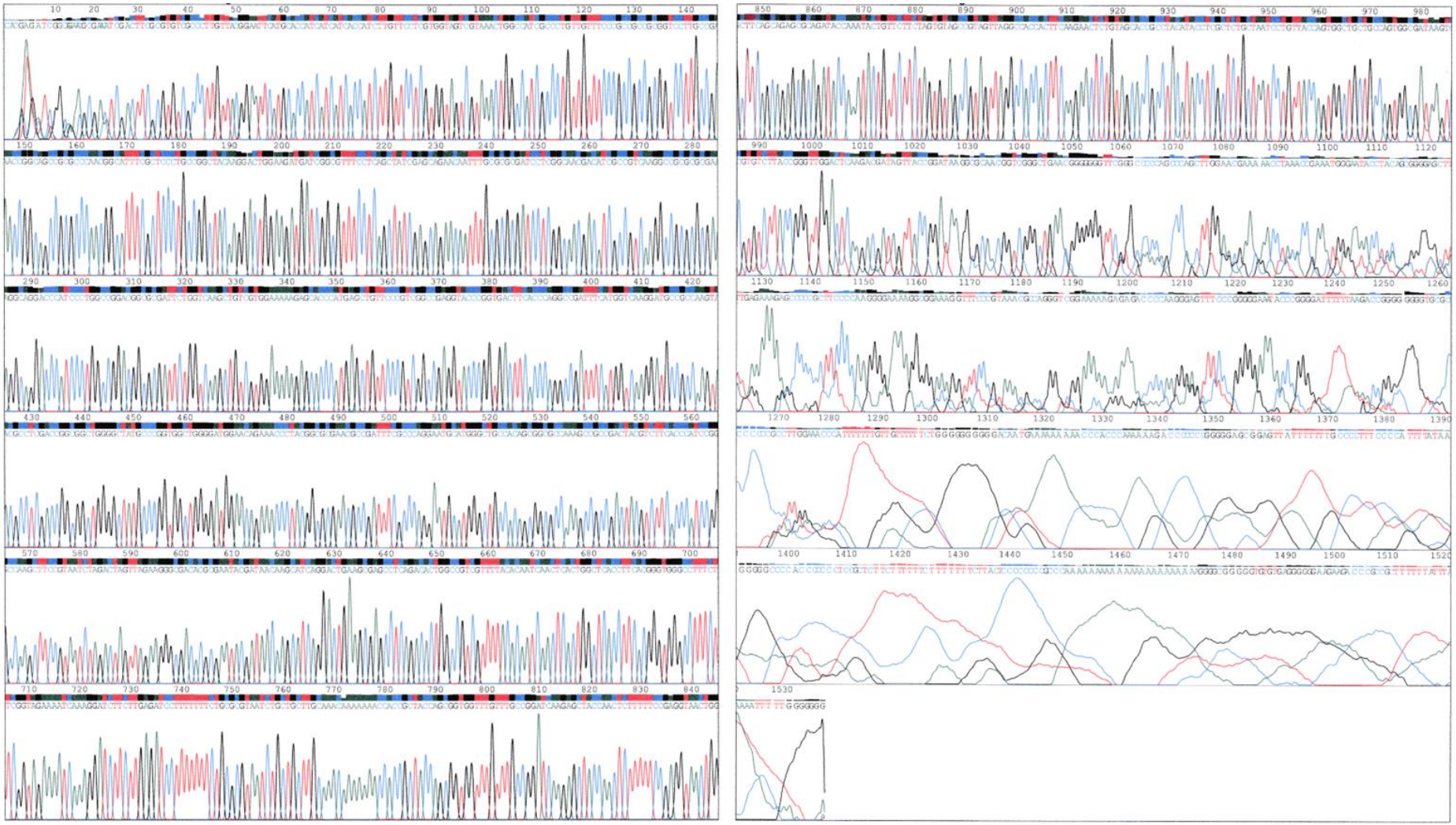

Figure A.7. Sequencing results showing the presence mutation R43A in *Mc*P460

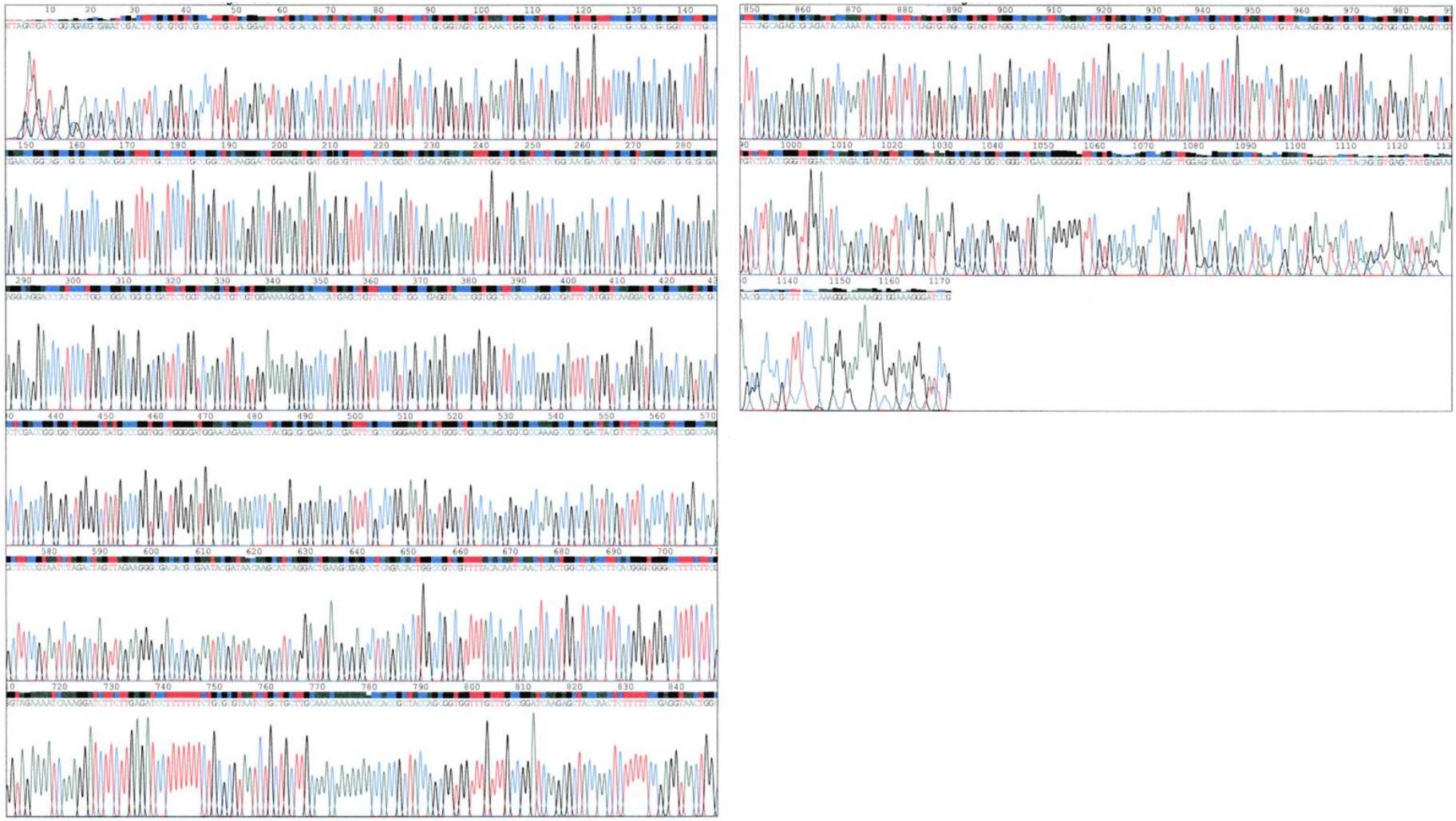

Figure A.8. Sequencing results showing the presence mutation R50A in *Mc*P460

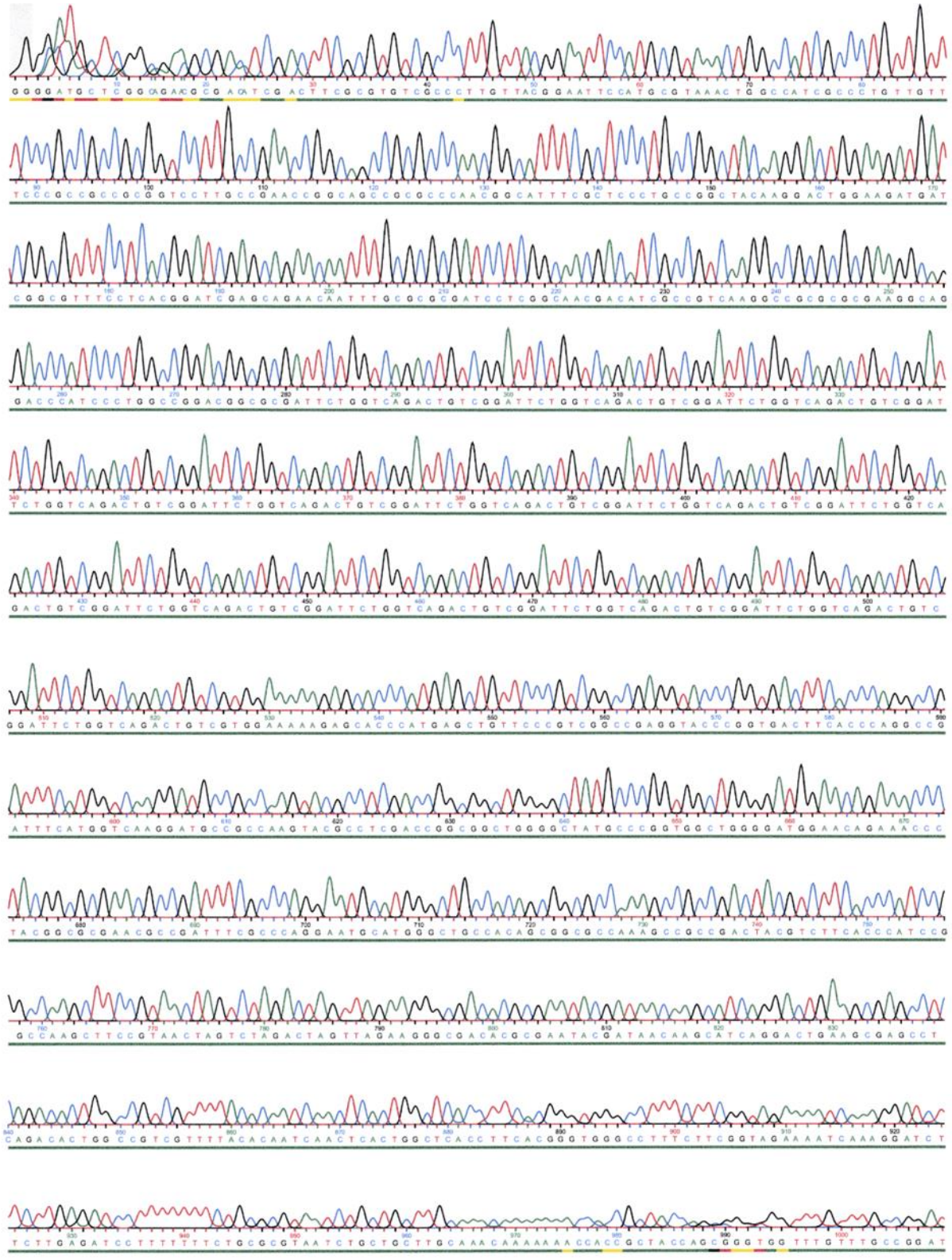

Figure A.9. Sequencing results showing the presence mutation K78R in *Mc*P460

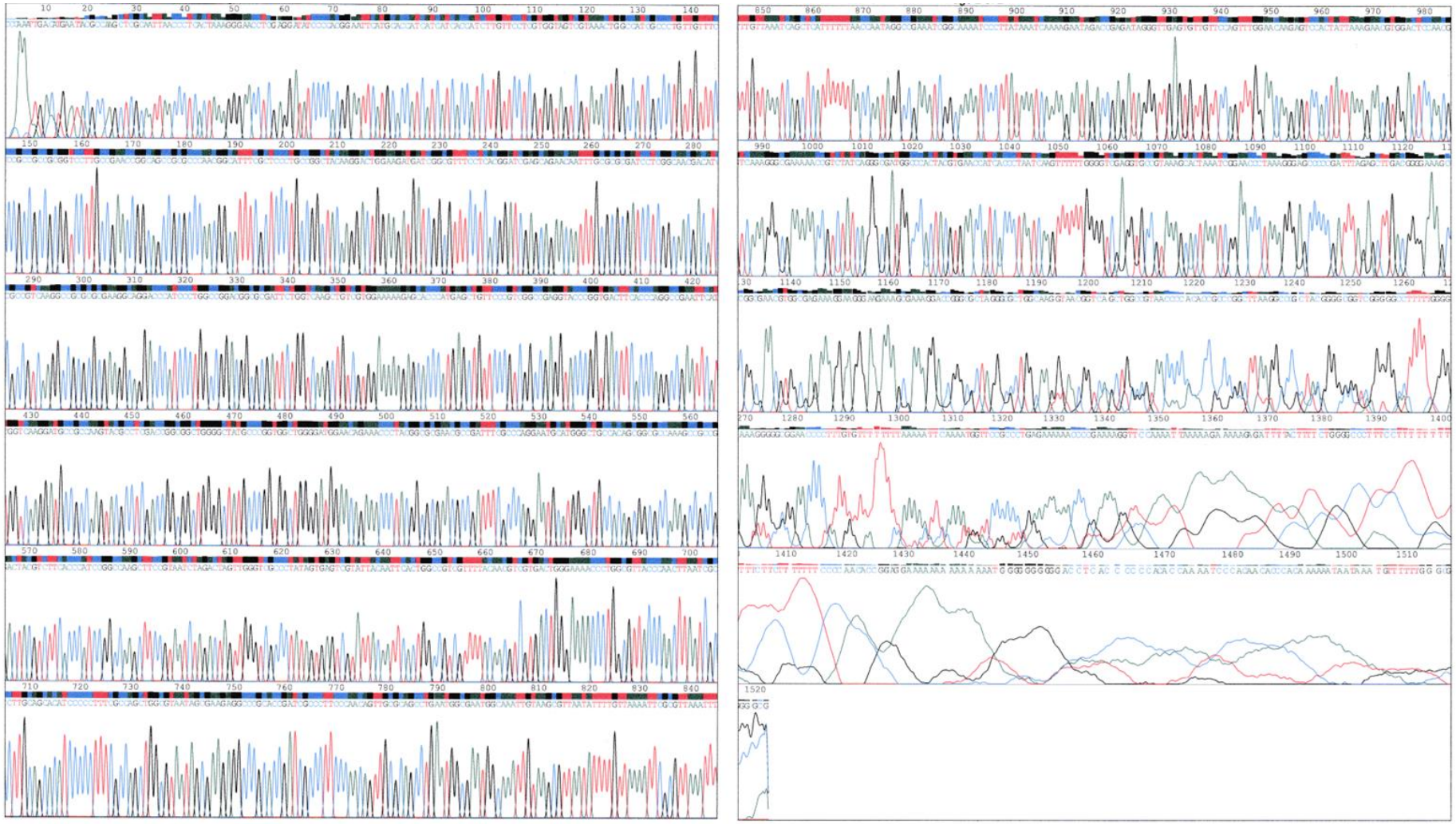

Figure A.10. Sequencing results showing the presence mutation D102E in *Mc*P460